NATIONAL AERONAUTICS AND SPACE ADMINISTRATION

Space Programs Summary 37-56, Vol. II

The Deep Space Network

For the Period January 1 to February 28, 1969

RECEIVED
JUN 27 1969
DEPT. OF AERONAUTICAL AND
ASTRONAUTICAL ENGINEERING
THE OHIO STATE UNIVERSITY

JET PROPULSION LABORATORY
CALIFORNIA INSTITUTE OF TECHNOLOGY
PASADENA, CALIFORNIA

March 31, 1969

NATIONAL AERONAUTICS AND SPACE ADMINISTRATION

Space Programs Summary 37-56, Vol. II

The Deep Space Network

For the Period January 1 to February 28, 1969

JET PROPULSION LABORATORY
CALIFORNIA INSTITUTE OF TECHNOLOGY
PASADENA, CALIFORNIA

March 31, 1969

SPACE PROGRAMS SUMMARY 37-56, VOL. II

Copyright © 1969
Jet Propulsion Laboratory
California Institute of Technology

Prepared Under Contract No. NAS 7-100
National Aeronautics and Space Administration

Preface

The Space Programs Summary is a multivolume, bimonthly publication that presents a review of technical information resulting from current engineering and scientific work performed, or managed, by the Jet Propulsion Laboratory for the National Aeronautics and Space Administration. The Space Programs Summary is currently composed of four volumes:

Vol. I. *Flight Projects* (Unclassified)

Vol. II. *The Deep Space Network* (Unclassified)

Vol. III. *Supporting Research and Advanced Development* (Unclassified)

Vol. IV. *Flight Projects and Supporting Research and Advanced Development* (Confidential)

Foreword

Volume II of the Space Programs Summary reports the results of work performed by the Deep Space Network (DSN). Information is presented, as appropriate, in the following categories:

Introduction
- Description of the DSN
- Description of DSN Systems

Mission Support
- Interplanetary Flight Projects
- Planetary Flight Projects
- Manned Space Flight Project
- Advanced Flight Projects

Advanced Engineering
- Tracking and Navigational Accuracy Analysis
- Communications System Research
- Communications Elements Research
- Supporting Research and Technology

Development and Implementation
- Space Flight Operations Facility Development
- Ground Communications Facility Development
- Deep Space Instrumentation Facility Development
- DSN Project and System Development

Operations and Facilities
- DSN Operations
- Space Flight Operations Facility Operations
- Ground Communications Facility Operations
- Deep Space Instrumentation Facility Operations
- Facility Engineering

In each issue, the section entitled "Description of DSN Systems" reports the current configuration of one of the six DSN systems (tracking, telemetry, command, monitoring, simulation, and operations control). The fundamental research carried out in support of the DSN is reported in Vol. III.

Contents

I. Introduction 1

A. Description of the DSN 1

B. Description of DSN Systems 3

1. Command System
W. J. Kinder and E. C. Gatz 3

II. Mission Support 9

A. Interplanetary Flight Projects 9

1. *Pioneer VIII* Mission Support
A. J. Siegmeth 9

B. Planetary Flight Projects 29

1. *Mariner* Mars 1971 Mission Support
D. J. Mudgway 29

C. Manned Space Flight Project 35

1. *Apollo* Mission Support
P. S. Goodwin 35

III. Advanced Engineering 43

A. Tracking and Navigational Accuracy Analysis 43

1. Introduction
T. W. Hamilton and D. W. Trask 43

2. DSS Location Solutions for Deep Space Missions, Using *Mariner IV*, *Mariner V*, and *Pioneer VII* Data
N. A. Mottinger 45

3. Comparison of Ionospheric Measurements for Evaluation of Techniques Used in Charged Particle Calibration of Radio Tracking Data, Preliminary Results
B. D. Mulhall and R. N. Wimberly 58

4. Charged Particle Effects to Radio Ranging and Doppler Tracking Signals in a Radially Outflowing Solar Wind
L. Efron and R. J. Lisowski 61

5. A Study of Polar Motion and Earthquakes for the Period 1904–1966
C. C. Chao and P. M. Muller 69

6. Lunar Landed *Surveyor*: SPODP Lunar Libration Sensitivities
F. B. Winn 74

7. The Capability of Estimating the Earth Gravitational Constant Through the Tracking of Synchronous Satellites
G. E. Pease 80

Contents (contd)

8. The Sensitivity Matrix Method for Orbit Determination Error Analysis, With Application to a Mars Orbiter
S. R. McReynolds 85

9. The Influence of Range Measurements on the State Information Contained in a Few Passes of Counted Doppler Data
J. F. Jordan 87

B. Communications Systems Research 90

1. Communication Statistics: Confidence Intervals for Probabilities Associated With the Normal Distribution
I. Eisenberger 90

2. Digital Telemetry and Command: Cycle Slipping in the Second-Order Loop With Limiting
R. C. Tausworthe 94

3. Digital Telemetry and Command: Steady-State Phase Probability Density of Cascaded Phase-Locked Loops
W. C. Lindsey 97

4. Information Systems: Efficiency of S/N Ratio Estimator
G. Lorden 98

C. Tracking and Data Acquisition Elements Research 101

1. Low-Noise Receivers: Microwave Maser Development
R. Berwin, R. Clauss, and E. Wiebe 101

2. Design of an Operational Atomic Hydrogen Frequency Standard
H. Erpenbach and C. Finnie 105

3. Improved RF Calibration Techniques: Scattering Matrix of a Reduced Multiport
T. Y. Otoshi 107

4. Improved RF Calibration Techniques: Operating Noise Temperature Calibrations of the JPL Research Cones
C. T. Stelzried 110

5. X- and K-Band Anechoic Antenna Range
D. E. Neff and S. A. Brunstein 113

6. *Pioneer* VI Solar Faraday Rotation Occultation Experiment
T. Sato and C. T. Stelzried 115

D. Supporting Research and Technology 115

1. Accuracy of Single Precision Univac 1108 Subroutine Library Functions
C. J. Devine, Jr., and C. L. Lawson 115

2. Tricone Multiple Cassegrain Feed System for the 210-ft Antenna
M. S. Katow and K. P. Bartos 121

3. Analysis of Bandpass Filtered Phase Modulation by a Non-Ideal Square Wave
R. C. Coffin 124

Contents (contd)

4. DSS 13 Operations
E. B. Jackson and J. D. Campbell 126

5. Cable-Driver Circuits
D. W. Slaughter 127

IV. Development and Implementation 131

A. DSIF Development 131

1. DSIF Systems Test Analysis and Verification
R. W. Burt 131

2. Programmable Frequency Divider and Pulse Generator for Receiver AGC Calibrations
A. C. Shallbetter 134

3. DSIF Monitor System Phase I Development
F. B. Leppla 139

4. Frequency and Timing Subsystem Phase II
P. C. Harrison 140

5. Clock-Synchronization System Performance
H. W. Baugh 142

6. Multiple-Mission Telemetry Baseband Signal Recording
J. McInnis 143

V. Operations and Facilities 148

A. DSN Operations 148

1. Radio-Science Support
J. R. Hall 148

B. Facility Engineering 148

1. 210-ft Antenna Overseas Projects
P. C. Doster 148

2. DSS 14 4-ft Time Sync Antenna Installation
M. Kron and V. B. Lobb 149

I. Introduction

A. Description of the DSN

The Deep Space Network (DSN), established by the NASA Office of Tracking and Data Acquisition under the system management and technical direction of JPL, is responsible for two-way communications with unmanned spacecraft traveling approximately 10,000 mi from earth to interplanetary distances. It supports, or has supported, the following NASA deep space exploration projects: *Ranger, Surveyor, Mariner* Venus 1962, *Mariner* Mars 1964, *Mariner* Venus 67, *Mariner* Mars 1969, *Mariner* Mars 1971, and *Mariner V* extended mission operations (JPL); *Lunar Orbiter* (Langley Research Center); *Pioneer* (Ames Research Center); and *Apollo* (Manned Spacecraft Center), as backup to the Manned Space Flight Network (MSFN).

The DSN is distinct from other NASA networks such as the MSFN, which has primary responsibility for tracking the manned spacecraft of the *Apollo* Project, and the Space Tracking and Data Acquisition Network (STADAN), which tracks earth-orbiting scientific and communications satellites. With no future unmanned lunar spacecraft presently planned, the primary objective of the DSN is to continue its support of planetary and interplanetary flight projects. Future activities may include support of certain foreign deep-space flight projects.

To provide this support of flight projects, the DSN simultaneously performs advanced engineering on components and systems, integrates proven equipment and methods into the network,[1] and provides direct support of each project through that project's Tracking and Data System. This management element and the project's Mission Operations System are responsible for the design and operation of the data system, software system, and operations system required in the conduct of mission operations. The organization and procedures necessary to carry out these activities were described in SPS 37-50, Vol. II, pp. 15–17.

In providing the direct support of a flight project, the DSN performs three basic functions:

(1) *Tracking:* locating the spacecraft; measuring its distance, velocity, and position; and following its course.

(2) *Data acquisition:* recovering information from the spacecraft in the form of telemetry, namely, engineering measurements and scientific data.

(3) *Command:* sending coded signals to the spacecraft to activate equipment to initiate spacecraft functions.

To accomplish these functions, six DSN systems have been established: (1) tracking, (2) telemetry, (3) command, (4) monitoring, (5) simulation, and (6) operations control.

[1]When a new piece of equipment or new method has been accepted for integration into the network, it is classed as Goldstone duplicate standard (GSDS), thus standardizing the design and operation of identical items throughout the network.

The DSN can be characterized as being comprised of three facilities: the Deep Space Instrumentation Facility (DSIF), the Ground Communications Facility (GCF), and the Space Flight Operations Facility (SFOF).

1. Deep Space Instrumentation Facility

a. Tracking and data acquisition facilities. A worldwide set of deep space stations (DSSs) with large antennas, low-noise phase-lock receiving systems, and high-power transmitters provide radio communications with spacecraft. The DSSs and the deep space communications complexes (DSCCs) they comprise are given in Table 1.

Radio contact with a spacecraft usually begins when the spacecraft is on the launch vehicle at Cape Kennedy, and it is maintained throughout the mission. The early part of the trajectory is covered by selected network stations of the Air Force Eastern Test Range (AFETR) and the MSFN of the Goddard Space Flight Center.[2] Normally, two-way communications are established between the spacecraft and the DSN within 30 min after the spacecraft has been injected into lunar, planetary, or interplanetary flight. A compatibility test station at Cape Kennedy (discussed later) monitors the spacecraft continuously during the launch phase until it passes over the local horizon. The deep space phase begins with acquisition by either the Johannesburg, Woomera, or Tidbinbilla DSS. These and the remaining DSSs given in Table 1 provide radio communications to the end of the flight.

To enable continuous radio contact with spacecraft, the DSSs are located approximately 120 deg apart in longitude; thus, a spacecraft in deep space flight is always within the field-of-view of at least one station, and for several hours each day may be seen by two stations. Furthermore, since most spacecraft on deep space missions travel within 30 deg of the equatorial plane, the DSSs are located within latitudes of 45 deg north or south of the equator. All DSSs operate at S-band frequencies: 2110–2120 MHz for earth-to-spacecraft transmission and 2290–2300 MHz for spacecraft-to-earth transmission.

To provide sufficient tracking capability to enable useful data returns from around the planets and from the edge of the solar system, a 210-ft-diam-antenna network will be

[2]The 30-ft-diam-antenna station established by the DSN on Ascension Island during 1965 to act in conjunction with the MSFN orbital support 30-ft-diam-antenna station was transferred to the MSFN in July 1968.

Table 1. Tracking and data acquisition stations of the DSIF

DSCC	Location	DSS	DSS serial designation	Antenna		Year of initial operation
				Diameter, ft	Type of mounting	
Goldstone	California	Pioneer	11	85	Polar	1958
		Echo[a]	12	85	Polar	1962
		(Venus)[b]	13	(85)	(Az–El)	(1962)
		Mars	14	210	Az–El	1966
Canberra	Australia	Woomera[c]	41	85	Polar	1960
		Tidbinbilla[c]	42	85	Polar	1965
—	South Africa	Johannesburg[c]	51	85	Polar	1961[d]
Madrid	Spain	Robledo[c]	61	85	Polar	1965
		Cebreros[c]	62	85	Polar	1967

[a]Established in 1959 to support NASA's *Echo* Project to explore the feasibility of transcontinental two-way communications using a passive satellite; the Echo DSS was originally configured with an 85-ft-diam Az-El-mounted antenna. In 1962, when the need arose for a second 85-ft-diam polar-mounted antenna at the Goldstone site, the 85-ft-diam Az-El-mounted antenna was moved to the Venus DSS, and an 85-ft-diam polar-mounted antenna was constructed at the Echo DSS.

[b]A research-and-development facility used to demonstrate the feasibility of new equipment and methods to be integrated into the operational network. Besides the 85-ft-diam Az-El-mounted antenna, the Venus DSS has a 30-ft-diam Az-El-mounted antenna that is used for testing the design and operation of the feed system for the Mars DSS 210-ft-diam antenna.

[c]Normally staffed and operated by government agencies of the respective countries (except for a temporary staff of the Madrid DSCC), with some assistance of U.S. support personnel.

[d]Between 1958 and 1962, a temporary mobile tracking station was located near Johannesburg to provide L-band communications required by the *Ranger* and *Mariner* Venus 1962 spacecraft.

required. Two additional 210-ft-diam-antenna DSSs are being established at Madrid and Canberra, starting in 1969. These DSSs, scheduled to be operational by early-1973, will operate in conjunction with the Mars DSS to provide this capability.

b. Compatibility test facilities. In 1959, a mobile L-band compatibility test station was established at Cape Kennedy to verify flight-spacecraft/DSN compatibility prior to the launch of the *Ranger* and *Mariner* Venus 1962 spacecraft. Experience revealed the need for a permanent facility at Cape Kennedy for this function. An S-band compatibility test station with a 4-ft-diam antenna became operational in 1965. In addition to supporting the preflight compatibility tests, this station monitors the spacecraft continuously during the launch phase until it passes over the local horizon.

Spacecraft telecommunications compatibility in the design and prototype development phases was formerly verified by tests at the Goldstone DSCC. To provide a more economical means for conducting such work and because of the increasing use of multiple-mission telemetry and command equipment by the DSN, a compatibility test area was established at JPL in 1968. In all essential characteristics, the configuration of this facility is identical to that of the 85- and 210-ft-diam-antenna stations.

The JPL compatibility test area is used during spacecraft system tests to establish the compatibility with the DSN of the proof test model and developmental models of spacecraft, and the Cape Kennedy compatibility test station is used for final flight spacecraft compatibility validation testing prior to launch.

2. Ground Communications Facility

The GCF, using, in part, facilities of the worldwide NASA Communications Facility (NASCOM),[3] provides voice, high-speed data, and teletype communications between the SFOF and all DSSs, except those of the Goldstone DSCC. Communications between the Goldstone DSCC and the SFOF are provided by a microwave link leased from a common carrier. Early missions were supported with voice and teletype circuits only, but increased data rates necessitated the use of wide-band circuits from all DSSs.

3. Space Flight Operations Facility

Network and mission control functions are performed by the SFOF at JPL. (Prior to 1964, these functions were performed in temporary facilities at JPL.) The SFOF receives data from all DSSs and processes that information required by the flight project to conduct mission operations. The following services are provided: (1) real-time processing and display of tracking data; (2) real-time and non-real-time processing and display of telemetry data; (3) simulation of flight operations; (4) near-real-time evaluation of DSN performance; (5) operations control, and status and operational data display; and (6) general support such as internal communications by telephone, intercom, public address, closed-circuit TV, documentation, and reproduction of data packages. Master data records of science data received from spacecraft are generated. Technical areas are provided for flight project personnel who analyze spacecraft performance, trajectories, and generation of commands.

The SFOF is equipped to support many spacecraft in flight and those under test in preparation for flight. Over a 24-hour period in 1967, as many as eight in-flight spacecraft or operational-readiness tests for flight were supported by the SFOF.

B. Description of DSN Systems

1. Command System, *W. J. Kinder and E. C. Gatz*

a. Background. As reported in SPS 37-52, Vol. II, pp. 3–5, no standard DSN command system configuration exists at the present time. Individual project procedures, mission-dependent equipment at the DSSs, and mission-dependent software in the SFOF are all characteristic of the present DSN command system. Requirements have now been published,[4] specifying a DSN command system with multiple-mission capability.

b. Objective. This system will provide the means to generate and transmit commands to spacecraft, and also provide related verification, display, and control functions to ensure and confirm the establishment of successful command operations. Specifically, the SFOF central processing system will be capable of supporting command operations for two spacecraft from one or two missions with adequate control and backup. Each DSS, except DSS 14, can command one spacecraft at a time. DSS 14 will have dual command capability.

c. Application. The command system is presently being implemented and will be made operational for the support of all missions in the two years following the

[3]Managed and directed by the Goddard Space Flight Center.

[4]Thatcher, J. W., *DSN Systems Requirements, DSN Command System (Through 1971)*, Feb. 15, 1969 (JPL internal document).

Mariner Mars 1969 mission. Included in these are the *Mariner* Mars 1971 mission and *Pioneer VI* through *IX* and *E* missions.

d. Functional requirements. Figure 1 displays the DSN command system general configuration and functions. Key characteristics of the DSN command system include the following:

(1) Centralized control of command generation/transmission/verification from the SFOF. To a project observer, the system will operate with minimum delays, and with error-free transmission to each DSS.

(2) Use of high-speed data lines for data transmission between the SFOF and DSSs as the prime mode. Teletype will be used as limited back-up; when teletype lines are used, delays will increase, but the system will be capable of performing all neccessary code/format conversions automatically so as to be invisible to the project users (except as reflected in increased delay). Voice circuits to each DSS with manual insertion of commands at the DSS will be provided as an emergency mode.

(3) Multiple-mission command capability at each DSS for:

  (a) Command waveform generation and verification.

  (b) Subcarrier modulation.

  (c) Phase-shift keying with or without transmitted reference.

  (d) Frequency-shift keying.

  (e) Use of project-supplied keys to ensure command transmission to the proper spacecraft when two or more are in the antenna beamwidth emergency-mode manual input.

(4) Generation of command standards and limits by the DSN command operations group.

(5) Real-time reporting of DSN command system status to DSN and mission control.

(6) Production of a DSN command master data record in real/near-real time.

(7) Simultaneous command and telemetry data handling/processing in each DSS telemetry and command data subsystem.

e. Operational description. A functional diagram depicting the DSN command system operation is shown in Fig. 2. The operation and control of the system will be characterized by a set of closed loops. Commands will be generated by the flight project in the SFOF and subjected to a project-specified approval and enabling process. Once this central project approval has been obtained, the command data will be presented to the DSN for encoding and formatting.

Command data will be sent from the SFOF by the DSN to the appropriate DSS, where they are reformatted and placed in temporary storage. A *verify* message, containing both the command data received from the SFOF and the actual constructed command bit sequence, will be returned to the SFOF. The *verify* message will be processed by the DSN (and the project at its option) in the SFOF to ensure that correct command data have been received and stored at the DSS.

After the above verification has been completed, an *enable* message will be composed and sent to the DSS, either automatically or on manual input, according to project option. The *enable* message will subsequently cause the verified command to be retrieved from temporary storage (at the time specified in the command message), to be converted to the proper composite format (i.e., proper waveform, subcarrier, etc.), and to be presented to the modulator and transmitter. The composite signal will be checked on a bit-by-bit basis against the verified format. Any failure in this comparison will cause immediate automatic interruption (*abort*) of transmission, and the generation of an *abort* message to the SFOF. If the comparison and transmission are successful, a *confirm* message will be returned to the SFOF.

It will be possible to abort the command process at any time with a *disable* signal from the SFOF, or with a manual insertion at the DSS. After any abort, the command message may be repeated by a new *enable* message, or a new command may be started by the standard initiation procedure.

As a limited backup, command data, *enable*, and *disable* messages may be entered manually at a DSS. This will be used as an emergency procedure only.

f. Performance parameters. The time required to initialize the DSN command system for a project being actively supported, resulting in a command message

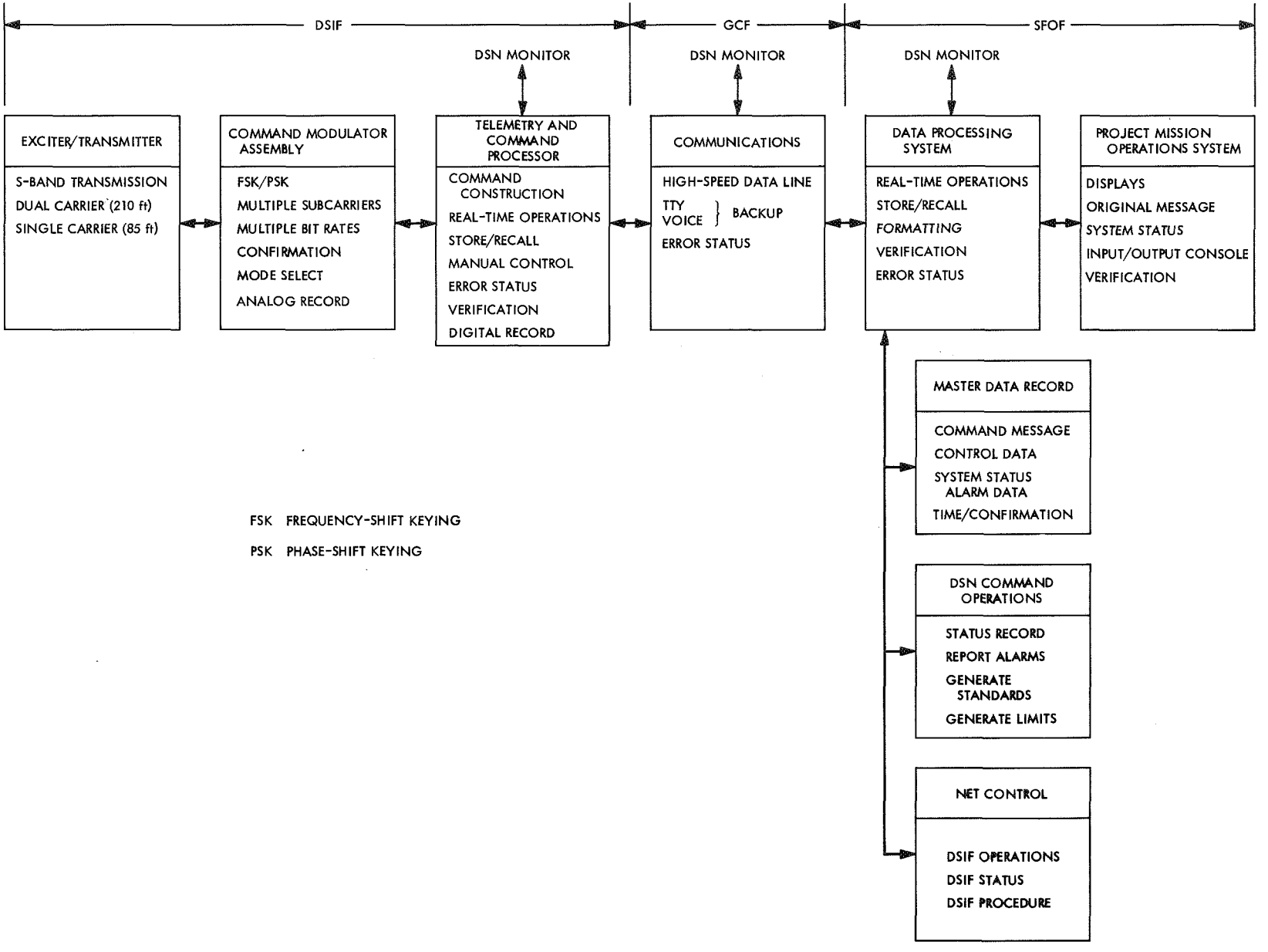

Fig. 1. DSN command system general configuration and functions

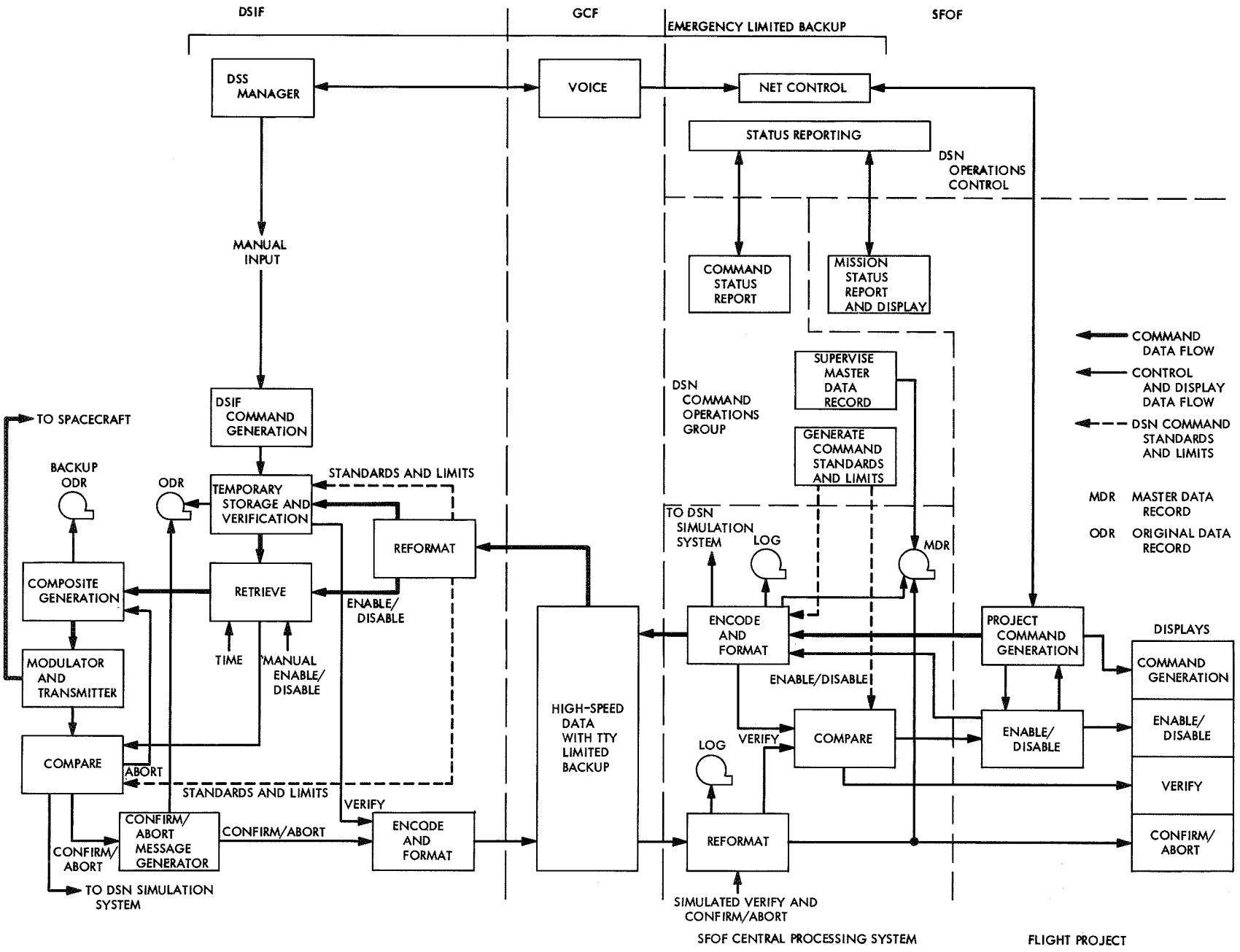

Fig. 2. DSN command system functional diagram

ready for transmission, will be less than 30 min. This time will be exclusive of the time required to establish two-way command lock. After system initialization, no more than 6 s will elapse between command transmission from the SFOF and start of command transmission to the spacecraft. The command word shall be transmitted from the DSS antenna to the spacecraft within 0.1 s of the Greenwich Mean Time.

A bit-error probability of less than 10^{-6} will be provided for the one-way high-speed data transmission of command system data between the SFOF and DSS. The command bit rate will be selectable in 1-bit/s steps from 1 to 20 bits/s, with future expansion to the range of 1 bit/min to 1000 bits/s.

The subcarrier will provide either sine-wave signals in the 100-Hz to 1-MHz range or square-wave signals, 1~ the range of 100 Hz to 100 kHz. Selection of phase-shift-keyed (with or without word or bit sync reference) or frequency-shift-keyed multiple subcarriers will be provided. Phase-shift-keyed modulation will be provided from zero to complete subcarrier suppression. The modulating signal will be provided with a 0.1-dB resolution to set the modulation index.

The carrier will be in the range of 2110- to 2120-MHz single frequency, except at DSS 14, which will have a dual-frequency capability. The 85-ft-antenna DSSs will transmit powers up to 10 kW. The 210-ft antenna station will have dual-carrier capability up to 40 kW, and single-carrier capability up to 400 kW.

The DSN command system master data record will be updated in near-real time and will contain a log of encoded command messages transmitted to the spacecraft, as well as command messages generated at the SFOF or DSS. All associated control data, time tags, status, and verification status will be included as part of the master data record. A separate master data record will be maintained for each mission and, at project option, for each spacecraft.

g. Constraints. The DSN command system will provide a multiple-mission capability consistent with the following constraints:

(1) No mission-dependent equipment or personnel will be required at the DSS for any mission supported by the DSN. This specifically includes present and planned *Pioneer* missions, the *Mariner* Mars 1971 mission, and extended *Mariner* Mars 1969 operations.

(2) The DSN command system will be automated to the maximum extent possible. Specifically, no additional (mission-independent) operator position will be required at the DSS for setup or operation of the system.

(3) The SFOF part of the DSN command system will reside in the SFOF central processing system.

(4) The command data handling and control software at each DSS will reside in the DSS telemetry and command data subsystem. Any mission-dependent initialization of automatic functions will be performed from the SFOF central processing system.

Page intentionally left blank

II. Mission Support

A. Interplanetary Flight Projects

1. *Pioneer VIII* Mission Support, *A. J. Siegmeth*

a. Introduction. SPS 37-50, Vol. II, pp. 17–27 contains a discussion of the DSN support services rendered for the *Pioneer VI* mission. A similar discussion covering the *Pioneer VII* mission is given in SPS 37-51, Vol. II, pp. 12–20. The third of the Ames Research Center's (ARC) *Pioneer* series is the *Pioneer VIII* mission, which was launched on December 13, 1967. This article describes the tracking and data acquisition (TDA) requirements, commitments, and support of the *Pioneer VIII* mission, elaborating on the near-earth and the deep space phases of the mission.

b. Mission objectives. The primary objective of the *Pioneer VIII* mission is to obtain scientific information on interplanetary phenomena in order to plan for future unmanned and manned interplanetary projects. Also, better understanding of the propagation of particles from the sun to the vicinity of the earth, and the exploration of effects caused by the dynamics of the surface of the sun, can lead to a better explanation of solar phenomena in general.

The detection of the solar and galactic magnetic fields has implications relative to the origin of cosmic rays and of the historic mechanism of the galaxy. The scientific information pertaining to the characteristics of solar radiation related to solar-flare prediction capability, and the information about the properties and distribution of particles in interplanetary space, are particularly important to the *Apollo* and planetary programs.

Pioneer VIII also performed an investigation of the magnetosheath and bow shock wave of the earth. The onboard plasma and magnetometer instruments were fully operational 3–3.5 h after launch, at an approximate altitude of 8–10 earth radii. In addition, *Pioneer VIII* met the objectives of an investigation of the geomagnetospheric tail. A syzygy distance of approximately 500 earth radii was reached as the spacecraft entered the earth's tail (created by the solar winds flowing around the earth's magnetic field) at a distance previously unexplored by any spacecraft. The reduction and analysis of these data will furnish new and valuable scientific information from this vicinity of the earth. Another objective of the *Pioneer VIII* mission was to achieve a heliocentric aphelion of 1.1 AU. The *Pioneer VIII* mission is also

making available near-real-time scientific data on the status of interplanetary fields and particles and is still fully operational. *Pioneer VIII* real-time telemetry data, after proper reduction and analysis, are included in a *Pioneer* Space Weather Report, which is regularly teletyped by the *Pioneer* Project to the Environmental Science Services Administration (ESSA) Space Disturbance Forecast Center, Boulder, Colorado.

c. Launch vehicle, test and training satellite, and spacecraft.

Launch vehicle. The *Pioneer VIII* spacecraft was launched into solar orbit with a *Delta-55* three-stage booster vehicle. The first stage was a modified liquid-propellant *Thor* unit powered by an MB-3 Block III Rocketdyne engine system rated at a 172,000-lb thrust at sea level. The first-stage booster thrust was augmented by three strapped-on Thiokol TX33-52 solid-propellant motors, each rated at a 54,000-lb thrust at sea level. This combination provided a lift-up thrust in excess of 330,000 lb. The second stage was an Aerojet General liquid propellant engine rated at a 7800-lb thrust in vacuum. The third stage contained a United Technology Center FW-4D solid propellant motor rated at a 6000-lb thrust at a 100,000-ft altitude. The third-stage–spacecraft assembly was enclosed in an improved *Delta* fairing.

The first and second stages were guided by two separately preprogrammed autopilot systems. The Western Electric Company provided a ground-based radio guidance system to make any necessary trajectory corrections during first- and second-stage powered flight. The third stage was spin-stabilized during the powered flight.

The launch vehicle's second and third stages were equipped with C-band radar beacons and VHF telemetry transmitters. The radar instrumentation was necessary to determine the near-earth phase trajectory of the stages, and also to establish the orbit parameters of the interplanetary solar injection of the spacecraft. This information established updated tracking prediction information to enable the DSN to make a reliable, early acquisition from the closest DSS. The purpose of the VHF telemetry transmitters was to monitor the performance of the launch vehicle.

Test and training satellite. The second stage of the booster vehicle carried piggyback a test and training satellite (TTS) equipped with a payload consisting of an S-band transponder compatible with the unified S-band system of the Manned Space Flight Network (MSFN). This earth satellite program was sponsored and directed by the Goddard Space Flight Center. In earth orbit, the TTS spacecraft provided an active target for the testing and training of the MSFN stations.

The TTS has an octahedron shape and weighs approximately 44 lb. The eight triangular sides of the TTS are covered with solar cells to provide power to a battery assembly, which consists of 10 nickel–cadmium cells and an appropriate charge regulator system. The batteries are designed to provide 3 h of continuous S-band transponder operation. They will require about 20 h of recharge time after maximum use. An S-band antenna is mounted at the top spacecraft apex, and the command receiver antenna is adjacent to the bottom apex. A fitting is located at the bottom apex for mounting and ejecting the spacecraft from its launch canister. The TTS was ejected from the second stage in an earth orbit after the third stage of the launch vehicle, together with the *Pioneer VIII* spacecraft, separated from the second stage.

Pioneer VIII spacecraft. The *Pioneer VIII* spacecraft has a cylindrical configuration approximately 35-in. high and 37 in. in diameter. In a folded configuration, the hinged spacecraft booms protrude from the cylinder and increase the overall spacecraft diameter to approximately 44 in. Three booms, each approximately 60-in. long, are folded into a tripod arrangement during the launch phase of the mission, and are supported by the antenna mast. The antenna increases the overall height of the spacecraft to about 87 in. All the basic scientific experiments and the spacecraft engineering equipment are mounted on an equipment platform inside of the spacecraft. Apertures for experiments are provided through the cylindrical body. The magnetometer is located on the end of one boom to minimize the effects of magnetic fields generated by the spacecraft equipment. The other two booms are provided to balance the spin-stabilized spacecraft. The second boom carries the orientation nozzle, and the third the wobble damper mechanism. The solar array, consisting of approximately 10,000 N–P-type solar cells, is mounted on the outer surface of the cylindrical spacecraft body.

The spacecraft contains five basic subsystems: thermal control, orientation control, communications, data handling, and power supply. The total spacecraft–third stage weight at lift-off was 890 lb including 665 lb for the third-stage motor, 144 lb for the spacecraft, and 81 lb for miscellaneous hardware and instrumentation.

The antenna complement of the *Pioneer VIII* spacecraft consists of one high-gain antenna and two omni-directional antennas. All three antennas are linear polarized. The high-gain antenna consists of a co-linear dipole array that provides a disk-like pattern in a plane perpendicular to the spin axis of the spacecraft. To make the spacecraft high-gain antenna application possible, the spin axis of the spacecraft must maintain a desired orientation; it is adjusted approximately perpendicular to the ecliptic plane and spacecraft sun line. In this position, the high-gain antenna's main lobe points toward the earth. The telemetry system of the spacecraft is capable of transmitting scientific and engineering data at five discrete bit rates ranging from 512 to 8 bits/s. The onboard data system uses pulse-code modulation/phase-shift keying/phase modulated S-band transmission. Scientific and engineering data are time multiplexed using five different formats to provide flexibility in the types of data being transmitted.

The *Pioneer VIII* spacecraft's seven scientific instruments and the names of the principal investigators and their affiliations are as follows:

(1) Cosmic-ray instrument – Dr. Webber, University of Minnesota.

(2) Magnetometer – Dr. Ness, NASA/Goddard Space Flight Center (GSFC).

(3) Cosmic-ray instrument – Dr. McCracken, University of South Carolina.

(4) Radio propagation instrument – Dr. Eshleman, Stanford University.

(5) Cosmic dust detector – Mr. Berg, GSFC.

(6) Plasma probe instrument – Dr. Wolfe, NASA/ARC.

(7) Electric field detector – Dr. Scarf, TRW Systems, Inc.

In addition, Dr. John D. Anderson of JPL is the principal investigator of the Celestial Mechanics Experiment. This experiment uses the S-band doppler tracking system as the precision data source.

d. Trajectory. During launch preparation for the *Pioneer VIII* mission, three trajectory blocks were developed. The objective was to achieve an aphelion of 1.1 AU, a period of 390 days with an inclination of less than 0.33 deg, and an earth-to-spacecraft distance at syzygy of 540 earth radii. The Block I trajectory required launch dates of December 13, 14, and 15, 1967, each date having an approximately 30-min launch window. The launch dates of the Block II trajectory were December 19, 20, 21, and 22, 1967, with daily launch windows of approximately 30 min. The Block III trajectory required launch dates of January 10, 11, 12, and 13, 1968, with daily launch windows of approximately 20 min.

All trajectory blocks were designed to have a fixed launch azimuth of 108 deg, and to achieve nominal heliocentric orbit parameters.

To achieve the *Pioneer VIII* planned heliocentric orbit, the guidance equipment aboard the *Delta* vehicle is adjustable for each trajectory block having a fixed launch azimuth and parking-orbit coast time. The launch vehicle boosts the third stage–spacecraft combination into a rather elliptical parking orbit. Near the end of the parking-orbit coast period, the third stage–spacecraft combination is spun off, second–third stage separation takes place, and the third stage is ignited. The third-stage burn has a fixed direction in space.

e. DSN TDA support requirements and plans. In view of the excellent flight performance of the *Pioneer VI* and *VII* missions, which have collected and delivered excellent fields and particles data beyond expectation (and are still continuing their operation), the TDA support requirements and commitments have been further extended for the *Pioneer VIII* mission. Prior to launch, the *Pioneer* Project outlined the TDA requirements of the *Pioneer* missions in the *Pioneer VI, VII,* and *C*[1] NASA Support Instrumentation Requirements Document (SIRD). In turn, JPL, being the TDA support center for all NASA deep space flight missions, outlined a NASA Support Plan (NSP) for *Pioneer VI, VII,* and *C*.

Since the *Pioneer VI* and *VII* spacecraft continue to operate in their heliocentric orbits, adding the *Pioneer VIII* spacecraft as an additional instrument platform trailing the earth's trajectory provides fields and particles instruments collecting scientific data at three independent points of the ecliptic plane. Therefore, the scientific investigators of the *Pioneer* Project expressed their desire to have daily tracking missions from all three *Pioneers* to make possible the correlation of these measurements, thus leading to a better understanding of the angular distribution of the fields and particles.

For this reason, the SIRD required the following DSN TDA support for the *Pioneer VIII* mission: 24-h full-time

[1]*Pioneer VIII* was known as *Pioneer C* prior to launch.

tracking coverage during the first month after launch, and, subsequently, a continuation of the full-time support with a minimum of two tracking passes per day coverage within the threshold capabilities of the DSN 85-ft antenna network. After phase-out of the 85-ft antenna network (approximately April 1, 1970), the DSN will be required to furnish one tracking pass per day coverage, with a minimum of three to four tracking passes per week, using the DSS 14 210-ft antenna. The *Pioneer VIII* extended mission would continue until such time as the spacecraft either fails to provide useful science data, or moves beyond the threshold of DSS 14.

The *Pioneer* Project also required the TDA support of special activities. The Type-II orientation maneuvers and special solar flares require continuous support; the flares require a minimum coverage of 30–50 h during the time the spacecraft is within the 85-ft antenna network capabilities. In order to see the effects of solar flares, two tracking passes covering two *Pioneers* back-to-back have been requested during the extended mission. For the geomagnetospheric tail analysis, 24-h coverage was required for 10–12 days for each *Pioneer* prior to and after the syzygy epoch. Continuous coverage within the constraints of facilities and capabilities is required during a possible lunar occultation or a solar superior conjunction.

The *Pioneer* Project also required DSS 14 to furnish daily TDA support for at least 3–4 h during the *Pioneer VI* extended mission. The *Pioneer VII* mission support at the same DSS should be rendered in the form of daily 4–8 h tracks.

The *Pioneer VI, VII,* and *C* NSP describes a detailed TDA support plan, listing all capabilities and facilities that will be available to meet the requirements of the *Pioneer VI, VII,* and *C* SIRD. Since the DSN is required to support all active deep space flight missions, facility and manpower limitations can cause support constraints making it impossible to meet all *Pioneer* Project requirements. To furnish the best service for all flight projects, the DSN makes every attempt to resolve these conflicts during the early planning activities. If the NASA flight project support priority guidelines do not provide the necessary tools to resolve the support conflicts, the DSN invites the corresponding Mission Operations System Managers to a conflict resolution conference to establish priorities and negotiate acceptable solutions.

f. TDA support during the near-earth phase. The near-earth phase of the *Pioneer VIII* mission started with the prelaunch preparations and tests and ended after the DSN established continuous TDA support.

For the *Pioneer VIII* mission Tracking and Data System (TDS) support, selected resources of the AFETR, MSFN, and the DSN have been included.

As an integral part of the preparation for the *Pioneer VIII* launch-readiness support, all selected resources of the TDS have been planned and the necessary training, acceptance, integration, verification, and operational readiness tests have been successfully completed.

The DSN/AFETR integration test was conducted on November 28, 1967 prior to the two *Pioneer* Project operational readiness tests. During the integration test, the AFETR provided simulated metric data. The DSN data were supplied to the AFETR in real time. No significant problems were encountered, and the test was considered successful. The operational readiness tests were conducted on December 4 and 8. During the full system test with all TDS elements participating, no significant problems were encountered and, at the conclusion of the test, the TDS was considered ready to support the launch.

The planned countdown for a December 13, 1967 launch included two built-in holds: one of 60 min at $T - 35$ min, and another of 5 min at $T - 5$ min. Lift-off was scheduled for 14:08 GMT with a flight azimuth of 108 deg. The launch window duration was 35 min.

Spacecraft power was applied approximately 9 h prior to the scheduled lift-off. No problems were experienced during the spacecraft countdown operations, and the spacecraft remained in a *go* condition throughout.

The launch-vehicle countdown was started on schedule at $T - 380$ min. Starting at $T - 345$ min, the DSN was considered to be in a *go* condition. Because of commercial power failures at the SFOF caused by locally severe weather conditions, the *W* string of the SFOF computers was dropped off-line at 10:45 GMT. At that time, a decision was made to assign the *X* computer string, which was operating on diesel-generated power, to *Pioneer VIII* mission support. Because of a maser failure at DSS 12, the DSN decided to support the initial flight phase operations from DSS 12 with a parametric amplifier. No other failures or anomalies occurred, and the DSN remained in a *go* condition through the countdown and launch.

The MSFN reported all stations and systems in a *go* condition, with the exception of Tananarive, which was qualified as providing limited metric support only.

The AFETR experienced no problems during the countdown and launch phase, and remained in a *go* condition throughout. The RF propagation forecast, which was received at $T - 105$ min, predicted good conditions for all high-frequency circuits.

The spacecraft terminal count was initiated at $T - 140$, and operations proceeded normally throughout liftoff (14:08:00.265 GMT).

The TDS configuration for the near-earth support of the *Pioneer VIII* mission is shown in Table 1. The earth track for the 108-deg flight azimuth, along with the anticipated coverage intervals, is illustrated in Fig. 1.

Table 1. TDS configuration for near-earth support of the *Pioneer VIII* mission

Station	Metric-tracking C-band radars	VHF telemetry	S-band spacecraft telemetry
AFETR			
Kennedy Space Center	X	X	X
Cape Kennedy	X	—	—
Patrick AFB	X	—	—
Grand Bahama Island	X	X	X
Grand Turk	X	—	X[a]
Antigua	X	X	X
Ascension	X	X	X
Twin Falls	X	X	X
Pretoria	X	X	X
MSFN			
Bermuda	—	X	—
Tananarive	X	X	—
Carnarvon	X	X	—
Guam	—	X	—
Hawaii	X	X	—
Guaymas	—	X	—
DSN			
DSS 71	—	—	X
DSS 51	X	—	X
DSS 41	X	—	X

[a]Engineering test basis.

All Class I metric coverage requirements were met, with the actual coverage either equaling or exceeding the estimate at most stations. Difficulty in obtaining valid third-stage tracking data is believed to have been caused by tumbling of the third stage following third-stage–spacecraft separation.

The AFETR C-band radar stations have processed the received tracking data in real time, and transmitted high-density time, azimuth, elevation, and range data in optimum form to the AFETR Real-Time Computer System (RTCS) via AFETR and NASA Communications Network (NASCOM) circuits, sub-cables and high-frequency communications. The RTCS transmitted, in decimal form, the best metric tracking data to the SFOF for further processing and predicts generation. The RTCS also computed the *Pioneer VIII* parking and solar orbits.

A parking orbit was computed using Antigua free-flight data. This solution indicated an almost nominal parking orbit. Table 2 illustrates the RTCS orbital computations for *Pioneer VIII.*

A theoretical transfer orbit was computed by the RTCS, using Antigua data plus nominal third-stage burn parameters. An inter-range vector, orbital elements, and DSN predicts for DSSs 51 and 41 were computed from this solution. The SFOF reported that its predicts agreed closely with the nominal predicts. Third-stage look angles for Tananarive and Carnarvon were also computed from this solution.

An initial transfer orbit was also computed by the RTCS using a 2-min span of radar data. An inter-range vector, orbital elements, and solar mapping were provided from this computation. The RTCS also computed DSN predicts for DSS 41, and updated look angles for Carnarvon. A second transfer orbit solution, based on Range Instrumentation Ship (RIS) Twin Falls data, was computed to verify the first radar solution.

The Tananarive and Carnarvon radars were scheduled to provide metric data during the transfer orbit. Tananarive did not acquire track, and no usable Carnarvon data were provided to the RTCS for orbital computations. The RTCS was also involved in the computation of actual spacecraft transfer orbits using 10 min of DSS 41 data. This solution was considered good.

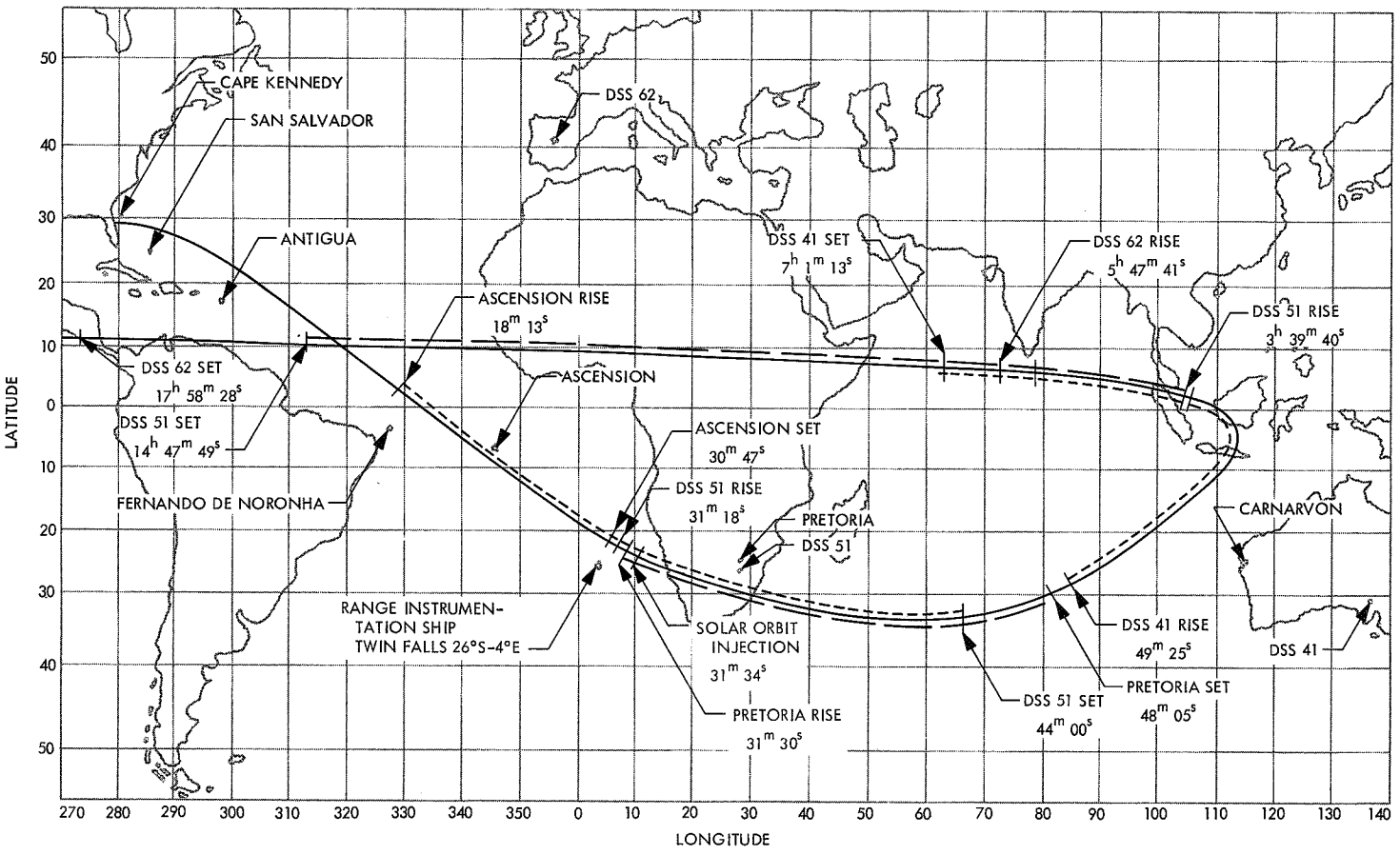

Fig. 1. *Pioneer VIII* earth track of parking and transfer orbit

Table 2. RTCS orbital computations for *Pioneer VIII*

Orbit	Epoch, s	Computation time, s	Data source	Quality
Initial parking orbit	L + 559	L + 840	Antigua	Good
Theoretical transfer orbit	L + 1890	L + 1140	Antigua plus nominal 3rd stage burn	Good
Transfer orbit	L + 1890	L + 3360	Pretoria	Fair
Actual spacecraft transfer orbit (1)	L + 1890	L + 6840	DSS 41 (10 min)	Fair
Actual spacecraft transfer orbit (2)	L + 1890	L + 9630	DSS 41 (45 min)	Good

The second actual spacecraft orbit, based on the 45 min of DSS 41 data, was computed by the RTCS. This solution was also considered good.

In general, the VHF telemetry coverage provided was quite good. Grand Bahama Island (GBI) 234-MHz link acquisition was approximately 5-min late due to operator error. Redundant and overlapping coverage from Tel-4 in Antigua was available during this period. Mark event times received and read out by AFETR stations are shown in Table 3. Usable data were obtained by Tel-4, GBI, Antigua, Ascension, Pretoria, and the RIS Twin Falls.

The MSFN C-band tracking and VHF telemetry acquisition stations, under the management of GSFC also participated in the *Pioneer VIII* near-earth support operations.

Tananarive, which was committed on a "best obtainable" basis, did not acquire track. This discrepancy was attributed to the probable tumbling of the third stage.

Table 3. *Pioneer VIII* in-flight events

Mark	Event	GMT	L + Time, s
—	Liftoff	1408:00.265	—
1	Solid-motor jettison	1409:10.55	70.28
2	Main-engine cutoff	1410:30.14	149.87
3	Second-stage ignition	1410:35.71	155.04
4	Shroud jettison	1411:08.39	188.11
5	Second-engine cutoff	1416:56.8	536.53
6	Third-stage spinup	1438:42.8	1841.81
7	Second/third stage separation	1438:45.1	1844.73
8	Third-stage ignition	1438:58.1	1891.77
9	Third-stage burnout (injection)	1439:31	1937.73
10	Third-stage/spacecraft separation	1440:20	1939.83
11	Spacecraft boom deployment	1440:20	1939.83

Carnarvon also did not acquire third-stage track. The station reported poor beacon returns. Since neither the GSFC acquisition message nor the AFETR look angles were received, it was necessary to use the acquisition-aid bus in order to achieve second-stage track.

Good second-stage telemetry data were received by the MSFN stations; however, the third-stage data were poor and unusable because of severe signal fluctuations.

The near-real-time trajectory information on the resultant parking orbit and on the third-stage–spacecraft injection solar orbit, supplied by the AFETR and MSFN radars, was used by the DSN to update the antenna-pointing information of the DSN acquisition DSS to make immediate acquisition of the spacecraft's S-band signal possible. The S-band frequency predicts for the same DSN acquisition DSS had been updated during the last phase of the prelaunch countdown by making systematic spacecraft frequency measurements. This action was required to shorten the time necessary for the S-band carrier frequency search at the acquisition DSS. In addition, the *Pioneer* Project provided the DSN with a real-time indication of the normality of the spacecraft injection into solar orbit.

The first DSN acquisition station was DSS 51. This station acquired the *Pioneer VIII* signal at 14:43 GMT and was in the one-way operational mode until 14:53 GMT. During this time, the DSS 51 transmitted, via teletype line, spacecraft engineering and science telemetry information to the SFOF for the assessment of the spacecraft's performance by the *Pioneer* Project Space Flight Operations Director (SFOD), the spacecraft performance analysis and command (SPAC) team, and the space science analysis and command (SSAC) group. Since DSS 51 had only a short view of the *Pioneer VIII* trajectory, the prime acquisition station was DSS 41. This station acquired a *Pioneer VIII* S-band signal at 14:55 GMT, and started the two-way tracking and data acquisition

operation at 15:11 GMT. Thus, the two-way tracking and data-acquisition support of *Pioneer VIII* started 63 min after launch. After two-way acquisition of the *Pioneer VIII* S-band signal was accomplished, *Pioneer* Project initiated the first spacecraft command, in order to check the automatic Type I orientation maneuver, and also began initiation procedures for the turn-on of all spacecraft scientific instruments. During the same period, two-way metric data collected by DSS 41 were used to make possible the final solar-orbit calculations.

Prelaunch spacecraft telemetry data were transmitted to the SFOF via the ground operating equipment (GOE) and the telemetry and command processor at DSS 71. The postlaunch near-earth phase requirements for DSSs 71 and 51 were on the "best obtainable" basis only. The DSS 71 received 9 min 10 s of postlaunch telemetry data, and DSS 51 received 11 min 10 s of data. The initial acquisition station, DSS 41, was to receive 5 min of telemetry data in a one-way mode before initiating the two-way mode.

The DSS 41 one-way receiver lock was obtained at 14:55 GMT (67 s earlier than predicted). At 15:03 GMT, the transmitter was turned on, and uplink acquisition commenced. Two-way lock occurred at 15:10 GMT; however, sideband and sidelobe lock-on problems were encountered. At 15:19 GMT, the station again performed the uplink acquisition sequence and, at 15:28 GMT, obtained good two-way lock.

The nominal and actual heliocentric orbital parameters of *Pioneer VIII* are shown in Table 4. These parameters have been calculated from 45 min of two-way tracking data furnished by DSS 41.

Table 4. Nominal and actual *Pioneer VIII* heliocentric-orbital parameters

Parameter	Nominal	Actual
Aphelion, AU	1.103	1.0880
Perihelion, AU	0.9895	0.98917
Period, days	390.9	386.6
Inclination, deg	0.33	0.0571
Earth-to-spacecraft distance at syzygy, earth radii	542	463.7
Time to syzygy, days	39	35 + 23 h
Spacecraft distance out of ecliptic at syzygy, earth radii	0.03	8.3

The TTS spacecraft nominal and actual orbital parameters are shown in Table 5.

Since DSS 41 had tracked *Pioneer VIII* in a two-way mode from 15:10 until 20:50 GMT, the continuous spacecraft signal TDA requirements were fulfilled and the near-earth phase of the *Pioneer VIII* mission support was successfully completed.

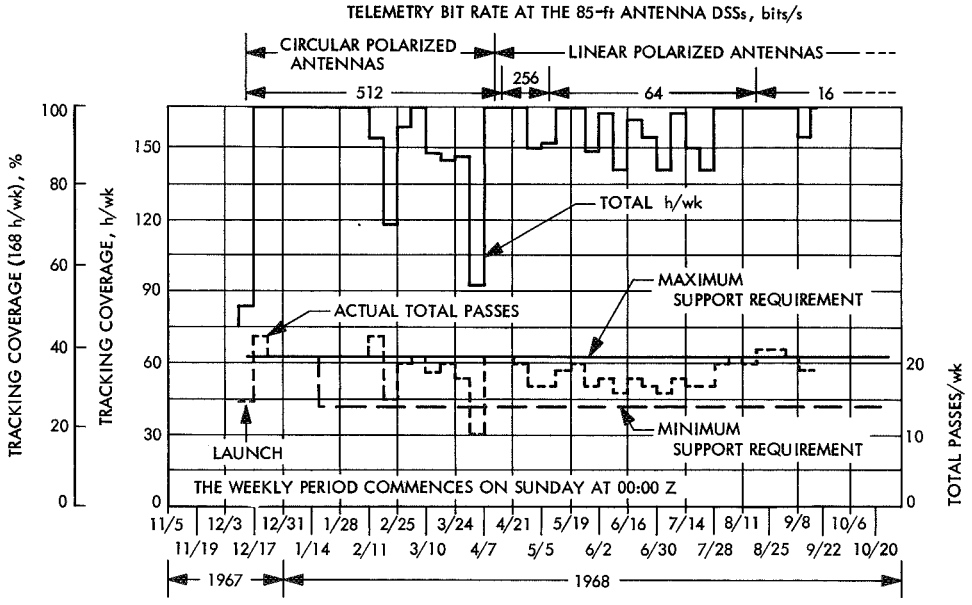

Fig. 2. *Pioneer VIII* nominal mission tracking and data acquisition support

Table 5. Nominal and actual TTS earth-orbital parameters

Parameter	Nominal	Actual
Apogee, nmi	320	264
Perigee, nmi	180	163
Inclination, deg	32.9	32.9
Period, min	93.9	92.46

g. TDA support performance during the deep space phase. The DSN TDA support was based on the application of the Unified S-Band System wherein a single coherent uplink and downlink carrier was used to provide both a two-way doppler and a data reference carrier. This carrier was modulated with command on the uplink and telemetry on the downlink. During this time, the DSN has made available almost continuous telemetry information with the lowest bit error rate, has sent all the necessary commands to the spacecraft, and has collected the required two-way precision doppler tracking data to update orbit parameters and to support *Pioneer* Project experimenters. In addition, the DSN has generated the antenna-pointing and tracking-frequency predictions for all stations, and has made available to the flight project an elaborate Mission Support Area (MSA) at the SFOF. This *Pioneer* MSA was used by the *Pioneer* Project Flight Operations Team during the prelaunch tests, launch operations, and during the first 5 days of the *Pioneer VIII* mission. The DSN also made available all required voice, teletype, and television services during this time, and provided sampled real-time spacecraft science telemetry data and decommutated and processed spacecraft engineering data in the form of teletype printouts at the SFOF. After the first critical days of the flight operations, *Pioneer* Project transferred the flight control activity to a Mission Operations Center (MOC) located at ARC. The real-time science and engineering teletype information was also supplied to this facility on a continuous basis. This real-time information was used by the *Pioneer* Project Space Flight Operations Team to continuously monitor spacecraft performance, engineering functions, and scientific instruments, and to make real-time decisions to send the commands necessary to make those configuration changes, adjustments, and calibrations to better utilize spacecraft capabilities. The real-time science data were also used by the flight project to generate, at regular intervals, solar weather forecasts to be used by ESSA and other flight projects, such as *Apollo*. The DSN has also provided the properly configured Original Data Records (ODR) for the *Pioneer* Project. These records consist of ½-in. wide analog, 7-channel magnetic tape recordings and logs of engineering measurements and calibration information required to analyze the performance of the DSN TDA support. The *Pioneer VIII* data packages containing the ODR have been carefully checked and validated by the DSN and forwarded to the flight project for further data processing and data reduction. From these ODRs, ARC generates the *Pioneer* Experimenter Records containing the spacecraft instrumentation data and information required by each *Pioneer* scientific investigator. These records also contain orbital information derived from *Pioneer VIII* trajectory tapes (also generated, edited, validated by the DSN), and provided to the flight project. The percentage of spacecraft telemetry data received in real time at the SFOF or at the ARC MOC using a 100 words/min teletype capability is as follows:

Bit rate	Percent received
512	3
256	8
64	31
16	100
8	100

DSN support performance quantitative analysis. The *Pioneer VIII* mission TDA support is presented in Fig. 2. This graph shows the actual number of tracking passes per week, the tracking hours per week, and the percentage of coverage per week. During the first 9 mo of the *Pioneer VIII* mission (which is equivalent approximately to 40 wk), the DSN furnished a total of 6236 h of TDA support. Since a total of 6720 h were available during this time, the DSN *Pioneer VIII* support coverage reached an average of 93% of the total available time. It should be noted that for a continuous 24-h/day, 7 days/wk coverage, 21 tracking passes/wk are required, which is equivalent to 168 h/wk of TDA support. To assure that no science and engineering data are lost during tracking-station switchover, 1-h tracking overlaps have also been provided. During the first 9 wk of the *Pioneer VIII* mission, the support was continuous and the DSN met the full requirements and commitments at that time. From the tenth to the fortieth week after launch, the support was sometimes below the full-time coverage, but generally well above the so-called "absolute minimum" requirements. Although the DSN made every attempt to continue the full-time *Pioneer VIII* coverage after the first 9 wk, this was not always possible. During the first

week in April, the DSN support was below the absolute minimum requirements due to *Apollo* launch activity.

The telemetry bit rate threshold points have been reached in accordance with the preflight engineering plans. During the first part of April, the DSN equipped the 85-ft antenna DSSs supporting *Pioneer VIII* with polarizer grids to convert the standard DSS circular antenna feed polarization to a linear mode in order to make it compatible with the spacecraft's linear polarized transmission, thus regaining a 3 dB polarization loss.

The fixed earth–sun-line heliocentric trajectory of *Pioneer VIII* is shown in Fig. 3. The time ticks drawn on the trajectory represent the spacecraft's position on the first day of each given month. The *Pioneer VIII* telemetry threshold ranges are displayed for the 85-ft antenna DSSs as well as for the 210-ft DSS 14 antenna. Most of the stations were operating in the linear polarized mode.

It should be noted that the *Pioneer VIII* threshold ranges have been 3 dB larger than those during the previous support of *Pioneer VI* and *VII*.

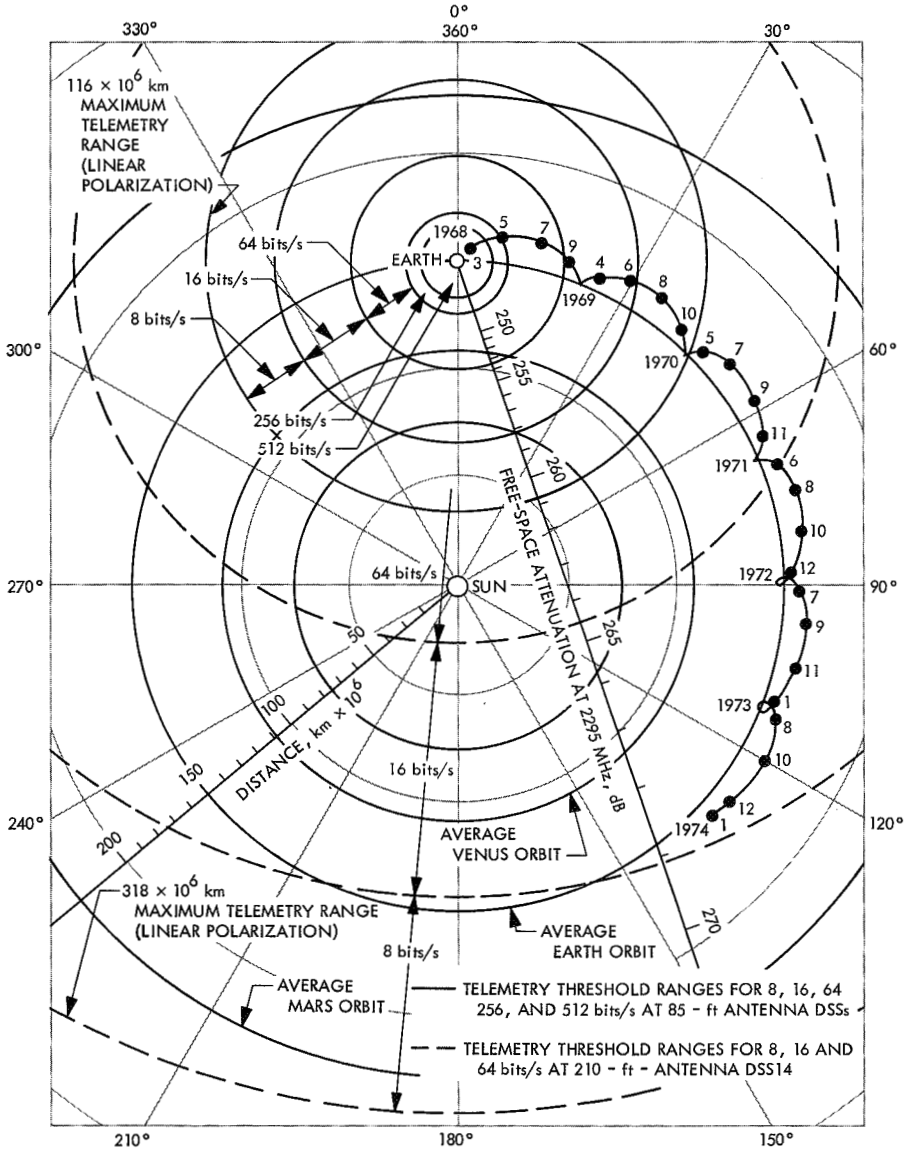

Fig. 3. Fixed earth–sun line trajectory

During the first 9 mo of the *Pioneer VIII* mission, the DSN furnished:

Real time TDA passes	669
Recording-mode TDA passes	122
Total TDA passes	791

an equivalent of 6150 h of TDA support.

Most of the recording-mode TDA passes have been made available from DSSs 41 and 42. The Australian DSSs have only one *Pioneer* GOE, which is required for real-time operations. For better utilization of the Australian DSSs, the DSN transferred the *Pioneer* GOE from DSS 41 to DSS 42 at the end of May 1968.

During the reported time frame, the average efficiency of the *Pioneer VIII* TDA support performance was as follows:

	Percentage
Actual versus scheduled TDA time	99.3
DSS receiver in lock versus actual time	99.9
GOE demodulator/bit synchronizer lock versus actual time	99.8
Telemetry command processor (TCP) in lock versus actual time	99.8
ODR versus actual time	99.9
DSS transmitter operating versus actual time	87.0
High-quality tracking data versus actual time	92.0
GCF throughput	98.0

During 9 mo, the DSN has recorded 2,610 ½-in., 7 channel analog magnetic tapes for the *Pioneer VIII* mission. On the average, 3.3 rolls of magnetic tape have been used for this purpose during each tracking pass. All the ODR tapes have been properly identified, checked, and validated before their shipment to the *Pioneer* Project. The DSN has also recorded a similar number of backup tapes, which are kept at the DSSs until the original tapes have been evaluated and processed by the *Pioneer* Project. In the event that no need for the backup tapes arises, degauss instructions are given to the DSSs.

The DSN has received, demodulated, and recorded 5783×10^6 telemetry bits during the first 9 mo of the *Pioneer VIII* mission. This figure breaks down as follows:

(1) 4700×10^6 bits at 512 bits/s.

(2) 520×10^6 bits at 256 bits/s.

(3) 525×10^6 bits at 64 bits/s.

(4) 38×10^6 bits at 16 bits/s.

Of the collected data bits, 72% contained scientific information originating from the spacecraft science flight instruments, 6% carried engineering information on spacecraft performance, and 22% have been used for parity check and data identification purposes.

The spacecraft duty cycle storage mode was used during the few times that the DSN was unable to furnish TDA support. The data received in this mode were, however, considerably less than 0.1 percent of the total.

During the period under discussion, the Space Flight Operations Control Team sent a total of 3,007 commands (equivalent to 69,161 1-s long command bits). All command activities have been nominal and no erroneous commands were received and/or accepted by the spacecraft.

All tracking station logs, science and engineering teletype printouts, ODR logs, and validation reports have been cataloged, and two sets of microfilms have been made. One set of records is available to the *Pioneer* Project, DSN, and experimenter personnel at the SFOF; the second set is stored in a fireproof vault.

DSN support performance qualitative analysis. Table 6 displays the cruise phase nominal design values of power levels, gains, and losses of the S-band telecommunications links. Design and measurement tolerances are omitted. Most of the listed quantities represent not only the hardware performance goals, but are also close to the actual average values.

In the telecommunications S-band uplink design section, the DSS transmitter output levels (1) are maximum values and can be reduced, if necessary, to avoid spacecraft receiver overloading. The transmitter circuit losses (2) and antenna gain (4) are measured quantities.

Table 6. *Pioneer VIII* S-band telecommunications design control table

Item	DSS 85-ft antenna[a]		DSS 210-ft antenna[a]	
	Spacecraft high-gain antenna	Spacecraft low-gain antenna	Spacecraft high-gain antenna	Spacecraft low-gain antenna
Telecommunications/uplink				
1. DSS transmitter power (10 kW maximum at the 85-ft antenna and 20 kW at the 210-ft antenna), dBmW	70.0	70.0	73.0	73.0
2. DSS transmitting circuit loss, dB	−0.4	−0.4	−0.4	−0.4
3. Carrier power vs transmitted total power (1.2 rad peak deviation), dB	−3.5	−3.5	−3.5	−3.5
4. DSS transmitting antenna gain, dB	51.2	51.2	60.0	60.0
5. Space attenuation (at 2110 MHz, 31.5×10^6 km), dB	−249.0	−249.0	−249.0	−249.0
6. Polarization and antenna pointing loss, dB	−0.5	−0.5	−0.5	−0.5
7. Spacecraft receiver antenna gain, dB	11.8	−1.3	11.8	−1.3
8. Spacecraft receiving circuit loss, dB	−1.0	−1.0	−1.0	−1.0
9. Spacecraft, received carrier power (sum of 1, 2, 3, 4, 5, 6, 7, and 8), dBmW	−121.4	−134.5	−109.6	−122.7
10. Spacecraft, received total power (sum of 1, 2, 4, 5, 6, 7, and 8), dBmW	−117.9	−131.0	−106.1	−119.2
Uplink carrier (Doppler) loop				
11. Spacecraft receiver noise spectral density, dBmW/Hz	−164.0	−164.0	−164.0	−164.0
12. Spacecraft receiver APC noise bandwidth ($2B_{L_0}$ = 20 Hz), dB Hz	13.0	13.0	13.0	13.0
13. Spacecraft receiver total noise power (sum of 11 and 12), dBmW	−151.0	−151.0	−151.0	−151.0
14. Received carrier S/N normalized to $2B_{L_0}$ (9 minus 13), dB	29.6	16.5	41.4	28.3
15. Required minimum S/N in spacecraft receiver, dB	6.0	6.0	6.0	6.0
16. Spacecraft carrier tracking loop margin (14 minus 15), dB	23.6	10.5	35.4	22.3
Uplink command data loop				
17. Data noise bandwidth (2 Hz–1 bit/s), dB Hz	3.0	3.0	3.0	3.0
18. Data noise power (sum of 11 and 17), dBmW	−161.0	−161.0	−161.0	−161.0
19. Data power/transmitted total power, dB	−3.3	−3.3	−3.3	−3.3
20. Spacecraft received data power (sum of 10 and 19), dBmW	−121.2	−134.3	−109.4	−122.5
21. Spacecraft command data S/N (20 minus 18), dB	39.8	26.7	51.6	38.5
22. Required command S/N (bit error: 10^{-5}), dB	13.5	13.5	13.5	13.5
23. Command margin (21 minus 22), dB	26.3	13.2	38.1	25.0

[a]With linear polarization.

NOTE: If DSSs use a circular polarized antenna feed, received power levels should be lowered by 3 dB. In this configuration, a 3-dB polarization loss exists since the spacecraft antenna is linearly polarized and the DSS antenna is circularly polarized.

Table 6 (contd)

Item	DSS 85-ft antenna[a]		DSS 210-ft antenna[a]	
	Spacecraft high-gain antenna	Spacecraft low-gain antenna	Spacecraft high-gain antenna	Spacecraft low-gain antenna
Telecommunications/downlink				
24. Total spacecraft transmitter power, dBmW	39.5	39.5	39.5	39.5
25. Carrier power vs total power (0.9 rad peak deviation), dB	−4.1	−4.1	−4.1	−4.1
26. Spacecraft transmitter feed losses, dB	−1.5	−2.1	−1.5	−2.1
27. Spacecraft transmitter antenna gain, dB	11.5	−0.4	11.1	−0.4
28. Spacecraft transmitter antenna and DSS pointing loss (average deviation from optimum), dB	−0.5	−0.5	−0.5	−0.5
29. Space attenuation (at 2298 MHz, 31.5×10^6 km), dB	−249.5	−249.5	−249.5	−249.5
30. DSS receiving antenna gain, dB	52.8	52.8	61.8	61.8
31. DSS received carrier power (sum of 24, 25, 26, 27, 28, 29, and 30), dBmW	−152.2	−163.8	−143.2	−154.8
32. DSS received total power (sum of 24, 26, 27, 28, 29, and 30), dBmW	−148.1	−159.7	−139.1	−150.7
Downlink carrier (Doppler) loop				
33. DSS receiver single-sided noise spectral density (45°K at the 85-ft antenna and 28°K at the 210-ft antenna), dBmW/Hz	−182.1	−182.1	−184.1	−184.1
34. DSS receiver noise bandwidth ($2B_{L_0}$), dB Hz	10.8	10.8	10.8	10.8
35. Receiver noise power (sum of 33 and 34), dBmW	−171.3	−171.3	−173.3	−173.3
36. Carrier S/N normalized to $2B_{L_0}$ (31 minus 35), dB	19.1	7.5	30.1	18.5
37. Required S/N in carrier loop, dB	6.0	6.0	6.0	6.0
38. Carrier tracking loop margin (36 minus 37), dB	13.1	1.5	24.1	12.5
Downlink telemetry data				
39. Subcarrier power vs total power, dB	−2.2	−2.2	−2.2	−2.2
40. DSS received subcarrier power (sum of 32 and 39), dBmW	−150.3	−161.9	−141.3	−152.9
41. Receiver and demodulator losses—limiter and demodulator/bit synchronizer, dB	−1.9	−1.9	−1.9	−1.9
42. Modulation loss caused by spacecraft jitter, dB	−0.4	−0.4	−0.4	−0.4
43. Effective data signal (subcarrier) power (sum of 40, 41, and 42), dBmW	−152.6	−164.2	−143.6	−155.2
44. Time duration of the data bits at 256 bits/s, dB s	−24.0	−24.0	−24.0	−24.0
45. Energy per bit: ST_b (sum of 43 and 44), dBmW s	−176.6	−188.2	−167.6	−179.2
46. Single-sided noise spectral density: N_0 (see item 33), dBmW/Hz	−182.1	−182.1	−184.1	−184.1
47. ST_b/N_0 (45 minus 46), dB	5.5	−6.1	16.5	6.9
48. Required ST_b/N_0 for *Pioneer VIII* with a $P_E = 10^{-2}$ at 256 bits/s, dB	5.2	5.2	5.2	5.2
49. 256 bits/s telemetry subcarrier margin with $P_E = 10^{-2}$ at 31.5×10^6 km (47 minus 48), dB	0.3	−11.3	11.3	1.7
50. P_E 256 bits/s	8.10^{-3}	—	No error	2.10^{-3}

The carrier power drop (3) is determined by the phase modulation index of 1.2-rad one-sided peak. The free space attenuation (5) is derived from

$$L_{FS} = 92.45 + 20 \log f + 20 \log d$$

where L_{FS} is in decibels, f in gigahertz, and d in kilometers (Ref. 1). The polarization and antenna-pointing loss (6) is a best estimate based on numerous measurements made on *Pioneer* uplink operations. The *Pioneer VIII* antenna gain and circuit losses (7 and 8) were carefully established during the engineering evaluation of the communications subsystem. The RF carrier power and the RF total power (9 and 10) at the spacecraft receiver input were calculated from items 1 to 8.

The nominal values of the spacecraft receiver uplink carrier (Doppler) loop have been based on preflight measurements of the noise spectral density (11) and automatic phase control (APC) noise bandwidth (12). To avoid a doppler cycle slipping, the required minimum signal-to-noise ratio (S/N) in the spacecraft receiver should be 6 dB (15) (Refs. 2 and 3). The spacecraft carrier tracking loop margin is calculated from the values given in items 11 to 15.

The uplink command loop parameters and the loop margin are based on preflight measurements (17).

The S-band telecommunications downlink parameters are calculated from preflight measurements made on the spacecraft transmitter and antenna (24, 25, 26, and 27). The carrier power drop of 4.1 dB (25) is a result of an 0.9-rad peak phase modulation deviation using a 2048 bits/s square-wave subcarrier. The antenna pointing loss (28) is a best estimate. This item also includes medium term variations of the spacecraft transmitter output power and the subcarrier modulation index. The free space attenuation (29) was derived from a formula on L_{FS} given above. The DSS receiving antenna gain (30) given is based on numerous validated precision measurements. The received S-band carrier power and total power at the input of a DSS receiver is calculated from the values given from items (24) to (30).

The S-band downlink carrier loop parameters have been established from precision system noise temperature (33) and receiver noise bandwidth (34) measurements at the DSS. The carrier tracking loop margin was calculated from items (33) to (37).

The determination of the downlink telemetry subcarrier loop design values require special attention. Good telemetry performance is one of the most important requirements of the *Pioneer* missions. The subcarrier or data power versus total power ratio (39) is a function of the 0.9-rad, one-sided peak phase-modulation index (25). The carrier power is 4.1 dB below the total power (25); the subcarrier power is 2.2 dB below the total power (39). The sum of the downlink carrier power (31) and subcarrier power (40) is equal to the total power (32). The *Pioneer* GOE demodulator/bit synchronizer and DSS receiver limiter losses (41) degrade the useful *Pioneer* subcarrier power by 1.9 dB at a telemetry bit rate of 256 bits/s. In addition, the phase jitter of the spacecraft downlink signal degrades the useful modulation index of the telemetered bit stream. The mean value of this loss is 0.4 dB at 256 bits/s. Nominal values of items 41 and 42 are given in Fig. 4. The effective data signal power (43) is the sum of items 40, 41, and 42. The required signal energy per bit per unit noise bandwidth (ST_B/N_0) is given in item 47. The ST_B/N_0 is calculated from items 44, 45, and 46 (Refs. 4 and 5). This is the subcarrier signal energy versus noise power/Hz available at the input of the lossless perfect coherent detector. These losses have already been accounted for in items 41 and 42. The single-sided noise spectral density (46) was based on system noise temperature (SNT) measurements. The bit-error rate P_E of an antipodal uncoded coherent phase-shift keyed (PSK) system using the non-return to zero–level (NRZ–L) data modulation scheme is given by

$$P_E = erfc\left(\frac{2\,ST_B}{N_0}\right)^{1/2}$$

The values of P_E versus ST_B/N_0, assuming perfect PSK coherent detection, can be depicted from Fig. 4.

Since *Pioneer VIII* uses the non-return to zero–mark (NRZ–M) data modulation scheme, the error rate for this system becomes (Ref. 4):

$$P_{E_{Pioneer\,VIII}} = 2\,P_E\,(1 - P_E)$$

Therefore, with a good approximation, all P_E readings displayed on Fig. 5 should be multiplied by two for *Pioneer VIII* application. The *Pioneer* parity error scale, ERR for *Pioneer VIII*, is already adjusted by this factor. Accordingly, ST_B/N_0 = 5.2 dB (48) for *Pioneer VIII* operating at a $P_E = 10^{-2}$. (In the convolutional-coded mode, *Pioneer IX* uses the NRZ-L format.)

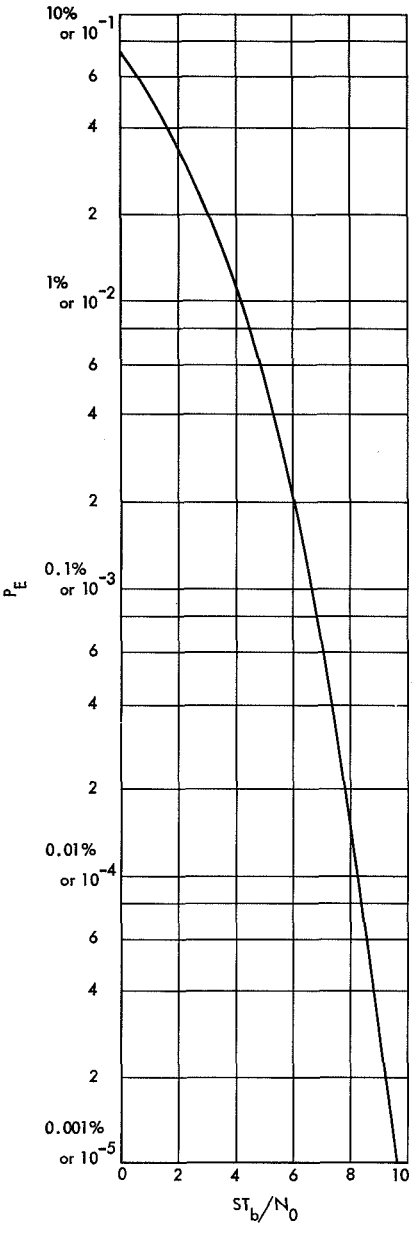

Fig. 4. Signal energy per bit/noise spectral density vs P_E

Table 6 shows that at a 31.5×10^6 km spacecraft–earth range, there is a 23.6-dB S-band uplink tracking loop, a 26.3-dB command, a 13.1-dB S-band downlink carrier loop margin, and a 0.3-dB subcarrier margin at a telemetry bit rate of 256 bits/s and $P_E = 10^{-2}$. All these margins apply to the 85-ft antenna DSSs operating in the linear-polarized configuration and the spacecraft switched to the high-gain antenna mode. It should be noted that the *Pioneer* Project requires almost errorless telemetry reception. Therefore, the general rule is that if P_E drops below $P_E = 10^{-3}$, or one error in 1000 detected bit level, the *Pioneer* Project Flight Controller commands the spacecraft to the next lower bit-rate configuration. In special cases, however, the *Pioneer* Project accepts a maximum P_E of $P_E = 10^{-2}$. In this case, however, the usefulness of some data points is questionable. The example shown in Table 6 portrays the 256 bit/s $P_E \approx 10^{-2}$ condition.

The uplink margins are considerably larger than the downlink margins. The S-band downlink performance is limited by the available spacecraft power, necessitating the use of large earth-based antenna installations. The performance differences of 85-ft and 210-ft antenna DSSs, and low- and high-gain spacecraft antennas, should also be noted.

S-band uplink carrier and subcarrier performance. The performance of the S-band uplink carrier was nominal during the time period covered by this article. During the first 2 mo of the mission, at *Pioneer* Project request, the DSN has lowered the uplink S-band power from the maximum value of 10 kW down to 0.1, 1, and 3 kW levels. This action was necessary to prevent spacecraft receiver overloading; excessive input signal levels can cause receiver saturation and cross-modulation. During the first 5 wk of the mission, the *Pioneer* Project operated both spacecraft S-band receivers from the low-gain spacecraft antennas. After the spacecraft communication link range increased, the channel 7 spacecraft receiver was connected to the spacecraft high-gain antenna.

Based on spacecraft receiver automatic gain control (AGC) information obtained using the spacecraft omni-antenna, the *Pioneer VIII* telecommunications uplink carrier performance was apparently 4 dB below nominal during the first 4 mo. During the second half of the time period covered in this article, the uplink performance changed, and the channel 6 spacecraft receiver using the omni-antenna showed AGC readings only approximately 1.5 dB below the nominal design values. On the other hand, the spacecraft channel 7 receiver, using the directional spacecraft antenna, showed performance approximately 2 dB above the nominal design values during May, June, and July. The quoted performance deviations are within the spacecraft receiver AGC calibration tolerances and the measurement tolerances of the DSS uplink power levels. Since the S-band uplink carrier performance using the spacecraft high-gain antenna has a margin approximately 10 dB above the downlink carrier performance margin, the mentioned performance deviations did not affect the quality of the uplink performance. The operation of the uplink side-band power

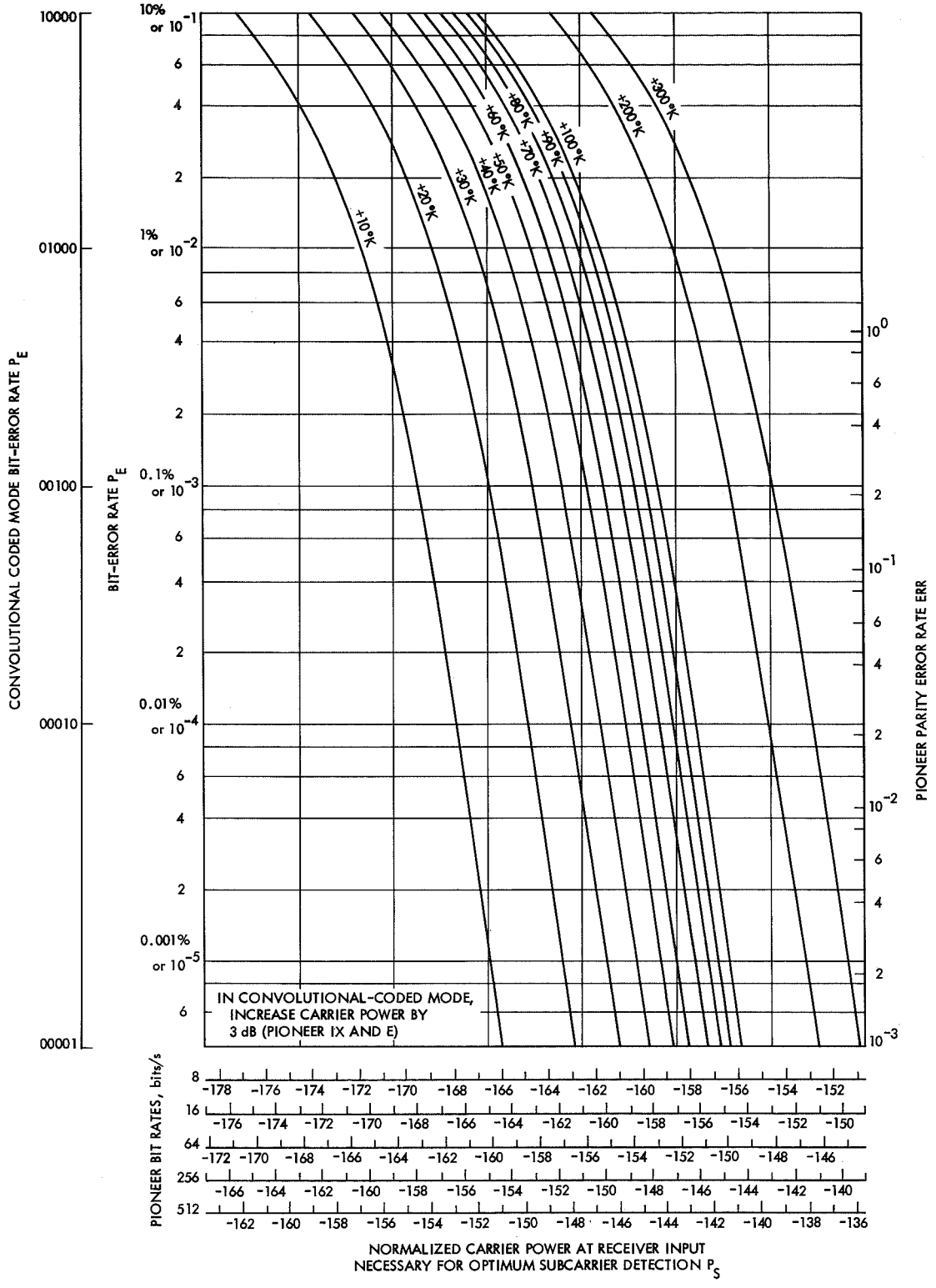

Fig. 5. Normalized carrier power necessary for optimum subcarrier performance

transmission and reception, carrying the command instructions to the spacecraft, was nominal and no erroneous commands have been detected by the spacecraft. The command side-band power margin, based on a bit-error rate of 10^{-5}, is approximately 3 dB higher than the margin of the uplink spacecraft carrier tracking loop.

Note that it is highly desirable to have high S/N prevailing in the spacecraft carrier tracking loop, which generates a best estimate of the S-band uplink carrier power received by the spacecraft receiver whose signal drives the downlink spacecraft transmitter. If the phase noise of the uplink signal best estimate can be kept low, the jitter modulation of the spacecraft downlink signal also will be low. This clear downlink S-band carrier signal is necessary not only to improve the precision of the two-way doppler spacecraft tracking signal, but also to improve the efficiency of the utilization of the downlink subcarrier power.

The spacecraft transmitter is driven by an auxiliary oscillator in the one-way downlink operational mode. This oscillator has a phase noise relatively higher than the best estimate of the uplink signal available at the output of the spacecraft receiver. Therefore, downlink jitter is generally less in the two-way mode than in the one-way mode. At increased spacecraft communications ranges, the S/N drops in the spacecraft receiver loop and the downlink phase jitter in the auxiliary oscillator one-way mode can be lower than in the two-way mode.

S-band downlink carrier and subcarrier performance. Since all *Pioneer* spacecraft are spin stabilized, their high-gain antennas always point toward earth after the completion of the Type II spin-axis orientation maneuver, and after the spacecraft is at least 2×10^6 to 3×10^6 km from earth. The radiated power level toward earth is, for many months, remarkably constant, and only very small antenna pointing errors, negligible output power fluctuations, and small subcarrier modulation index variations are present. Therefore, it was possible to develop the given analysis of the S-band downlink carrier and subcarrier power transfer efficiency. It should be noted, that the implementation of this technique in the DSN Monitoring System would make possible the near-real-time generation of *Pioneer* downlink performance residuals. This information would be not only useful for the preventive-type performance control of the DSN support, but can also be readily used by the *Pioneer* Project in the case of non-standard mission behavior. The study of the DSN performance residuals variations can help the task of isolating possible telecommunications downlink perturbances from other performance variations. In addition, the application of a similar method can also be used to normalize the DSN support performance analysis included in the quarterly DSN reports and the TDA final reports.

To obtain the telecommunications downlink performance efficiency values, the power levels, gains, and losses of all elements of the downlink have to be established and measured. All measurements are carried out with instruments calibrated by secondary standards. The calibration of the secondary standards is traced back to the primary standards in the possession of the National Bureau of Standards.

Every measurement has a tolerance that is the maximum deviation allowed from the specified nominal, or true, value. The tolerance is generally a function of the design complexity, precision, and configuration. It can also be affected by power-source voltage variations, temperature variations, and any physical changes (aging effects) that can affect, on a short- or long-term basis, the components of the equipment. The actual measured values are, in most cases, well within the extreme limits of the tolerance values.

The error in the given measurement may be defined as the difference between the value indicated by the measuring instrument and the "true" value of the measured quantity.

$$x = U_{\text{measured}} - U_{\text{true}}$$

The purpose of error analysis is to provide a description of the error that will permit its magnitude to be estimated for any set of operating conditions without running calibrations of tests for all possible combinations of conditions that may be encountered. In general, the error will vary with the time at which the measurement is made, the value of the quantity to be measured, and with the environmental conditions.

It is common practice to divide errors into systematic (or bias) and random (noise or accidental) components. The former are characterized by their predictability and may be corrected, at least partially, by a process of calibration applied to the instrument before and after the measurement. One calibration can determine the value of the initial bias error and will perhaps permit the reduction of the residual bias error to zero. Sometimes the error will assume some value within a limited range of values

centered around a mean error. For any measured set of n error values, the mean error can be determined using

$$\bar{x} = \frac{1}{n} \sum_{i=1}^{i=n} x_i$$

Other terms used to describe the magnitude of the error include the maximum (or peak) error Xm, the peak-to-peak error $Xp - p$, and the rms error X_{rms}. The latter is the square root of the mean value of the square of the individual error values.

To assess the S-band carrier and subcarrier performance of the *Pioneer* communications downlink, an attempt is made to analyze the correlation between the measured actual downlink carrier power P_A and actual SNT obtained by the DSN and the measured telemetry P_E or ERR generated by the TCP computer using a project-dependent program. All these measurements are constrained by measuring errors. To make the modeling of these errors possible, "normalized values" are used. Thus, by applying normalized references, which are not affected by systematic and random errors, the generation of carrier and subcarrier performance residuals has been made possible. Also, high confidence can be placed in the described performance analysis since the two variables, the downlink carrier power and the system noise temperature, are derived from three independent and semi-redundant measurements.

The performance of the *Pioneer VIII* telecommunications downlink can be analyzed from the data shown in Fig. 6. The actual P_A measurements made by the 85-ft antenna DSSs have been averaged for each pass and the weekly mean values have been calculated and displayed for a communications range of 2.5×10^6 to 60×10^6 km. The spread of these measurements is caused by the systematic and random measurement errors of the complex test equipment used. The solid line shown on the graph represents the planned nominal downlink carrier power versus the spacecraft/earth communications range in millions of kilometers. This line has been derived from Table 6. The same line is also used for the determination of the normalized downlink carrier power P_C levels. The P_C is the best estimate of the truth and it is also the mean value of all measurements made by the DSN during the first 9 mo.

The tolerance of downlink carrier power measurements is $\pm$ 2 dB. The bulk of the actual data points are well within this tolerance and, by using the P_C line, it can be stated that best estimates of the real value of the spacecraft signal power are within a band of $\pm$ 0.5 dB measured from the shown straight line. During the first 9 mo of the mission, the spacecraft high-gain antenna was pointing continuously toward the earth and the transmitter power output was constant. A regression analysis using least-square methods can further narrow the uncertainties. By using the P_C concept, it is possible to make visible the systematic and random errors of power measurements. The "normalized straight line" can also be used to pinpoint the presence of possible excess tolerances in the calibration of DSS equipment, as well as help to locate any man-made errors experienced in making a large number of complex precision measurements.

The SNT is measured (in °K) before, during, and after each *Pioneer* pass. The tolerance of these measurements around 45°K is approximately $\pm$ 0.5 dB. The assessment of SNT is necessary to establish the S/N between downlink carrier power and receiver noise power.

In order to make possible the analysis of the downlink subcarrier power performance of the *Pioneer VIII* spacecraft, two basic relationships should be noted. First, the *Pioneer VIII* spacecraft uses a 2048 Hz square-wave subcarrier signal with a constant phase modulation index of 0.9-rad peak. This subcarrier is phase-shift switched on telemetry bit rates of 512, 256, 64, 16 and 8 bits/s. Because of a constant PSK peak deviation of the carrier, there is a fixed relationship between the S-band downlink carrier and subcarrier power (subcarrier power is equal to the carrier power plus 1.9 dB). Second, the subcarrier ST_B/N_0 is a direct function of the telemetry P_E or ERR. Since the *Pioneer VIII* TCP program automatically monitors the telemetry words having a parity error, a direct measure of the ST_B/N_0 relationship is available. The subcarrier ST_B is proportional with the subcarrier power (Table 6), which in turn is also proportional with the carrier power. The subcarrier ST_B can be directly referenced to the carrier power. Also, the N_0 is a fixed function of the S/N. For any bit rate, a carrier power level can be established, which is necessary for optimum subcarrier detection P_S.

The *Pioneer VIII* P_E is determined by the ERR, which is equal with the number of telemetry word parity errors divided by the number of telemetry frames. The ERR of 0.116 is equal to a P_E of five errors in 10,000 bits, or 5×10^{-4}. The computer detects and accumulates the parity errors for 12 min, and the teletype printout appears at the end of each computation.

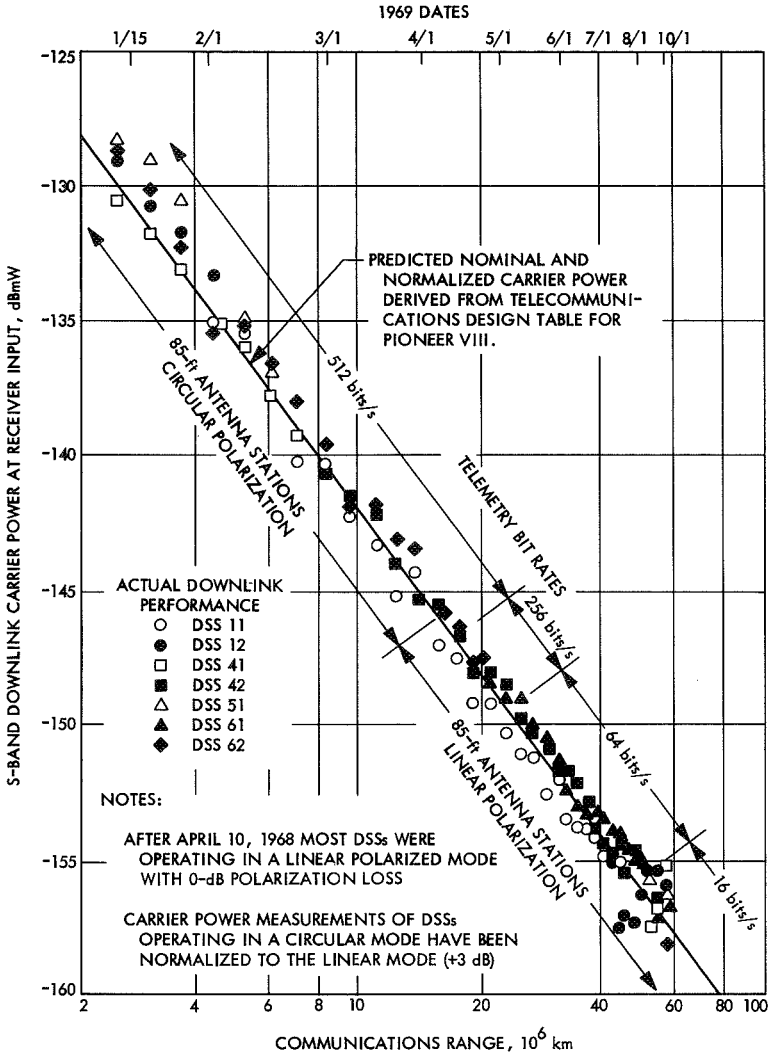

Fig. 6. Normalized carrier power necessary for optimum telecommunications downlink performance of *Pioneer VIII*

Figure 5 depicts the P_C necessary for P_S performance analysis for *Pioneer VIII*. The right side vertical scale includes all possible *Pioneer VIII* ERR values. This scale can be converted to P_E using the left vertical scale. The bottom horizontal scales indicate the P_C levels at the receiver input necessary for P_S. For each *Pioneer VIII* telemetry bit rate, a separate scale is made available. The slanted curves are given to cover SNT from 10 to 300°K.

Figure 7 indicates the normalized additional power required above perfect PSK coherent detection for *Pioneer VIII*. The solid lines are a measure of the additional sideband power required to compensate for S/N degradation of the *Pioneer* GOE demodulator/bit synchronizer and DSS receiver band limiter (Ref. 4). The dotted lines represent the normalized additional sideband power required to compensate for sideband power drop caused by two-way uplink–downlink jitter, one-way downlink jitter, charged-particles jitter, and additional sun noise. This value has been determined by numerous measurements made during *Pioneer VI, VII* and *VIII* tracks and is a normalized best estimate.

The total additional normalized sideband power required above the perfect PSK coherent detection is given for each *Pioneer* telemetry bit rate by the round dots on Fig. 7. This additional sideband power is required above the ST_B/N_0 perfect detection values shown in Fig. 4. The P_C scales of Fig. 5 have been computed from the ST_B/N_0 values, and the additional power as shown in Fig. 7 has

Table 7. *Pioneer VIII* S-band telecommunications downlink performance analysis

Date	DSS	Bit rate, bits/s	Communications range[a], 10^6 km (±0.1 dB)[b]	DSS antenna polarization[c] (±0.1 dB)	SNT[d], °K (±0.5 dB)	ERR[d] (±1.5 dB)	Carrier power			Performance residuals	
							Actual measured at DSS[d], dBmW P_A (±2 dB)	Normalized for optimum performance			
								Carrier[e], dBmW P_C (±0.5 dB)	Subcarrier[f], dBmW P_S (±0.2 dB)	Carrier[g], dB $P_A - P_C$ (±2 dB)	Subcarrier[g], dB $P_C - P_S$ (±1.5 dB)
3/22	61	512	12.3	C	51.5	0.186	−146.7	−147.0	−147.2	0.3	0.2
4/1	62	512	14.5	C	43	0.179	−147.2	−148.1	−148.0	0.9	−0.1
4/11	62	512	17.0	L	47	0.034	−145.8	−146.7	−146.6	0.9	−0.1
4/17	62	512	18.5	L	46	0.181	−147.1	−147.7	−147.8	0.6	0.1
4/25	62	256	20.6	L	46	0.005	−147.8	−148.2	−148.8	0.5	0.6
7/29	42	64	46.8	L	48	0.110	−156.0	−155.2	−155.7	−0.8	−0.5
8/10	12	64	48.5	L	42	0.090	−155.5	−155.9	−155.3	0.4	−0.6
8/12	61	16	48.9	C	46	0.010	−158.5	−159.0	−159.1	0.5	0.1
8/13	42	64	49.1	L	39.8	0.036	−156.1	−156.0	−155.7	−0.1	−0.3
8/15	61	16	49.5	C	45	0.007	−158.5	−159.1	−158.9	0.6	−0.2
8/16	62	64	49.6	L	38	0.136	−156.3	−156.0	−155.6	−0.3	−0.4
8/18	42	64	50.2	L	48	0.100	−155.7	−156.2	−155.6	0.5	−0.6
8/19	62	64	50.1	L	38.9	0.179	−157.1	−156.2	−157.1	−0.9	0.9
9/1	12	64	52.2	L	42.4	0.160	−155.6	−156.5	−156.6	0.9	0.1
9/19	51	16	56.9	C	40.4	0.009	−159.3	−160.2	−159.7	0.9	−0.5

[a]From trajectory tables.

[b]The values in parentheses are tolerances.

[c]C indicates circular (−3 dB) polarization mode. L indicates linear (0 dB) polarization mode.

[d]Measured at DSS.

[e]From chart: Normalized carrier power necessary for optimum *Pioneer* telecommunications downlink performance.

[f]Normalized carrier power necessary for optimum *Pioneer* subcarrier detection performance.

[g]Carrier mean value of fifteen TDA tracks is 0.3. Subcarrier mean value is −0.1.

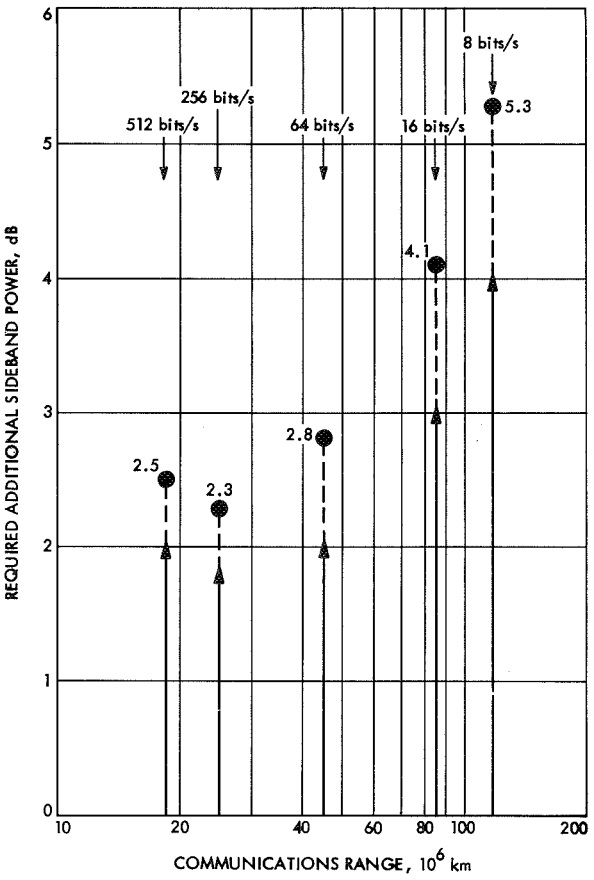

Fig. 7. *Pioneer VIII* additional sideband power required above perfect PSK coherent detection

been added. Thus, the subcarrier power levels have been converted to carrier power values.

Table 7 shows the performance evaluation of 15 typical *Pioneer VIII* passes. After listing the spacecraft number, date, pass number, DSS number and bit rate, the communications ranges have been taken from the *Pioneer VIII* trajectory tables generated by the DSN. It should be noted that there is a difference between polarization modes. The carrier and subcarrier power levels are 3 dB lower in the circular polarized receiving mode than in the linear mode. The SNT is a regular DSS measurement; the ERR is taken from the *Pioneer* engineering telemetry teletype printout. The P_A is depicted from the DSN logs. The P_C necessary for optimum carrier performance is taken from Fig. 6. The P_S is taken from Fig. 5. The performance residuals for the carrier and subcarrier are computed from $P_A - P_C$ and $P_C - P_S$. If these residuals are within a predetermined limit range governed by the given tolerances, the DSN performance status is *green* (as was the case for the 15 passes evaluated in Table 7). In this case, it can be stated that the performance of the complete telecommunications downlink was nominal and all communications elements of the spacecraft and DSN were functioning within the predicted performance limits. If the performance status is *red*, the trend of the discrepancies can indicate the possible causes of telecommunications link degradation. Using the described performance analysis, it can be stated that during the first 9 mo of the *Pioneer VIII* mission, the downlink carrier and subcarrier performance was nominal and the DSN has met its commitments pertaining to the quality of the downlink TDA services.

References

1. *Reference Data for Radio Engineers*, Fifth Edition. Howard W. Sams & Co., Inc., Indianapolis, Ind. 1968.
2. Tausworthe, R. C., *Theory and Practical Design of Phase-Locked Receivers: Volume I*, Technical Report 32-819. Jet Propulsion Laboratory, Pasadena, Calif., Feb. 15, 1966.
3. Tausworthe, R. C., "Cycle Slipping in Phase Locked Loop," *IEEE Trans. Commun. Technol.*, Vol. Com-15, No. 3, June 1967.
4. Lindsey, W. C., *Performance of Phase-Coherent Receivers Preceded by Band Pass Limiters*, Technical Report 32-1162. Jet Propulsion Laboratory, Pasadena, Calif., Sept. 15, 1967.
5. Viterbi, A. J., *Principles of Coherent Communication*. McGraw-Hill Book Co., Inc., New York, 1966.

B. Planetary Flight Projects

1. *Mariner* Mars 1971 Mission Support, D. J. Mudgway

a. Introduction. During the current reporting period, the DSN continued activity in the planning and coordination phases of support for the *Mariner* Mars 1971 orbiter project. At the present time, there are several very active project working groups in operation, all of which are supported by the DSN. It is through these groups that the processes of negotiation and iteration to match the DSN capability with the project's requirements are accomplished.

b. Planning. The DSN plans to support *Mariner* Mars 1971 deep space operations with DSSs 14 (210-ft-diam antenna), 12, 41, and 62. Subject to other NASA projects' requirements, an additional set of 85-ft-diam antenna stations may be available for a few weeks prior to orbit insertion to provide capability for obtaining two-way doppler and command capability to both spacecraft simultaneously.

The 210-ft-diam antenna station will have the capability to receive telemetry at all bit rates, both coded and uncoded, from two spacecraft simultaneously. It will also be able to command and obtain metric data from both spacecraft simultaneously. It will not be able to receive two 16-kbps coded data streams at the same time that it is commanding two spacecraft simultaneously.

The 85-ft-diam antenna network can receive coded data from both spacecraft simultaneously, and can command and receive metric data from one spacecraft at a time. It is, however, constrained by the telecommunications link design to an upper limit of 2 kbps for coded data.

All video data from the 210-ft-diam antenna station will be delivered to the mission support area in the SFOF in real time or near-real time (20-min delay). Telemetry and metric data will arrive in real time. One 2-kbps video data stream only will be available in real time from the 85-ft-diam antenna stations; the other video data stream will be recorded at the station and played back after the pass. In all cases, the DSN expects to deliver the video data to the SFOF within 14 h of receipt. Metric and low-rate telemetry data from the 85-ft-diam antenna stations will be available in real time, as for the 210-ft-diam antenna station.

The *Mariner* Mars 1971/DSN capabilities planning team has completed its task of designing the baseline capabilities of each of the DSN systems required for *Mariner* Mars 1971 support. Functional diagrams with descriptive material for software and hardware, together with a set of technical performance criteria, now exist for each of the DSN telemetry, tracking, command, monitor, and simulation systems. These are used as inputs representing *Mariner* Mars 1971 requirements to the DSN system requirements series of documents. The functional diagrams for the telemetry system are presented in Fig. 8 (85-ft-diam antenna network) and Fig. 9 (DSS 14). The functional diagrams for the other DSN systems will be presented in subsequent SPS issues. These are working diagrams in the sense that they will be modified occasionally as the system design is solidified.

Figure 8 is divided (left to right) into DSIF, GCF, and SFOF. Figure 9 is divided (left to right) into DSIF, GCF, CTA, and SFOF. Each facility is shown as a group of component subsystems connected with data flow paths. Table 8 lists nomenclature used in Figs. 8 and 9 and Tables 9–12. Table 9 provides numbered notes (①, ②, etc.) which describe the contents of data flow paths in Fig. 8. Table 10 provides alphabetic notes (A, B, etc.) which describe hardware/subsystem capabilities in Fig. 8. Table 11 describes data flow paths in Fig. 9, and Table 12 describes hardware/subsystem capabilities in Fig. 9.

Table 8. Nomenclature

ADC	analog-to-digital converter
AGC	automatic gain control
BMXR	block multiplexer
BSMF	bit sync matched filter
CP	communications processor
CTA	compatibility test area
DEMXR	demultiplexer
DTSS	DSIF tracking subsystem
HSD	high-speed data
I/O	input/output
MDR	master data record
MUX	multiplexer
ODR	original data record
SDA	subcarrier demodulation assembly
S/N	signal-to-noise ratio
SPE	static phase error
SSMF	symbol sync matched filter
TTY	teletype

In cases where the appropriate facility representative to the capabilities planning team determined that a specific hardware item would be used in the *Mariner* Mars 1971 time frame, that item is shown in Figs. 8 and 9, for example: 920, 7044, M-BOX, CP, and BMXR. In other cases, more general functional descriptions are used, for example: DTSS, DEMXR, and command waveform generator and mode control.

c. Schedules. Implementation schedules for the tracking and data acquisition system, the Deep Space Network, and the near-earth phase have been published.

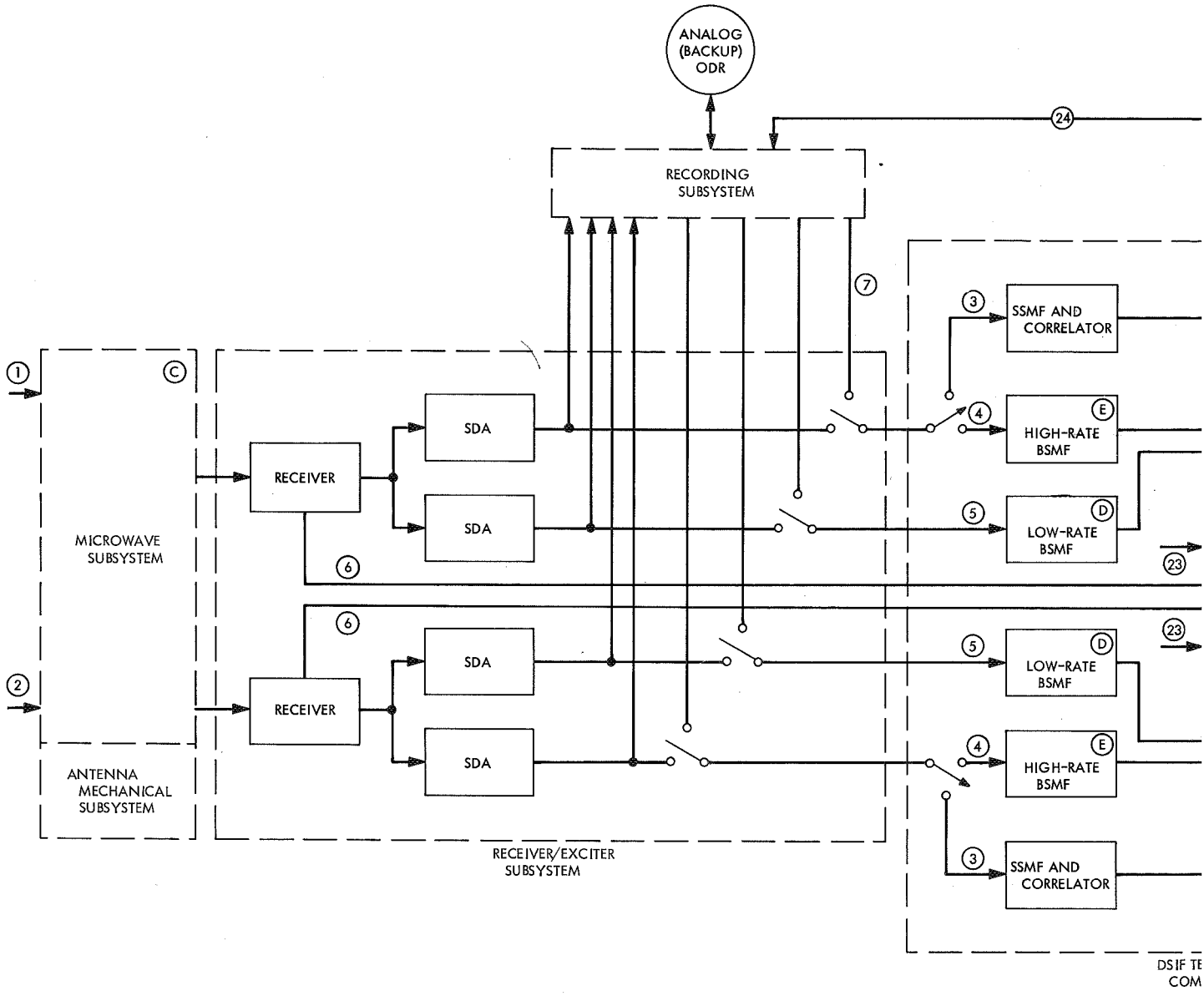
ANALOG (BACKUP) ODR
RECORDING SUBSYSTEM
24
7
3
SSMF AND CORRELATOR
1
C
SDA
4
E
HIGH-RATE BSMF
RECEIVER
SDA
5
D
LOW-RATE BSMF
MICROWAVE SUBSYSTEM
6
23
6
23
SDA
5
D
LOW-RATE BSMF
2
RECEIVER
SDA
4
E
HIGH-RATE BSMF
ANTENNA MECHANICAL SUBSYSTEM
3
SSMF AND CORRELATOR
RECEIVER/EXCITER SUBSYSTEM
DSIF TE
COM

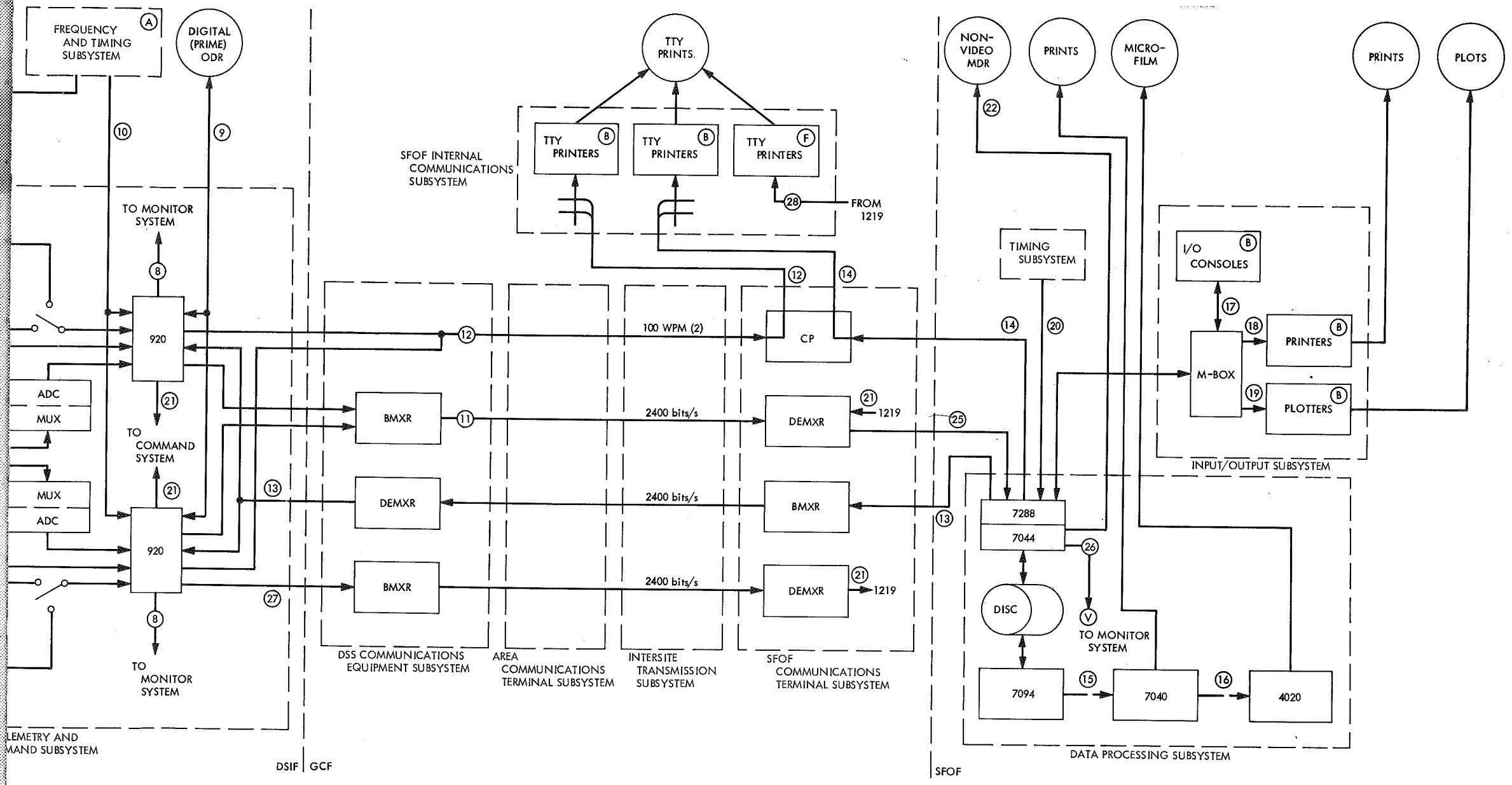

Fig. 8. Telemetry system for 85-ft-diam antenna network

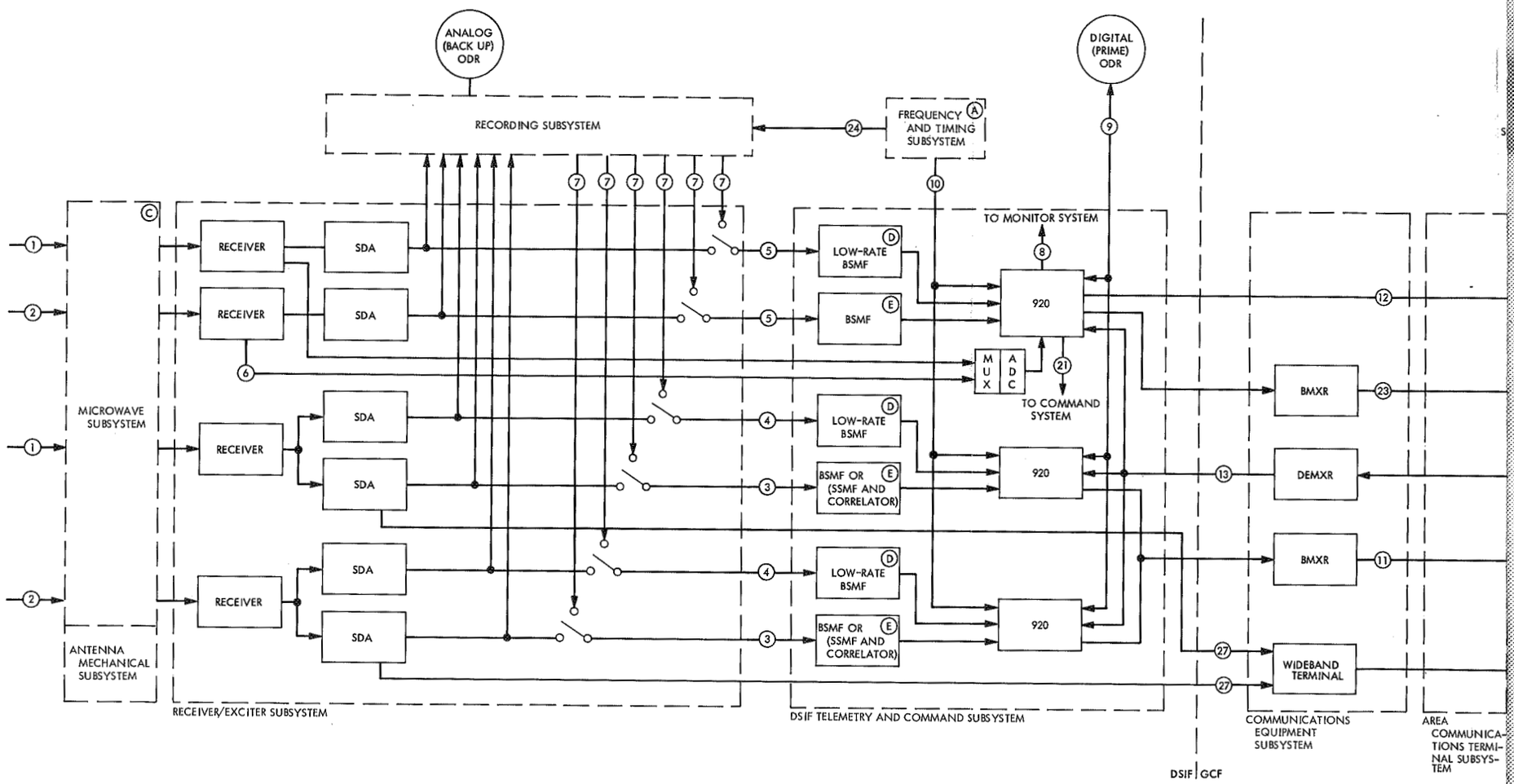

Fig. 9. DSS 14 orbital phase telemetry system

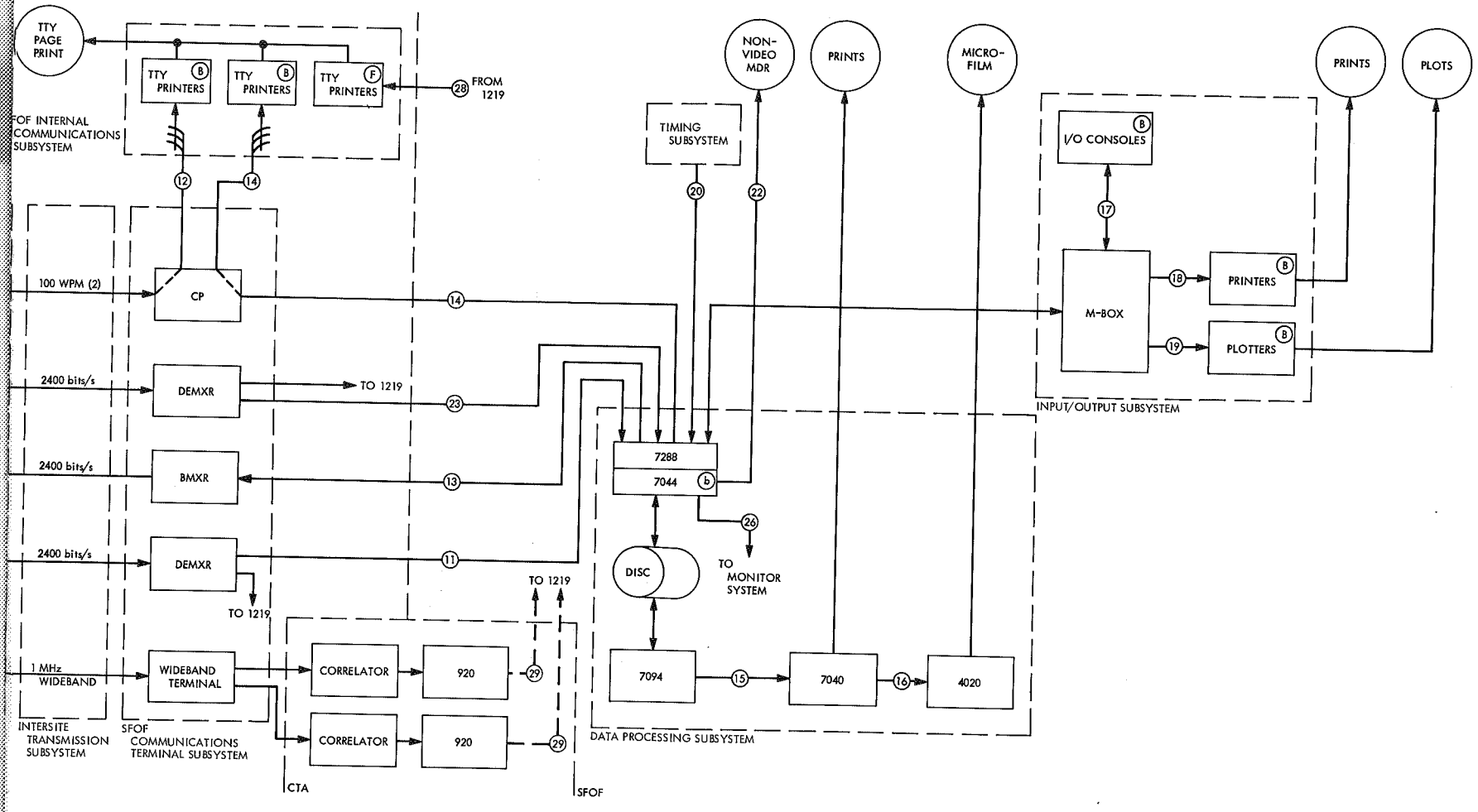
TTY PAGE PRINT
TTY PRINTERS B
TTY PRINTERS B
TTY PRINTERS F
28 FROM 1219
FOF INTERNAL COMMUNICATIONS SUBSYSTEM
12
14
100 WPM (2)
CP
14
2400 bits/s
DEMXR
TO 1219
23
2400 bits/s
BMXR
13
2400 bits/s
DEMXR
11
TO 1219
TO 1219
1 MHz WIDEBAND
WIDEBAND TERMINAL
CORRELATOR
920
29
CORRELATOR
920
29
INTERSITE TRANSMISSION SUBSYSTEM
SFOF COMMUNICATIONS TERMINAL SUBSYSTEM
CTA
SFOF
NON-VIDEO MDR
PRINTS
MICRO-FILM
TIMING SUBSYSTEM
20
22
7288
7044 b
26
DISC
TO MONITOR SYSTEM
7094
15
7040
16
4020
DATA PROCESSING SUBSYSTEM
I/O CONSOLES B
17
M-BOX
18
PRINTERS B
19
PLOTTERS B
INPUT/OUTPUT SUBSYSTEM
PRINTS
PLOTS

Table 9. Description of data flow paths for 85-ft-diam antenna telemetry system (Fig. 8)

Number	Data flow path description	Number	Data flow path description
(1)	Carrier from spacecraft 1	(14)	TTY page printer output from 7044
(2)	Carrier from spacecraft 2	(15)	Manual movement of digital tapes, for printing and plotting
(3)	2.025-kbps or 1.0125-kbps video data (coded)	(16)	Manual movement of digital tapes, formatted for microfilm prints and plots
(4)	8⅓- or 133⅓-bps science data (uncoded)	(17)	Processing control messages and status
(5)	33⅓- or 8⅓-bps engineering data (uncoded)	(18)	3070 printer outputs from 7044
(6)	Ground AGC (analog) and SPE (analog)	(19)	30 × 30 plotter outputs from 7044
(7)	Playback of previously recorded SDA outputs	(20)	Time
(8)	Computer-to-computer outputs: periodic status (bit, word, and frame sync; data output and recording frame/block totals, etc.), spacecraft AGC and SPE, S/N data, data loss alarm, tape loss alarm, and other required alarms	(21)	Spacecraft AGC, SPE, and other parameters for telemetry data for command system—teletype form
(9)	Digital recording of all 920 data inputs—one for recording each spacecraft. Prime ODR for both video and non-video data. Also, replay of ODR.	(22)	Non-video MDR data (may require subsequent supplementing with ODR)
(10)	Time for time-tagging data	(23)	At present, cross-connected ground AGC and SPE
(11)	HSD to SFOF: (1) engineering data from both spacecraft; (2) science data from both spacecraft, video data from one 920 only; (3) replay of ODR; (4) DSS telemetry system partial status, consisting of ground AGC and SPE from both receivers and selected hardware status data	(24)	Time for time-track of recording
		(25)	Same as (11) without video
		(26)	SFOF telemetry system alarms: periodic status (sync, data output, number of records made, data block errors detected, etc.); data loss alarms (tape, display, to communications, or in certain programs)
(12)	TTY to SFOF—raw digitized engineering data from both spacecraft (backup only)	(27)	One 2.025- or 1.0125-kbps video stream
(13)	HSD from SFOF to DSIF: (1) Telemetry standards and limits, (2) DSS initialization	(28)	Error messages from GCF error detection process performed by 1219 for DSN

Table 10. Description of subsystem/equipment capabilities for 85-ft-diam antenna telemetry system (Fig. 8)

Letter	Subsystem/equipment capability
(A)	Output time accurate to 10 ms
(B)	Located in mission support areas and DSN telemetry operations area in the following quantities:

Equipment	Project	DSN
Printer	6	1
Plotter	4	1
7044 TTY	24	6
TTY	5	2
I/O console	3	1

(C)	System temperature: 65°K or less at 10 deg or more above horizon
(D)	8⅓ to 33⅓ bps (uncoded)
(E)	8⅓ to 2000 bps (uncoded)
(F)	TTY page printers located in DSN telemetry area and GCF control

Table 11. Description of data flow paths for DSS 14 orbital phase telemetry system (Fig. 9)[a]

Number	Data flow path description
①	Carrier from spacecraft 1
②	Carrier from spacecraft 2
③	16.2-, 8.1-, 4.05-, 2.025-, or 1.0125-kbps video data (coded), or 133⅓-bps uncoded science data
④	8⅓-bps science data (uncoded)
⑤	33⅓- or 8⅓-bps engineering data (uncoded)
⑥	Ground AGC (analog) and SPE (analog)
⑦	Playback of previously recorded SDA outputs
⑧	Computer-to-computer outputs: spacecraft AGC and SPE, S/N data, and other required alarms
⑨	Digital recordings (3) of all 920 data inputs, one recording for each 920; prime ODR for video and non-video data; replay of ODR
⑩	Time for time-tagging data
⑪	HSD to SFOF, maximum of: (1) engineering data from both spacecraft; (2) science data from both spacecraft, no coded video; (3) replay of ODR (not simultaneous with 1 and 2); (4) DSS telemetry system partial status, consisting of ground AGC and SPE from two receivers and selected hardware status data
⑫	TTY to SFOF—raw digitized engineering data from both spacecraft (backup only)
⑬	HSD from SFOF to DSIF: (1) telemetry standards and limits, (2) DSS initialization
⑭	TTY page printer output from 7044
⑮	Manual movement of digital tapes, for printing and plotting
⑯	Manual movement of digital tapes, formatted for microfilm prints and plots
⑰	Processing control messages and status
⑱	3070 printer outputs from 7044
⑲	30 × 30 plotter outputs from 7044
⑳	Time
㉑	Spacecraft AGC, SPE, and other parameters for telemetry data for command system—teletype form
㉒	Non-video MDR data (may require later supplementing with ODR)
㉓	HSD to SFOF: engineering data from both spacecraft, AGC and SPE from both receivers, and hardware status data, in real time or ODR replay
㉔	Time for time-track of recording
㉕	Not used
㉖	SFOF telemetry system alarms: periodic status (sync, data output, number of records made, data block errors detected, etc.); data loss alarms (tape, display, to communications, or in certain programs).
㉗	Coded video data (analog)
㉘	Error messages from GCF error detection process performed by 1219 for DSN
㉙	Digital recording of video data, manually transported from CTA to 1219

[a]Cruise phase is identical with 85-ft-diam antenna telemetry system (Fig. 8).

Table 12. Description of subsystem/equipment capabilities for DSS 14 orbital phase telemetry system (Fig. 9)

Letter	Subsystem/equipment capability
Ⓐ	Output time accurate to 10 ms
Ⓑ	Located in mission support areas and DSN telemetry operations area in the following quantities:

Equipment	Project	DSN
Printer	6	1
Plotter	4	1
7044 TTY	24	6
TTY	5	2
I/O console	3	1

Ⓒ	System temperature: 45°K or less at 10 deg or more elevation
Ⓓ	8⅓ or 33⅓ bps (uncoded)
Ⓔ	8⅓ to 133⅓ bps (uncoded) in BSMF mode; 16.2 kbps maximum (coded) in SSMF plus cross correlator mode
Ⓕ	TTY page printers located in DSN telemetry area and GCF control

These schedules are keyed to the mission operations system and spacecraft system schedules and provide for achieving operational readiness of the DSN in December 1970, at which time the network will be made available to the project for training and testing on an operational basis in preparation for launch readiness in May 1971.

The second project quarterly review was held. A preliminary issue of the DSN Operations Plan, Volume I, was published, describing the estimated tracking support which will be available during the *Mariner* Mars 1971 period.

C. Manned Space Flight Project

1. Apollo Mission Support, P. S. Goodwin

a. Introduction. The DSN support provided to the MSFN during the first manned flight (*Apollo* 7) was described in SPS 37-55, Vol. II, pp. 8–10. The support provided during the second manned mission (*Apollo* 8, AS-503) is described here.

b. Apollo 8 mission description. While *Apollo* 8 was the second manned *Apollo* mission, it was the first manned *Apollo* mission flown aboard the three-stage *Saturn* V launch vehicle, and it carried astronauts Frank Borman (spacecraft commander), James A. Lovell, Jr. (command module pilot), and lunar module pilot William A. Anders on an historic flight to the vicinity of the moon and ten lunar orbits before returning to a successful splashdown in the Pacific Ocean 147 h later.

Apollo 8 was launched from Pad 39-A at Cape Kennedy on December 21, 1968, at 12:51:00.92 GMT on a launch azimuth of 72.12 deg. It was inserted into a 103-nmi circular earth orbit by a complete burn of the *S-IC* booster stage, followed by a complete burn of the *S-II* second stage, and a partial burn of the *S-IVB* third-stage vehicle. During the second revolution, the *S-IVB* stage was reignited over the Pacific Ocean and *Apollo* 8 was injected into a lunar transfer orbit. After injection into lunar transfer orbit, the command service module (CSM) separated from the *S-IVB* third stage and performed a practice transposition maneuver with the *S-IVB* stage that will be required on later missions when the lunar module is actually carried aboard the interstage adapter between the *S-IVB* third stage and the command service module. The lunar module was not carried aboard *Apollo* 8.

Following a separation maneuver and two small midcourse corrections, *Apollo* 8 deboosted into an elliptical lunar orbit measuring approximately 60 by 170 nmi. After two such elliptical orbits around the moon, the *Apollo* 8 service propulsion system was burned again to place it into a circular lunar orbit of about 60 nmi. This was followed by eight additional orbits around the moon, then an additional burn of the service propulsion system aboard the command service module for injection into an earth transfer orbit. The trajectory was so precise that only one midcourse correction was required on the return flight.

Prior to reentering the earth's atmosphere, the command module portion of the CSM separated from the service module portion and assumed a proper attitude for entering the earth's atmosphere in the planned aerodynamic skip profile, which was so precise that the command module splashed down a mere 5,000 yd from the carrier U.S.S. Yorktown, southwest of Hawaii. The separated service module portion entered the atmosphere on a ballistic trajectory and was consumed by heat. Upon arrival of the three astronauts aboard the carrier Yorktown on December 28, 1968, the first attempt to reach the vicinity of the moon by manned flight was successfully completed. A listing of the significant events of this journey is shown in Table 13, expressed as ground-elapsed time or time from launch.

c. Requirement for DSS 14 210-ft-diam antenna. The successful checkout of the *Apollo* CSM during the *Apollo* 7 mission (SPS 37-55, Vol. II) created confidence that the *Apollo* 8 mission could be upgraded from an earth-orbital mission to a lunar-orbital mission. There was, however, one item aboard the CSM that had not been previously checked out in space – the spacecraft's multiple beamwidth high-gain antenna system. Should this system fail while the *Apollo* spacecraft was near the moon, there would be insufficient signal strength received by the 85-ft-diam antenna MSFN/DSN ground stations to detect the *Apollo* high bit-rate telemetry signal. Since such a situation was considered undesirable, NASA Headquarters decided to guard against this possibility by requesting support from the DSS 14 210-ft-diam antenna during the *Apollo* 8 mission.

d. Reconfiguration of DSS 14 for Apollo 8. When the *Apollo* requirement was received, DSS 14 control room equipment was being moved from the antenna pedestal to a new control room. To support *Apollo* 8, it became necessary to accelerate portions of this move as well as to improvise temporary arrangements. In addition, a

Table 13. *Apollo 8* sequence of events (nominal mission)

Time from lift-off,[a] h:m:s	Event[a]
00:00:00	Lift-off
00:01:17	Maximum dynamic pressure
00:02:06	*S-IC* center engine cutoff
00:02:31	*S-IC* outboard engine cutoff
00:02:32	*S-IC/S-II* separation
00:02:33	*S-II* ignition
00:02:55	Camera capsule ejection
00:03:07	Launch escape tower jettison
	Mode I/mode II abort changeover
00:08:40	*S-II* cutoff
00:08:41	*S-II/S-IVB* separation
00:08:44	*S-IVB* ignition
00:10:06	Mode IV capability begins
00:10:18	Mode II/mode III abort changeover
00:11:32	Insertion into earth parking orbit
02:50:31	Translunar injection ignition
02:55:43	Translunar injection cutoff
	Translunar coast begins
03:09:14	*S-IVB*/CSM separation
04:44:54	Begin maneuver to slingshot attitude
05:07:54	Liquid oxygen dump begins
05:12:54	Liquid oxygen dump ends
(*TLI* + 6 h)	Midcourse correction 1
(*TLI* + 25 h)	Midcourse correction 2
69:07:29	Lunar orbit insertion (LOI_1) initiation
69:11:35	Lunar orbit insertion (LOI_1) termination
73:30:53	Lunar orbit insertion (LOI_1) initiation
73:31:03	Lunar orbit insertion (LOI_1) termination
89:15:07	Trans-earth injection initiate
89:18:33	Trans-earth injection terminate
(TEI + 15 h)	Midcourse correction
146:49:00	Entry interface
147:00:00	Splashdown

[a]TLI = translunar injection; LOI = lunar orbit insertion; TEI = trans-earth injection.

workable interface between DSS 14 and the MSFN *Apollo* prime station at Goldstone had to be developed to deliver the signals received by DSS 14 to the MSFN for processing and subsequent remoting to the Mission Control Center at Houston. Since there was insufficient time to install a new microwave link for this purpose, it was necessary to use existing facilities.

Unfortunately, the existing DSS intersite microwave system at Goldstone did not have passband characteristics such that the raw *Apollo* signals could be simply remoted to the MSFN *Apollo* prime station for demodulation and decommutation. A cooperative effort was then undertaken wherein both the MSFN and the DSN pooled their resources and efforts in an attempt to find a quick solution to the problem. An *Apollo* signal data demodulator subsystem (SDDS) was borrowed from the MSFN *Apollo* prime station and placed in the communications room in the basement of the new control building at DSS 14 (Fig. 10). The SDDS provided a suitable interface between the DSS 14 receivers and the DSIF Goldstone intersite microwave system. This interface, together with the microwave routing employed for *Apollo 8*, is shown in block diagram form in Fig. 11.

The *Apollo 8* requirement also imposed two new operational interfaces. First, the DSS 14 antenna feed system does not have auto-track capability. It was, therefore, necessary to make arrangements to have the MSFN and/or the Manned Spacecraft Center provide timely spacecraft state vectors in order that the SFOF might generate station predictions and/or drive tapes for each phase of the *Apollo 8* mission that required DSS 14 support. This support was required whenever the *Apollo 8* spacecraft was at a range of 50,000 mi or more from the earth. New state vectors would be needed after every engine burn by the *Apollo* spacecraft. Both preflight nominal and inflight actual state vectors were received during the *Apollo 8* mission via the interface routing indicated in Fig. 11.

The other operational interface requirement resulted from the fact that DSS 14 personnel had no previous operational experience in a manned mission and there was insufficient time for them to undergo formal training prior to launch. DSS 14 and the *Apollo* prime station exchanged selected personnel who conducted accelerated briefings on the operational use and techniques of their respective networks. Also, arrangements were made to exchange high-level "interpreters" who would be stationed at the other's facility during the mission to explain proceedings and coordinate combined efforts.

e. DSN support for Apollo 8 mission operations. *Apollo 8* was the first mission wherein all of the supporting DSSs were fully committed to the mission. In the

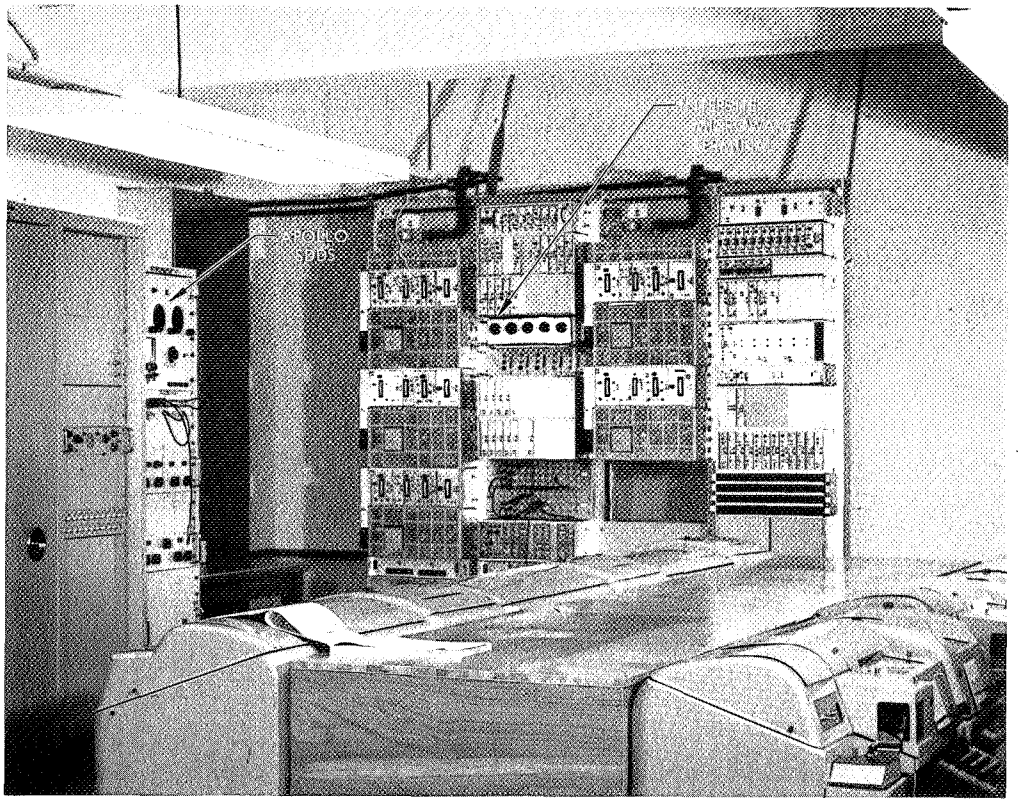

Fig. 10. *Apollo* signal data demodulator subsystem installed in DSS 14 communications room

previous *Apollo* missions, this support was on a best-efforts basis and used for training purposes. When *Apollo 8* became a lunar-orbital mission, support from the DSSs became a first requirement and a formal commitment was made to support the mission. This support is best described by the phases of the *Apollo* mission.

Launch phase. The Cape Kennedy compatibility test station (CTS) supported the *Apollo 8* prelaunch and launch activities in a manner identical with the support previously provided for *Apollos 4, 5, 6,* and 7. The station was configured in a manner identical to that for the *Apollo 4* mission (SPS 37-50, Vol. II, pp. 27–33), i.e., the CSM S-band downlink was received at the Cape Kennedy CTS and the detected phase-modulated telemetry baseband was relayed to the MSFN station on Merritt Island for processing. This arrangement provides backup during launch in case the MSFN Merritt Island station experiences signal-level difficulties due to either multipath propagation phenomena or flame attenuation phenomenon from liftoff to horizon loss of signal.

The Cape Kennedy CTS participated in the prelaunch countdown demonstration test and proceeded to provide support through the terminal count and subsequent launch of *Apollo 8* at 12:51:00.92 GMT on December 21, 1968. The received signal strength at the Cape Kennedy CTS from launch to horizon loss is shown in Table 14. No anomalies were experienced and the mission support from the Cape Kennedy CTS was terminated at horizon loss of signal on the launch phase.

Earth-orbital phase. The subearth tracks of the first two revolutions of *Apollo 8* were such that the spacecraft was seen briefly by DSSs 42 and 11, but not by DSS 61. Though these stations are not formally committed to support the earth-orbital phase of *Apollo* missions, the stations do participate in the terminal count and attempt to acquire the spacecraft during those earth-orbital passes that are within view of the station.

Experience on previous *Apollo* flights has shown that the angular rates while in earth-orbit frequently exceed the rate capability of these antennas. Such was the case during *Apollo 8* revolution 1 over DSS 42. In addition, that station simultaneously experienced an overloading of the receiver front end due to a combination of strong received signal strength from the spacecraft together with a gain saturation created by the installation, just prior to the mission, of a transistor follow-on amplifier behind the

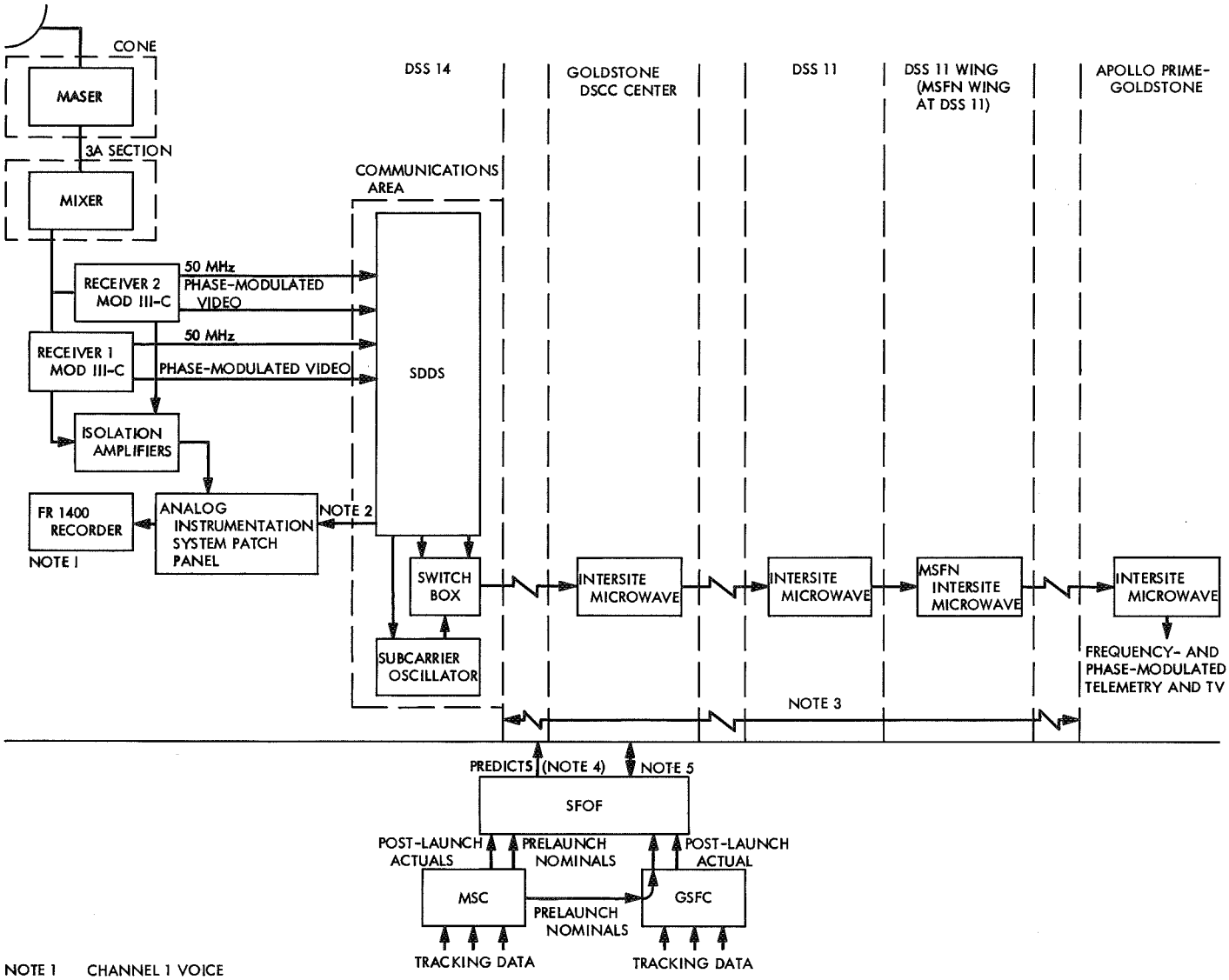

NOTE 1
CHANNEL 1 VOICE
CHANNEL 2 51.2-kbit STREAM
CHANNEL 3 SPACECRAFT VOICE (RECEIVER 1, PHASE MODULATED)
CHANNEL 4 36-bit SERIAL TIME
CHANNEL 5 SPACECRAFT VOICE (RECEIVER 2, FREQUENCY MODULATED)
CHANNEL 6 51.2-kbit STREAM
CHANNEL 7 STATION PARAMETERS

NOTE 2
PHASE-MODULATED TELEMETRY
PHASE-MODULATED VOICE
FREQUENCY-MODULATED TELEMETRY
FREQUENCY-MODULATED VOICE

NOTE 3
29-pt ACQUISITION MESSAGE TELETYPE
HOUSTON-MSFN COORDINATION
VOICE, SPACECRAFT EMERGENCY VOICE, HOUSTON-SPACECRAFT NET 1
MAINTENANCE ORDER WIRE
VOICE, HOTLINE MAINTENANCE AND OPERATIONS SUPERVISOR
VOICE, RECEIVER OPERATIONS COORDINATION (UNIFIED S-BAND)

NOTE 4
STATE VECTORS FROM MSC AND GSFC ARE CONVERTED TO DSS 14 PREDICTS IN INERTIAL CARTESIAN COORDINATES

NOTE 5
COMMUNICATIONS COORDINATION NET FOR JPL TRACK

Fig. 11. Special DSS 14 configuration for *Apollo 8*

Table 14. *Apollo* 8 Cape Kennedy CTS launch support[a]

Time, GMT	Receiver 1 automatic gain control, dBm
12:51:00	−68.8
12:51:30	−65.4
12:52:00	−66.9
12:52:30	−69.2
12:53:00	−83.9
12:53:30	−97.5
12:54:00	−111.6
12:54:30	−118.4
12:55:00	−121.2
12:55:30	−120.9
12:56:00	−121.0
12:56:30	−122.6
12:57:00	−125.1
12:57:30	−128.7
12:58:00	−135.0
12:58:30	−141.6
12:58:33	Receiver 1 out of lock
12:58:42	Receiver 1 in lock
12:59:00	−136.0
12:59:10	Receiver 1 out of lock

[a]No anomalies were experienced.

maser. The combination of these two effects gave rise to an unstable antenna angular track, which was more severe than had been experienced on previous earth-orbital tracks. This phenomenon was self-correcting in that DSS 42 did not have a viewperiod for revolution 2 so that, when the station reacquired after translunar injection, the signal strengths had decreased to a tolerable level and the high-rate dynamic instability had disappeared. Remedial action was, therefore, deferred until after the mission.

The high angular tracking rate problem was not experienced at DSS 11 because the spacecraft elevation angles were sufficiently low to avoid the problem. However, DSS 11 did experience two minor anomalies: During revolution 1, extreme weather conditions caused a nylon chain on the pre- and final-limit control boxes of the antenna servo system to break. No loss of data resulted and the chains were repaired prior to revolution 2. During revolution 2, the low-speed clutch on the hour-angle axis became inoperative and it was necessary to switch to the high-speed mode. However, no degradation in tracking or data acquisition resulted.

Translunar phase. The *Apollo* 8 mission was designed to have injection into a lunar transfer trajectory occur over Hawaii in the Pacific Ocean. As a result, the stations in the Goldstone DSCC were the first to acquire *Apollo* 8 after translunar injection. DSS 11 acquired *Apollo* 8 at horizon rise of the spacecraft. DSS 14 acquired *Apollo* 8 some 8 min later (Fig. 12), using preflight nominal predictions and drive tapes. However, the received signal was so strong as to overload the receiver, with the result that it was 3 to 4 h before the correct angle offsets could be punched into the servo control unit to accurately peak the 0.15-deg beamwidth of the 210-ft-diam antenna onto the spacecraft and obtain a meaningful signal-strength reading. When obtained, the reading was found to agree with the expected 8- to 10-dB improvement over the 85-ft-diam antenna stations.

The earth tracking of *Apollo* 8 carried it eastward over the United States and it reached its synchronous altitude point approximately over Bermuda where the earth track reversed direction, starting in a westerly direction (with respect to Goldstone) back across the United States to final set over the Pacific. The Goldstone stations, therefore, experienced the same long postinjection track as is normally experienced by DSS 51 on unmanned launches with Atlantic injections.

During this time period, and on subsequent lunar passes, the MSFN *Apollo* prime station had a choice of "the best of three" data sources to process and remote to the Mission Control Center at Houston, namely, *Apollo* prime station data, DSS 11/MSFN wing data, or DSS 14 data. Much of this was automatically selected by computers, so an accurate time history of which data were used is difficult to ascertain. However, as the spacecraft distance from earth increased, the DSS 14 high bit-rate telemetry reception data became more and more useful due to what is known as the "rotisserie" or "barbecue" effect: To keep thermal balance throughout the spacecraft, the *Apollo* mission was designed so that the spacecraft rotated slowly about its roll axis to keep uniform illumination from the sun. This necessitated the astronauts to select between the four omniantennas as the rotation proceeded. A typical resulting received signal-strength pattern at DSS 14 would show the signal strength dropping slowly some 30 to 35 dB and then reinstating itself suddenly as the antennas on the spacecraft were switched. As the spacecraft neared the moon,

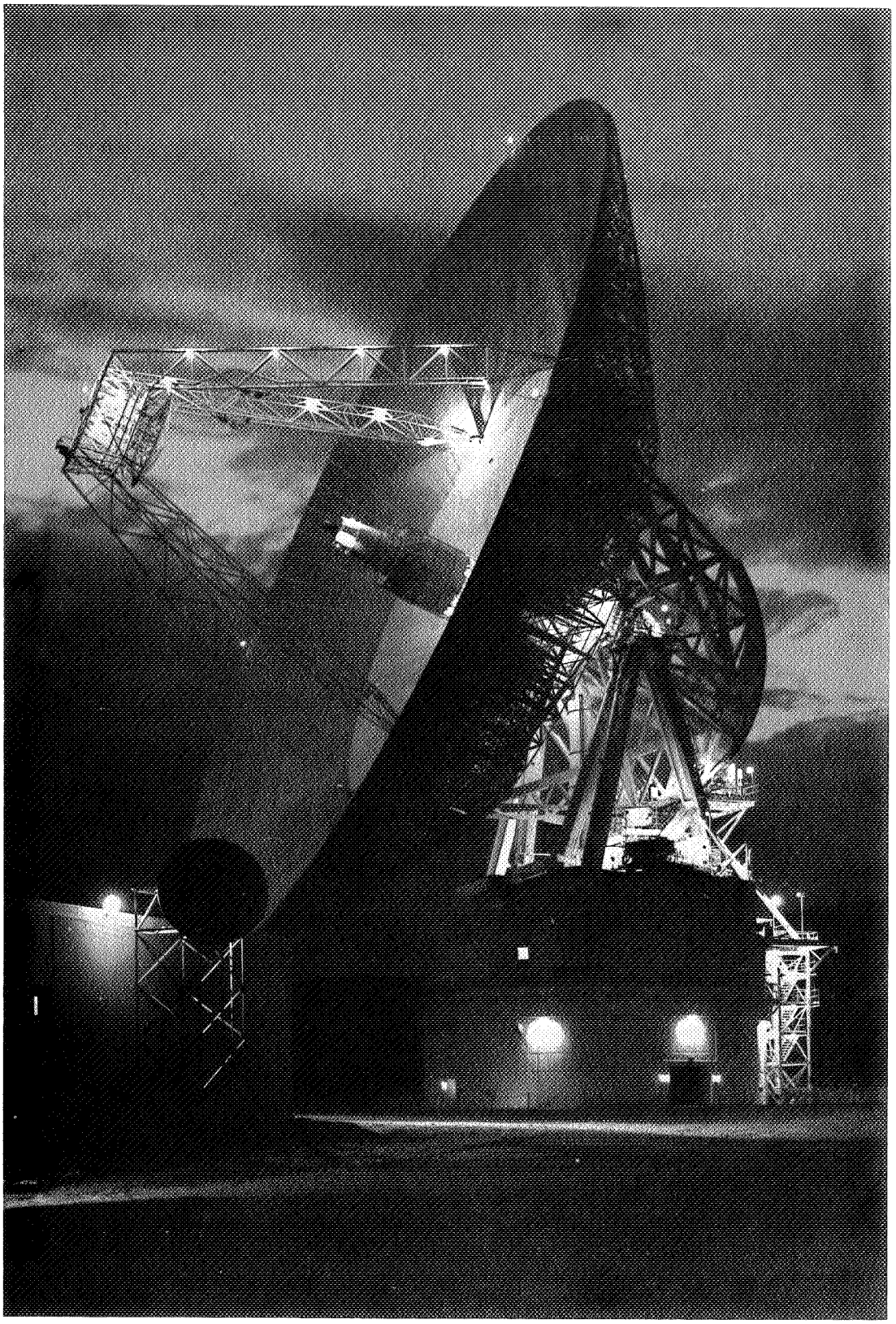

Fig. 12. DSS 14 210-ft-diam antenna tracking *Apollo 8*

this drop in signal strength would cause the signal to fall below the 51.2-kbps high bit-rate telemetry threshold at the 85-ft-diam antenna stations but not below the threshold at the DSS 14 210-ft-diam antenna station. By selecting the DSS 14 telemetry data for processing and remoting to Houston, many unnecessary commands to change to low bit-rate telemetry were avoided while the *Apollo 8* spacecraft was in view of Goldstone.

Fortunately for the many TV viewers throughout Europe, the United States, and Japan, the *Apollo 8* multibeamwidth high-gain antenna worked 100% successfully during the mission, which permitted TV transmission from the spacecraft to be obtained at the 85-ft-diam antenna stations in Madrid and Goldstone for relay to Houston and subsequent distribution through commercial TV channels. The TV transmission signal strengths were in the vicinity of −95 dBm, which produced a very acceptable signal into the 85-ft-diam antennas. Because of this and also because of a very slight degradation of TV picture quality over the Goldstone intersite microwave link (Fig. 11), *Apollo 8* TV signals from DSS 14 were not used during the mission.

During the translunar midcourse maneuver and coast phases, the MSFN wings at DSSs 11, 42, and 61 provided continuous coverage of the *Apollo 8* spacecraft in both the two-way and three-way mode of operation. Scheduled commands and voice were successfully uplinked through these wings to the *Apollo 8* spacecraft during portions of this period, which ended with the successful arrival of *Apollo 8* in the vicinity of the moon on Christmas Eve while the spacecraft was in view of DSS 42.

Lunar phase. The beginning of the *Apollo 8* lunar-orbital phase started on December 24 at 09:49:08 GMT with spacecraft occultation behind the moon as viewed from DSS 42. *Apollo 8* exited occultation from behind the moon at 10:23 GMT, at which time DSS 42 tracked lunar orbit 1, which ended at 11:47 GMT with the second lunar occultation. The beginning of the second lunar orbit was viewed simultaneously by DSSs 42 and 61. *Apollo 8* set on the DSS 42 horizon at 12:41 GMT. The coverage was continued at DSS 61 through lunar orbits 2–6, which were tracked without anomaly and reported signal-strength readings in the range of −102 to −126 dBm. *Apollo 8* lunar orbit coverage continued during the Goldstone visibility and on into the DSS 42 visibility for orbits 8, 9, and 10. *Apollo 8* experienced its last lunar occultation on orbit 10 on December 25 at 05:42 GMT. The *Apollo 8* service propulsion system trans-earth injection burn occurred while the spacecraft was occulted behind the moon during orbit 10.

Trans-earth phase. The trans-earth phase of *Apollo 8* commenced on December 25 with acquisition by DSS 42 at 06:19:46 GMT and continued at this station until loss of signal due to horizon set at 12:42 GMT that day. However, DSS 61 had acquired *Apollo 8* at 12:03 GMT in a three-way mode so there was no loss of data during the handover. DSS 61 viewperiod extended to 22:54 GMT on December 25 with the entire pass being in the three-way mode. DSS 61 viewperiod overlapped that of the Goldstone stations supporting *Apollo*.

The DSS 11 viewperiod was from December 25 at 19:41 GMT through December 26 at 06:25 GMT. During this time period, the station reported both one-way and three-way tracks without anomalies. The Goldstone tracks overlapped those of DSS 42, which acquired *Apollo 8* in a three-way mode on December 26 at 01:38 GMT. DSS 42 alternated between three-way and two-way modes of operation over this pass, which ended at 12:54 GMT with no anomalies being reported. This was followed by an overlapping viewperiod with DSS 61, which remained in the three-way mode for the entire pass, which ended at 22:54 GMT on December 26.

Overlap with Goldstone commenced at 19:51 GMT on December 26. DSS 11 operated in both one-way and three-way modes throughout the entire pass, which ended on December 27 at 07:06 GMT without any anomaly. Since the *Apollo* return trajectory was such that Goldstone would not have another viewperiod, DSS 11 was relieved of further *Apollo* support at the end of this pass.

The succeeding December 27 tracks by DSSs 42 and 61 similarly concluded participation in the *Apollo 8* mission since these tracks were the last ones for these stations before spacecraft splashdown. The end of track occurred at 13:04 GMT for DSS 42, and at 14:53 GMT for DSS 61. No problems were reported by either station on this final track in support of the *Apollo 8* mission.

f. Conclusion. The support provided to *Apollo 8* by all participating stations in the MSFN and in the DSN was excellent throughout the mission. Messages congratulating all participating stations on their fine performance during the mission were sent by the Manned Spacecraft Center at Houston, Texas, and by the Manned Flight Operations Directorate at the Goddard Space Flight Center.

III. Advanced Engineering

A. Tracking and Navigational Accuracy Analysis

1. Introduction, *T. W. Hamilton and D. W. Trask*

The DSN Inherent Accuracy Project was formally established by the DSN Executive Committee in July 1965. The objectives of the project are:

(1) Determination (and verification) of the inherent accuracy of the DSN as a radio navigation instrument for lunar and planetary missions.

(2) Formulation of designs and plans for refining this accuracy to its practical limits.

Achievement of these goals is the joint responsibility of the Telecommunications and Systems Divisions of JPL. To this end, regular monthly meetings are held to coordinate and initiate relevant activities. The project leader and his assistant (from the Systems and Telecommunications Divisions, respectively) report to the DSN Executive Committee, and are authorized to task project members to (1) conduct analyses of proposed experiments, (2) prepare reports on current work, and (3) write descriptions of proposed experiments. The project is further authorized to deal directly with those flight projects using the DSN regarding data-gathering procedures that bear on inherent accuracy.

The various data types and tracking modes provided by the DSIF in support of lunar and planetary missions are discussed in SPS 37-39, Vol. III, pp. 6–8. Technical work directly related to the Inherent Accuracy Project is presented in SPS 37-38, Vol. III, and in subsequent *Deep Space Network* SPS volumes, and is continued in the following subsections of this volume.

To meet the navigational goals under consideration for some planetary projects, the uncertainties in DSS longitude and the distance off the earth's spin axis must be known on the order of 1 m. Previous articles have discussed this dependence (SPS 37-44, Vol. III, pp. 4–11) as well as the status in obtaining DSS locations from radio tracking data. *Subsection 2* reports the latest progress in these determinations. Specifically selected portions of the *Mariner IV* and *V* and the *Pioneer VII* missions have been analyzed. The significant result of this analysis is the reduced scatter among the solutions as compared to earlier work. As an example, spin-axis solutions fall within 3 m of the mean for DSS 12 for this analysis while they fell within 12 m of the mean for the *Ranger* Block III analysis reported in SPS 37-43, Vol. III, pp. 3–18. Another significant difference between the two analyses lies in a 20-m discrepancy between the "planetary" and "lunar" longitude solutions. This discrepancy is traced to a basic

incompatibility between the lunar and planetary ephemerides.

During this reporting period, the results of the above work were provided to the *Apollo* navigation working group (ANWG). In particular, the ANWG was provided with a best estimate of the locations for DSSs 11, 42, and 61. These DSS locations were adjusted to be applicable for real-time *Apollo 8* support. These adjustments included accounting for the difference of equinox between the planetary and lunar ephemerides to be used during *Apollo 8* (as well as other differences between the JPL software and that to be used for *Apollo 8*), predicting the position of the pole during *Apollo 8*, and the change in definition of UT1 disseminated by the U.S. Naval Observatory after January 1, 1968. Unfortunately, MSFN location solutions based on radio tracking data are not yet available. Therefore, geodetic survey locations have been used in the past even though, for example, longitude differences between Spain and Australia as derived from the geodetic surveys differ by 200 m from those derived from radio tracking data for the DSS. The ANWG was particularly concerned over the effect of possible station location errors during the lunar approach phase. Analysis by JPL and the Manned Spacecraft Center showed that during similar phases of past lunar missions (*Surveyor* and Langley *Lunar Orbiter*) the navigation accuracy would have been seriously degraded if the geodetic locations had been used instead of the DSS locations determined from radio tracking data. In addition, tracking data was simulated for the approach phase of *Apollo 8* and the effect of station location errors representative of the differences between the geodetic and radio determinations was analyzed. It was found that such errors would seriously increase the risk of an otherwise unnecessary aborting of the *Apollo 8* mission during the lunar approach phase. The Goddard Space Flight Center, which is responsible for specifying the MSFN station locations, derived the MSFN locations for *Apollo 8* by applying geodetic survey differentials to the DSS locations determined by radio tracking data where MSFN and DSN stations were co-located on the same geodetic datum. Their decision was based on the above analysis plus the fact that current work being performed at the Goddard Space Flight Center on Fisher's modified Mercury 1968 datum tends to agree with the radio tracking results.

Not only must our knowledge in DSS locations be improved, but related to this effort, the effects of the charged particles must also be calibrated out of the tracking data to realize the navigation accuracy goals currently under consideration. In addition, it should be noted that the quality of the DSS locations determined during postflight analysis depends on the ability to calibrate the radio tracking data for charged-particle effects. For the *Mariner* 1969 mission to Mars, the navigational errors incurred by ignoring the effect of the ionosphere will exceed the total error budget allocated to the ground-based system during support of the planetary encounter phase. Consequently, the effect of charged particles will be modeled/calibrated out of the tracking data for the *Mariner* Mars 1969 mission. *Subsection 3* compares three methods of measuring the total electron content in the ionosphere; namely, ionosonde data from ESSA, Faraday rotation data obtained at Stanford University while tracking geostationary satellites, and data from the Stanford University dual-frequency experiment carried aboard the *Mariner V* spacecraft. The latter measurement provides a measure of the charged-particle effect along the probe's ray path. This article is a preliminary evaluation of the techniques employed to map an ionospheric measurement made at one location to the ray path of the radio signal of the deep space probe being tracked. The ionosonde and Faraday rotation measurements are obtained at a constant elevation angle (fixed geometry while the elevation angle is constantly changing for the dual-frequency measurements) and the conversion to the desired ray path is the most difficult part of the charged-particle calibration for probes not carrying an experiment which directly measures charged particles along their ray path.

Although the *Mariner* Mars 1969 mission is most sensitive to the charged particles present in the ionosphere, charged particles are also present in the space plasma, and space plasma effects do become a limiting error source for missions to the outer planets. *Subsection 4* illustrates the effect on tracking data for various missions, assuming a steady-state inverse square law for the density of the charged particle emanating from the sun. Therefore, the effect of the charged particles increases with earth–probe distance and as the sun–earth–probe angle decreases. For example, in the case of a spacecraft approaching Jupiter, the dominant error in a ranging measurement will be due to charged particles for a sun–earth–probe angle less than 90 deg.

A recent article in *J. Geophys. Res.* (Smylie, D. E., and Mansinha, L., Vol. 73, No. 24, p. 7661, Dec. 15, 1968) concluded that large earthquakes correlate with small changes in the curvature of the polar motion and that apparently earthquakes excite the polar motion. Uncertainties in polar motion represent one of the inherent limitations to navigational accuracy, and a major portion

of this uncertainty is incurred during the process of extrapolating the polar motion from the time of the last measurement to the current date during real-time navigation operations. Therefore, if such correlations do exist between polar motion and earthquakes, they are of interest because it may be possible to provide a model for more accurately predicting polar motion in support of the planetary missions of the 1970s. A check was made of the existing earthquake data, as reported in *Subsection 5*, and although it was found that there are interesting correlations between the average earthquake energy and the Chandler motion of the pole, it seems more likely that either the Chandler motion excites the earthquakes, or that both are excited by the same phenomena, than that the earthquakes are exciting the Chandler motion.

The landed *Surveyor* two-way doppler "observed minus computed" residuals exhibit long-term periodicity and diurnal signatures as previously reported in SPS 37-50, Vol. II, pp. 110–125, and SPS 37-51, Vol. II, pp. 42–50. The long-term periodicities are lunar-ephemeris dependent, while the diurnal signature has a number of suspected causes, among which are the imperfections in the tropospheric refraction corrections applied to the doppler and ionospheric charged-particle effects (discussed in previous SPS issues). *Subsection 6* demonstrates the impact of the existing physical libration model used in the reduction of the landed *Surveyor* tracking data, along with a proposed improved model and no model at all. The variation of libration modeling induced significant influences upon the *Surveyor* data reductions. It is of interest to note that all libration algorithms employed in this study exhibited time-dependent or lunar-coordinate-dependent characteristics. No one libration model "best" fitted all *Surveyors* utilized in the study.

Generally, reductions from earth–satellite tracking data result in high correlations between the gravitational mass of the earth $GM_\oplus$ and the scale of the coordinate system (i.e., linear coordinates of the tracking stations). This is especially true in the case of optical data that rely on an independent determination of $GM_\oplus$. To provide the scale of quantities that involve linear dimensions to date, the most accurate $GM_\oplus$ determinations have been provided from radio tracking data of deep space probes, such as those reported in SPS 37-43, Vol. III, pp. 3–18 and SPS 37-44, Vol. III, pp. 11–28. At present, these $GM_\oplus$ determinations from deep-space-probe data have no close competitors in that their claimed uncertainty is an order of magnitude less than that provided by previous techniques. In a previous article (SPS 37-53, Vol. II, pp. 16–20), it was shown that a moderate altitude satellite carrying a DSN-type transponder could provide a $GM_\oplus$ determination competitive to that obtained from deep space missions. *Subsection 7* studies a family of three high-altitude satellites, including the synchronous satellite *SYNCOM II* plus one with ¾ and another with ½ the semimajor axis of the synchronous satellite. $GM_\oplus$ is well determined in all three cases but improves as the altitude of the satellite decreases.

Subsection 8 is a report on a new technique, the sensitivity matrix method, useful for performing orbit determination error analysis. The method computes the partial derivatives of the estimates with respect to parameter errors. The technique is used to analyze some of the error sources in the orbit determination of a Mars orbiter.

Subsection 9 considers the influence of range measurements on the information contained in a few passes of doppler data and is an extension of the work in SPS 37-52, Vol. II, pp. 37–44. It is shown that the range data improve the ability to estimate the magnitude of a velocity component normal to the earth probe line $\vec{\nu}$. Furthermore, uncertainty of $\vec{\nu}$ varies as a reciprocal of the magnitude of $\vec{\nu}$ and is independent of its direction. In fact, range data do not improve the ability to estimate the direction of $\vec{\nu}$. As long as the accuracy of the range measurement σ_ρ significantly exceeds the accuracy of the range estimate determined from doppler only ($\sigma_\rho < 10$ km) and is not so accurate that differenced range measurements have an accuracy competitive with that of doppler data ($\sigma_\rho > 10$ m), then σ_ν is independent of σ_ρ.

2. DSS Location Solutions for Deep Space Probe Missions, Using *Mariner IV*, *Mariner V*, and *Pioneer VII* Data,

N. A. Mottinger

a. Introduction. As discussed by Mottinger and Trask in SPS 37-48, Vol. II, pp. 12–22, the uncertainties in DSS locations can become limiting factors to the navigational accuracy obtainable with earth-based radio tracking data. To meet the navigational goals under consideration for some planetary projects, the uncertainties in the DSS longitude σ_λ and the distance off the earth's spin axis[1] σ_{r_s} must be known on the order of 1 m. In an earlier article by Hamilton, Grimes, and Trask (SPS 37-44, Vol. III, pp. 4–11), an approximate method for determining the navigational accuracy obtainable during the encounter phase of a mission is presented, where the

[1] r_s = geocentric radius times the cosine of the geocentric latitude.

dependence of this accuracy on station location uncertainties is discussed.

A general discussion of DSS location solutions obtained from postflight analyses is presented in SPS 37-48, Vol. II. SPS 37-49, Vol. II, pp. 10–23, gives the solutions for DSS locations obtained in processing the *Mariner V* data at about the same time the mission was in progress.[2] The present article discusses recent advancements in solving for station locations, using the deep space radio data from the *Mariner IV*, *Mariner V*, and *Pioneer VII* missions when the encounter and zero declination data are reduced with the single-precision orbit determination program (SPODP, Ref. 1).

Although the SPODP lacks the precision required for computing DSS locations to the 1-m level,[3] the results obtained for r_s and λ agree to 4 m and better for selected portions of the missions as opposed to the 20- to 40-m scatter obtained for solutions discussed previously. The forthcoming double-precision orbit determination program (DPODP, SPS 37-38, Vol. III, pp. 24–27) will aid in obtaining the 1-m goal since it contains extended precision of arithmetic operations and will include models for antenna motion, polar motion, ionosphere, etc., which are not in the SPODP.[3]

b. Determining data to be reduced. One of the distinguishing characteristics of the DSS location solutions presented by Mottinger and Trask (SPS 37-48, Vol. II) is their scatter. Inconsistencies can be noted which either appear or do not appear to be a function of the mission type. That is, in some cases the solutions obtained from planetary missions are different than those obtained from lunar missions, or within a set of lunar missions there may be a variety of solutions. Relative as well as absolute locations may also vary between the flights, both lunar and planetary. The scatter in the absolute locations can be the result of errors in the ephemeris, time determination, polar motion, unknown atmospheric conditions, and perhaps from other error sources not realized at this time. Relative locations are not dependent upon the ephemeris; hence only atmospheric conditions, time synchronization, polar motion, or such parameters may be responsible for the deviations among these solutions. With the cancellation of ephemeris errors and certain timing relationship errors, radio tracking can determine relative locations (longitude) better than any other station location parameter. Even with remaining error sources, the scatter of solutions obtained by radio tracking is significantly less than that for absolute longitudes.[4]

The ionosphere could cause false station locations. Without a model for it in the SPODP, its effects on the radio signal could cause an erroneous location to be computed. Earlier spacecraft missions, primarily the lunar *Ranger* Block III (*Ranger VI, VII, VIII,* and *IX*) and *Mariner II* (Venus) missions, used L-band data, whereas all other missions used S-band. It is known that L-band data is approximately six times more sensitive to the ionosphere than S-band. This means that individual *Ranger* Block III station locations could be in error as much as 5–10 m in r_s and 10–20 m in longitude due to ionospheric effects (SPS 37-43, Vol. III, pp. 3–18). Reduction of S-band data should produce station locations significantly better than those obtained from L-band data.

There are, however, two other important items to consider when reducing the lunar and planetary data for station locations. These items help to explain why there might be a scatter between the various solutions. Possibly of greatest interest is the work of Dr. Van Flandern (U.S. Naval Observatory), who reports (Ref. 2) that there is an approximate 1.44-s (in time) difference between the FK4 equinox and the assumed equinox used by Brown in the lunar theory. To first-order approximations, this would remove the 20–25 m difference between the combined *Ranger* Block III and other lunar mission longitudes and the longitude solutions obtained when processing the planetary encounter data, i.e., *Mariner IV* and *V*. The JPL lunar ephemerides are based upon the Brown lunar theory, and the planetary ephemerides are based upon radar and optical observations, the latter being used to relate the system to the FK4 star catalog equinox. It is possible that a difference between the equinoxes of the lunar and planetary ephemerides would preclude agreement between the DSS longitude solutions for lunar and planetary flights. Van Flandern's work, which includes identifying the exact location of Brown's equinox and transferring it (the theory) to the FK4 star catalog system equinox, is currently being incorporated into the JPL lunar ephemerides.

To check the expected results of correcting the lunar equinox, an ephemeris was provided with a 1.44-s (in time) offset to the lunar longitude. This was expected to produce a westward shift of 24 m in the DSS longitudes,

[2]More detail on the *Mariner V* orbit determination results, including solutions for station locations, appears in an article by G. E. Pease (SPS 37-50, Vol. II, pp. 125–140).

[3]See SPS 37-48 and 37-49, Vol. II.

[4]For examples, see SPS 37-48, Vol. II.

thereby bringing the planetary and lunar longitude solutions to much closer agreement. To test this, postmidcourse doppler and range data, as discussed by Mottinger and Sjogren in SPS 37-46, Vol. II, pp. 18–26, was used with this ephemeris. The reduction gave a 28-m shift, which, in light of the numerical and physical limitations of the SPODP and the distance from the moon at which the free flight ends (3000 km), would tend to confirm the expected results. However, additional fits of the entire translunar data for this mission, using only the two-way doppler, produced twice the expected shift in DSS longitudes and also produced unrealistic solutions for the physical constants $GM_{\oplus}$ and $GM_{\mathfrak{D}}$ being estimated. It was decided to wait until Van Flandern's complete set of corrections could be incorporated into the ephemeris before resuming the reduction of *Lunar Orbiter* and other lunar data for station locations and physical constants.

Until reduction of lunar data is resumed using the corrected lunar ephemeris, it is difficult to forecast to the 1-m level how the planetary longitude solutions will compare with the lunar solutions. If the equinox of the planetary ephemeris also coincides with the FK4 equinox, then, in theory, the longitude solutions should be the same. However, any difference between the actual position of the equinox in the planetary ephemeris (assumed to be the FK4 equinox but in reality having an uncertainty associated with it) and the FK4 equinox will prohibit exact agreement of the two longitude solutions. The inclusion of radar bounce data in the compilation of the advanced planetary ephemerides (such as those currently being used for data reduction) determines the relative location of the "target" body with respect to the earth about two orders of magnitude better (to approximately 5 km) than it aids in determining their absolute position. Therefore, there is a definite possibility that the present errors in the knowledge of absolute planetary locations will limit the agreement between the "planetary" and "lunar" DSS longitude solutions.

Since an immediate goal was to provide the most accurate station locations possible for the *Mariner* Mars 1969 mission, a decision was made to concentrate on the reduction of the planetary data currently available.

Reducing planetary data can be regarded a difficult task due to the extreme distance between the spacecraft and any attracting bodies. During the cruise phase of the mission, the extreme distance between the probe and the sun would be expected to degrade the determination of DSS longitudes since it is the gravitational attraction of the primary attracting body on the spacecraft which permits significant longitude determination. When the probe is under stronger gravitational attractions during the encounter phase, the right ascension of the probe is determined from the known right ascension of the target. Then the longitude of the tracking station can be determined. To obtain reliable DSS longitude solutions, the *Mariner IV* and *V* encounter data appear to be the best to reduce.

Examination of the Hamilton–Melbourne parameterization of the information content of a pass of doppler data from a distant spacecraft (SPS 37-39, Vol. III, pp. 18–24) reveals a configuration in which r_s can be determined independently of the need for an encounter situation. In their model of the information content of the doppler data, there is a quantity b which is naturally determined by radio tracking. The parameter b equals the product of the earth's angular rotation rate r_s and the cosine of the probe declination. From the expression for Δb, one can note that the strength for determining r_s lies in the zero-declination data because (1) Δr_s, hence r_s, is well defined by $\omega_{\oplus}$ since cosine δ is practically invariant near 0 deg, and (2) the sine δ term nullifies the effects of any uncertainties in probe position upon Δb.

$$\Delta b = \omega_{\oplus}(\cos \delta \, \Delta r_s - r_s \sin \delta \Delta \delta)$$

Therefore, when solving for station locations, the best times to obtain an r_s solution would be when the probe is near zero declination and at encounter when the declination is known.

Realizing the importance of the zero-declination data, the trajectories of *Mariners IV* and *V* and the other planetary mission (*Pioneer*) were checked for zero-declination configurations. Plots of the declination for portions of these two *Mariner* missions and *Pioneer VII* are shown in Fig. 1. Many of the lunar missions reported in SPS 37-48, Vol. II are not at this optimum configuration. However, the gravitational attraction by the moon should be pertinent in determining station locations. Once work is resumed on the lunar data, items such as this will be more closely investigated. The *Mariner V* plot in Fig. 1a is of special interest since the probe passes through zero declination twice, once in August during the cruise phase and again after encounter in November. *Mariner V* encounter occurred in October at +6 deg; *Mariner IV* encounter occurred at −3-deg declination. The sun–earth–probe angles shown in Fig. 1 will be pertinent when analyzing ionospheric and space plasma effects on the radio signal.

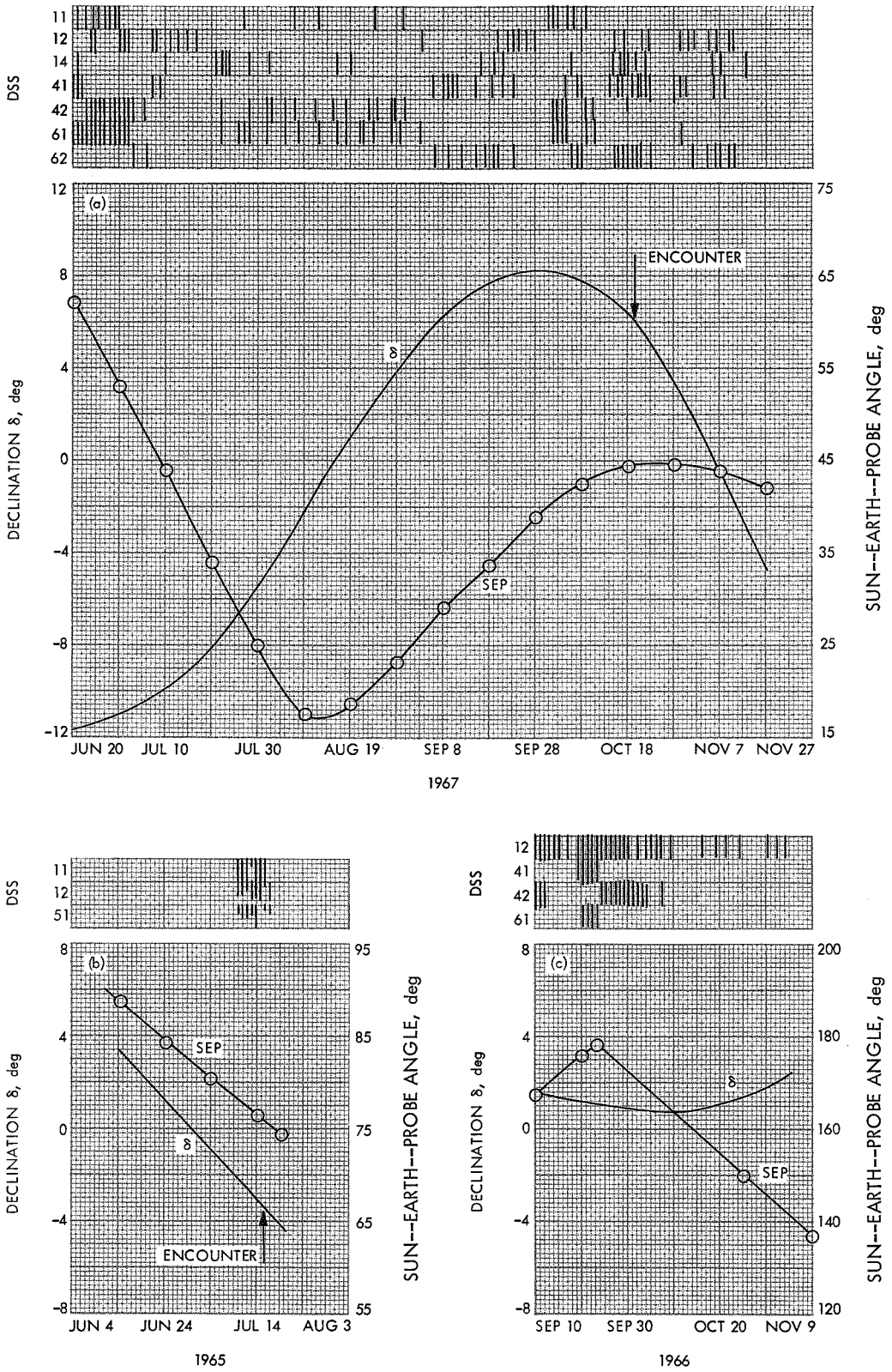

Fig. 1. Data reduction times, declination, and sun–earth–probe (SEP) angle: (a) *Mariner V*, (b) *Mariner IV*, (c) *Pioneer VII*

The hash marks shown in Fig. 1 indicate times during DSS tracking when data was reduced. Table 1 gives the tracking spans. In Fig. 1b, only encounter reduction times are shown for *Mariner IV*. Partial hash marks given for *Mariner IV* indicate incomplete passes of data (a pass is approximately 8 h). However, full hash marks on the *Mariner V* and *Pioneer VII* plates (Figs. 1a and c) do not always mean that a complete pass was available for data reduction. For *Pioneer VII*, only DSS 12 data was used in the reduction reported in this article, but passes of data from other stations are included because these may be considered in future analyses.

c. Ephemeris used to reduce the data. Table 1 contains a summary of the data spans which have been used to solve for r_s and longitude in the small-declination and encounter portions of the three missions. All the reductions were performed with Development Ephemeris (DE) 40, which contains Lunar Ephemeris (LE) 4 (Ref. 3; SPS 37-51, Vol. III, pp. 4–13). DE 40 is one of JPL's latest planetary ephemerides, incorporating newly adopted IAU masses along with radar data for Venus. The ephemeris which is being used in the *Mariner* Mars 1969 mission is similar to DE 40. Since inconsistencies exist between the current lunar and planetary ephemerides, it is desirable to restrict the efforts of solving for station locations to fitting the existing planetary data to the ephemeris chosen by the mission. A similar argument would hold for reducing data for a lunar mission requiring station locations accurate below the 10-m level. Hopefully, however, with improved ephemerides this qualification can be removed.

d. Results from fitting Mariner and Pioneer data to DE 40. The station location solutions obtained when using the 0-deg declination and encounter data with DE 40 are remarkably consistent. Typical results are shown in Figs. 2 and 3 for r_s and longitude solutions for DSS 12 at the Goldstone DSCC. DSS 12 was chosen since it has tracked more than any other Goldstone station and has become a standard for comparison with other location solutions, such as those obtained by Smithsonian Astrophysical Observatory (SAO) from tracking satellites with Baker–Nunn cameras. Also, the solved-for location of any station at Goldstone DSCC can be transferred to DSS 12 by using the relative first-order land survey station location solutions determined by William Bollinger and Teledyne (Footnote d, Table 2). Land survey techniques were used to extend the Coast and Geodetic first-order survey to the physical point on each antenna which is defined as the station location. For these reasons, a particular reduction may contain two or more solutions for DSS 12 (Figs. 2 and 3). One may be the direct solution and the other a DSS 14 or DSS 11 solution transferred to DSS 12. Note that the scale of the r_s and λ plots has been changed by an order of magnitude (2 m per division instead of 20) with respect to those appearing in previous articles.

The uncertainties shown in Figs. 2 and 3 are the 1-σ statistics computed by the SPODP. Other known contributing error sources, which are not considered in the program for lack of a model or other reasons, indicate that the true uncertainty should be larger. Later in this article, some indication of their contribution is given.

Shown in Fig. 2 are the spin-axis solutions obtained from three phases of *Mariner V*: the two zero-declination crossings (cruise and postencounter) and the encounter solution. Numerous transferring of solutions from DSSs 11 and 14 has been done to show how direct solutions compare with the indirect. The encounter solutions agree most closely with those cruise solutions which are transferred from the station tracking closest to the zero-declination moment. The scatter among these three solutions is about 1.5 m as compared to the 20-m scatter shown in previous articles.

Some of the *Mariner IV* encounter spin-axis solutions exhibit disagreement with the *Mariner V* and *Pioneer* values. The *Mariner IV* data is quite sensitive to the tropospheric refraction model and the stations used in the reduction. Improved values of the tropospheric index of refraction were prepared by A. Liu (SPS 37-50, Vol. II, pp. 93–97). The r_s solutions for fits using all three DSSs (11, 42, and 51) and using DSS 11 and 42 data show agreement apart from those solutions obtained fitting the DSS 11 data only or DSS 11 and 51 data. The latter two solutions are more in line with the *Mariner V* and *Pioneer* results. It is interesting that the solution for the r_s of DSS 51 is the same whether fitting all three stations or only DSSs 11 and 51.

The longitude solutions behave quite similarly. The DSS 11 only and the DSS 11 and 51 solutions agree precisely with the *Mariner V* encounter solutions, but fitting all three stations or DSSs 11 and 42 produces solutions which disagree. It appears that the DSS 42 data may be responsible for these inconsistencies. None of these later fits have been performed using the nominal indices of refraction since it has been observed from other reductions that a better fit is obtained using Liu's values.

Table 1. Flight analysis summary

Flight	Tracking type	Tracking span, days	Ephemeris			SPODP mod	ET–UTC, s	UT1–UTC, ms	Effective data weights		Instantaneous pole position (IPMS), m				Declination δ, deg	Sun–earth–probe angle, deg
			DE	LE	JPL tape				Doppler (1 pt/min), mm/s	Range, km	x, m	Change in x, m	y, m	Change in y, m		
Mariner V																
Cruise	Doppler and range	60 (July 23–Sept. 19, 1967)	40	4	5953	VI	Start 38.069 End 38.222	45 91	3	6	0.92	1.6	5.91	1.2	−8 to 8	35–20–35
Encounter	Doppler and range	10 (Oct. 14–24, 1967)	40	4	5953	V	38.202	89	3	11	−0.94	0.4	7.19	0.3	6	45
Post-encounter	Doppler and range	16 (Oct. 28–Nov. 13, 1967)	40	4	5953	VI	38.350	86	5	11	−1.38	0.6	7.68	0.5	2 to −2	43
Mariner IV																
Encounter	Doppler	7 (July 10–17, 1965)	40	4	4904	VI	36.280	5.7	3	—	1.2	0.9	13.6	0.1	−3	77
Pioneer VII	Doppler	60 (Sept. 10–Nov. 3, 1966)	40	4	4904	VI	Not available	Not available	Not available	—	2.5	1.6	9.8	1.4	1.7 to 2.4	180–140

Table 2. New best set of station locations and their sources[a]

DSS	r_s, km	Source[b]	$\Delta\lambda$, deg (DSS − 12)	Source	λ, deg E lat	Source	Z, km	RI geocentric radius, km	ϕ geocentric latitude, deg
12	5212.0497	Weighted average of *Mariner V* cruise and postencounter 0-δ and encounter solution			243.19463	*Mariner V* encounter *Mariner IV* encounter[c]	3665.624[c,f]	6371.9904	35.118642
11	5206.3381	DSS 12, using Bollinger's deltas[d]	−0.04393	[d]	243.15070	DSS 12	3673.759[c,f]	6372.0061	35.208019
14[k]	5203.9949	Same as DSS 11	−0.08404	[e]	243.11059	DSS 12	3677.0480[e,f]	6371.9891	35.244331
41	5450.1978	*Mariner V* postencounter	−106.30702	*Mariner V* post-encounter	136.88759	DSS 12	−3302.238[f]	6372.5530	−31.211388
42	5205.3497	*Mariner V* cruise	−94.21326	*Mariner V* cruise	148.98137	DSS 12	−3674.628[i]	6371.6997	−35.219528
51	5742.9412[g]	*Mariner IV* encounter (DSSs 11 and 51 only)	−215.50915[h]	*Mariner IV* encounter (DSSs 11 and 51 only)	27.68548[h]	DSS 12	−2768.760[f]	6375.5318	−25.739428
61	4862.6044	*Mariner V* cruise	112.55646	*Mariner V* cruise	355.75109	DSS 12	4114.829[i]	6369.9874	40.238538
62	4860.8158	*Mariner V* postencounter	112.43763	*Mariner V* post-encounter	355.63226	DSS 12	4116.950[i]	6369.9927	40.263494

[a]See Table 1 for more information on sources.

[b]r_s sources refer to zero-declination passage or encounter; see Table 1.

[c]Obtained by using data from DSSs 11 and 51 only.

[d]William Bollinger's relative locations at the Goldstone DSCC are: $\Delta r_{s_{11-12}}$ − 5.7116 km, $\Delta\lambda_{11-12}$ − 0.04393 deg, ΔZ_{11-12} + 8.1354 km, $\Delta r_{s_{14-12}}$ − 8.0548 km, $\Delta\lambda_{14-12}$ − 0.08404 deg, ΔZ_{14-12} + 11.4238 km.

[e]DSS 14 relative locations are obtained from Teledyne.

[f]SAO Standard Earth, 1966, Vol. III, Table 9.

[g]Erroneously entered as 5742.9370 in Ref. 4.

[h]Erroneously entered as −215.50917 in Ref. 4, creating absolute longitude of 27.68546.

[i]See Source column.

[j]Geocentric radius and latitude included for completeness only.

[k]DSS 13 at Goldstone DSCC also used footnote d for relative location: r_s = 5215.4862, λ = 243.20523, Z = 3660.952, RI = 6372.1163, ϕ = 35.066505.

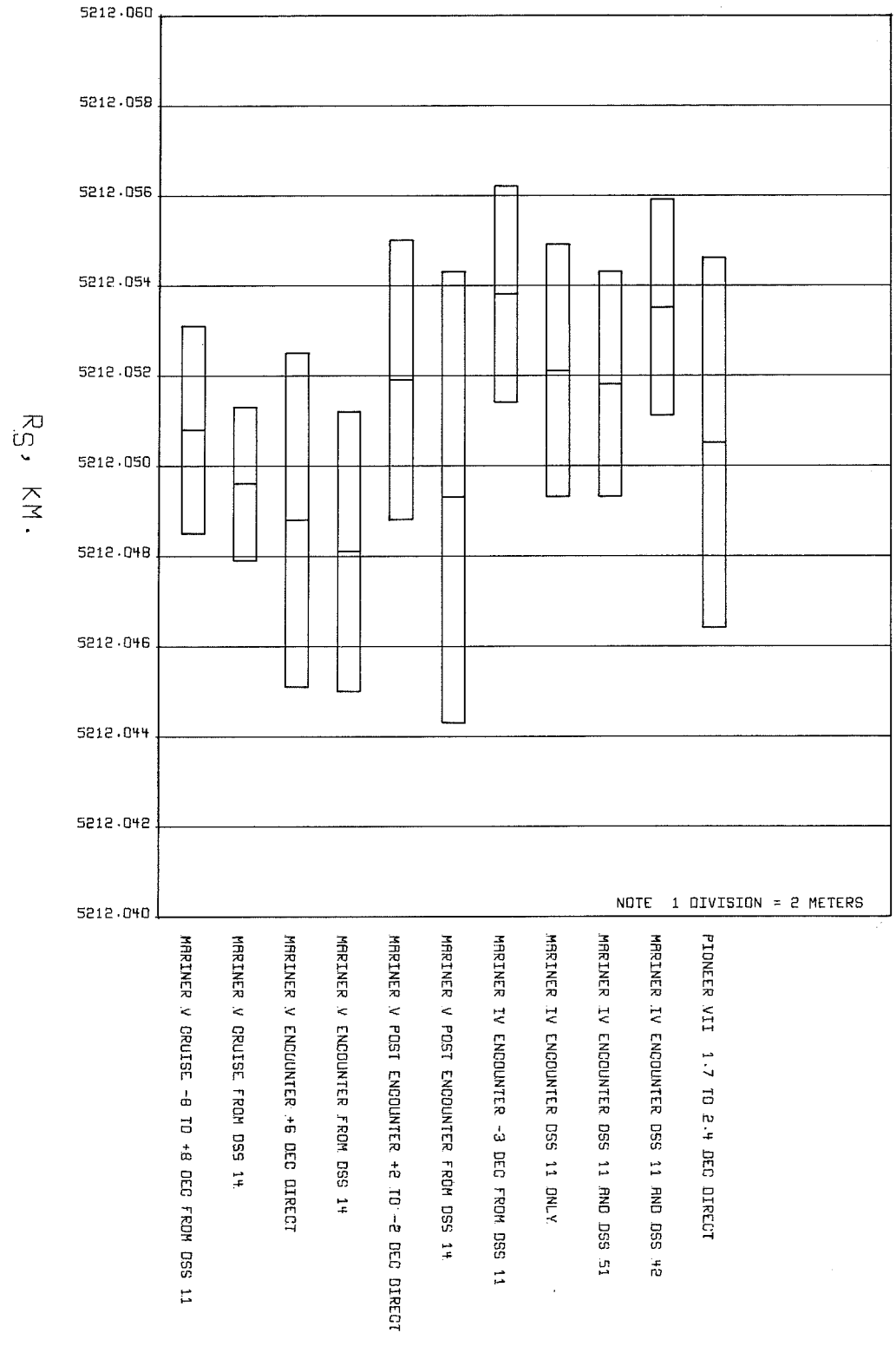
5212.060
5212.058
5212.056
5212.054
5212.052
5212.050
5212.048
5212.046
5212.044
5212.042
5212.040
RS, KM.
NOTE 1 DIVISION = 2 METERS
MARINER V CRUISE -8 TO +8 DEC FROM DSS 11
MARINER V CRUISE FROM DSS 14
MARINER V ENCOUNTER +8 DEC DIRECT
MARINER V ENCOUNTER FROM DSS 14
MARINER V POST ENCOUNTER +2 TO -2 DEC DIRECT
MARINER V POST ENCOUNTER FROM DSS 14
MARINER IV ENCOUNTER -3 DEC FROM DSS 11
MARINER IV ENCOUNTER DSS 11 ONLY
MARINER IV ENCOUNTER DSS 11 AND DSS 51
MARINER IV ENCOUNTER DSS 11 AND DSS 42
PIONEER VII 1.7 TO 2.4 DEC DIRECT

Fig. 2. Distance off spin axis, earth-fixed system (1903.0 pole), DSS 12

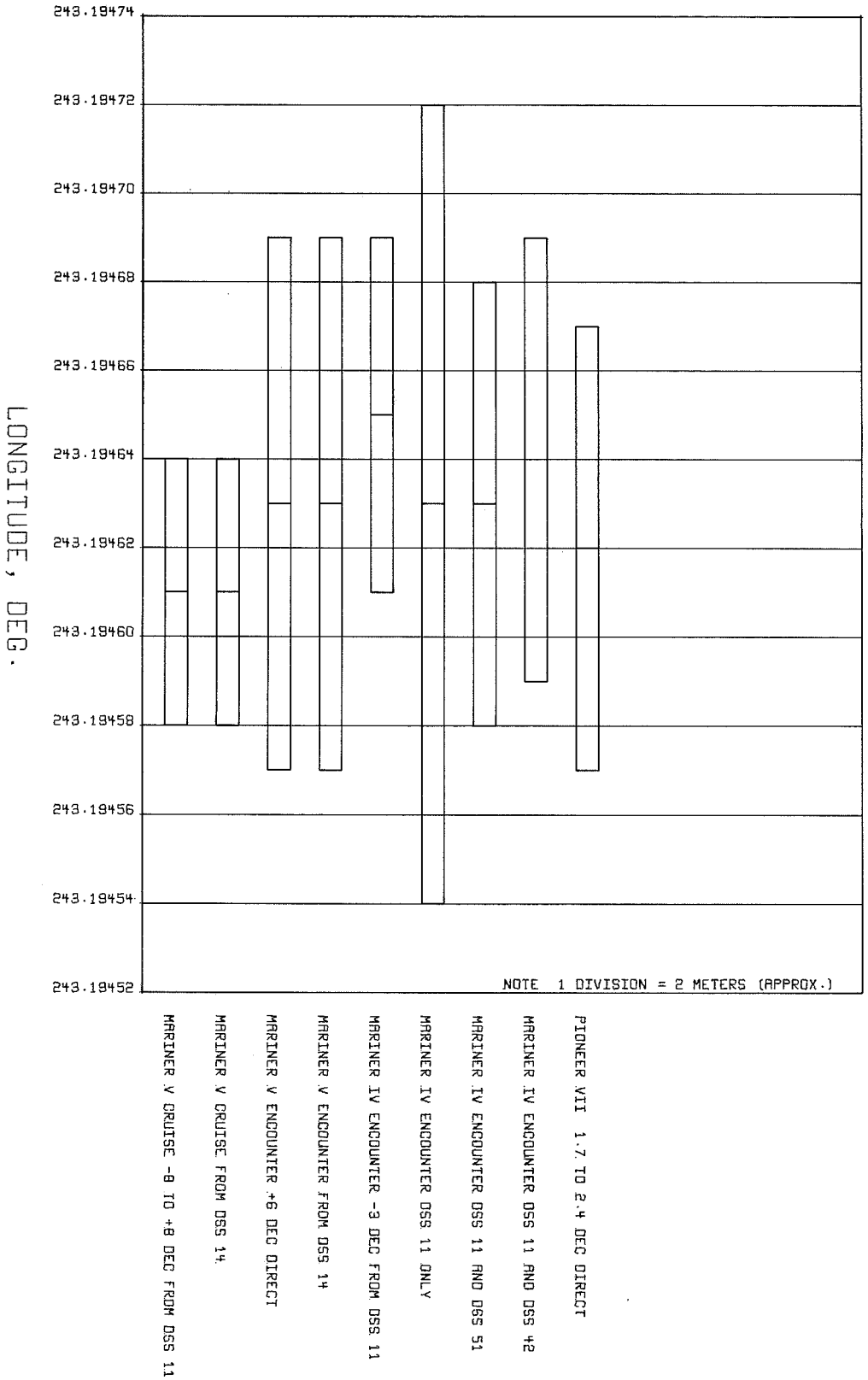

Fig. 3. Geocentric longitude, earth-fixed system (1903.0 pole), DSS 12

It may be that the nominal troposphere was cancelling ionospheric effects. Improving the troposphere model could then permit the ionospheric effects to produce the changes discussed earlier. Since DSS 42 had the smallest change of any of the stations in index of refraction (30 vs 100 units) one would not believe that this is responsible for the sensitivity of the DSS 11 and 51 station location solutions to the inclusion or omission of DSS 42. Other factors not yet considered may be responsible. Also, the limitations of the SPODP may preclude the resolution of these problems. Sensitivity at the meter level is beyond the capability of this program.

An item which definitely must be given more attention is the elevation-angle history for each station. The low-elevation data is very important for estimating r_s. This can be noted in the reductions of the DSS 11 and 51 data for *Mariner IV* encounter. If one rejects some of the low-elevation data on the basis that it appears to be biased about 0.03 Hz, the solution for r_s nears the value obtained when fitting all three stations and rejecting the data on an elevation criterion. Apparently, even biased data can be significant for some circumstances when estimating this parameter.[5] This information, combined with knowing which station(s) tracked the closest to the zero-declination passage, is of importance in determining just which solutions may be more significant than others.

As opposed to the 40-m spread in longitude solutions reported in SPS 37-48, Vol. II, the *Mariner IV* and *V* encounter reductions have given solutions agreeing exactly (Fig. 3). Longitude solutions agreeing to 1 or 2 m with these encounter solutions have also been obtained when fitting portions of the cruise phase of *Mariner V* and *Pioneer VII*. It has been assumed that longitude could not be well determined during the cruise phase of a planetary mission. However, these fits indicate that good longitude determination can be attained from fitting relative long arcs of cruise data. A minimum of 60 days of *Mariner V* cruise data is needed to obtain agreement with encounter longitudes. Fitting the *Pioneer VII* data for an r_s determination has also produced a longitude solution which agrees within 1 or 2 m of the encounter values. In this case, 60 days of data were fit. However, the problem of longitude determination during cruise is perplexing and requires further study.

[5]For the report on the recommended indices of tropospheric refraction and their effect on the *Lunar Orbiter II* translunar data and the landed *Surveyor* analysis, see articles by Mottinger and Winn (SPS 37-50, Vol. II, pp. 97–104, 110–125).

The longitude plot (Fig. 3) shows that the referenced and direct *Mariner V* solutions for DSS 12 are the same. This illustrates that excellent relative longitudes are obtained within a complex, even though it is unusual to have any two stations tracking on successive days. Atmospheric disturbances are assumed to be the same for all Goldstone stations, whereas between complexes (continents) local atmospheric effects could cause the relative solutions to be erroneous.

e. Compiling a "best" set of station locations. From the two zero-declination portions of the *Mariner V* mission, it is possible to find a time when all but one station in the DSN were tracking very close, if not exactly at the time of passage, through zero declination. For the stations at the Goldstone DSCC, a solution for one is sufficient because it can be transferred to the remaining stations. These solutions are reduced to the 1903.0 pole using International Polar Motion Service (IPMS) pole positions. From these same fits (reduced to 1903.0) used to determine r_s, it is also possible to determine the relative longitudes between the stations.[6] Table 2 lists the phases and the solutions of the missions analyzed for the absolute and relative locations. By choosing the longitude for one station from an encounter reduction and applying the relative longitudes, the set (denoted by the mnemonic LS14 for location set n) is complete for the spin axis and longitude components. The absolute spin axis and the relative longitude from the *Mariner IV* encounter reduction fitting DSS 11 and 51 data were used to tie DSS 51 into the network.

A process similar to that described above was performed using the radio solutions available to determine relative distance off the spin axis and relative distance off the equator plane, as well as relative longitude for the DSN stations. These relative locations were computed from *Mariner IV* and *V* results which were reported in the first two articles of this series (SPS 37-48 and 37-49, Vol. II). These were connected to the combined *Ranger* solutions for DSSs 12, 41, and 51 and were denoted by the mnemonic LS4. The combined *Ranger* locations were chosen as the base since the data comprising their reduction has been the most thoroughly analyzed to date and has been used as the standard for the physical constants

[6]It is not the intention of this article to present a rigorous discussion of relative longitudes. These values have been chosen from the *Mariner IV* and *V* missions since they have shown remarkable consistency among numerous reductions performed. Although other errors are induced by spanning continents, the relative locations are still considered to be of fine quality. It will be the goal of future analyses to investigate these quantities more closely.

Table 3. Previous best set minus new set (LS4 − LS14)[a]

DSS	$r_{s_{LS4}}$, km	λ_{LS4}, deg	$\Delta\lambda_{LS4}$, deg[b]	$r_{s_{LS14}}$, km	λ_{LS14}, deg	$\Delta\lambda_{LS14}$, deg[b]	$r_{s_{LS14}} - r_{s_{LS4}}$, m	$\lambda_{LS14} - \lambda_{LS4}$, 1 m ≃ 10^{-5} deg	$\Delta\lambda_{LS14} - \Delta\lambda_{LS4}$, ~ m[b]
12	5212.0392	243.19483	—	5212.0497	243.19463	—	10.5	−20	—
11	5206.3300	243.15090	−0.04393	5206.3381	243.15070	−0.04393	8.1	−20	0
14	5203.9855	243.11079	−0.08404	5203.9949	243.11059	−0.08404	9.4	−20	0
41	5450.1987	136.88783	−106.30700	5450.1978	136.88759	−106.30704	−0.9	−24	4
42	5205.3403	148.98157	−94.21326	5205.3497	148.98137	−94.21326	9.4	−20	0
51	5742.9815	27.68572	−215.50911	5742.9412	27.68548	−215.50915	9.7	−24	4
61	4862.5986	355.75122	112.55639	4862.6044	355.75109	112.55646	5.8	−13	7
62	4860.8115	355.63250	112.43767	4860.8158	355.63226	112.43763	4.3	−24	−4

[a]These mnemonics are used to designate particular sets of station location solutions. LS14 values are those appearing in Ref. 4, and as noted in footnotes g and h of Table 2; LS4 denotes the previous best set.

[b]DSS 12.

$GM_{\oplus}$ and $GM_{\mathfrak{D}}$ as well as the station locations. Table 3 shows the differences in the absolute and relative locations of the LS14 and LS4 sets. There is an approximate 10-m difference in the r_s solutions (excepting DSS 41) and a 13- to 25-m difference in absolute longitudes. This latter difference would be expected since the previous values were based upon lunar missions and the new values on planetary missions, so it is not justifiable to say that the LS4 longitudes were really incorrect by this amount.

The locations identified as LS14, with some minor exceptions noted in Table 2, appear in Ref. 4. Although these are regarded as the "best", one must understand how the word "best" is used in this context. These solutions are "best" for DE 40, using the U. S. Naval Observatory universal time coordinated (UTC) and other inputs to TPOLY[7] for reducing the data. For reductions of lunar data using the present lunar ephemerides, these need not be the "best" station locations. The spin axis values would probably be acceptable, but the longitudes definitely would not. For the "best" station locations for reducing lunar data, the longitudes in set LS14 would have to be increased by ~20 m (1 m ≅ 10^{-5} deg). However, even with the corrected (Van Flandern) ephemeris discussed earlier, it is not possible to guarantee that the planetary longitudes would be the "best". One must take careful note of the context surrounding "best". Each set of station locations is a function of several items. Newer ephemerides with improved absolute locations of the planets could be expected to change the DSS longitude solution. Any changes in the time would produce longitude shifts. A change in pole positions would affect spin axis as well as longitude solutions. Within the DSN, UTC time tags are attached to the data as it is received. When the data is reduced with the SPODP, TPOLY calculates the corresponding UT1 for determining the position of the tracking station in space. The final longitude estimate obtained is corrected using the IPMS[8] pole reports. Since the SPODP lacks a model for the polar motion, it is necessary to assume that for an extended flight the motion is averaged in the final solution obtained. To correct for the polar motion, it too is averaged over this same time. The pole positions used to correct the SPODP estimate should be the same as those used by the time agency for predicting UT1.

Prior to January 1, 1968, the U. S. Naval Observatory has used BIH[9] pole position reports for determining UT. To be consistent in our reductions, the BIH pole should have been used. The difference may be as much as 3 m. The conversion to IPMS pole by the Naval Observatory has produced an 8-ms jump in UT1. Although this jump is in the 1968 TPOLY polynomial coefficient computations, data reduced prior to 1968 has not affected. Currently, Naval Observatory data is being reduced after

[7]As described by Muller in SPS 37-41, Vol. III, pp. 18–24, TPOLY is a program which accepts U. S. Naval Observatory time bulletin data and produces a set of polynomials which fit the data and are used in the SPODP for necessary UT1, UTC, and ET time transformations.

[8]IPMS = International Polar Motion Service.

[9]The International Bureau of Time (Bureau International de l'Heure) in Paris is the coordinating agency for time transmission and related matters. The results of all communications are published in the *Bulletin Horaire*.

having defined a new pole prior to 1962. This eliminates the 1968 jump in UT1 and will yield a pole and timing system that are consistent. When this is available, it will be used to reprocess this data.

It is also necessary to quote a guide to the uncertainties in our station locations r_s and longitude. In some instances, the formal statistics produced by the SPODP are unrealistic in light of known factors affecting the station locations. Some of these items have been mentioned. They generally are those which are not modeled in the ODP. For extended flights, the polar motion causes the DSS r_s and longitude to change; ionospheric and tropospheric effects on the signal also affect the position determined as the station location. As discussed previously, a computer program is being used to model these contributing error sources in the form of a post-reduction corruption of the accumulated normal equation matrix prior to its inversion.

Initial results from this program are producing more realistic statistics. Whereas earlier attempts for achieving credible uncertainties have involved a simple rms of assumed equivalent errors in station locations due to polar motion, ionosphere, ephemeris, etc., this program calculates the effects of these items on the doppler data and puts the values into the normal equation matrix (J). Other values are computed for errors in doppler due to software integration error, troposphere, space plasma, transmitter stability, and time synchronization; these values are also inserted in the J matrix. Inversion of this expanded matrix is then performed to obtain the uncertainties and correlations on the parameters desired. At the same time, it is also possible to scale the weights used in the original SPODP run so that they are more indicative of the noise of the data. Weights actually used in the SPODP are larger than the noise on the data since it is necessary to off-weight the data to account for these error sources. However, with the models present for the error sources in this separate program, it is possible to use a more realistic weight. This has been done and has given an initial estimate of the uncertainties to be associated with the station locations. These uncertainties are listed in Table 4.

Future plans include a statistical combination of these results which would serve to reduce the uncertainties even further. It is also a definite objective to try and explain the scatter among these various solutions. With the uncertainties approaching the 1-m level, these differences among the solutions will have to be explained before the statistic can be accepted with complete confidence. Hopefully, the collection of additional data for calibrating out the effects of the ionosphere and troposphere will lead towards improving the agreement exhibited in Figs. 2 and 3.

f. Comparison of LS14 with SAO Baker–Nunn data. Table 5 shows the comparison of the LS14 set with the values for DSN stations obtained by SAO using the Baker–Nunn optical data and with the combined *Ranger* solutions by Vegos and Trask (SPS 37-43, Vol. III, pp. 3–18). For the spin axis and absolute longitude solutions, there is a 1- to 7-m improvement in the agreement of the SAO and JPL r_s and approximately a 20- to 30-m improvement in absolute longitude agreement. Relative longitudes fluctuate from decreasing to increasing agreement of 3 to 6 m, respectively. This represents an improvement in some respect, but the large disagreement between the JPL and SAO absolute longitudes prohibits the direct combination of the two solutions. Even the

Table 4. Approximate station location uncertainties[a]

Parameter	Uncertainty, m
Relative longitudes[b]	~ 3.5
Absolute longitudes	~ 5
Distance off spin axis	~ 5

[a]For stations at Goldstone, California, Woomera and Canberra, Australia, Madrid, Spain, and Johannesburg, South Africa.

[b]Between complexes (continents).

Table 5. Comparison of SAO Standard Earth, 1966 DSN locations with combined *Ranger* results and new best set (LS14)

DSS parameter	SAO	LS14	SAO − LS14, m	SAO − *Ranger*, m
$r_{s_{12}}$	5212.0635	5212.0497	13.8	23.5
$r_{s_{41}}$	5450.1820	5450.1978	−15.8	−17.7
$r_{s_{51}}$	5742.9360	5742.9412	−5.2	4.0
λ_{12}	243.19431	243.19463	−32	−51
λ_{41}	136.88701	136.88761	−60	−80
λ_{51}	27.68500	27.68548	−48	−71
$\Delta\lambda_{12-41}$	106.30730	106.30702	28	29
$\Delta\lambda_{41-51}$	109.20201	109.20213	−12	−9
$\Delta\lambda_{12-51}$	215.50931	215.50915	16	20

disagreement between the relative longitude solutions is overly large when one considers that this is the best determined quantity from radio tracking. The absolute longitudes may disagree due to the differences in BIH time and the U. S. Naval Observatory time used in the respective reductions. Known differences of 25 ms could account for 10 m of this. The discussed possibility of an inconsistency between the FK4 star catalog system and the current JPL ephemerides could also be responsible. Other items which should be considered are the amount of tracking performed by the SAO cameras. Is a tie between cameras established in the same sense as between DSN stations? Until these matters can be resolved, JPL's contributions to the SAO work would best be limited to supplying r_s and relative longitude.

SAO solutions are currently being used for the component of station locations along the earth's axis of rotation Z. Since radio tracking is insensitive to Z, another source must be used if one wishes to produce a complete set of coordinates containing the best solutions for all stations. The Z values chosen are taken from SAO Standard Earth, Vol. III, 1966, Table 9. Solutions are available only for DSSs 12, 41, and 51. This means that all the stations at the Goldstone DSCC will have the Z component based upon the SAO results for DSS 12, using the known survey differences in station locations. Since there presently is not a first-order tie between DSSs 41 and 42, a radio solution will be retained for DSS 42. Similarly, for the Madrid stations, DSSs 61 and 62, it will be necessary to wait until the survey work is completed to the standards required: the existing first-order geodetic control must be carried to the point defined as the station location—the point on the polar axis nearest the declination axis. Until this is done for all the stations in the DSN, following the pattern set by William Bollinger at the Goldstone DSCC, radio tracking cannot successfully utilize results such as those provided by SAO. Hopefully, the SAO Standard Earth, 1969 can be used to establish the Z component, in addition to possibly updating those listed in the SAO Standard Earth, 1966 for the remaining DSN stations as soon as they are properly surveyed into the control system.

Geocentric radius and latitude components for r_s are given only as an aid to those requiring input for computer programs in this format. It is extremely important to remember that only r_s and λ have been determined by the radio tracking of deep space probes. Should others desire to compare their values with ours, the only valid comparison to make for r_s is to compute their geocentric radius times the cosine of their geocentric latitude and compare this with our r_s. As more analysis is performed and a better understanding of the SAO work is acquired, it may be possible to attach more significance to all three components of station locations.

g. Conclusion. Having tentatively identified the cause for the disagreement between the planetary and lunar longitude solutions and realizing that the zero-declination and encounter data are well suited for estimating distance off the spin axis, significant advancement has been made in the reduction of deep space probe radio data when solving for DSS locations. The accuracies achieved probably have approached the limits of the single-precision orbit determination program. To make significant improvements again will require the double-precision program with its increased numerical accuracy and better models. The consistency obtained using DE 40 to reduce the *Mariner IV* and *V* and the *Pioneer VII* data indicates that it appears to be one of the best ephemerides to date.

In the future, station location reductions will entail reducing the lunar data, some of which has never been examined, and will involve the corrected lunar ephemeris. Improved agreement between the lunar and planetary solutions is expected. Techniques to calibrate the atmospheric effects will also be a requirement for meeting the goals of the future. With the creation of improved models for the troposphere and the ionosphere, it should be possible to reprocess the earlier data and obtain some consistent results.

The LS14 set of station locations is qualified as the present "best" set of station locations which have been obtained using the planetary ephemeris contained in DE 40. These solutions also represent reductions performed using U. S. Naval Observatory time signals and International Polar Motion Service pole position reports. Before comparing these locations with those derived, either a different time source or pole motion service would require adjustment of the solutions to put them on a common basis.

References

1. Warner, M. R., and Nead, M. W., *SPODP — Single Precision Orbit Determination Program,* Technical Memorandum 33-204. Jet Propulsion Laboratory, Pasadena, Calif., Feb. 15, 1965.
2. *Proceedings of the JPL Seminar on Uncertainties in the Lunar Ephemeris.* Edited by J. D. Mulholland, Technical Report 32-1247. Jet Propulsion Laboratory, Pasadena, Calif., May 1, 1968.

References (contd)

3. Mulholland, J. D., and Block, N., *JPL Lunar Ephemeris Number 4*, Technical Memorandum 33-346. Jet Propulsion Laboratory, Pasadena, Calif., Aug. 1, 1967.

4. Melbourne, W. G., et al., *Constants and Related Information for Astrodynamic Calculations, 1968*. Technical Report 32-1306. Jet Propulsion Laboratory, Pasadena, Calif., July 15, 1968.

3. Comparison of Ionospheric Measurements for Evaluation of Techniques Used in Charged Particle Calibration of Radio Tracking Data, Preliminary Results, *B. D. Mulhall and R. N. Wimberly*[10]

a. Introduction. The capability to calibrate radio tracking data of deep space probes for charged particle effects is being developed. The calibration procedure is to compute the phase-path length decrease due to charged particles and apply this quantity as a correction to the observed doppler. The group-path delay is also computed and used as a correction to ranging data. The corrections are computed from charged particle measurements or by using a model to predict the medium through which the tracking radio signal passes. The charged particles acting upon a probe's radio signal exist in the interplanetary space plasma, the earth's ionosphere, and during encounter, the ionosphere of the other planet. This article is concerned with the calibration of the effect due to the earth's ionosphere.

b. Ionospheric data. Three major sources of charged particle data for the earth's ionosphere are:

(1) Faraday rotation measurements made from earth satellites.

(2) Ionosonde measurements made by ESSA.[11]

(3) Dual-frequency experiments carried on deep space probes.

Faraday rotation data (SPS 37-55, Vol. II, pp. 15–19) provide measures of the charged particles between a satellite and an observer. Faraday rotation measurements indicate the change in the number of charged particles but do not provide a measure of absolute content, which must be estimated. To use Faraday rotation data to calibrate tracking data, the measurement must be mapped from the satellite–observer line of sight to the ray path between the probe and the deep space station. Adjustments must be made in the mapping for differences in elevation angle, longitude, and latitude (SPS 37-55, Vol. II, pp. 13–15 and 19–22.

Ionosonde measurements (Ref. 1) are made by recording reflection from the ionosphere of radio signals transmitted vertically. This provides a measure of the electron content of the lower ionosphere. The upper portion must be extrapolated. Like Faraday rotation measurements, ionosonde data must be mapped from the observer's direction of measurement, in this case his zenith, to the probe's ray path.

Dual-frequency experiments (Ref. 2) carried on *Mariner V* and *Pioneers* provide a direct measure of all the charged particles (both interplanetary and earth's ionosphere) between the transmitter at Stanford University and the probe. This data type can be used with very little adjustment to calibrate the tracking data measured at the Goldstone DSCC because of the geographic proximity of Goldstone and Stanford.

c. Comparisons of measurements. Comparisons of these three ionospheric measurements are being made to evaluate the accuracy of the mapping techniques used in the ionospheric calibration program. Figure 4 shows the electron content[12] measured by the Stanford Electronics Laboratory using Faraday rotations of radio signals from the *Syncom III* satellite versus time and ionosonde measurements made by ESSA at Point Arguello, California. The Stanford–*Syncom III* measurements have been mapped to the Point Arguello zenith. Short-term divergences between measurements may be caused by inaccurate estimates of the upper profile for ionosonde data or by errors in the Faraday rotation measurements. They may also be caused by local, short-term fluctuations seen only along one ray path. They are not believed to be caused by the mapping technique. On the other hand, the bias error between the two measurements (Fig. 4) is probably caused by inaccuracies in mapping technique, although it may be caused by errors in estimating the absolute level of Faraday rotation measurements.

Table 6 lists the sample mean and standard deviation of the difference between the two measurements. The

[10]We would like to acknowledge the assistance of Mr. T. Croft and Mr. M. Davies of Stanford Electronics Laboratory, who provided the dual-frequency and Faraday rotation data, respectively, and Miss L. Wescott of the Telecommunication Laboratory, ESSA, Boulder, Colorado, who provided the ionosonde data.

[11]ESSA is Environmental Science Services Administration, Boulder, Colorado.

[12]At S-band, 1.14×10^{17} electrons/m^2 cause an increase in phase-path length of 1 m.

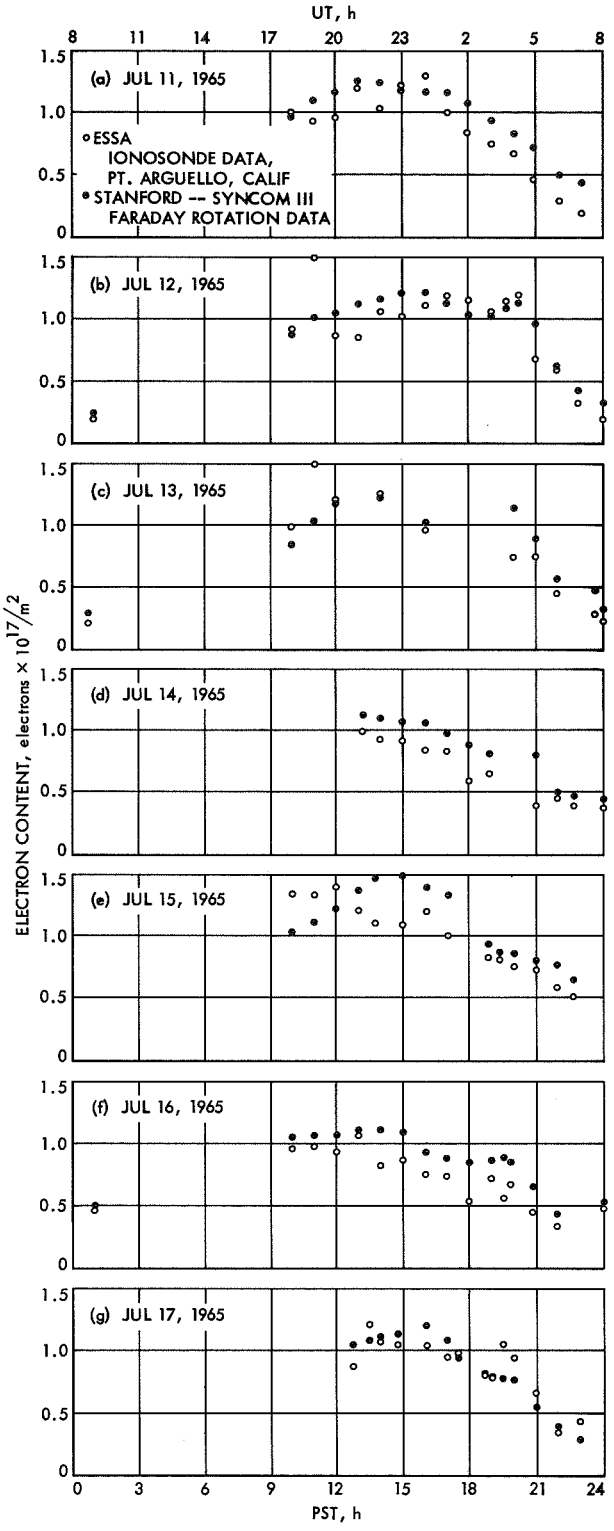
UT, h
8 11 14 17 20 23 2 5 8
(a) JUL 11, 1965
°ESSA IONOSONDE DATA, PT. ARGUELLO, CALIF
• STANFORD -- SYNCOM III FARADAY ROTATION DATA
(b) JUL 12, 1965
(c) JUL 13, 1965
(d) JUL 14, 1965
(e) JUL 15, 1965
(f) JUL 16, 1965
(g) JUL 17, 1965
ELECTRON CONTENT, electrons × $10^{17}/m^2$
1.5
1.0
0.5
0
0 3 6 9 12 15 18 21 24
PST, h

Fig. 4. Ionospheric measurements: ionosonde and Faraday rotation data (Stanford–*Syncom III* data mapped to Point Arguello zenith)

Table 6. Differences between ionosonde and Faraday rotation measurements of the ionosphere (Stanford–*Syncom III* Faraday rotation measurements mapped to the Point Arguello zenith)

Date (Jul 65)	Number of data points	Sample mean, 10^{17} electrons/m^2	Standard deviation (unbiased), 10^{17} electrons/m^2
11	14	−0.1361	0.1240
12	17	−0.0338	0.1826
13	11	−0.0399	0.2188
14	11	−0.5173	0.6417
15	14	−0.1031	0.2117
16	16	−0.1609	0.0919
17	14	0.0193	0.1371
18	1	−0.0262	—
19	2	−0.1971	0.0428
24	1	−0.1377	—
25	1	−0.0892	—
27	2	0.0685	0.1332
28	4	0.2029	0.0793
29	4	0.0034	0.1031
30	2	−0.2642	0.1266
	Total: 114	Average: −0.1238	

negative overall average of the bias for this period indicates that the mapping technique underestimates the ionosphere at high elevation angles.

Figure 5 shows Stanford–ATS-1 Faraday rotation[13] and *Mariner V* dual-frequency measurements. The Stanford–ATS-1 measurements are mapped to the *Mariner V*–Stanford line of sight. The large variation in electron content is due to the variation in elevation angle during the pass.

Since the dual-freqency measurements include space plasma and the Faraday rotation measurements do not, there is an offset between the two measurements. This bias is caused in part by the space plasma, and partially by mapping errors. The space plasma effect should grow as the earth–probe distance increases. Figure 6 is a plot of this bias versus mission time. The center of the bars indicates the average difference. The length of the bars is $\pm$ 1σ. The fluctuations in the bias are to be expected since the space plasma is not isotropically radiated from

[13]ATS-1 = *Applications Technology Satellite 1.*

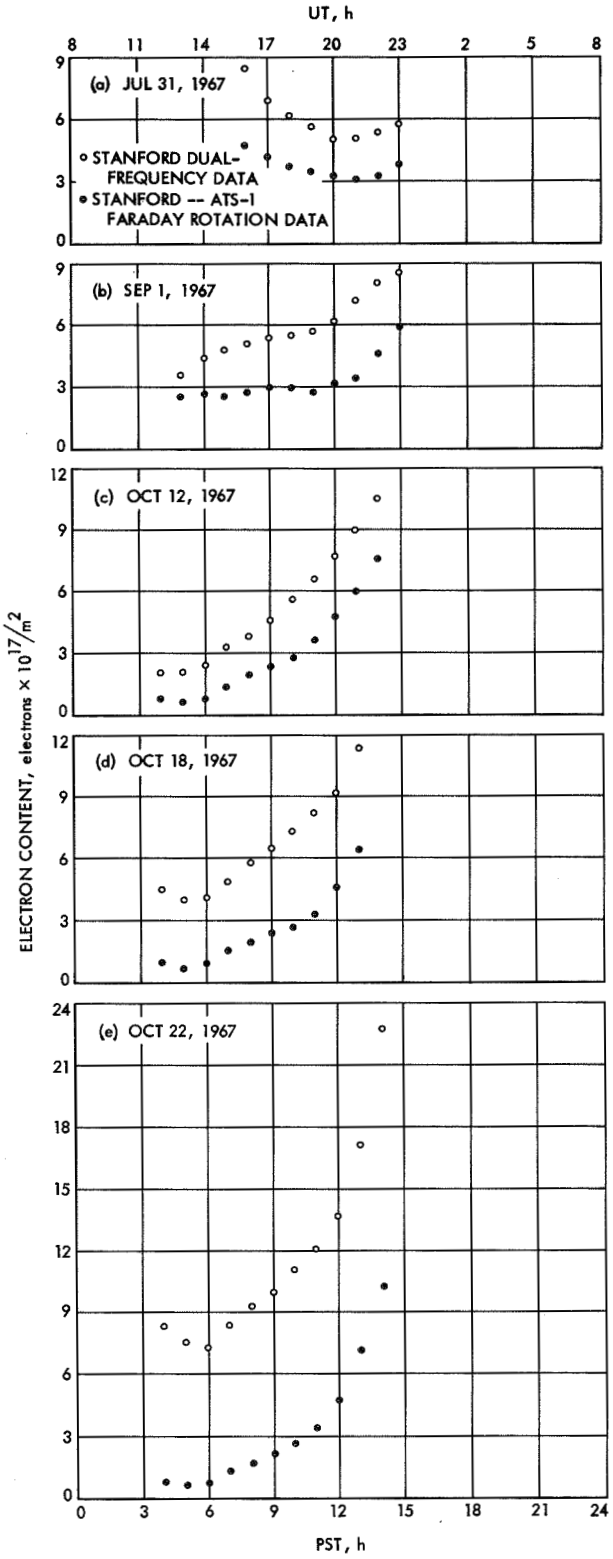
UT, h
8 11 14 17 20 23 2 5 8
(a) JUL 31, 1967
○ STANFORD DUAL-FREQUENCY DATA
● STANFORD -- ATS-1 FARADAY ROTATION DATA
(b) SEP 1, 1967
(c) OCT 12, 1967
(d) OCT 18, 1967
(e) OCT 22, 1967
ELECTRON CONTENT, electrons × $10^{17}/m^2$
0 3 6 9 12 15 18 21 24
PST, h

Fig. 5. Charged particle measurements: dual-frequency and Faraday rotation data (Stanford–ATS-1 data mapped to *Mariner V* ray path)

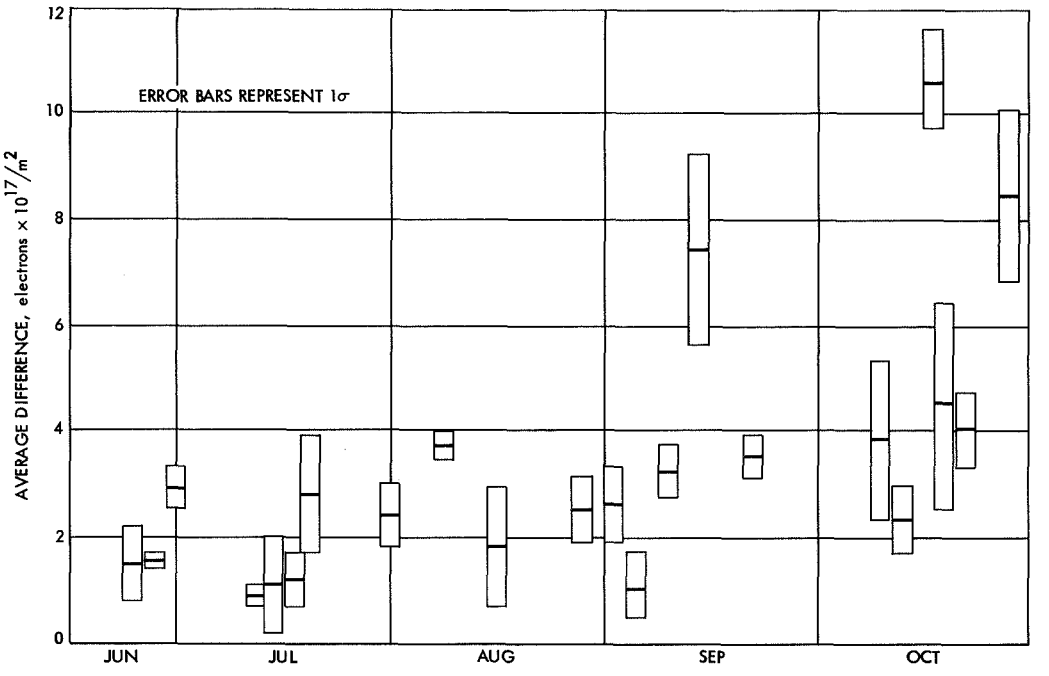

Fig. 6. Difference between *Mariner V* dual-frequency data and Stanford–ATS-1 Faraday rotation data vs mission time

the sun; on the contrary, plasma pulses are frequently observed (Ref. 2).

Figure 5 shows that the difference in measurements increases consistently at the end of each pass when the probe is at low elevation angles. This divergence is undoubtedly caused by errors in the mapping technique which grow as elevation angle decreases.

The close similarity in the shape of the two measurements shows that a doppler correction, which is computed by differencing the electron content over intervals of 1 to 10 min, will be quite accurate.

d. Future studies. These preliminary results indicate that there is very good agreement between the various data sources when mapped to the same ray path. However, more work is required to determine measurement errors so that mapping errors can be isolated and eliminated.

The computer program developed to produce the analyses described in this article will be used to perform more comparisons of measurements to determine and eliminate the inaccuracies of the mapping technique used in the charged particle calibration of tracking data.

Analysis will also be undertaken to determine the distance across the earth's surface that an ionospheric measurement can be mapped with usable accuracy.

References

1. Davies, K., *Ionospheric Radio Propagation*, Monograph 80. National Bureau of Standards, Washington, D.C., April 1, 1965.

2. Koehler, R. L., "Radio Propagation Measurements of Pulsed Plasma Streams from the Sun Using Pioneer Spacecraft," *J. Geophys. Res., Space Physics*, Vol. 73, No. 15, pp. 4883–4894, Aug. 1, 1968.

4. Charged Particle Effects to Radio Ranging and Doppler Tracking Signals in a Radially Outflowing Solar Wind,

L. Efron and R. J. Lisowski

Radio signal ranging and doppler errors due to ray path and phase change effects resulting from the presence of charged particles can be calculated by determining the total electron content and its time rate of change along the ray path between the tracking station and the spacecraft. The charged particles through which tracking signals propagate lie in three distinct regions: the earth's ionosphere, the interplanetary medium, and (during tracking near solar occultation) the solar corona.

Current ranging systems accuracies are quoted as being ± 15 m. It is the intent of this article to show that the uncalibrated effect of charged particles in the interplanetary medium may introduce bias errors an order of magnitude greater than this during radio tracking when the signal ray path is well outside the solar corona.

When contrasted with the ionosphere, which exhibits large diurnal variations, the interplanetary medium is closer to being a steady-state environment during a tracking pass at any DSN station. However, anomalies occur due to the pin-wheel-like streamers in the solar wind and, even more drastically, as a result of sudden outbursts of plasma from solar flares. This article only considers the case of a steady-state, isotropic solar wind.

Continuity of plasma flux for a radially outflowing solar wind yields a local electron density N_e inversely proportional to the square of the distance from the sun:

$$N_e = \frac{N_1}{r^2} \tag{1}$$

where r is the heliocentric distance and N_1 is the local electron density at unit heliocentric distance ($r = 1$). Refraction (bending) of the S-band signal ray path in the interplanetary region is negligible. Figure 7 illustrates the two possible cases of sun–earth–spacecraft geometry for straight-line propagation paths.

Let

- b = impact parameter of ray path to sun (ray path closest approach distance to sun for straight-line ray propagation)
- ρ = geocentric range to spacecraft
- r_1 = heliocentric distance to earth
- r_2 = heliocentric distance to spacecraft
- λ = relative heliocentric longitude of earth and spacecraft
- α = sun–earth–probe angle
- s = arc length along ray path $\bar{\rho}$

Let I_e be the total electron content along the ray path outside the ionosphere. Then

$$I_e = \int N_e \, ds \tag{2}$$

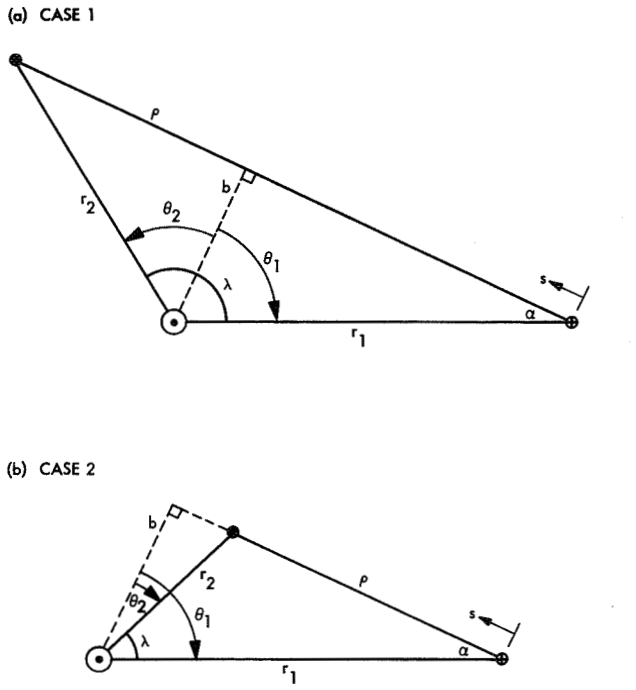

Fig. 7. Two cases of typical sun–earth–probe geometry

and, for the inverse-square solar-wind electron density distribution, we have

$$I_e = \int \frac{N_1}{r^2} \, ds = \int_{\theta_2}^{\theta_1} \frac{N_1}{b} \, d\theta$$

In terms of the relative heliocentric longitude of the earth and spacecraft, the solution in both cases is

$$I_e = \frac{N_1}{b} \lambda = N_1 \frac{\rho}{r_1 r_2} \frac{\lambda}{\sin \lambda} \tag{3}$$

From the triangle relations between the geocentric range ρ and the heliocentric distances r_1 and r_2, we have the results:

$$I_e = \frac{N_1}{r_1} \frac{\lambda}{\sin \alpha} \tag{4}$$

$$\lambda = \sin^{-1}\left[\frac{\rho \sin \alpha}{(r_1^2 + \rho^2 - 2 r_1 \rho \cos \alpha)^{1/2}}\right] \tag{5}$$

$$\lambda \leq 90 \text{ deg if } \rho \leq \frac{r_1}{\cos \alpha} \tag{6}$$

Equation (4) permits calculation of the total electron content in terms of geocentric quantities. The result is

noteworthy in that it may be scaled by the electron density at unit distance. However, the result is indeterminate for $\alpha = 0, 180$ deg. Here, we have

$$\lim_{\alpha \to 0} I_e = \frac{N_1}{r_1} \frac{\rho}{(r_1 - \rho)}, \qquad \rho < r_1 \tag{7}$$

$$\lim_{\alpha \to \pi} I_e = \frac{N_1}{r_1} \frac{\rho}{(r_1 + \rho)} \tag{8}$$

It is convenient to express distances in AU, charged particle densities in electrons/cm^3, λ in radians, and I_e in units of electrons/m^2. With this choice, Eqs. (4), (7), and (8) become

$$I_e = 1.5 \times 10^{17} \frac{N_1}{r_1} \frac{\lambda}{\sin \alpha} \tag{9a}$$

$$I_{e_{\alpha=0}} = 1.5 \times 10^{17} \frac{N_1}{r_1} \frac{\rho}{r_1 - \rho}, \qquad \rho < r_1 \tag{9b}$$

$$I_{e_{\alpha=180}} = 1.5 \times 10^{17} \frac{N_1}{r_1} \frac{\rho}{r_1 + \rho} \tag{9c}$$

Equations (9a, b, c) are plotted in Figs. 8 and 9 as I_e versus ρ for fixed values of α and λ with $N_1 = 1.0$

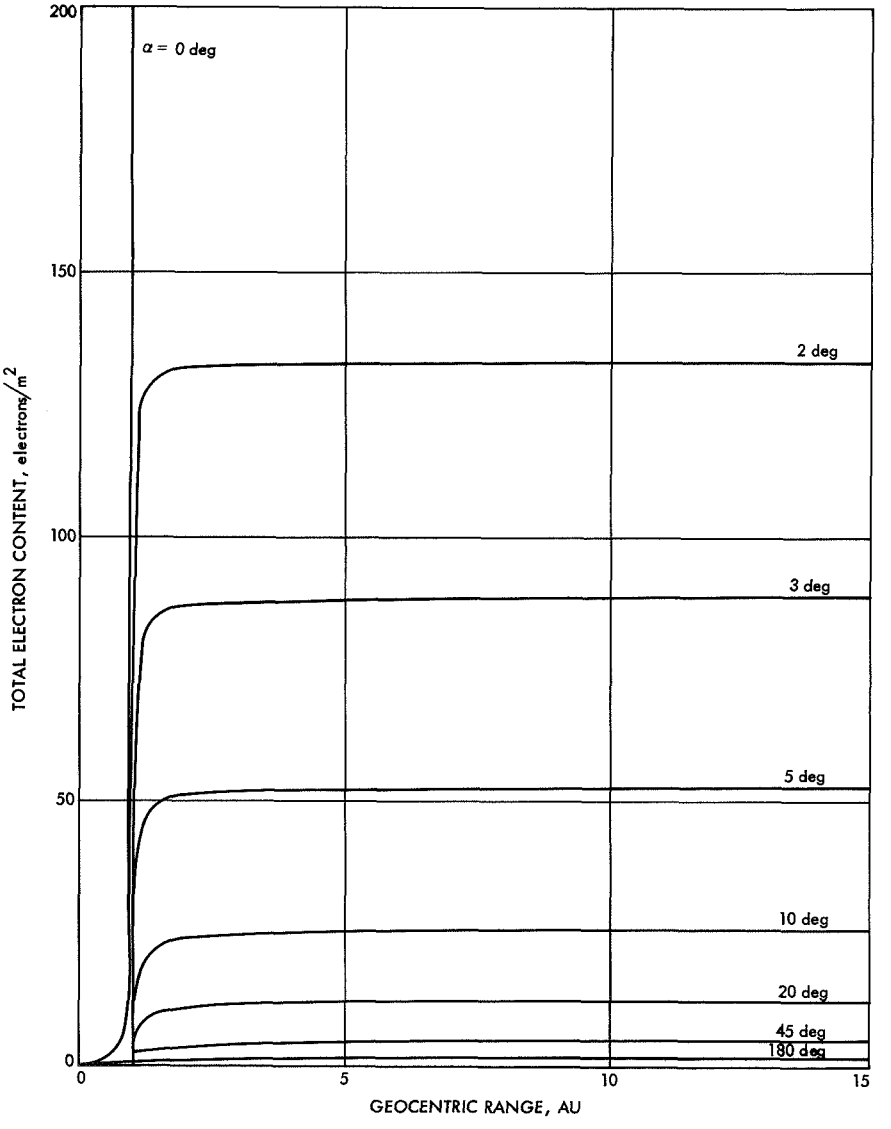

Fig. 8. Total electron content vs geocentric range for various sun–earth–probe angles α in a solar wind with an electron density of 1/cm^3 at 1 AU

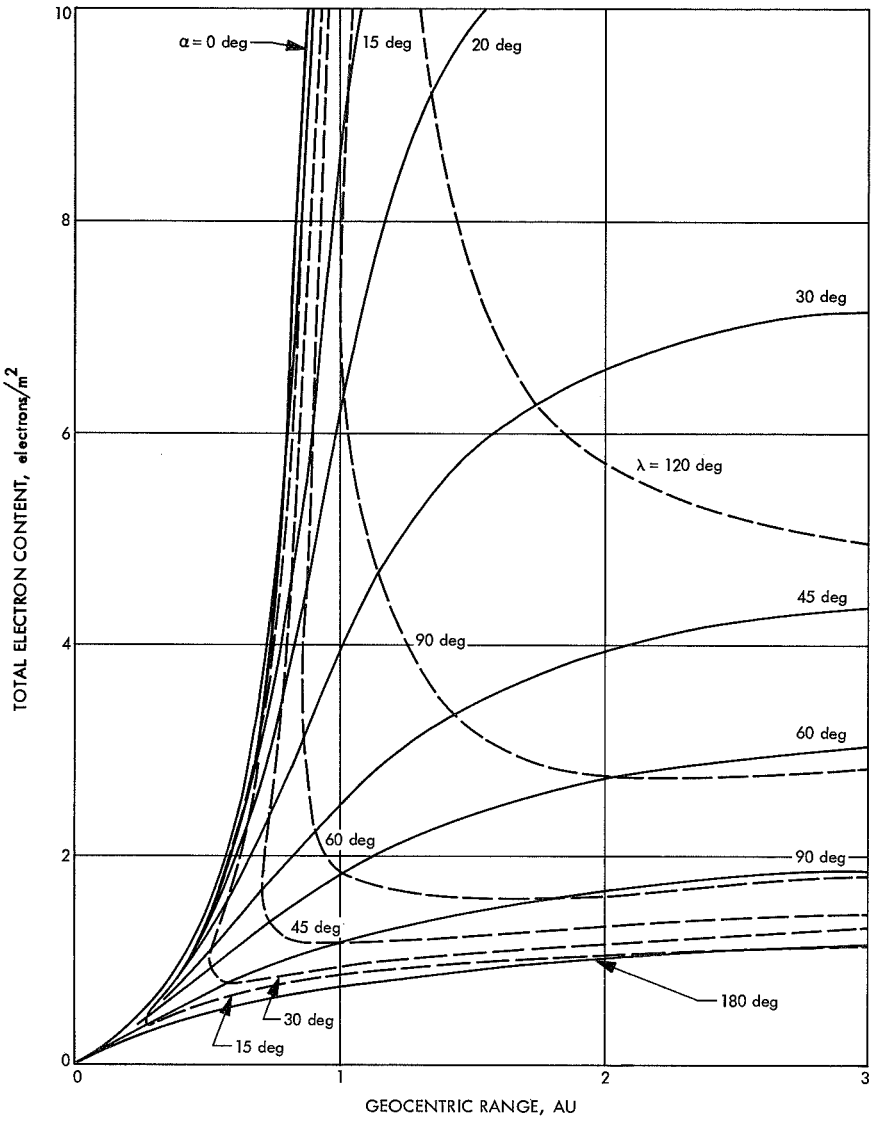

Fig. 9. Total electron content vs geocentric range for various sun—earth—probe angles α and relative heliocentric longitudes λ in a solar wind with an electron density of 1/cm³ at 1 AU

electron/cm³ and $r_1 \equiv 1$ AU. The ordinate may be scaled for any other value of N_1. From Fig. 8, we note that I_e (α = constant) is very nearly constant for geocentric range greater than 5 AU.

Contours of constant I_e are shown on a polar plot in Fig. 10. The curves are, of course, symmetric about the 0–180-deg axis.

Since r_1 is nearly constant, we have, from Eq. (4), that

$$\frac{dI_e}{dt} = \frac{\partial I_e}{\partial \alpha}\dot{\alpha} + \frac{\partial I_e}{\partial \lambda}\dot{\lambda} \tag{10a}$$

or

$$\frac{dI_e}{dt} = \left[\frac{\partial I_e}{\partial \alpha} + \frac{\partial I_e}{\partial \lambda}\frac{\partial \lambda}{\partial \alpha}\right]\dot{\alpha} + \frac{\partial I_e}{\partial \lambda}\frac{\partial \lambda}{\partial \rho}\dot{\rho} \tag{10b}$$

where

$$\frac{\partial \lambda}{\partial \rho} = \frac{r_1 \sin \alpha}{r_1^2 + \rho^2 - 2r_1\rho\cos\alpha} = \frac{b}{r_2^2} \tag{11a}$$

$$\frac{\partial \lambda}{\partial \alpha} = \frac{\rho(r_1\cos\alpha - \rho)}{r_1^2 + \rho^2 - 2r_1\rho\cos\alpha} = \frac{\rho(r_1\cos\alpha - \rho)}{r_2^2} \tag{11b}$$

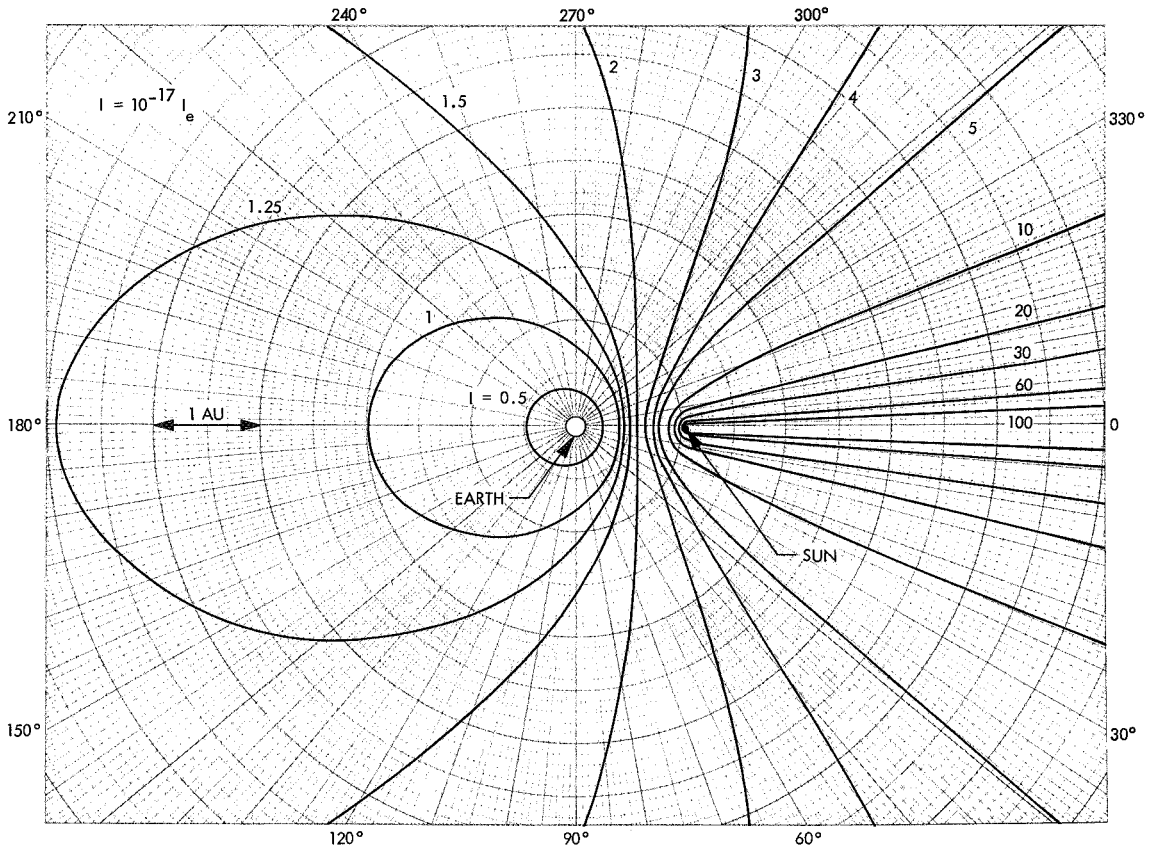

Fig. 10. Contours of constant total electron content in a solar wind with an electron density of 1/cm³ at 1 AU

$$\frac{\partial I_e}{\partial \alpha} = -\frac{N_1 \lambda \cos \alpha}{r_1 \sin^2 \alpha} = \frac{N_1 \lambda}{b \tan \alpha} \tag{11c}$$

$$\frac{\partial I_e}{\partial \lambda} = \frac{N_1}{r_1 \sin \alpha} = \frac{N_1}{b} \tag{11d}$$

From Figs. 8–10, we have already seen that the time rate of change of the total electron content along a signal ray path will only be of significance when the propagation path has a close approach to the sun. This condition is satisfied near solar occultation (superior conjunction with the sun) and for any inferior conjunction with $\rho \approx r_1$. Unless the object being tracked has a high eccentricity, these geometries result in $\dot{\rho} \approx 0$ during the pertinent periods.

Further simplification occurs at $\alpha \approx 0$ because we have

$$\dot{\alpha} = \frac{r_1 - \rho}{\rho} \dot{\lambda}$$

and, hence,

$$\frac{dI_e}{dt_{\alpha \approx 0}} = \left[\frac{\partial I_e}{\partial \lambda} - \left(1 - \frac{r_1}{\rho}\right) \frac{\partial I_e}{\partial \alpha}\right] \dot{\lambda}$$

$$= \frac{N_1}{b}\left[1 + \left(1 - \frac{r_1}{\rho}\right) \frac{\lambda}{\tan \alpha}\right] \dot{\lambda}$$

Near inferior conjunction, we have

$$\frac{\lambda}{\tan \alpha} \approx \frac{\rho}{r_1 - \rho}$$

and

$$\left.\frac{dI_e}{dt_{\alpha = 0}}\right|_{\rho < r_1} = 0$$

as expected from the symmetry noted in Fig. 10.

Let us now investigate the implications of this simple steady-state model of the radially outflowing interplanetary plasma to S-band radio ranging and doppler tracking signals.

The plasma-induced decrease in the tracking-signal group-path propagation velocity (SPS 37-41, Vol. III, pp. 3–11) results in a retardation of the ranging signal. The increased transit time results in an observed range (assuming a constant propagation speed c equal to the speed of light in a vacuum) which is too great by an amount $\Delta\rho$. For a frequency f(Hz), the range error $\Delta\rho$ (meters) is given by

$$\Delta\rho = \frac{40.3}{f^2} \int N_e \, ds$$

$$= \frac{40.3}{f^2} I_e$$

Table 7 indicates the columnar electron content which will induce a 1-m ranging error for a one-way passage of radio signal at nominal S-band uplink and downlink frequencies.

Table 7. Columnar electron content ($I_e \sim$ electrons/m^2) per 1-m one-way path range error

Parameter	Value, MHz	I_e/1-m one-way path error, electrons/m^2
Typical uplink frequency f_u	2110	1.11×10^{17}
Typical downlink frequency f_d	2295	1.31×10^{17}
Two-way frequency f_{eff}	—[a]	1.14×10^{17}

[a] $\frac{1}{f^2_{eff}} = \frac{1}{2}\left[\frac{k}{f_u^2} + \frac{1}{f_d^2}\right]$, $k = 240/221$

It now becomes a simple task to convert the plots of I_e versus geocentric range (Figs. 8–10) into plots of range error versus geocentric range. This, however, necessitates knowing the proper value of N_1 for use in scaling the ordinate. Solar-wind electron density at 1 AU heliocentric distance has been deduced from the dual-frequency radio propagation experiment aboard the *Pioneer* series of spacecraft. From information currently available (Ref. 1), Table 8 provides a basis for estimating N_1.

Table 8. Electron density at 1 AU from dual-frequency experiment data

Parameter	*Pioneer VI*	*Pioneer VII*
Data span	Dec 65–May 66	Aug 66–Mar 67
Geocentric range, km	to 75×10^6	to 85×10^6
N_1 (for an r^{-2} distribution), electrons/cm^3	4.3 ± 3.6	8.7 ± 4.0
Smoothed sunspot index range	23–46	63–85

During two-way S-band radio tracking, the plasma-induced doppler errors on the uplink signal will be multiplied by the spacecraft transponder multiplier (240/221). For a nominal uplink frequency of 2110 MHz, an electron-content time rate of change equal to 1.14×10^{17} electrons/m^2/s will result in a 1-m/s range rate error. Hence, for $N_1 = 6$ electrons/cm^3, the ordinate scale on Figs. 8–10 may be multiplied by a factor of 5 to yield an approximate quick-look range error.

As noted, the plasma decreases the group-path propagation speed. The phase-path velocity, however, is increased and, hence, the observed geocentric range rate (positive away from the earth) is decreased by an amount equal to the time rate of change of the range error. Since $I_e > 0$, we have a time varying range bias and a range rate error with a mean near zero (neglecting solar cycle variation effects) over the earth–spacecraft synodic period.

In spite of our imperfect knowledge of N_1 and its time (and spatial) variation, it is of interest to plot the geocentric trajectories of *Pioneer* and *Mariner* spacecraft to get some measure of the role played by plasma effects in past and future missions. To see the effects that may be present when tracking a planetary orbiter (such as *Mariner* 1971 in orbit about Mars), it is convenient to treat both the earth and the several planets of interest as moving along heliocentric circular orbits. These results are shown in Figs. 11 and 12.

S-band signal retardation $\Delta\rho$ greater than 10 m may occur for $\alpha < 90$ deg for all missions inside Jupiter's orbit. Significant effects ($\Delta\rho > 100$ m) occur for any interplanetary mission ($\rho > 1$ AU) for $\alpha < 15$ deg. These observations are based on using Figs. 8–12 with $N_1 \approx 6$ electrons/cm^3. The results are valid for sun–earth–probe angles greater than approximately 2 deg (8 solar radii) when $\rho > r_1$. For lesser values of α, the signal ray path passes through some portion of the solar

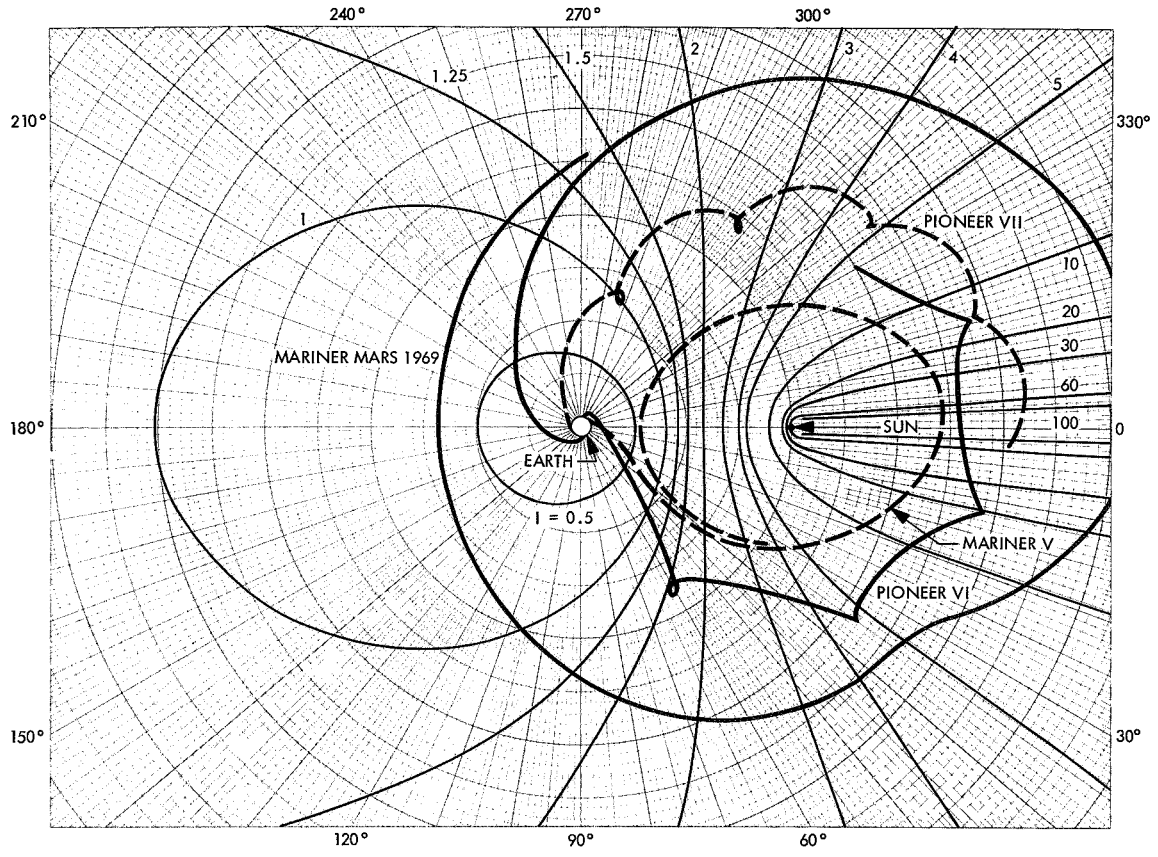

Fig. 11. Trajectories of *Mariner V*, *Mariner* Mars 1969, and *Pioneers VI* and *VII* in a solar wind with an electron density of 1/cm³ at 1 AU

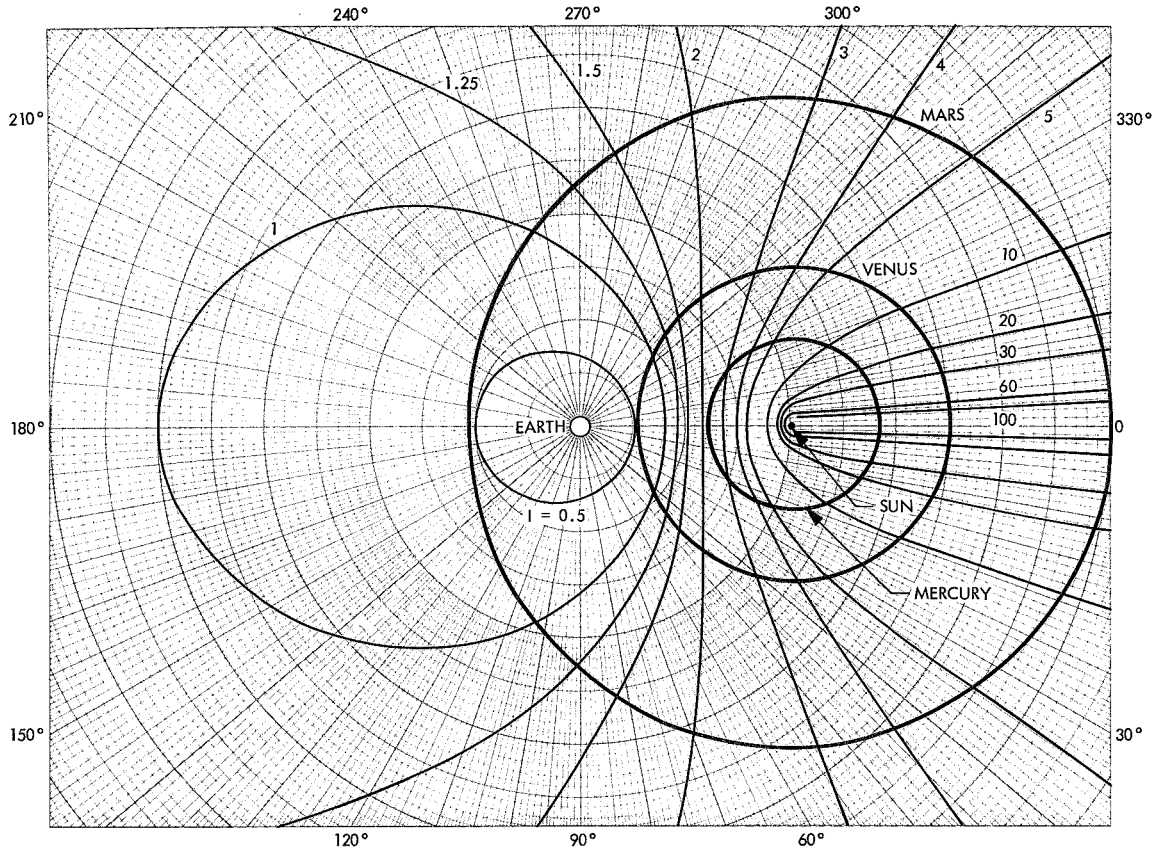

Fig. 12. Orbits of the inner planets, treated as being circular, in a solar wind with an electron density of 1/cm³ at 1 AU

corona where solar magnetic field effects and other mechanisms, although not fully understood, yield observed electron densities indicating an r^{-6} dependence with a solar surface electron density of approximately (1.0–1.5) $\times$ 10^8 electrons/cm^3.

The coronal electron effect and the variations in I_e as a result of $N_1 = N_1(t)$ and radially expanding pin-wheel streamers of high electron density emitted from a rotating sun will be discussed in a subsequent article.

Reference

1. Koehler, R. L., *Interplanetary Electron Content Measured Between Earth and the Pioneers VI and VII Spacecraft Using Radio Propagation Effects,"* Radio Science Laboratory Report SU-SEL-67-051. Stanford Electronics Laboratory, Stanford University, Palo Alto, California, May 1967.

5. A Study of Polar Motion and Earthquakes for the Period 1904–1966, C. C. Chao and P. M. Muller

a. Introduction. Possible correlations between the polar motion and earthquakes are investigated. If such correlations do exist, it may be possible to construct a model which will provide the necessary capability to predict polar motion for support of the navigational accuracy requirements of the planetary missions of the 1970s. The planetary encounter phase of a deep-space-probe mission generally requires a precise knowledge of the probe position with respect to the target planet. Usually, during real-time operations this information is desired before the gravitational field of the target planet has sufficiently perturbed the tracking data to allow the orbit of the spacecraft to be adequately determined with respect to the target body. Therefore, the relative target-body probe position must be inferred from the knowledge of the ephemeris of the target planet and the position (right ascension, declination) of the probe with respect to earth.

The role that the uncertainty in DSS locations plays in defining these angular relationships has been previously discussed by Hamilton and Melbourne in SPS 37-39, Vol. III, pp. 18–23, and applied to the particular case of *Mariner* Mars 1969 by Hamilton, Grimes, and Trask in SPS 37-44, Vol. III, pp. 4–11. Although the DSS locations may be relatively well fixed on the earth's crust, it is the stations' coordinates with respect to the earth's instantaneous spin axis, and with respect to the equatorial plane defined by that spin axis, which are important for navigational accuracy considerations. The earth's axis of figure is not fixed with respect to the spin axis, and it is this so-called polar motion (the motion of the earth's crust with respect to the spin axis) which causes the DSS locations with respect to the spin axis to be a function of time. This polar motion, as discussed by Muller in SPS 37-45, Vol. III, pp. 10–14, can cause DSS coordinates to change by up to 20 m over a period of 6 mo.

The uncertainty in the position of the pole is one of the major error sources limiting navigational accuracy. This uncertainty can be thought of as arising in two ways. The first is the basic ability to determine the position of the pole through the analysis of measurements. Two separate organizations are currently engaged in this work, and although their agreement is generally good, the position of the pole as defined by these organizations may differ by up to 3 m. This is large compared to the goal of reducing the uncertainty to the order of 0.5 m if it is to be compatible with the other error sources for planetary missions of the 1970s. The second arises during the process of extrapolating the polar motion from the time of the last measurement to the current date during real-time navigation operations. This time interval may be as much as 3 mo.

A recent article in the Journal of Geophysical Research (Ref. 1) concludes that large earthquakes correlate with small changes in the curvature of the polar motion and that apparently earthquakes excite the polar motion. In illustrating this correlation, Ref. 1 also indicates that the polar motion as determined by one of the services was definitely superior to the other. If such correlations do exist between polar motion and earthquakes, they are of interest because it may be possible to provide a model for more accurately predicting polar motion in support of the planetary missions. Furthermore, if it is obtainable, an insight into the accuracy of the polar motion as determined by the two services is valuable both for expressing the accuracy of results from postflight analysis of tracking data (i.e., DSS location solutions), which depend upon knowing the polar motion, and for predicting navigational accuracy capabilities for future missions.

b. Background. The question of the earth's polar motion has interested astronomers and geophysicists alike for more than a century. Many spirited controversies have resulted from the studies because of different interpretations made by various scientists. It was first shown by L. Euler in 1765 that the axis of figure (principal moment of inertia axis) could have an oscillation about the axis of rotation of a rigid earth with a period of approximately

300 days, which could be observed as a variation in observed astronomical latitude. Reference 2 and SPS 37-45, Vol. III, pp. 10–14, contain more detailed definitions and explanations which relate to basic understanding of the polar motion, and subsequent references cited in this article deal with more detailed facets of the associated problems.

In 1891, S. C. Chandler (Ref. 3) announced that a periodic oscillation of the instantaneous pole about a mean position had been observed with a period of about 427 days, and an amplitude of approximately 0.5 arc sec. The difference between the observed and Euler's theoretical period was explained by S. Newcomb (Ref. 4) as being due to the elastic deformation of the earth.

The problem of modeling the motion remains particularly tantalizing to this day because neither a definite conclusion nor a well-defined theory regarding the causes of the polar motion has been obtained.

A possible connection between earthquakes and polar motion had been suggested very early in the history of latitude observations (Ref. 5). More recently, D. E. Smylie and L. Mansinha (Ref. 1) have shown evidence that the largest earthquakes correlate with small changes in the curvature of the polar path. They further conclude that earthquakes excite the polar motion.

S. K. Runcorn (Ref. 6) concluded recently that the energy available from earthquakes was not sufficient to excite the polar motion, and suggested instead that the cause arises from magneto-hydrodynamic torque between the core and mantle of the earth. G. Colombo and I. Shapiro (Ref. 7) have proposed a model attributing excitation to the differential luni-solar gravitational torques, acting on the core and mantle, which occur somewhere between the depths of about 400 and 1000 km.

c. Nature of the earthquake and polar motion data. The polar motion is measured independently by two organizations. The International Polar Motion Service (formerly International Latitude Service) utilizes measurements taken from five observatories which are at the same latitude and share the same catalogue. Reference 8 gives a complete explanation of the methods of observation and reduction currently employed. We used the polar motion data as reduced to a common set of references by S. Iijima (Ref. 9). Figure 13 was abstracted from Iijima's data and includes plots of observed polar motion and its secular, annual, and Chandler components.

The polar motion is also determined by the Bureau International de l'Heure (BIH, Ref. 10), which prepares global averages of over 25 stations with distinct catalogues and latitudes. These BIH data were used in Ref. 1 because they produced superior results in the analysis. The long-term (1900–1968) polar motion is not available from BIH, and, in any event, the long-period components are not significantly different as reported by the two agencies.

SPS 37-45, Vol. III, pp. 10–14, contains a plot of the actual polar path from 1955 to 1967, and this plot reveals the essentially circular nature of the motion, its 1.2-yr period, and the modulation in amplitude with a period of approximately 6.7 yr (average) caused by the beat-frequency between the annual and Chandler terms shown in Fig. 13. Iijima's work in Ref. 9 on the periodic components of the polar motion reveals three distinct components whose sum is an adequate representation of the observed motion. These secular, annual, and Chandler ($\sim$14-mo period) components are shown in Fig. 13 for the period 1900–1966.

We obtained the earthquake data from B. Gutenberg (Ref. 11) and from bulletins of the U. S. Coast and Geodetic Survey for earthquakes after 1954. Earthquake energy release was obtained from equations in Ref. 11, p. 19.

d. The correlation analysis. The three basic components in the polar motion have been noted above. We studied possible correlations between these three terms plus two derived from them and earthquakes. The additional terms were simply the rate of the Chandler component (because of uniform angular velocity of the pole, equal to the envelope of this term as shown in Fig. 13) and the polar rate itself, determined by considering the velocity of the actual observed pole (directional derivative or rate of motion along the curve of the amplitude of the polar motion). The polar rate or the amplitude appears in Fig. 14, the Chandler rate or envelope in Fig. 15.

Figure 14 plots yearly energy release in all earthquakes against rate of the pole. It was the apparent visual correlation between these two functions over the period 1950–1966 that originally generated interest in this study. While excellent over this period, it can be seen that similar correlation does not exist for the previous period 1905–1920. It is easily noted, however, that when the 6.7-yr terms are large in amplitude (as they are during

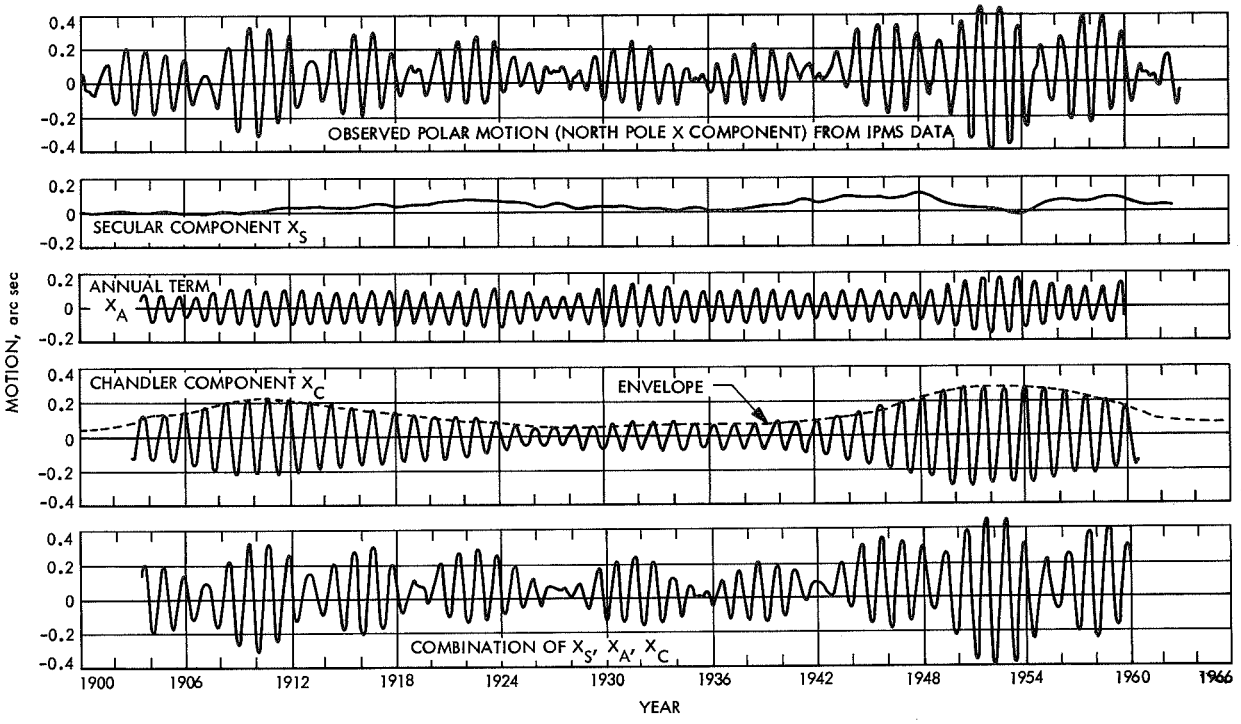

Fig. 13. Observed polar motion and its secular, annual, and Chandler components

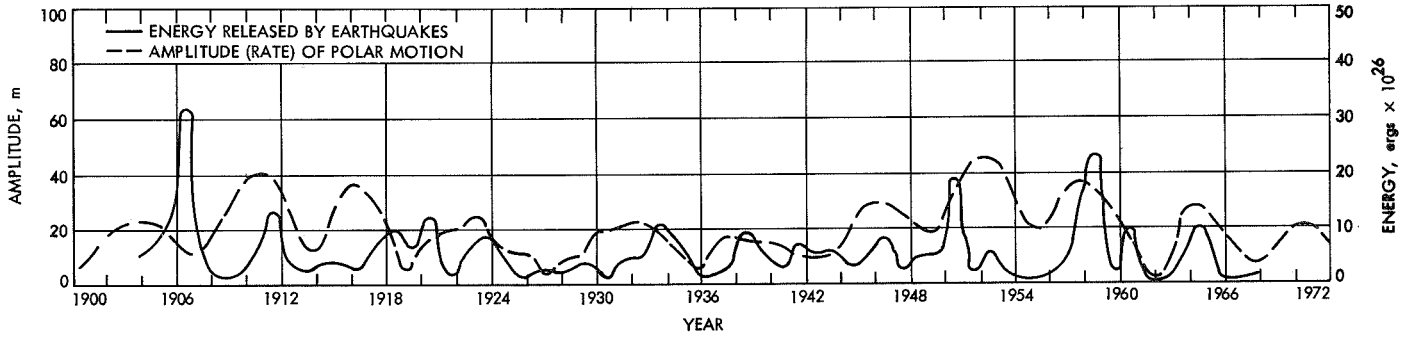

Fig. 14. Comparison between polar motion amplitude (rate) and energy released by earthquakes

these two periods), earthquake bunching does occur, while during the longer minimum (roughly 1920–1945), there are no big years, and the earthquakes happen less frequently and with lesser amplitudes.

The above observation suggested comparison of earthquake energy release with the rate in the Chandler component (which is responsible for the long-period approximately 45-yr polar variation noted). Figure 15 plots the envelope of the Chandler component taken from Fig. 13 versus 10-yr averages in earthquake energy release, as well as the yearly totals for earthquake energy. There are 50 to 100% increases in the 10-yr mean rate of earthquake energy release over that during the long minimum. On the other hand, such relatively modest changes in long-term earthquake energy dissipation, coupled with our having only 1.5 periods of the Chandler term for examination, makes us hesitant to ascribe anything approaching certainty to this correlation.

Qualitatively, it appears from Fig. 15 that the large integrated energy released over the 1904–1920 period is correlated with the smaller maximum of the Chandler wobble in that period, where the reverse is true in the 1942–1964 period. To explain such qualitative inconsistency, one must be aware of the fact that the energy

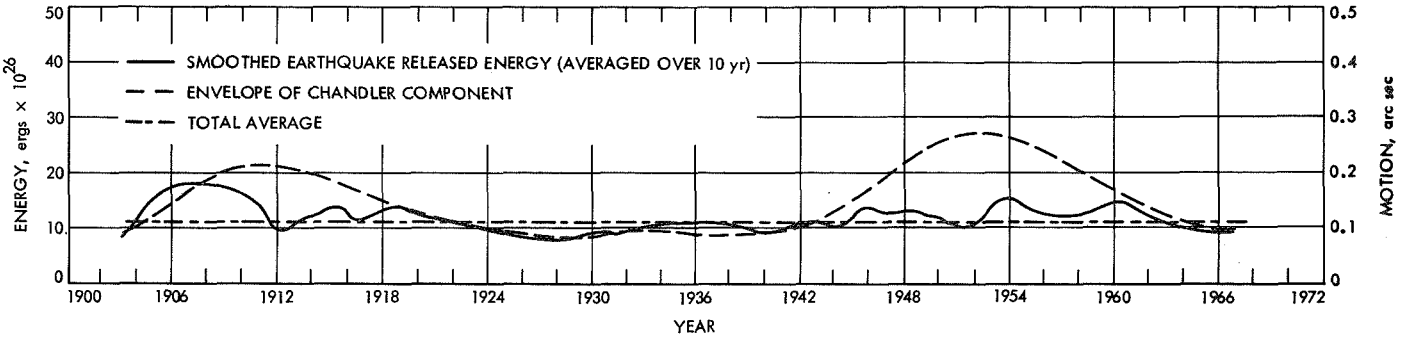

Fig. 15. Comparison between smoothed earthquake released energy and envelope of Chandler component

released during earthquakes depends on many parameters, such as local crust strain, the nonequilibrium of volcanic fluid and gases, and the depth of the earthquake. Thus, Fig. 15 indicates only that the excitation of earthquakes may be due to the Chandler wobble or that they may be caused by the same source. But once the earthquake is excited, the energy released will depend on the parameters given above and, therefore, may not be consistent with the amplitude of the "triggering source".

We might ask the question – Why does the average energy expended in earthquakes remain relatively constant when there are such obvious peaks of short-term behavior as shown for years 1906, 1911, 1920, 1950, 1958, 1960, and 1964? The answer is clear, because the big years are almost invariably followed by the lowest minima, and the long-term (10-yr) averages become relatively uniform. One should note that, during the so-called minimum, the energy release is more uniform and the peaks and minima are both less pronounced than in the other periods. Intuitively, this suggests that earthquakes tend to be triggered by whatever energizes the polar motion.

We can now attempt to place these observations on a more analytical basis. If we agree that a correlation has been shown to exist between average energy expenditure in earthquakes and Chandler motion, and also between earthquake rates and Chandler motion, then the following reasoning applies. Assume that this regular behavior of the Chandler term is a real, 45-yr, periodic effect (we have only 1.5 periods, and any assumption that we have enough data span to be sure is at least potentially dangerous). Further, accept the intuitively reasonable assumption that individual earthquakes should appear random in the absence of a global "causative" or "triggering" phenomenon (since individual earthquakes are known to be releases of *locally* contained energy in faults and slips, etc.). Then, given truth of the correlations mentioned, we can conclude that earthquakes do not cause or excite the Chandler component of polar motion. It is not necessarily true that the polar motion excites or triggers earthquakes, since these two phenomena may simply *both* be due to, or be triggered by, some other effect, such as the mantle forces suggested in Refs. 6 and 7.

In fact, Ref. 7 gives good dynamical reasons for believing that the 45-yr Chandler component is an effect related to the core–mantle forces, and this was, in fact, their conclusion. Iijima (Ref. 9) also gives good reasons for believing that the Chandler component's 45-yr term is real and reliable beyond the simple observations, which are subject to uncertainty because of the short relative period covered. There are, therefore, earlier analyses which support the assumptions necessary to the argument cited above. It, therefore, appears that the argument is analytically sound.

We were intrigued by the suggestion in Ref. 7 that forces in the upper mantle might be responsible for Chandler motion, and, therefore, by the above argument, for earthquake triggering as well. It was logical to investigate whether depth and/or magnitude of earthquakes exhibited any correlations.

We took the half-amplitude points on the Chandler component as indicating the divisions in time between maximum and minimum motion. The three semi-periods (two maxima and one minimum) were found to be as indicated in Table 9, noting that intervals were designated A, B, and C. Shocks were counted in each interval according to the depth h definitions given in Ref. 9 and the amplitude M as noted in the appropriate column of Table 9. We computed a frequency factor (F), as indicated on the last line of Table 9, which measures the ratio of earthquake frequency during maxima to that

Table 9. Count of earthquakes vs Chandler period

Period[a]	Shallow ($0 \leq h < 70$ km)		Intermediate ($70 \leq h < 300$ km)		Deep ($h \geq 300$ km)		Deep ($h \geq 400$ km)
	$M \geq 7.75$	$M \geq 7.00$	$M \geq 7.50$	$M \geq 7.00$	$M \geq 7.25$	$M \geq 7.00$	$M \geq 7.00$
A	45	—[b]	30	89	18	26	17
B	49	418	15	120	9	27	17
C	25	223	13	77	8	21	19
F[d]	1.28	0.96[c]	2.58	1.25	2.6	1.57	1.9

[a] *A* = 1904 to 1918 = 15 yr; *B* = 1919 to 1945 = 27 yr; C = 1946 to 1960 = 15 yr.
[b] Data not available.
[c] C substituted for *A* in formula for frequency factor.
[d] $F = 27/30\ [(A + C)/B]$.

during minima, normalized for the small difference between the number of years in two maxima as compared with the one minimum (B). To wit:

$$F = \frac{27}{30}\left(\frac{A + C}{B}\right)$$

A value near 1.0 for F indicates that earthquakes of that particular type were not correlated with the Chandler component, while a number significantly larger than 1.0 indicates a positive correlation.

The conclusion that earthquakes correlate with the Chandler term only if they are either large or deep is quite apparent. The suggestion that polar excitation comes from a depth of 400–1000 km is consistent with the definition of deep shocks (300 to 700 km).

The lack of correlation between smaller shocks ($M < 7.0$) and the Chandler term supports what one would intuitively expect, as noted above, that earthquakes in the absence of a global trigger would be expected to behave randomly since they are local phenomena, namely, the release of locally contained energy in faults and slips. Because the smaller shocks, as we observed, occur much more frequently and randomly, the time for the formation of conditions which make smaller earthquakes inevitable must be small compared to the 45-yr term, and so the long-period trigger has little effect on the rate.

e. Conclusion. Correlation between earthquake rates (for large, deep, and intermediate shocks) and the Chandler component of the polar motion has been demonstrated. The correlation does not exist for all small earthquakes, nor for moderate shallow and intermediate depth shocks. Total energy release appears to be correlated with the Chandler component.

The correlation between the deeper shocks and polar motion seems to give support to theories placing polar excitation in the upper mantle (400–700 km). The results strongly suggest that earthquakes, which are local phenomena (release of locally contained energy), do not themselves excite the Chandler term of the polar motion.

To specifically quote the steps of the last argument, we must proceed as follows:

(1) The Chandler component is a real, regular, 45-yr term, which would damp out in the absence of a regular, global cause.

(2) One agrees that correlation has been demonstrated between the long-period aspects of earthquake behavior and polar motion.

(3) One agrees that earthquakes should be random in the absence of a global trigger.

The conclusion is that: (1) earthquakes are not responsible for exciting the Chandler term; and (2) in fact, either the reverse is true, or both earthquakes and Chandler motion are excited by the same global causative.

Finally, we can conclude that it is impossible to predict polar motion from earthquakes within required accuracy, but earthquakes may be predicted in a long-term average sense from the polar motion data. Therefore, the solution of polar-motion prediction has to be

approached with different methods. One promising way is to study the correlation between mantle–core torques and the polar motion. An empirical curve-fitting technique may be more time-saving and reliable to predict the pole for future missions. Since we have just passed the irregular transition period (1967), the empirically predicted data are expected to be good in the next 5 yr.

References

1. Smylie, D. E., and Mansinha, L., "Earthquakes and the Observed Motion of the Rotation Pole," *J. Geophys. Res.*, Vol. 73, No. 24, p. 7661, Dec. 15, 1968.
2. Melbourne, W. G., et al., *Constants and Related Information for Astrodynamic Calculations, 1968*, Technical Report 32-1306. Jet Propulsion Laboratory, Pasadena, Calif., Jul. 15, 1968.
3. Chandler, S. C., *Astron. J.*, Vol. 11, p. 65, 1891.
4. Newcomb, S., *Astron. J.*, Vol. 11, p. 81, 1891.
5. Milne, J., "Bakerian Lecture of the Royal Society," *Proc. Roy. Soc. London, Ser. A*, Vol. 77, p. 365, 1906.
6. Runcorn, S. K., "Continental Drift, Secular Motion of the Pole, and Rotation of the Earth," in *Proceedings of IAU Symposium Number 32, Stresa, Italy, March 21, 1967*, p. 80. Verlag Publishers, Inc., New York, N. Y., 1968.
7. Colombo, G., and Shapiro, I., "Theoretical Model for the Chandler Wobble," *Nature*, Vol. 217, p. 156, Jan. 13, 1968.
8. Yumi, S., *Annual Report of the International Polar Motion Service for the Year 1962*, Mizusawa, Japan, 1964.
9. Iijima, S., *On the Yearly Trend of the Periodic Components of the Polar Motion*, March 11, 1965.
10. *Bulletin Horaire*, Bureau International De L'Heure, Paris, France.
11. Gutenberg, B., *Seismicity of the Earth and Associated Phenomena*. Princeton University Press, Princeton, N. J., 1954.

6. Lunar Landed *Surveyor*: SPODP Lunar Libration Sensitivities, *F. B. Winn*

The purpose of this article is to demonstrate the impact of the existing single precision orbit determination program (SPODP, Ref. 1) physical libration algorithm on the postlunar landed *Surveyor* tracking data reductions. The accuracies and magnitudes of the forced lunar librations as defined by the SPODP have been investigated by V. C. Clarke, and he terminated his study with the suggestion that perhaps abandonment of the existing SPODP libration model might be advisable (private communication).

In this presentation, it will be shown that:

(1) The SPODP forced lunar libration model does fail.

(2) The Heyn and Eckhardt physical libration coefficients, when employed in the SPODP libration algorithm, demonstrate accuracies which are space and/or time-dependent.

(3) The sum of the squares of the weighted residuals which result from *Surveyor* tracking data adjustments are significantly influenced as the SPODP libration model is zeroed out or scaled by Heyn or Eckhardt lunar physical libration coefficients, and, accordingly, the differential adjustments to the solution parameters are also significantly modified.

The existing SPODP forced libration model is (Ref. 2)

$$\sigma \sin I = C_1 \sin g + C_2 \sin (g + 2\omega) + C_3 \sin (2g + 2\omega) \tag{1}$$

$$\tau = C_4 \sin g + C_5 \sin g' + C_6 \sin 2\omega \tag{2}$$

$$\rho = C_7 \cos g + C_8 \cos (g + 2\omega) + C_9 \cos (2g + 2\omega) \tag{3}$$

where σ, τ, and ρ are small perturbations in the mean motions of the lunar ascending node $\bar{\Omega}$, lunar longitude $\mathfrak{D}$, and lunar equatorial plane inclination relative to the ecliptic I, respectively (Fig. 16), and g = lunar mean anomaly, ω = argument of perigee of the moon, and g' = solar mean anomaly.

The libration coefficients C_1 through C_9, which are incorporated within the SPODP, are those of Heyn (Ref. 3) and are tabulated in Table 10. These coefficients are the result of old observations of the moon, which were reduced by hand calculations involving several approximations. Dr. Eckhardt (Refs. 4 and 5) of the Air Force Cambridge Research Laboratory employed a computer algorithm which used Koziel's heliometer observations as the observable to be fitted in an integration of the differential equations of the librations. The C_1 through C_9 coefficients emerging from this differential adjustment are also tabulated in Table 10. These coefficients were substituted for Heyn's values in three of the *Surveyor* data reductions presented. Heyn's coefficients were also set to zero in three of the *Surveyor* data reductions. This effectively removes all libration modeling from these three data fits.

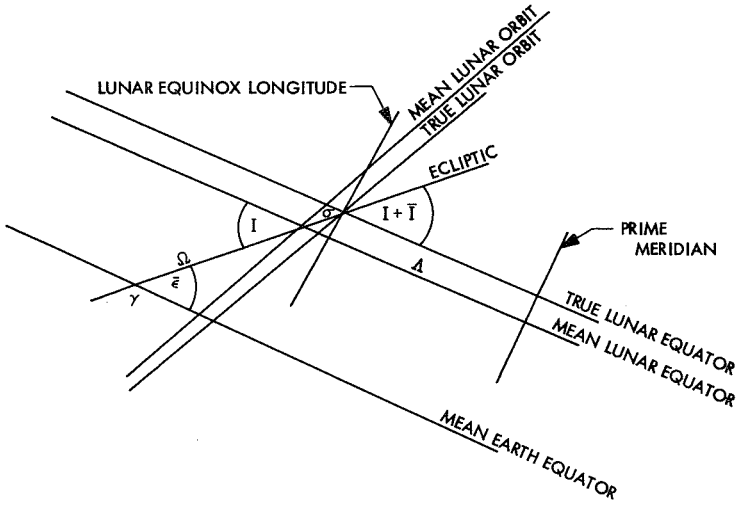

Fig. 16. Lunar physical libration geometry

Table 10. Libration coefficients

Coefficient	Zero	Heyn	Eckhardt
C_1	0″	−109.″0	−100.″7
C_2	0″	37.″0	23.″8
C_3	0″	−11.″0	−10.″6
C_4	0″	−12.″0	−16.″9
C_5	0″	59.″0	91.″7
C_6	0″	18.″0	15.″3
C_7	0″	−107.″0	−98.″5
C_8	0″	37.″0	23.″9
C_9	0″	−11.″0	−11.″0

Table 11. *Surveyor* coordinates and time span

Surveyor	Selenocentric coordinates		Lunar life span	
	λ	φ	Start	Stop
I	316.°6	−2.°5	Jun. 3, 1966	Jun. 14, 1966
VI	358.°6	0.°5	Nov. 10, 1967	Nov. 25, 1967
VII	348.°5	−40.°9	Jan. 10, 1968	Jan. 23, 1968

Postlunar landed tracking data were collected by three DSSs from five *Surveyors*. In the name of economy, however, only the data from DSS 42 collected from *Surveyors I, VI,* and *VII* are used in this study. The decision to utilize DSS 42 data stemmed from DSS 42's fairly consistent density and cleanness in the tracking data from *Surveyors I, VI,* and *VII*. The three *Surveyors* were chosen for study because of their time and selenocentric coordinate separation (Table 11).

Each *Surveyor* data sample was reduced by the SPODP three times. In each case, only the first lunar day tracking data were fit. The only variant was the forced lunar libration model coefficients. The influence of the zero, Heyn, and Eckhardt coefficients on the *Surveyor* two-way doppler function is deducible from the combined interpretation of the "observed minus computed" (O − C) residuals, from the "sum of the squares" (SOS), and from the differential solution parameter adjustments.

A visual inspection of the three O − C residual plots per *Surveyor* (Figs. 17–19) does not provide any significant evidence as to which residual set is representative of the "best" fit to the data; but it would be naive to assume, strictly on this basis, that the libration modeling is of no consequence since the parameter adjustments and the SOS do demonstrate significant sensitivity. A closer look at the *Surveyor I* O − C residual sets is obtained in Fig. 20. All three profiles exhibit the same frequency ($\sim 14^d$) and the daily O − C residual means show a scatter of ~0.1 mm/s at the maximum amplitude. The maximum amplitude is 0.3 mm/s.

It is apparent that $C_3 \cos(2g + 2\omega)/\sin I$ has a 14-day period; the term's amplitude is ~500.″0 (probe's angular displacement as seen from moon's center). If the libration coefficients had undergone differential adjustment in the

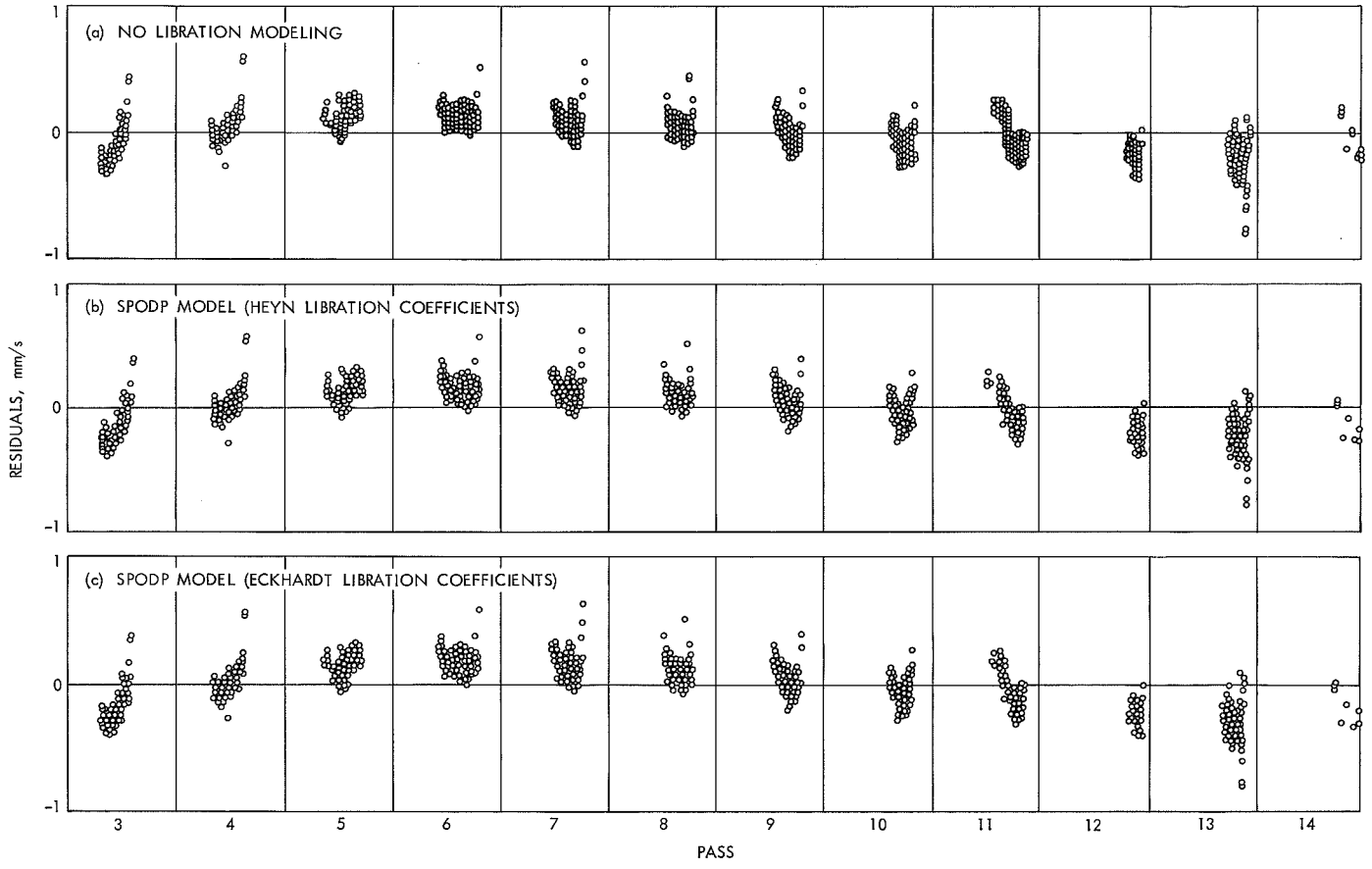

Fig. 17. *Surveyor I*: O — C residuals of DSS 42

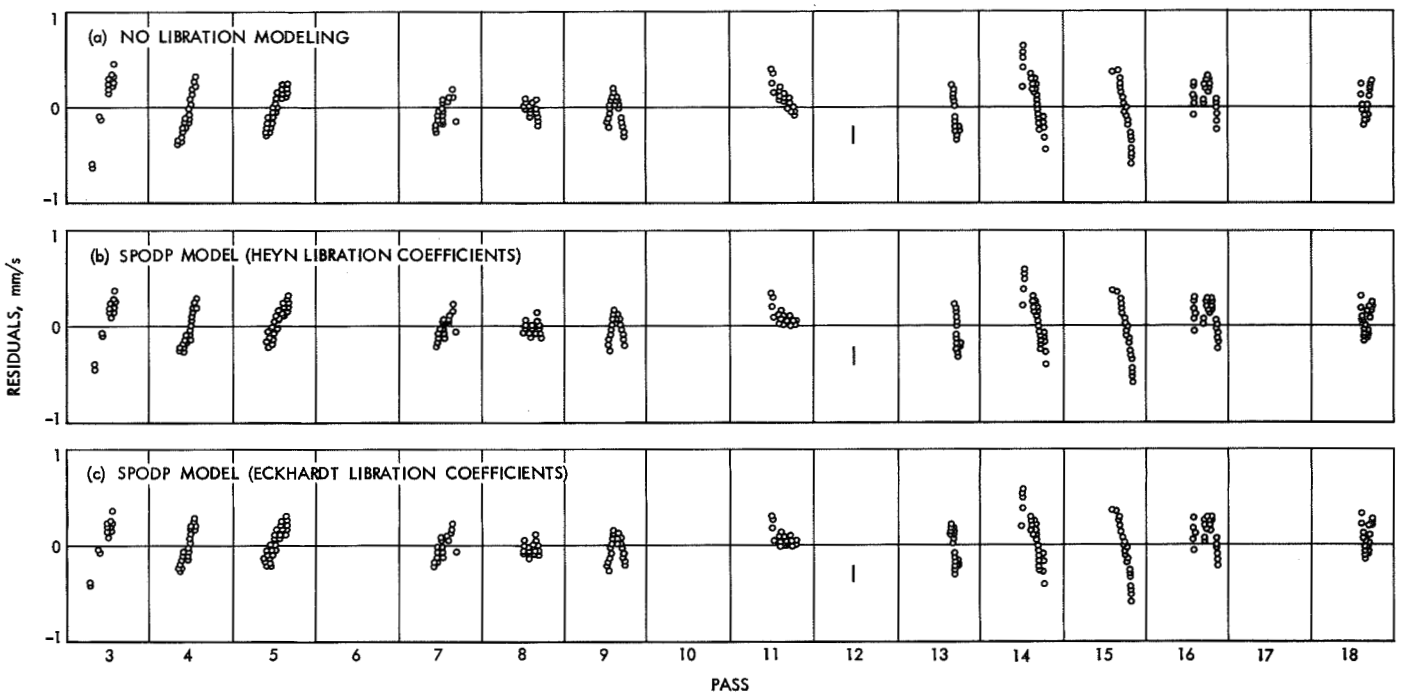
(a) NO LIBRATION MODELING
(b) SPODP MODEL (HEYN LIBRATION COEFFICIENTS)
(c) SPODP MODEL (ECKHARDT LIBRATION COEFFICIENTS)
RESIDUALS, mm/s
1
0
-1
3 4 5 6 7 8 9 10 11 12 13 14 15 16 17 18
PASS

Fig. 18. *Surveyor VI*: O — C residuals of DSS 42

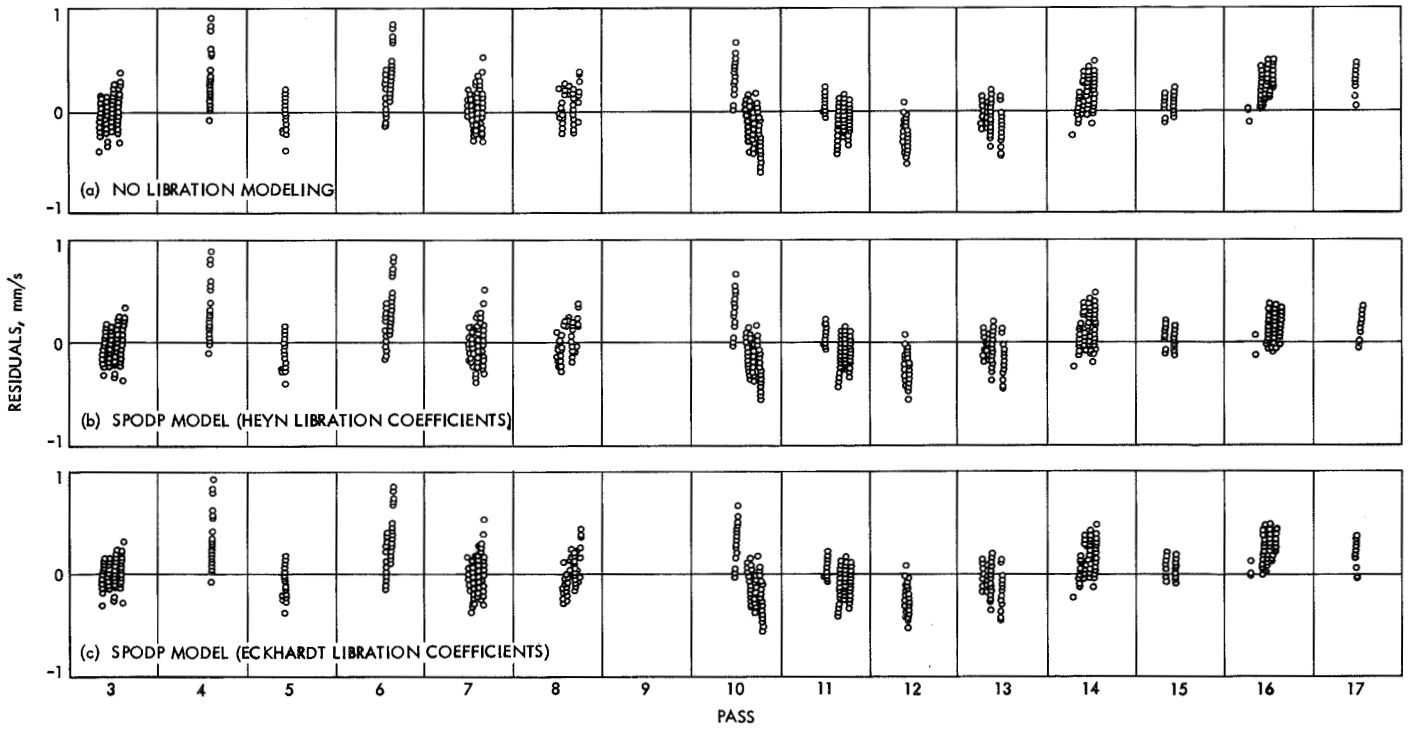
(a) NO LIBRATION MODELING
(b) SPODP MODEL (HEYN LIBRATION COEFFICIENTS)
(c) SPODP MODEL (ECKHARDT LIBRATION COEFFICIENTS)
RESIDUALS, mm/s
1
0
-1
3 4 5 6 7 8 9 10 11 12 13 14 15 16 17
PASS

Fig. 19. *Surveyor VII*: O — C residuals of DSS 42

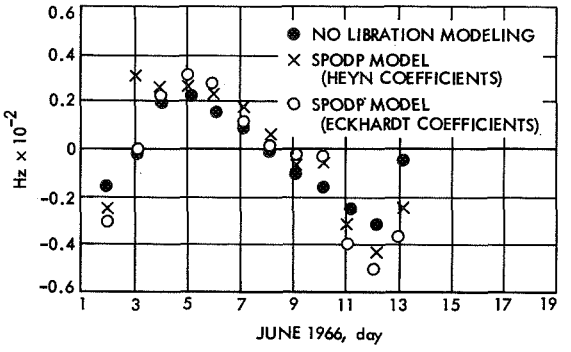

Fig. 20. *Surveyor I*: residual first moments

course of the *Surveyor* data fits, undoubtedly the C_3 coefficient would have been forced to absorb the 14-day, 0.3-mm/s signature presented in Fig. 19.

The minimizations of the SOS of the weighted residuals (Table 12) imply that the existing SPODP libration model is failing. The extent and nature of the required refinement are presently under investigation. The "best" fit resulted, for each *Surveyor*, with a different libration scheme (Table 12). The percentage differences between the SOS of the data fits per *Surveyor* are tabulated in Table 13.

Table 13. SOS percentage differences

Surveyor	Zero–Heyn, %	Zero-Eckhardt, %	Heyn–Eckhardt, %
I	2	4	2
VI	18	25	7
VII	34	28	−6

One possible explanation of the relative abilities of the three libration schemes to minimize the SOS associated with the *Surveyor* data sets is to be found in Fig. 21. The operational lives of the *Surveyors* in this study are indicated. Note that all the periodic functions are near zero

Table 12. Libration influences on differential parameter adjustments

Surveyor	Parameter[a]	Zero	Heyn	Eckhardt	Cruise	Whitaker	ACIC[b]
I	SOS	0.158	0.161	0.165	—	—	—
	R	1736.364	1736.317	1736.282	—	—	1736.5
	ϕ	−2.51835	−2.47889	−2.48392	−2.46	−2.45	—
	λ	316.65169	316.64940	316.63678	316.49	316.78	—
	R_I	6371.699	6371.698	6371.706	—	—	—
	LO	148.98169	148.98168	148.98170	—	—	—
VI	SOS	0.016	0.013	0.012	—	—	—
	R	1736.078	1736.052	1736.049	—	—	1736.0
	ϕ	0.47215	0.47442	0.47831	0.437	0.53	—
	λ	358.65066	358.63204	358.64180	358.63	358.60	—
	R_I	6371.683	6371.685	6371.685	—	—	—
	LO	148.98108	148.98122	148.98122	—	—	—
VII	SOS	0.038	0.025	0.027	—	—	—
	R	1739.032	1739.014	1739.018	—	—	1739.0
	ϕ	−40.92759	−40.93310	−40.92628	−41.1	−40.86	—
	λ	348.48559	348.49719	348.49182	348.56	348.53	—
	R_I	6371.689	6371.688	6371.688	—	—	—
	LO	148.98167	148.98153	148.98157	—	—	—

[a]SOS = sum of the squares of the weighted residuals (normalized); R = lunar radius at *Surveyor* lunar site; ϕ = selenocentric latitude of *Surveyor*; λ = selenocentric longitude of *Surveyor*; R_I = geocentric distance of DSS 42; LO = geocentric longitude of DSS 42.

[b]Air Force Charting and Information Center.

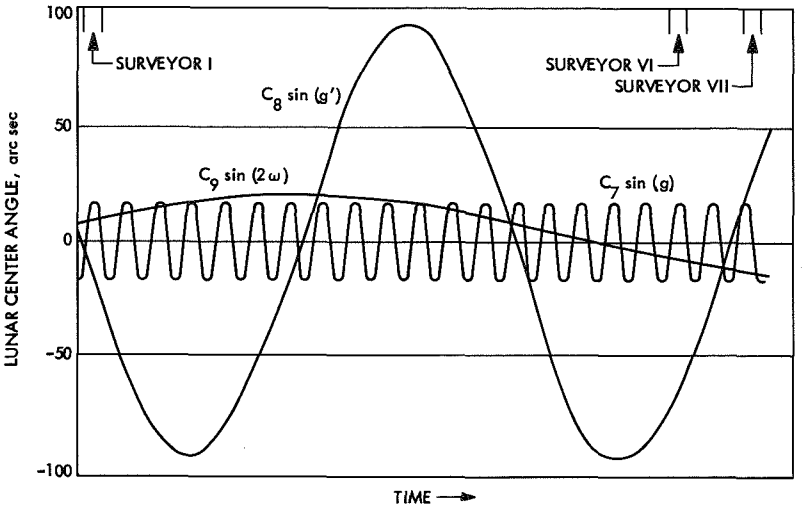

Fig. 21. SPODP librational terms that sum to π

at the time of *Surveyor I*. Thus, the magnitude of the *Surveyor I* librational terms is also near zero, but apparently not close enough since no libration model "best" fitted the *Surveyor I* data. The Eckhardt coefficients in the SPODP libration model "best" fitted the *Surveyor VI* data. *Surveyor VI* was in operation at a time when the C_8 sin g' term was near maximum amplitude, and, accordingly, any error in C_8 will have a maximum influence on τ, the physical libration in mean lunar longitude.

The differential parameter adjustments are another index by which the libration model can be evaluated. Table 12 presents the *Surveyor* lunar surface coordinates of E. Whitaker (from *Lunar Orbiter* photographs of *Surveyor* lunar sites, Ref. 4) of the translunar cruise *Surveyor* data (Ref. 3) in the company of these nine libration variant solutions. Also, the normalized SOSs of the weighted residuals are tabulated.

Extraction of information from Table 12, concerning the libration algorithm influences on the parameters sets, requires knowledge of the initial parameter constraints and the parameter correlations. All parameters were unconstrained. The parameter correlations for the three *Surveyors* are tabulated in Table 14. Table 14 shows that the parameter adjustments have been appreciably altered with the libration modeling changes.

The demonstrated sensitivity of the *Surveyor* two-way doppler function to libration modeling indicates the strength of the *Surveyor* data in solving for the libration coefficients. However, such a solution would be of questionable value, due to the excessive correlation between

Table 14. Parameter correlations

Surveyor	Parameter	R	ϕ	λ	R_I	LO
I	*R*	1	−0.04	0.06	0.07	0.10
	ϕ		1	0.46	−0.49	0.43
	λ			1	0.20	−0.98
	R_I				1	−0.20
	LO					1
VI	*R*	1	0.28	−0.22	0.13	0.22
	ϕ		1	−0.45	0.88	0.40
	λ			1	−0.44	−0.99
	R_I				1	0.40
	LO					1
VII	*R*	1	0.32	0.05	0.02	0.01
	ϕ		1	0.84	0.50	0.88
	λ			1	−0.44	−0.99
	R_I				1	0.41
	LO					1

the libration coefficients. That is, all libration coefficients are functionally defined in terms of three parameters: lunar inclination I and the lunar figure parameters J_2 and C_{22}. Computer programs are currently being developed by Georgia Dvornychenko which will evaluate the partials of the *Surveyor* two-way doppler function with respect to the total librations of the node, inclination, and longitude for the entire 610-day life of the *Surveyor* program. Cliff Cary has completed the analysis and is

presently developing the software which will provide the functional relationship between total librations and the I, J_2, C_{22} parameters. The *Surveyor* tracking data will be used to solve for the lunar parameters that induce the libration.

References

1. Warner, M. R., and Nead, M. W., *SPODP — Single Precision Orbit Determination Program,* Technical Memorandum 33-204. Jet Propulsion Laboratory, Pasadena, Calif., Feb. 15, 1965.
2. White, R. J., et al., *SPACE — Single Precision Cowell Trajectory Program,* Technical Memorandum 33-198. Jet Propulsion Laboratory, Pasadena, Calif., Jan. 15, 1965.
3. *Surveyor VII Mission Report. Part I. Mission Description and Performance,* Technical Report 32-1264. Jet Propulsion Laboratory, Pasadena, Calif., Feb. 15, 1969.
4. *Measure of the Moon.* Edited by Z. Kopal and C. L. Goudas. D. Reidel Publishing Co., Dordrecht, Holland, 1967.
5. Melbourne, W. G., et al., *Constants and Related Information for Astrodynamic Calculations, 1968,* Technical Report 32-1306. Jet Propulsion Laboratory, Pasadena, Calif., Jul. 15, 1968.
6. Whitaker, E., "Television Observations from Surveyor," *Surveyor VI Mission Report. Part II. Science Results,* Technical Report 32-1262. Jet Propulsion Laboratory, Pasadena, Calif., Jan. 10, 1968.

7. The Capability of Estimating the Earth Gravitational Constant Through the Tracking of Synchronous Satellites,

G. E. Pease

a. Introduction. In a previous article (SPS 37-53, Vol. II, pp. 16–20), the possibility of obtaining an accurate value of the earth gravitational constant through the tracking of moderate-altitude satellites was discussed. Such a determination was indicated to be feasible, provided the satellite is equipped with a ranging transponder. The scarcity of moderate-altitude satellites equipped for ranging data, however, brings up the question of whether or not it is practical to use synchronous communications satellites for this purpose.

The high altitude of the synchronous satellite frees the solution from the effects of high-order gravitational harmonics, atmospheric drag, and small errors in the distances of the tracking stations from earth's rotational axis. However, with a synchronous satellite the diurnal doppler signature from earth rotation vanishes. Normally, this is of great value in determining the right ascension, declination, and range-rate of a distant spacecraft from radio doppler tracking (SPS 37-39, Vol. III, pp. 18–23). This same consideration, of course, restricts the earth track and tracking geometry very highly. The 24-h orbit also causes resonance with the low-order tesseral harmonics, most notably the sectorial C_{22} and C_{33} terms. The resultant tangential accelerations cause a secularly increasing longitude error if not perfectly modeled in the parameter estimation process (Ref. 1). Lastly, the synchronous communications satellites are subjected to station-keeping maneuvers at intervals, so that the data span suitable for orbit determination is restricted to the interval between maneuvers. In practice, this does not appear to be a problem, since the results of this article indicate only a day or so of tracking to be sufficient, whereas station-keeping maneuvers are usually separated by several weeks.

The synchronous satellite orbit chosen for analysis in this article is that of *Syncom II* (6331a). The following elements were kindly supplied by R. J. Anderle of the U. S. Naval Weapons Laboratory:

Epoch	J. D. 39976.88074421
a	6.61047522 earth radii
e	0°0007058
i	29°507
M	339°1902
ω	334°9893
Ω	291°9411

b. Tracking model. As in SPS 37-53, Vol. II, simulated range and range-rate data were used with respective standard deviations of 25 m and 5 mm/s for a data rate of 1 point/min, assuming zero-mean uncorrelated gaussian noise. Simulated tracking stations were DSSs 11, 42, and 51.

c. Statistical analysis. The JPL single precision orbit determination program (SPODP, Ref. 2) was used to numerically integrate a trajectory by the Cowell method and to compute partial derivatives of the ρ and $\dot{\rho}$ data types with respect to the estimated parameters listed below.

x, y, z, $\dot{x}$, $\dot{y}$, $\dot{z}$ — geocentric equatorial position and velocity at epoch

GM earth gravitational constant

J_2 second-order earth zonal harmonic coefficient

The following quantities are estimated for each tracking station:

r_s perpendicular distance of station from rotational axis of earth

z_s perpendicular distance of station from earth equator

λ east longitude of station from Greenwich meridian

A covariance matrix Γ is formed from the vector of partial derivatives ϕ_i and data weight w_i at the ith observation as follows:

$$\Gamma = \left(\sum_{i=1}^{N} \phi_i w_i^{-1} \phi_i^T \right)^{-1}$$

This has been computed at intervals through use of the JPL double precision matrix program[14]. No *a priori* knowledge was assumed for any of the estimated parameters.

d. Syncom II statistical analysis. Table 15 shows the statistical results of simulated tracking of *Syncom II* for 36 h with DSSs 11 and 42, but not DSS 51. DSS 11 was in view of the satellite continuously during this period, whereas DSS 42 was within view slightly less than half the time. Also shown are results from high-altitude satellites having many of the same orbital characteristics as *Syncom II*, but only ¾ and ½ the semimajor axis of a synchronous satellite. All three tracking stations were used in these latter runs. Table 15 indicates an extremely accurate solution for GM and J_2 in all cases, but in actual fact, such accuracies are not attainable because of unmodeled error sources, such as the tesseral harmonics,

[14]Hilt, D. E., *Double Precision Matrix Manipulation Program*, Apr. 1, 1968 (JPL internal document).

Table 15. Standard deviations of estimated parameters after 36 h of tracking *Syncom II* (results for satellites at 3/4 and 1/2 synchronous altitudes also shown)

Parameter	Standard deviation after 36 h of tracking					
	Range and range-rate data [σ_ρ = 25 m, $\sigma_{\dot\rho}$ = 5 mm/s (1 point/min)]			Range-rate data only [$\sigma_{\dot\rho}$ = 5 mm/s (1 point/min)]		
	Syncom II	3/4 a	1/2 a	*Syncom II*	3/4 a	1/2 a
x, km	9.772	0.456	0.045	47.141	2.093	0.114
y, km	6.381	0.540	0.544	30.783	2.477	1.471
z, km	0.016	0.012	0.015	0.085	0.029	0.024
$\dot{x}$, m/s	0.585	0.063	0.123	2.823	0.286	0.335
$\dot{y}$, m/s	0.692	0.041	0.0030	3.336	0.187	0.0084
$\dot{z}$, m/s	0.00075	0.00115	0.0014	0.00426	0.00279	0.0041
GM, km^3/s^2 × 10^3	0.400	0.020	0.0018	2.182	0.060	0.0046
J_2 × 10^6	0.130	0.0112	0.00032	0.328	0.0149	0.00048
r_s (DSS 11), m	1.44	9.42	2.12	49.15	15.89	4.96
z_s (DSS 11), m	3.64	29.01	6.68	12.48	69.83	11.59
λ (DSS 11), deg	0.0174	0.0013	0.0017	0.084	0.0061	0.0045
r_s (DSS 42), m	9.99	2.71	2.11	25.68	10.59	6.58
z_s (DSS 42), m	11.47	4.88	5.35	49.87	7.81	12.43
λ (DSS 42), deg	0.0175	0.0013	0.0017	0.085	0.0060	0.0046
r_s (DSS 51), m	—	1.33	2.46	—	9.49	5.81
z_s (DSS 51), m	—	4.63	7.44	—	11.62	14.22
λ (DSS 51), deg	—	0.0013	0.0017	—	0.0061	0.0045

mentioned in the introduction. Comparison between solutions may be made with some validity, however.

Because of the peculiarities of the synchronous orbit mentioned in the introduction, the solution is not as accurate as for the nonsynchronous high-altitude satellites at ¾ and ½ *a*. This is especially seen in the poor tracking station longitude solutions in the synchronous case. Normally, these would be constrained to a 1-σ *a priori* of 0.5×10^{-3} deg or better. However, the correlations between *GM* and other parameters in the covariance matrix, including station longitudes, are quite small. An exception is J_2, which is somewhat negatively correlated with *GM* in the covariance matrix.

Figure 22 shows the standard deviation of *GM* obtained from *Syncom II* as a function of tracking time. *GM* standard deviations from lunar and planetary flights typically lie between 0.3 and 1 km^3/s^2. The standard deviations obtained from a 9000-km satellite (SPS 37-53, Vol. II) also level off in this range. For *Syncom II*, the *GM* uncertainty levels off after 3 days of tracking to an indicated 0.6×10^{-8} km^3/s^2 with ranging data and to 0.2×10^{-7} km^3/s^2 with doppler data only. It appears, therefore, that the potentially best *GM* solution is from a high-altitude satellite, although the required tracking time at synchronous altitude is double or more than in SPS 37-53, Vol. II, for a 9000-km satellite. Of course, omissions in the SPODP model of uncertainties in tesseral

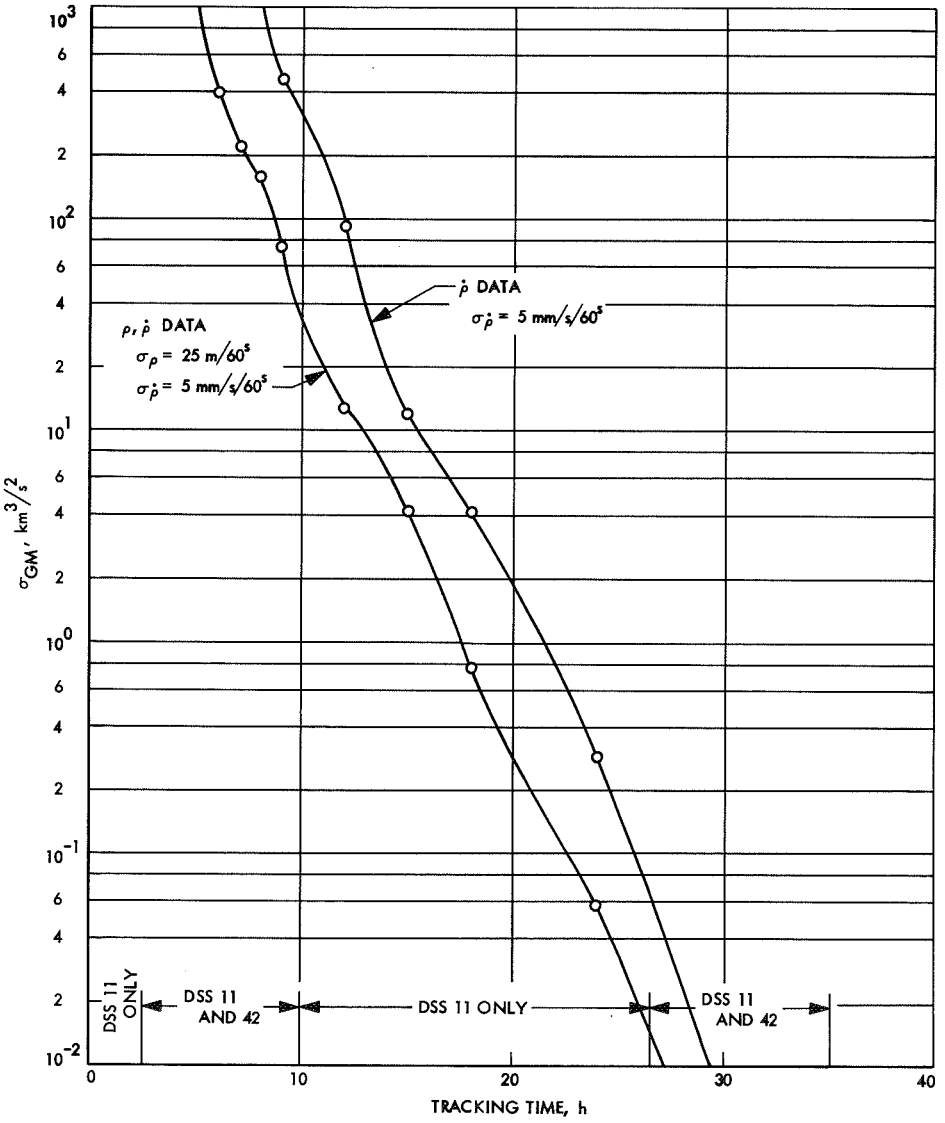

Fig. 22. Uncertainty in earth gravitational constant as a function of tracking *Syncom II*

harmonic coefficients and other error sources make such figures as 10^{-7} km^3/s^2 unrealistic and certainly unobtainable at present. However, a very definite improvement over existing values is clearly indicated.

Figure 23 shows the J_2 uncertainty as a function of tracking *Syncom II*. The accuracy attainable here is somewhat surprising for such a high-altitude satellite. Since the actual value of J_2 is about 10^{-3} for earth, an uncertainty of 10^{-6}, attained in less than 30 h, is certainly acceptable. Both Figs. 22 and 23, in addition to Table 15, indicate that ranging is not necessary to attain very high accuracies in GM and J_2 with high-altitude satellites. In general, equivalent accuracies are obtainable if an extra three hours of doppler tracking is obtained. However, in the presence of model errors, ranging data may be of considerable importance.

e. Comparison with high-altitude subsynchronous orbits. From Table 15, it is seen that the orbits at ½ and ¾ synchronous altitude lend themselves to more precise initial orbit determination than a synchronous orbit. The GM uncertainty is also reduced more quickly, although at ½ a the uncertainty levels off after 3 days to an indicated 0.7×10^{-6} km^3/s^2 with ranging, 0.3×10^{-5} km^3/s^2 with doppler tracking only. As in the synchronous case, these figures are unrealistic because of

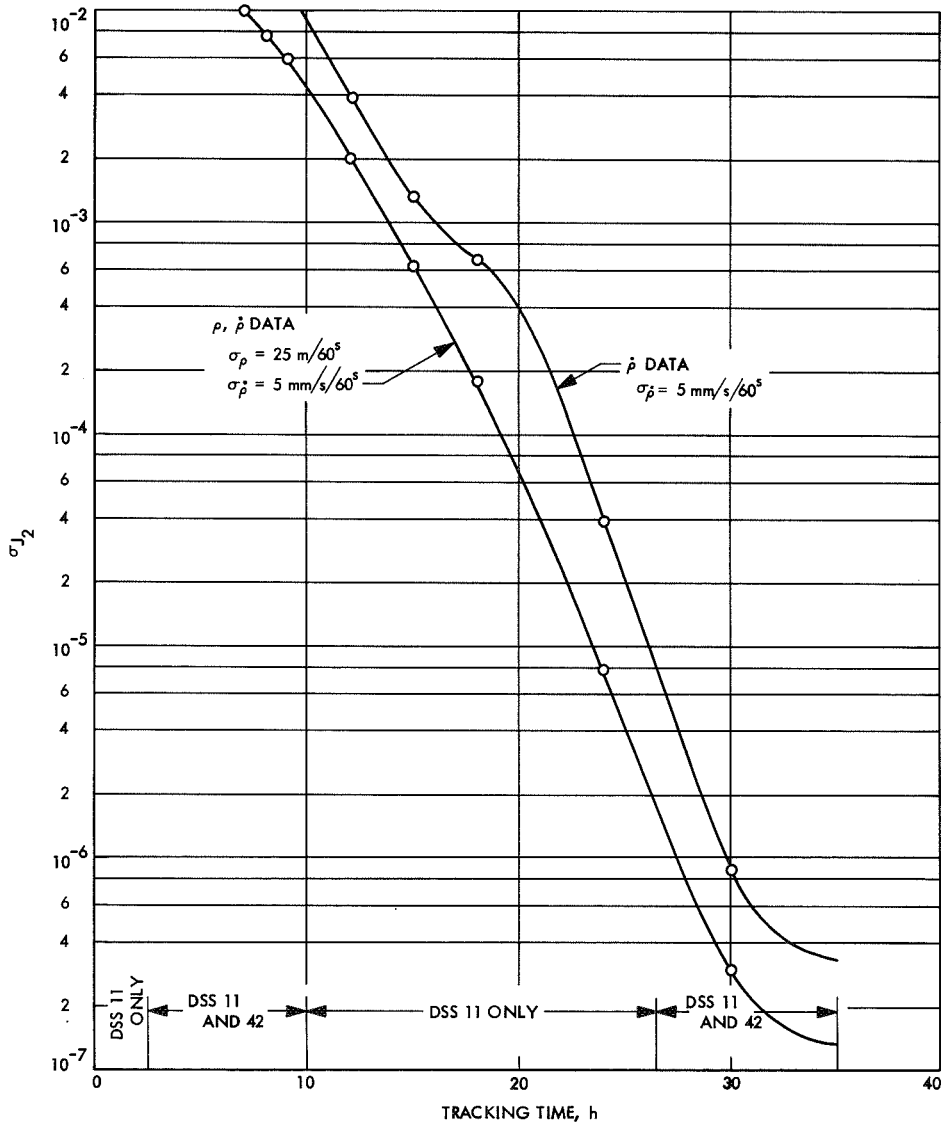

Fig. 23. Uncertainty in earth oblateness coefficient as a function of tracking *Syncom II*

unmodeled error sources, but are two orders of magnitude worse than at synchronous altitude. It appears that σ_{GM} is better determined initially with the lower orbits, but the higher ultimate accuracy is attained at synchronous altitude. This is confirmed in SPS 37-53, Vol. II, for the 9000-km satellite. The *GM* uncertainty here levels off very rapidly (in less than 10 h), but at $\sigma_{GM} = 0.27$ km^3/s^2 in the best case.

Figures 24a and 24b illustrate the *GM* uncertainty as a function of orbital semimajor altitude for various data spans. Figure 24a shows the profile for range and doppler tracking, while Fig. 24b is plotted for doppler tracking only. In either case, it is seen that the slopes are steep and remain more or less constant in the region of interest between 8 and 18 h of tracking. The most attractive orbits for the purpose of estimating *GM* are thus indicated to lie roughly in the region between ¼ and ½ synchronous altitude. This region does not seem practical for most other considerations, however. The effect of neglected uncertainties in high-order harmonic coefficients favors higher altitude satellites, furthermore. Of the existing satellites, those at synchronous altitude show the most promise in determining *GM*.

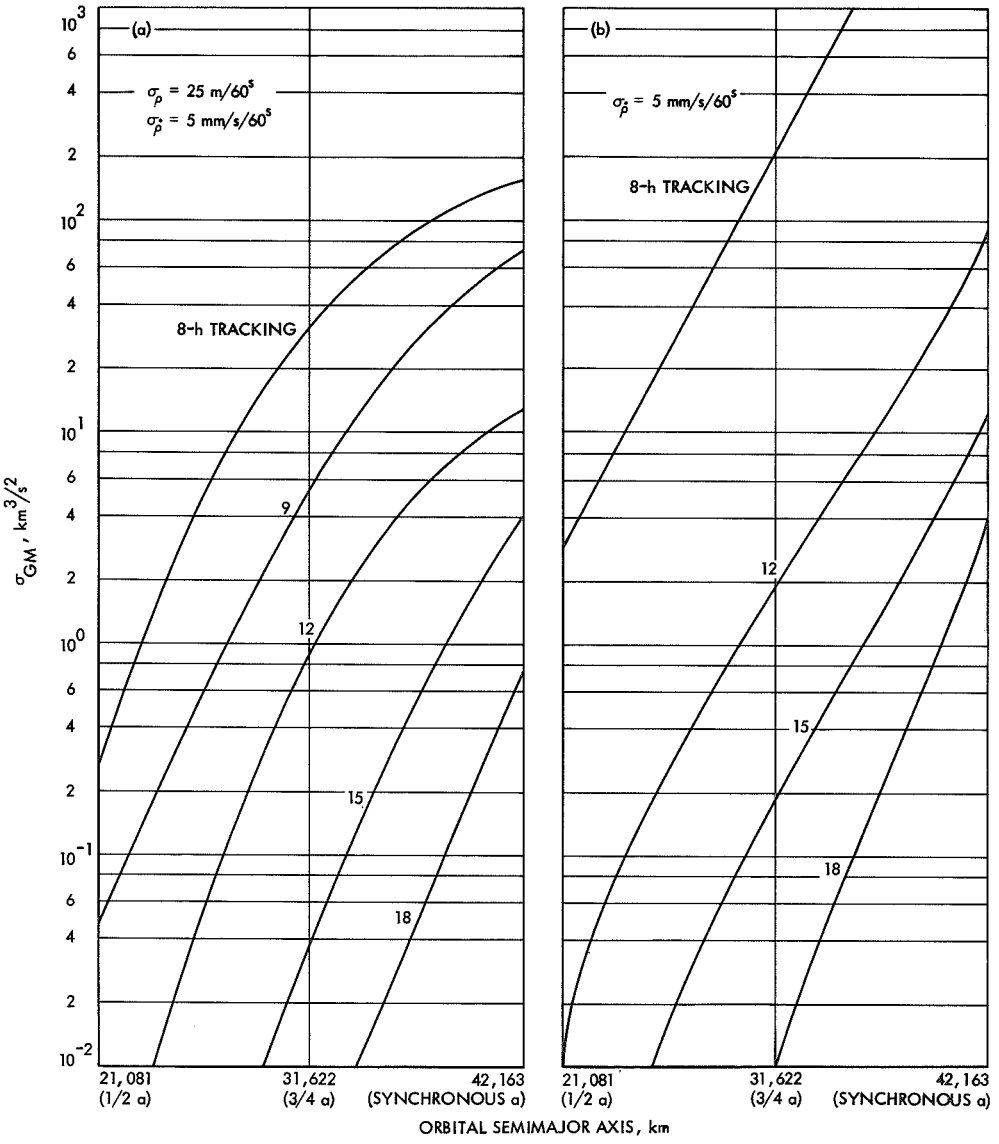

Fig. 24. Uncertainty in earth gravitational constant as a function of orbital altitude: (a) ρ, $\dot\rho$ tracking data, (b) $\dot\rho$ tracking data

References

1. Balsam, R. E., and Dunin, S. E., "Orbit Determination for Stationary Satellites," *Space Flights Mechanics Specialist Symposium, Vol. II*, p. 125, American Astronautical Society, 1967.
2. Warner, M. R., Nead, M. W., and Hudson, R. H., *The Orbit Determination Program of the Jet Propulsion Laboratory*, Technical Memorandum 33-169. Jet Propulsion Laboratory, Pasadena, Calif., Mar. 18, 1964.

8. The Sensitivity Matrix Method for Orbit Determination Error Analysis, With Application to a Mars Orbiter,

S. R. McReynolds

a. Introduction. The major task of orbit determination error analysis is to determine whether a mathematical model will permit the achievement of a given level of accuracy. The first step in the error analysis is to isolate the major error sources. To evaluate these error sources, they have to be modeled mathematically. Next, a study of the effects of these error sources on the estimate must be made. It is this latter topic that shall be considered here.

The traditional approach to orbit determination error analysis is the consider option, a feature built into the orbit determination programs at JPL. The consider option computes the "true" covariance of the estimate due to random errors in certain constant parameters. The weakness of this technique is that a new computer run is required to determine the effects of a specific parameter. To separate the effects of many error sources with a single computer run, an additional quantity should be computed, which is referred to here as the sensitivity matrix. This quantity is usually computed as an intermediate quantity in the consider option.

b. The sensitivity matrix. Let us introduce the following notation:

$\mathbf{x} = (x_1, \cdots, x_n)^T$, the velocity of estimated parameters

$\bar{\mathbf{x}}$ = the estimate of $\mathbf{x}$

$\mathbf{y} = (y_1, \cdots, y_m)^T$, the vector of consider parameters

$\mathbf{w} = (w_1, \cdots, w_m)^T$, data noise

S = the sensitivity matrix $(n \times m)$

The estimate is a function of $\mathbf{x}$, $\mathbf{y}$, and $\mathbf{w}$. The sensitivity matrix is defined by

$$S = \frac{\partial \bar{\mathbf{x}}}{\partial \mathbf{y}} \tag{1}$$

A formula for the sensitivity matrix shall be developed next. Consider the problem of estimating an n-dimension vector $\mathbf{x}$ from measurements, denoted by the p vector $\mathbf{z}$. The measurements are assumed to have the following linearized form:

$$\mathbf{z} = A\mathbf{x} + G\mathbf{y} + \mathbf{w} \tag{2}$$

where

$A = p \times n$ matrix

$G = p \times m$ matrix

Normally, $\mathbf{y} = 0$ in the model. However, in practice $\mathbf{y}$ will deviate from zero. Regarded as a random vector, $\mathbf{y}$ is assumed to have mean zero and covariance Λ_y. The vector $\mathbf{w}$ will be assumed to be independent gaussian error measurements with standard deviation σ_w.

The standard least-squares estimator for x minimizes

$$Q = \frac{1}{\sigma_w^2} ||\mathbf{z} - A\mathbf{x}||^2$$

This yields the estimate

$$\bar{\mathbf{x}} = (A^T A)^{-1} A^T \mathbf{z} \tag{3}$$

Now, since $\mathbf{z}$ is given by Eq. (2), one obtains

$$\bar{\mathbf{x}} = \mathbf{x} + S\mathbf{y} + B\mathbf{w} \tag{4}$$

where

$$S = (A^T A)^{-1} A^T G \tag{5}$$

$$B = (A^T A)^{-1} A^T \tag{6}$$

S is the desired sensitivity matrix. Next, we show how the consider covariance may be computed from S.

c. The total error — the consider covariance. Thus, the estimate $\bar{\mathbf{x}}$ will differ from the true value of $\mathbf{x}$ due to two error sources:

(1) A model error, $\varepsilon_1 = S\mathbf{y}$, which is caused by a departure of $\mathbf{y}$ from the nominal value.

(2) Measurement errors, $\varepsilon_2 = B\mathbf{w}$.

If $\mathbf{y}$ and $\mathbf{w}$ are considered to be independent random variables, it is clear that the estimate is unbiased, i.e.,

$$E(\bar{\mathbf{x}}) = \mathbf{x} \tag{7}$$

The covariance of the estimate is given by

$$E(\bar{x} - x)^2 = \Gamma_x = \Gamma_1 + \Gamma_2 \tag{8}$$

where

$$\Gamma_1 = E(\varepsilon_1^2) = S\Gamma_y S^T. \tag{9}$$

$$\Gamma_2 = E(\varepsilon_2^2) = \sigma_w^2 (A^T A)^{-1} \tag{10}$$

Γ_2 is the covariance on the estimate, ignoring the presence of y altogether. This is computed normally; the consider option is not employed. Γ_x is the consider covariance obtained from an orbit determination study when employing the consider covariance.

The sensitivity matrix may be computed from a least-squares estimator easily if the estimator can estimate the consider parameters. Partition the information matrix as follows:

$$J = \left[\begin{array}{c|c} J_x & J_{xy} \\ \hline J_{xy}^T & J_y \end{array}\right] \tag{11}$$

where

J_x = part of the information matrix associated with x

J_y = part of the information matrix associated with y

Table 16. Covariance matrix

Keplerian elements[a]	a	e	T_p	Ω	ω	i	Standard deviations
a	0.1628D−05	0.1439D−10	0.2022D−07	−0.7285D−10	−0.6064D−10	0.6500D−11	0.1276D−02
e	0.1439D−10	0.1271D−15	0.1786D−12	−0.6435D−15	−0.5356D−15	0.5743D−16	0.1127D−07
T_p	0.2022D−07	0.1786D−12	0.2511D−09	−0.9044D−12	−0.7525D−12	0.8076D−13	0.1584D−04
Ω	−0.7285D−10	−0.6435D−15	−0.9044D−12	0.3259D−14	0.2715D−14	−0.2902D−15	0.5709D−07
ω	−0.6064D−10	−0.5356D−15	−0.7525D−12	0.2715D−14	0.2268D−14	−0.2404D−15	0.4762D−07
i	0.6500D−11	0.5743D−16	0.8076D−13	−0.2902D−15	−0.2404D−15	0.2616D−16	0.5115D−08

[a]a = semimajor axis, e = eccentricity, T_p = time of periapsis, Ω = longitude of ascending node, ω = longitude of periapsis, i = inclination.

Table 17. Sensitivity matrix

Keplerian elements	Harmonic coefficients							
	J_1	J_2	J_3	J_4	C_{11}	S_{11}	C_{21}	C_{22}
a	−0.3651D 05	0.4688D 05	0.1367D 05	−0.3035D 05	0.2296D 05	0.4532D 04	0.9967D 05	−0.4907D 05
e	−0.3198D 00	0.4145D 00	0.1191D 00	−0.2671D 00	0.2115D 00	0.3803D−01	0.8685D 00	−0.4373D 00
T_p	0.5082D 04	0.2164D 03	−0.1782D 04	0.1404D 04	0.8214D 04	0.3191D 04	−0.9252D 04	0.6034D 04
Ω	0.1618D 01	−0.2000D 01	−0.6706D 00	0.1347D 01	−0.6369D 00	−0.3155D 00	−0.4864D 01	0.1771D 01
ω	0.4795D 01	−0.1633D 01	−0.1925D 01	0.2200D 01	0.5171D 01	0.1932D 01	−0.1112D 02	0.5421D 01
i	−0.6745D−02	0.2365D 00	−0.2702D−01	−0.8441D−01	0.4572D 00	0.1518D 00	0.2244D−01	−0.7956D−01
	C_{41}	C_{42}	C_{43}	C_{51}	C_{54}	C_{55}	S_{21}	S_{22}
a	0.1759D 05	−0.2175D 06	0.1520D 07	0.4620D 05	0.2015D 07	0.1952D 08	0.8626D 05	0.1420D 06
e	0.1566D 00	−0.1886D 01	0.1335D 02	0.4035D 00	0.1752D 02	0.1707D 03	0.7605D 00	0.1256D 01
T_p	0.1878D 04	0.2087D 05	−0.1731D 05	−0.5383D 04	0.1746D 06	−0.5742D 06	−0.3264D 04	0.1245D 05
Ω	−0.6883D 00	0.1131D 02	−0.7046D 02	−0.2197D 01	−0.1064D 03	−0.9462D 03	−0.3718D 01	−0.6316D 01
ω	0.8024D 00	0.2633D 02	−0.8159D 02	−0.5837D 01	0.3025D 00	−0.1341D 04	−0.5496D 01	0.2303D 01
i	0.1879D 00	0.1981D 00	0.5246D 01	−0.2779D−01	0.1177D 02	0.4769D 02	0.3091D 00	0.1045D 01

Now

$$\Gamma_2 = J_x^{-1} \tag{12}$$

Thus

$$S = \Gamma_2 J_{xy} \tag{13}$$

It should be noted that S is independent of the data weight σ_w.

d. Example: a Mars orbiter. In order to employ the sensitivity matrix method to analyze orbit determination of a Mars orbiter, a special computer program was written by Peter Dyer and Melba Nead. The program manipulates partial derivatives from a DPODP REGRESS tape. This program was applied to a Mars orbiter with a trajectory similar to one that is being considered for the *Viking* orbiter. Doppler points were sampled every half hour. After 48 h, which constitute approximately two orbits, the standard covariance in classic plane-of-sky Keplerian elements is given in Table 16. The S matrix for certain parameters is given in Table 17. The actual perturbations using reasonable values for the perturbing parameter are given in Table 18. These results indicate that gravitational perturbations will be the dominant source of estimation errors.

e. Conclusion. A new method, the sensitivity matrix method, was introduced and related to the consider option. The advantage of the sensitivity matrix method is that it allows one to perform an error analysis of many error sources simultaneously and to distinguish among different effects. The method was applied to a Mars orbiter and the results showed that gravitational perturbations were the major source of errors.

9. The Influence of Range Measurements on the State Information Contained in a Few Passes of Counted Doppler Data, *J. F. Jordan*

a. Introduction. In SPS 37-52, Vol. II, pp. 37–44, the accuracy of the continuous minimum variance estimate of the state of a distance space probe was studied over several successive passes of counted doppler data. Dependency of the estimation accuracies on the velocity and position of the probe and the variance of the data noise was noted, and a set of empirical formulas for the estimation sigmas was presented, which illustrated these dependencies.

In this article, the influence of range data on the estimation accuracies is studied, and the dependency of the state estimation sigmas on both the earth–probe geometry and the accuracy of the range measurements is noted. Plots are presented which illustrate the various dependencies, and empirical formulas for the accuracies of the affected state parameters are set forth.

Table 18. Perturbations due to consider parameters

Keplerian elements	Harmonic coefficients							
	J_1	J_2	J_3	J_4	C_{11}	S_{11}	C_{21}	C_{22}
a	−0.3651D 00	0.1031D 01	0.1777D 00	−0.2276D 00	0.9185D 00	0.1812D 00	0.1295D 01	−0.3190D 00
e	−0.3198D−05	0.9120D−05	0.1549D−05	−0.2003D−05	0.8463D−05	0.1521D−05	0.1129D−04	−0.2842D−05
T_p	0.5082D−01	0.4761D−02	−0.2316D−01	0.1053D−01	0.3285D 00	0.1276D 00	−0.1202D 00	0.3922D−01
Ω	0.1618D−04	−0.4400D−04	−0.8717D−05	0.1010D−04	−0.2547D−04	−0.1262D−04	−0.6324D−04	0.1151D−04
ω	0.4795D−04	−0.3593D−04	−0.2502D−04	0.1650D−04	0.2068D−03	0.7728D−04	−0.1445D−03	0.3524D−04
i	−0.6754D−07	0.5203D−05	−0.3512D−06	−0.6331D−06	0.1828D−04	0.6073D−05	0.2917D−06	−0.5172D−06
	C_{41}	C_{42}	C_{43}	C_{51}	C_{54}	C_{55}	S_{21}	S_{22}
a	0.4223D−01	−0.1087D 00	0.2280D 00	0.6930D−01	0.2620D−01	0.1171D 00	0.1121D 01	0.9235D 00
e	0.3759D−06	−0.9431D−06	0.2003D−05	0.6052D−06	0.2277D−06	0.1024D−05	0.9887D−05	0.8168D−05
T_p	0.4508D−02	0.1043D−01	−0.2597D−02	−0.8074D−02	0.2270D−02	−0.3445D−02	−0.4243D−01	0.8095D−01
Ω	−0.1651D−05	0.5657D−05	−0.1057D−04	−0.3295D−05	−0.1383D−05	−0.5677D−05	−0.4834D−04	−0.4105D−04
ω	0.1925D−05	0.1316D−04	−0.1223D−04	−0.8756D−05	0.3933D−08	−0.8051D−05	−0.7145D−04	0.1497D−04
i	0.4510D−06	0.9906D−07	0.7869D−06	−0.4168D−07	0.1531D−06	0.2861D−06	0.4018D−05	0.6794D−05

b. The model. The theoretical development coincides with that presented in SPS 37-52, Vol. II, where a station on the earth's equator observes a distant space probe over successive passes of data. The probe travels with geocentric velocity $\vec{v}$ and is at a great enough distance r such that solar gravitational forces do not affect the state estimation accuracies over several passes of data. The counted doppler data noise model is exponentially correlated gaussian, with a constant standard deviation of 1 m. The correlation time is 1000 s. A single range measurement is made by the station at the end of each pass of data. It is assumed that the accuracy of the range data is not great enough for the range data to compete with the counted doppler data for range-rate information. That is, the range measurements cannot be differenced to obtain range-rate values, whose accuracy is comparable to that derived from the counted doppler data.

The state estimates are formed in the equatorial plane of the sky coordinate system illustrated in Fig. 25, where u is the component of probe velocity along the earth probe line, v is the component of velocity perpendicular to u and parallel to the equatorial plane (velocity in the right ascension direction), and w is perpendicular to both u and v (declination velocity). $\vec{\nu}$ is the vector projection of $\vec{v}$ in the y, z plane, and it represents the component of probe velocity which is at right angles to the earth–probe line.

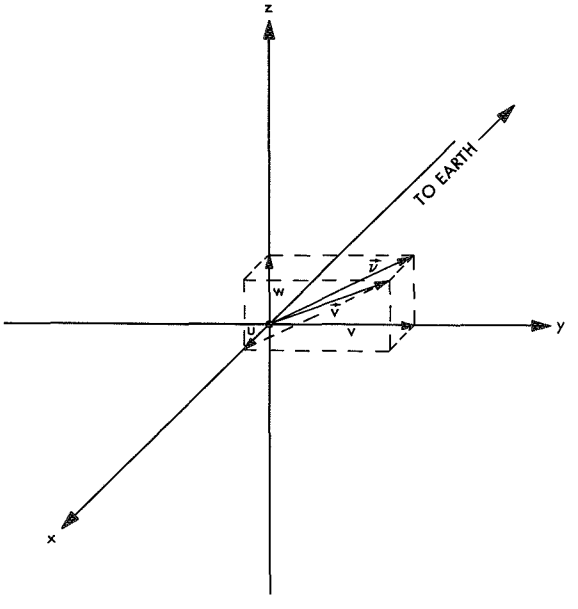

Fig. 25. Problem geometry (position of probe is at origin)

c. Results. The following properties of the contribution of range data to the counted doppler data accuracies have been obtained from the integration of a matrix Riccati equation for the covariance matrix of errors in the state estimates. Integration of the Riccati equation was carried out by the continuous estimation program (SPS 37-48, Vol. II, pp. 23–27). The properties of the range-data contributions are:

(1) The standard deviation of the inertial range is improved to the accuracy of the range measurements and decreases after the first pass of data as the reciprocal of the square root of the number of passes completed.

(2) If the magnitude of $\vec{\nu}$ [$\nu = (v^2 + w^2)^{1/2}$] is nonzero, then the range data improves the accuracy of the

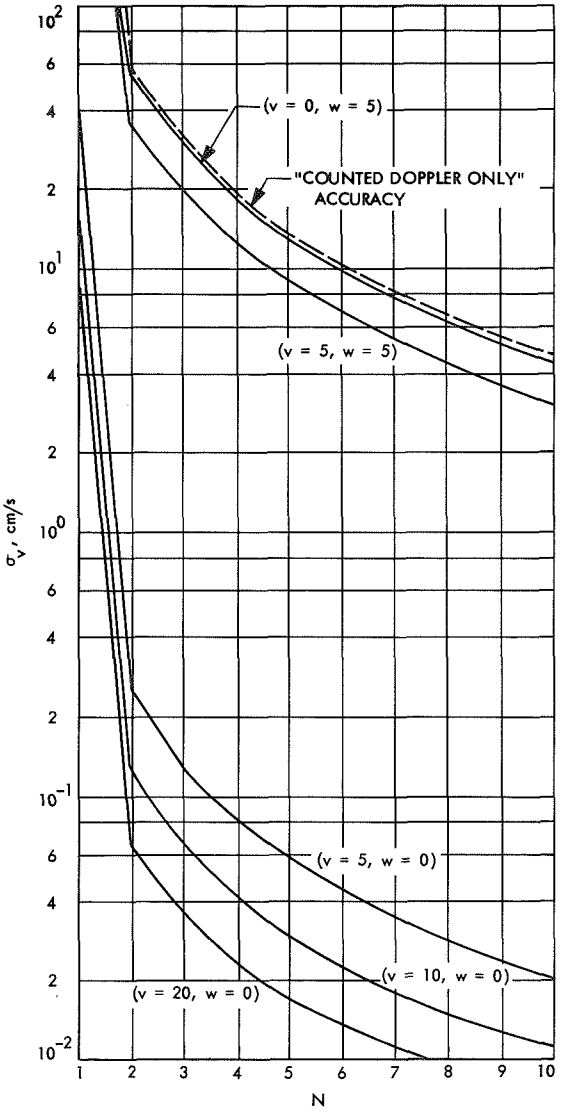

Fig. 26. Lateral velocity accuracy time history

magnitude of $\vec{v}$, but does not improve the accuracy of the direction of $\vec{v}$. It should be noted that this phenomenon was also recognized by Curkendall and McReynolds (Ref. 1).

(3) The standard deviation of v, σ_v, varies as the reciprocal of v, and is independent of the direction of $\vec{v}$. This property is illustrated in Fig. 26, where σ_v is plotted as a function of the number of completed passes N for a probe observed over 10 passes of data. A range measurement of 10-m accuracy is made at the end of each pass. Curves are shown for the following sets of (velocity components) v and w: $v = 0$, $w = 5$ km/s; $v = 5$ km/s, $w = 5$ km/s; $v = 5$ km/s, $w = 0$; $v = 10$ km/s, $w = 0$; and $v = 20$ km/s, $w = 0$. When $w = 0$, v becomes v and is observed very well, but when $v = 0$, σ_v is not improved over the "doppler only" value. When v and w are both nonzero, only slight improvement occurs. This behavior is consistent with property (2).

(4) The accuracy of v is proportional to the earth–probe distance r but is not affected by the value of the geocentric declination δ_0. The accuracy of v decreases with the number of completed passes by the factor $(2/N)^{3/2}$

(5) As long as the accuracy of the range measurement σ_ρ is between 10 m and 10 km, σ_v is independent of σ_ρ. This is illustrated in Fig. 27, where σ_v is plotted versus σ_ρ. Curves are shown for $v = 5$ km/s, and 10 km/s when $w = 0$; hence $v = v$. In Fig. 27, it is seen that when the accuracy of the range measurements is approximately the accuracy to which x can be measured from the counted doppler data alone (about 10^7 m) the accuracy of v is slightly improved. σ_v continues to decrease as σ_ρ is decreased until σ_ρ reaches 10^4 m, where the information about v becomes saturated. Improving σ_ρ beyond this point will only decrease σ_x, but not σ_v.

(6) The accuracies of the rest of the state parameters u, y, and z are not affected by the addition of range measurements to the counted doppler information, and σ_u, σ_y, and σ_z still obey the empirical formulas set forth in SPS 37-52, Vol. II.

d. Conclusions. The properties discussed in *Paragraph c* indicate that when the accuracy of range measurements is between 10 m and 10 km, the uncertainty in inertial range, σ_x, and the uncertainty in the magnitude of the lateral velocity, σ_v, obey the following respective empirical formulas

$$\sigma_x = \frac{1}{(N)^{1/2}}\,\sigma_\rho \quad \text{m} \tag{1}$$

$$\sigma_v = \left[\left(\frac{2}{N}\right)^3\right]^{1/2} r\,\frac{1.3 \times 10^{-10}}{(v^2 + w^2)^{1/2}} \quad \text{m/s} \tag{2}$$

where r and σ_ρ are specified in meters and v and w are specified in m/s. Equations (1) and (2) are valid up to about 15 passes of data and for values of v between 1 km/s and 30 km/s. The uncertainty in the magnitude of

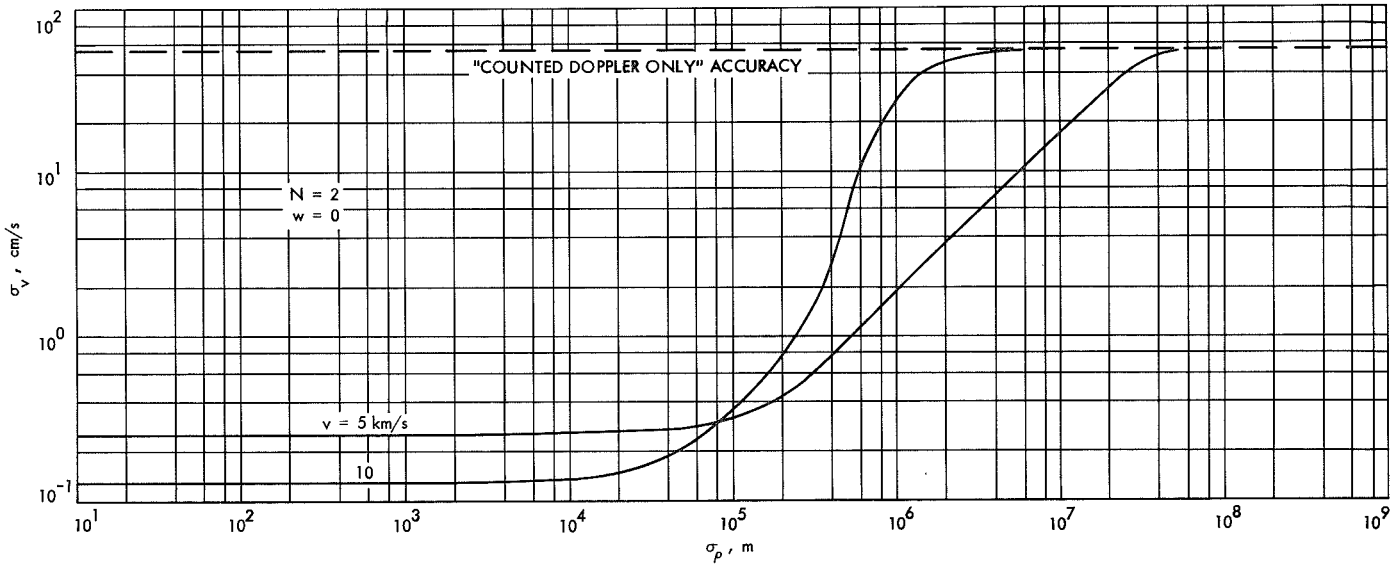

Fig. 27. Lateral velocity accuracy vs accuracy of range measurement

the lateral velocity component perpendicular to $\vec{v}$, v', is not affected by range data and can be computed from the relation

$$\sigma_{v'} = \left\{ \left(\frac{2}{N}\right)^3 \frac{r^2}{v^2 + w^2} \left[w^2 (0.5 \times 10^{-11})^2 + \frac{v^2}{(\sin \delta_0)^2} (0.2 \times 10^{-11})^2 \right] \right\}^{1/2} \text{ m/s} \quad (3)$$

It should be noted that the uncertainty in v and the uncertainty in v' are uncorrelated; thus, the covariance of estimation errors in v and w can be found from the following matrix mapping:

$$\begin{bmatrix} \sigma_v^2 & \gamma_{vw} \\ \gamma_{vw} & \sigma_w^2 \end{bmatrix} = A \begin{bmatrix} \sigma_v^2 & 0 \\ 0 & \sigma_v^2 \end{bmatrix} A^T \quad (4)$$

where

$$A = \frac{1}{(v^2 + w^2)^{1/2}} \begin{bmatrix} v & -w \\ w & v \end{bmatrix} \quad (5)$$

Although the formulas given above indicate the improvement in state estimation accuracies due to range measurements made over a short span of time, no results were given for large data spans. Also, no study was performed regarding the influence of range data on the counted doppler accuracies where random forces act on the space probe. These problem areas will be the subject of future investigation.

Reference

1. Curkendall, D. W., and McReynolds, S. R., "A Simplified Approach for Determining the Information Content of Radio Tracking Data," Presented at the AAS/AIAA Conference, Jackson Hole, Wyoming, Sep. 3–5, 1968.

B. Communications Systems Research

1. Communication Statistics: Confidence Intervals for Probabilities Associated With the Normal Distribution,

I. Eisenberger

a. Introduction. In estimating the probability of success of the DSN system during a mission, it is useful to have reliability estimates for the subsystems involved. Making such estimates brings up the problem of finding confidence intervals for the unknown parameters in such probability distributions. One method of doing this is applied here to a normal distribution.

Let x be a normally distributed random variable with mean μ_0 and variance σ_0^2. The typical problem in reliability which we consider is to try and determine the probability that a sample value taken from a population with such a distribution will not exceed a certain value, say k. If μ_0 and σ_0 are known, this is easily accomplished. One has

$$P = \text{Prob}\,(x < k) = \text{Prob}\left(y < \frac{k - \mu_0}{\sigma_0}\right) \quad (1)$$

where y is distributed $N(0,1)$. The value of P is determined from a table of areas under the standard normal curve. However, when μ_0 and σ_0 are unknown, as is usually the case, the parameters must be estimated from a set of n sample values drawn from the population. One then usually obtains the unbiased estimation

$$\hat{\mu}_0 = \bar{x} = \frac{1}{n} \sum_{i=1}^{n} x_i$$

$$\hat{\sigma}_0 = s = \left[\frac{1}{n-1} \sum_{i=1}^{n} (x_i - \bar{x})^2 \right]^{1/2}$$

Substituting $\hat{\mu}_0$ and $\hat{\sigma}_0$ for μ_0 and σ_0 in Eq. (1) results in the point estimate of P given by

$$\hat{P} = \text{Prob}\left(y < \frac{k - \bar{x}}{s}\right)$$

The purpose of this article is to provide a confidence interval for P of the form

$$P_{\min} < P < P_{\max}$$

such that the probability statement

$$\text{Prob}\,(P_{\min} < P < P_{\max}) \geqq \alpha \quad (2)$$

can be made.

The type of probability statement given by Inequality (2) can also be used in connection with certain other distributions which are related to the normal. For example, the distribution of the time before failure due to wearout for certain electronic components can often be closely approximated by the lognormal distribution. A random variable z is said to have the lognormal distribution with parameters μ and σ if $x = \ln z$ is $N(\mu, \sigma^2)$. For this case, the probability that $z < e^k$ is equivalent to the probability that $x < k$.

b. A confidence region for the joint estimation of μ_0 and σ_0. The confidence interval for P given in Inequality (2) will be obtained by considering a confidence region for the joint estimation of μ_0 and σ_0, which will be determined by a method suggested in Ref. 1.

Let $1 - \varepsilon = (\alpha)^{1/2}$. We can find numbers $z_{\varepsilon/2}$, $\chi^2_{\varepsilon/2}$, and $\chi^2_{1-\varepsilon/2}$, where $z_{\varepsilon/2}$ is the quantile of order $1 - \varepsilon/2$ of the standard normal distribution, $\chi^2_{\varepsilon/2}$ and $\chi^2_{1-\varepsilon/2}$ are the quantiles of orders $1 - \varepsilon/2$ and $\varepsilon/2$, respectively, of the χ^2 distribution with $n - 1$ degrees of freedom, such that

$$\text{Prob}\left(-z_{\varepsilon/2} < \frac{\bar{x} - \mu_0}{\sigma_0/(n)^{1/2}} < z_{\varepsilon/2}\right) = 1 - \varepsilon$$

$$\text{Prob}\left(\chi^2_{1-\varepsilon/2} < \frac{(n-1)s^2}{\sigma_0^2} < \chi^2_{\varepsilon/2}\right) = 1 - \varepsilon$$

Since $\bar{x}$ and s^2 are independently distributed, it follows that the joint probability

$$\text{Prob}\left(-z_{\varepsilon/2} < \frac{\bar{x} - \mu_0}{\sigma_0/(n)^{1/2}} < z_{\varepsilon/2},\ \chi^2_{1-\varepsilon/2} < \frac{(n-1)s^2}{\sigma_0^2} < \chi^2_{\varepsilon/2}\right) = (1 - \varepsilon)^2 = \alpha \tag{3}$$

The four inequalities in Expression (3) determine a joint α confidence region in the parameter space (μ,σ), which can be found by plotting its boundaries. By replacing the inequality signs in Expression (3) by equality signs, one finds that the boundaries of the confidence region for the joint estimation of μ_0 and σ_0 are the four straight lines

$$\sigma = a_1 s$$

$$\sigma = a_2 s$$

and

$$\mu = \bar{x} \pm b\sigma, \qquad \sigma > 0$$

where

$$a_1 = \left(\frac{n-1}{\chi^2_{1-\varepsilon/2}}\right)^{1/2}$$

$$a_2 = \left(\frac{n-1}{\chi^2_{\varepsilon/2}}\right)^{1/2}$$

$$b = \frac{z_{\varepsilon/2}}{(n)^{1/2}}$$

This confidence region is shown as the shaded area in Fig. 28.

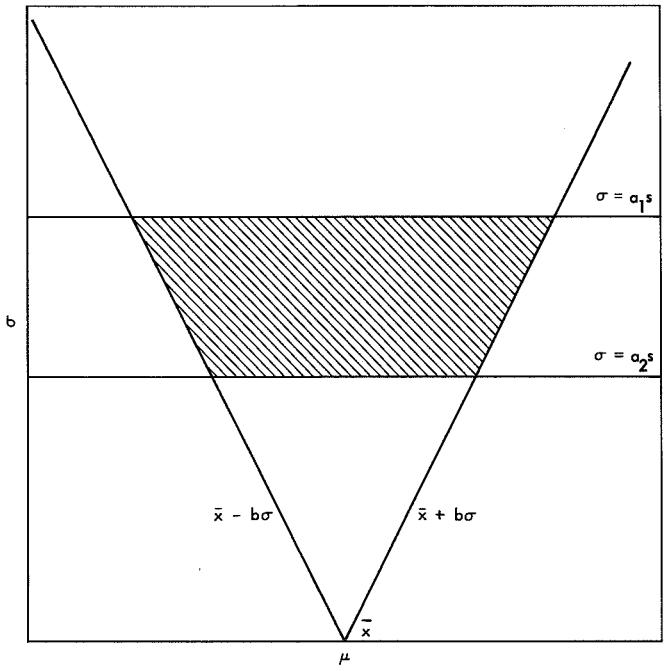

Fig. 28. A confidence region for (μ_0, σ_0)

c. A confidence interval for P. By virtue of the method used in the construction of the confidence region for μ_0 and σ_0, the probability that the region includes the true parameter point (μ_0,σ_0) is α. Moreover, since

$$F\left(\frac{k-\mu}{\sigma}\right) = \text{Prob}\left(y < \frac{k-\mu}{\sigma}\right)$$

is a monotone increasing function of its argument, the point in the region which maximizes (minimizes) $v = (k-\mu)/\sigma$ will also maximize (minimize) $F(v)$. Thus, by determining the point (μ_1,σ_1) which minimizes v and the point (μ_2,σ_2) which maximizes v in the region and setting

$$P_{\min} = F\left(\frac{k-\mu_1}{\sigma_1}\right), P_{\max} = F\left(\frac{k-\mu_2}{\sigma_2}\right),$$

and

$$P = F\left(\frac{k-\mu_0}{\sigma_0}\right)$$

one has

$$P_{\min} < P < P_{\max}$$

with probability at least equal to α.

To determine (μ_1,σ_1), we first observe that μ_1 must be a maximum and, hence, the point (μ_1,σ_1) must lie on the line $\mu = \bar{x} + b\sigma$. Then one has

$$v = \frac{k-\mu_1}{\sigma_1} = \frac{k-\bar{x}-b\sigma_1}{\sigma_1} = \frac{k-\bar{x}}{\sigma_1} - b$$

Therefore, if $k - \bar{x} > 0$, $\sigma_1 = a_1 s$ will minimize v, while if $k - \bar{x} < 0$, $\sigma_1 = a_2 s$ will minimize v. Similarly, we find that in order to maximize v, (μ_2,σ_2) must be on the line $\mu = \bar{x} - b\sigma$ and for $k - \bar{x} > 0$, $\sigma_2 = a_2 s$ will maximize v, while for $k - \bar{x} < 0$, $\sigma_2 = a_1 s$ will maximize v. In summary, we have

$$P_{\min} = F\left(\frac{k-\mu_1}{\sigma_1}\right)$$

where

$$\sigma_1 = \begin{cases} a_1 s, & k-\bar{x} > 0 \\ a_2 s, & k-\bar{x} < 0 \end{cases}$$

$$\mu_1 = \bar{x} + b\sigma_1$$

and

$$P_{\max} = F\left(\frac{k-\mu_2}{\sigma_2}\right)$$

where

$$\sigma_2 = \begin{cases} a_2 s, & k-\bar{x} > 0 \\ a_1 s, & k-\bar{x} < 0 \end{cases}$$

$$\mu_2 = \bar{x} - b\sigma_2$$

If, for all points (μ_0,σ_0) outside the confidence region, P did not lie in the interval $(P_{\min}, P_{\max})$, one would have

$$\text{Prob}\,(P_{\min} < P < P_{\max}) = \alpha$$

However, this is not necessarily so. Let $k - \bar{x} > 0$ and consider a point (μ_0,σ_0) on the line $\mu = \bar{x} + \delta + b\sigma$. Then, for values of δ such that

$$(k-\bar{x})\left(1-\frac{\sigma_0}{a_2 s}\right) - 2b\sigma_0 < \delta < (k-\bar{x})\left(1-\frac{\sigma_0}{a_1 s}\right) \tag{4}$$

one has, after some algebraic manipulation,

$$\frac{k-\bar{x}}{a_1 s} - b < \frac{k-(\bar{x}-\delta)}{\sigma_0} - b < \frac{k-\bar{x}}{a_2 s} + b$$

or

$$\frac{k-\mu_1}{\sigma_1} < \frac{k-\mu_0}{\sigma_0} < \frac{k-\mu_2}{\sigma_2}$$

which implies that

$$P_{\min} < P < P_{\max}$$

Restricting δ to positive values so that (μ_0,σ_0) lies to the right of the confidence region, Inequality (4) becomes

$$0 < \delta < (k-\bar{x})\left(1-\frac{\sigma_0}{a_1 s}\right) \tag{5}$$

Thus, for any value of σ_0 such that $0 < \sigma_0 < a_1 s$, and for all values of δ satisfying Inequality (5), the points (μ_0,σ_0) on the lines $\mu = \bar{x} + \delta + b\sigma$ have the property that

$$P_{\min} < P < P_{\max}$$

Similarly, it can be shown that if $(k - \bar{x}) < 0$, for any value of σ_0 such that $0 < \sigma_0 < a_1 s$, and for all values of δ satisfying

$$(k - \bar{x})\left(1 - \frac{\sigma_0}{\sigma_1 s}\right) < \delta < 0$$

all the points on the lines $\mu = \bar{x} + \delta - b\sigma$ lie to the left of the confidence region and the points (μ_0,σ_0) have the property that

$$P_{\min} < P < P_{\max}$$

Thus, with respect to the confidence interval for P, one can only state that

$$\text{Prob}\,(P_{\min} < P < P_{\max}) \geqq \alpha$$

It may be that one is interested in the probability

$$\begin{aligned} P &= \text{Prob}\,(k_1 < x < k_2) \\ &= \text{Prob}\left(\frac{k_1 - \mu}{\sigma} < y < \frac{k_2 - \mu}{\sigma}\right) \\ &= \text{Prob}\left(y < \frac{k_2 - \mu}{\sigma}\right) - \text{Prob}\left(y < \frac{k_1 - \mu}{\sigma}\right) \\ &= P' - P'' \end{aligned}$$

A point estimate of P is, of course, provided by

$$\hat{P} = \hat{P}' - \hat{P}''$$

A confidence interval for P can be established from the confidence intervals for P' and P''. Suppose the point (μ_0,σ_0) lies in the α confidence region. Then the joint event

$$(P'_{\min} < P' < P'_{\max}, P''_{\min} < P'' < P''_{\max})$$

will occur with probability one, and it follows that $P' - P''$ will lie in the interval

$$(P'_{\min} - P''_{\max}, P'_{\max} - P''_{\min})$$

However, even if P' or P'', or both, lie outside of their respective confidence intervals, the probability is not zero that $P' - P''$ will lie inside of

$$(P'_{\min} - P''_{\max}, P'_{\max} - P''_{\min})$$

Thus, one can make the statement that

$$\text{Prob}\,(P'_{\min} - P''_{\max} < P' - P'' < P'_{\max} - P''_{\min}) > \alpha$$

d. Establishing confidence intervals for P using real data. Five sets of 100 sample values each and six sets of 50 sample values each were drawn from a table of

Table 19. Confidence intervals $(P_{\min}, P_{\max})$ for $P = \text{Prob}\left(y < \frac{k - \mu}{\sigma}\right)$ and point estimates $\hat{P} = \text{Prob}\left(y < \frac{k - \bar{x}}{s}\right)$ when $\mu = 0$, $\sigma = 1$, $\alpha = 0.9$

n	k	$\bar{x}$	s	$\hat{P}$	$P_{\min}$	P	$P_{\max}$
100	0	−0.112	1.016	0.544	0.461	0.5	0.625
100	2.0	−0.112	1.016	0.981	0.946	0.977	0.995
100	0	−0.013	0.894	0.506	0.428	0.5	0.583
100	0	−0.122	0.982	0.550	0.466	0.5	0.632
100	0	0.164	1.024	0.436	0.345	0.5	0.522
100	0	−0.019	0.990	0.508	0.430	0.5	0.585
50	0	0.229	0.873	0.397	0.279	0.5	0.525
50	0	−0.271	0.900	0.618	0.498	0.5	0.737
50	0	−0.075	1.0	0.530	0.416	0.5	0.641
50	0	0.041	0.935	0.483	0.373	0.5	0.594
50	0	−0.249	0.942	0.604	0.476	0.5	0.722
50	0	0.193	1.109	0.431	0.315	0.5	0.553

random numbers in which the entries are distributed $N(0,1)$. Values of $\bar{x}$, s, $\hat{P}$, $P_{\min}$, and $P_{\max}$ were computed for all cases with $k = 0$ and $\alpha = 0.9$. In addition, for one case k was taken to be 2.0. The results are given in Table 19. In all cases, the interval $(P_{\min}, P_{\max})$ includes P, although in one case just barely.

Reference

1. Mood, A. M., *Introduction to the Theory of Statistics*, pp. 227–229. McGraw-Hill Book Co., New York, N. Y., 1950.

2. Digital Telemetry and Command: Cycle Slipping in the Second-Order Loop With Limiting, R. C. Tausworthe

a. Introduction. In Ref. 1, the author developed an approximate double integral expression for the slip-rate of a second-order phase-locked loop. Later studies (SPS 37-43, Vol. III, pp. 76–80) verified that the expression was indeed valid, even at low loop signal-to-noise ratios (SNRs). This article gives simplified formulas for the slip-rate in the threshold region of operation, with a special evaluation when the loop is preceded by a hard limiter.

b. Approximate behavior as a function of loop damping. The curves published in Ref. 1 indicate very strongly, in the region for which the parameter ρ, given by

$$\rho = \frac{A^2}{N_0 w_L} \tag{1}$$

in which A is the rms signal amplitude, N_0 is the two-sided noise density ($= kT/2$), and w_L is the two-sided loop bandwidth, that the mean first-slip T is very nearly of the form

$$T = \frac{c}{w_L} \exp(a\rho) \tag{2}$$

The parameters c and a are functions of the loop damping parameter

$$r = \frac{AK\tau_2^2}{\tau_1} \approx 4\zeta^2 \tag{3}$$

in the notation of Ref. 2, but almost independent of ρ. Based on the results in Ref. 1 and SPS 37-43, Vol. III, both c and a can be tabulated. Figure 29 shows a plot

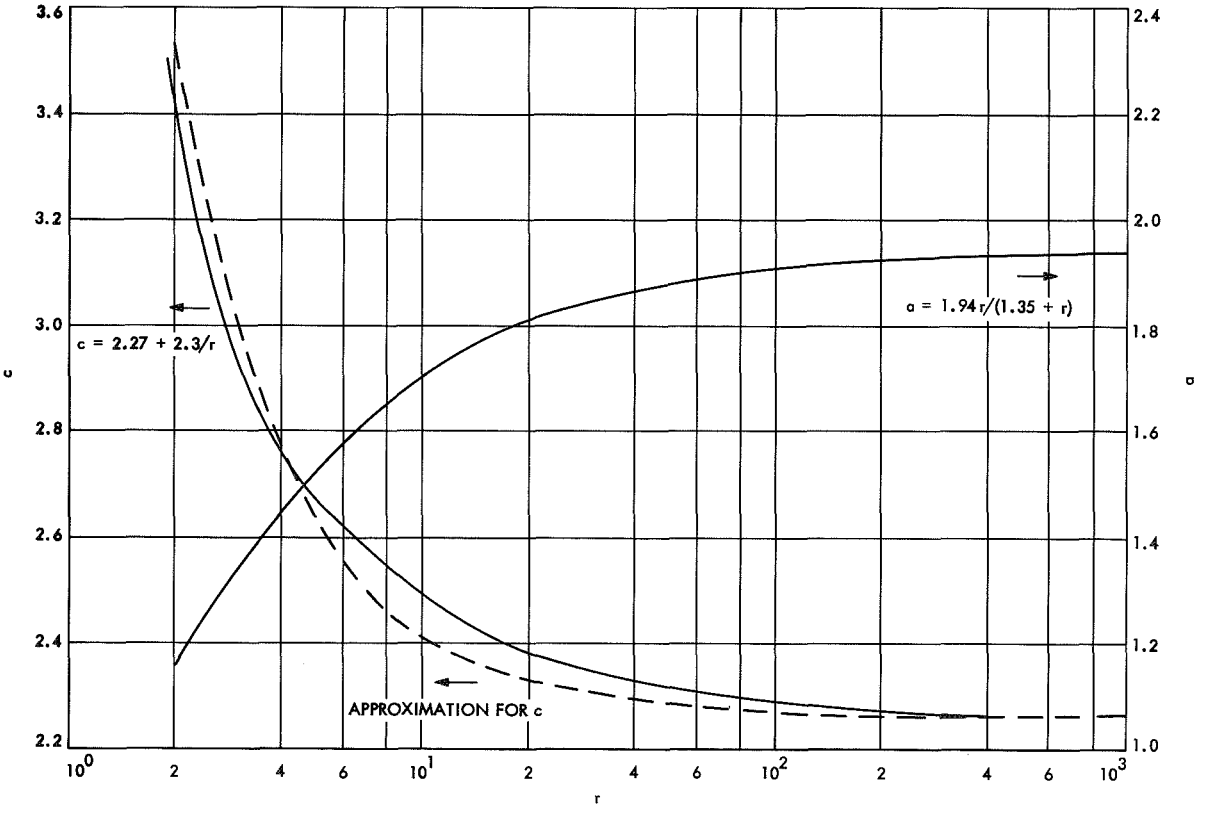

Fig. 29. Variation of the slip-time parameters c and a as a function of the damping parameter r

of the exponent a and constant c as a function of r, along with simple approximations. It is noteworthy that the simplified expression for a is indistinguishable on the figure from the actual computed value of a in the region shown. The approximation for c lies within 4% of its computed values. The simplified expressions are

$$c = 2.27 + \frac{2.3}{r}$$
$$a = \frac{1.94r}{1.35 + r} \tag{4}$$

c. The limiter-loop. As the loop input A^2/N_0 varies, the linear loop bandwidth w_L changes accordingly:

$$w_L = w_{L_0}\left[\frac{1 + \left(\frac{\alpha}{\alpha_0}\right) r_0}{1 + r_0}\right] \tag{5}$$

in terms of design-point values of loop bandwidth and damping parameter, w_{L_0} and r_0. The parameter α is the limiter suppression factor (Ref. 2), and α_0 is its value at design point. In the signal-suppression region of limiter operation, we have very nearly

$$\frac{\alpha}{\alpha_0} = \frac{A}{A_0} = m^{1/2} \tag{6}$$

The parameter $m = A^2/A_0^2$ is defined as the *loop margin.* The relevant expression for ρ can then be written as

$$\rho = \frac{m\rho_0}{\Gamma}\left[\frac{1 + r_0}{1 + m^{1/2}r_0}\right] \tag{7}$$

in the region for which Eq. (6) is valid. The value ρ_0 is the *design-point loop SNR,* and Γ is the limiter performance factor. In the region of interest

$$\Gamma = \frac{1}{0.862} \tag{8}$$

As a function of margin, then, the mean first-slip time is approximately

$$T = \frac{\left(2.27 + \frac{2.3}{m^{1/2}r_0}\right)(1 + r_0)}{w_{L_0}(1 + m^{1/2}r_0)} \exp\left[\frac{1.94\, m^{3/2}r_0\, \rho_0\, (1 + r_0)}{(1.35 + m^{1/2}r_0)(1 + m^{1/2}\, r_0)}\right] \tag{9}$$

A plot of Tw_{L_0} appears in Fig. 30, and Table 20 gives a tabulation of the various loop performance parameters. In both of these, the design-point values r_0 and ρ_0 are

$$r_0 = 2, \qquad \zeta = 0.707$$
$$\rho_0 = 2, \qquad \text{unity SNR in receiver passband} \tag{10}$$

d. Measurement of mean slip time. As was shown in SPS 37-43, Vol. III, the distribution of the first-slip times t_s is very nearly Poisson, so the standard deviation of t_s about its mean value T is equal to T; hence, the larger that T is, the more samples that must be examined to estimate T absolutely from measured slip times t_s. Defining the sample mean slip time as

$$\hat{T} = \frac{1}{N}\sum_{n=1}^{N} t_{s,n} \tag{11}$$

we find that the statistics of $\hat{T}$ are

$$E(\hat{T}) = T$$
$$\text{var}\,(\hat{T}) = \frac{T^2}{N} \tag{12}$$

The number of samples required to make var $(\hat{T}) = \varepsilon$ is then

$$N = \frac{T^2}{\varepsilon} \tag{13}$$

However, the number of samples required to make var $(\hat{T})/E^2(\hat{T}) = \varepsilon$ is only

$$N = \frac{1}{\varepsilon} \tag{14}$$

Table 20. Normalized first-slip time for loop with limiter

Margin, dB	ρ	ρ, dB	r	Tw_{L_0}	Tw_{L_0}, dB
0.000	2.000	3.001	2.000	25.12	14.00
1.000	2.328	3.659	2.244	34.53	15.38
2.000	2.703	4.305	2.518	51.28	17.10
3.000	3.130	4.939	2.825	83.09	19.20
4.000	3.614	5.562	3.170	148.57	21.72
5.000	4.164	6.175	3.557	296.83	24.72
6.000	4.786	6.778	3.991	671.67	28.27
7.000	5.490	7.372	4.477	1747.81	32.42
8.000	6.285	7.957	5.024	5317.84	37.26
9.000	7.181	8.534	5.637	19271.53	42.85

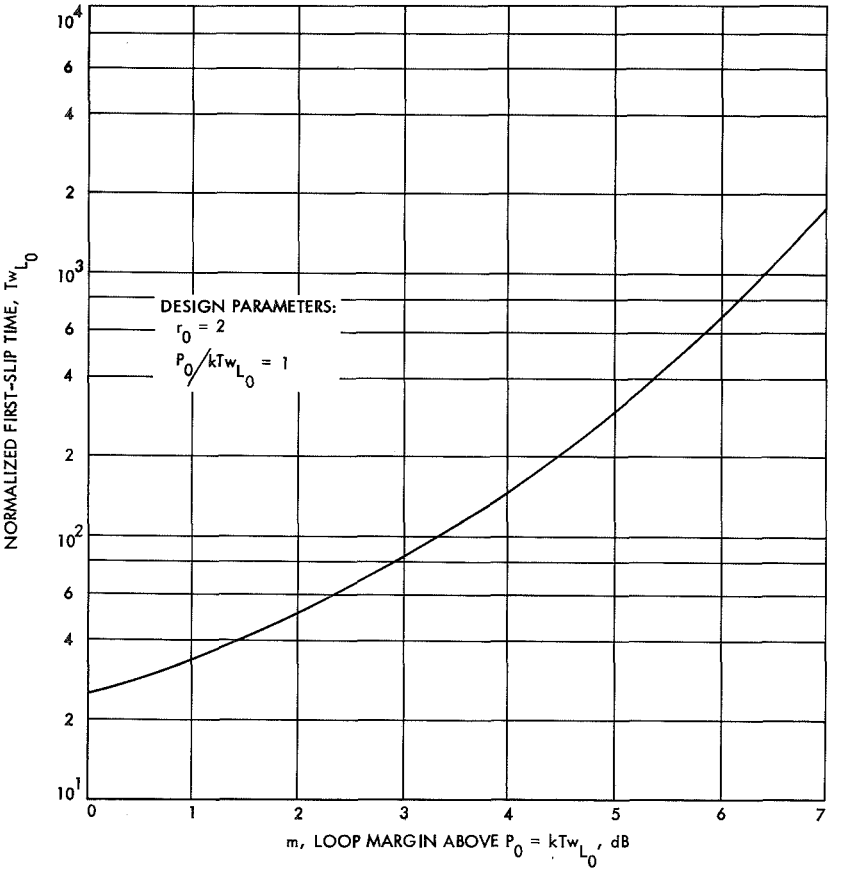

Fig. 30. Normalized first-slip time of a phase-locked loop with limiter

The obvious conclusion from this is that T is much quicker to estimate within a given *percent* than it is *absolutely*, when $T > 1$.

References

1. Tausworthe, R. C., "Cycle Slipping in Phase Locked Loops," *IEEE Trans. Commun. Technol.*, Vol. COM-15, No. 3, pp. 417–421, Jun. 1967.

2. Tausworthe, R. C., *Theory and Practical Design of Phase-Locked Receivers, Vol. I*, Technical Report 32-819. Jet Propulsion Laboratory, Pasadena, Calif., Feb. 15, 1966.

3. Digital Telemetry and Command: Steady-State Phase Probability Density of Cascaded Phase-Locked Loops,

W. C. Lindsey[15]

a. Introduction. Based upon methods outlined in Ref. 1, we present here the steady-state probability density function of a phase measurement made by two first-order phase-locked loops in cascade. In Ref. 2, it was shown that the joint probability density function $p(\hat{\theta}_1,\hat{\theta}_2)$ of the phase estimate $\hat{\theta}_1$ of θ_1 in loop one and the phase estimate $\hat{\theta}_2$ of θ_2 in loop two satisfies the Fokker–Planck equation (zero detuning assumed in both loops):

$$-A_1K_1\frac{\partial}{\partial\hat{\theta}_1}\left[\sin\hat{\theta}_1 p_{\hat{\theta}}\right] - A_2K_2\frac{\partial}{\partial\hat{\theta}_2}\left[\sin(\hat{\theta}_2-\hat{\theta}_1)p_{\hat{\theta}}\right] + \frac{K_1^2N_{01}}{4}\frac{\partial^2 p_{\hat{\theta}}}{\partial\hat{\theta}_1^2} + \frac{K_2^2N_{02}}{4}\frac{\partial^2 p_{\hat{\theta}}}{\partial\hat{\theta}_2^2} = \frac{\partial p_{\hat{\theta}}}{\partial t} \tag{1}$$

where $p_{\hat{\theta}} = p(\hat{\theta}_1,\hat{\theta}_2,t)$. In Eq. (1), A_k^2, $k = 1$ or 2, represents the power received in the respective loops, K_k represents their respective loop gains. N_{0k} represents the single-sided spectral densities of the white gaussian noise sources perturbing the inputs to the two loops.

b. The new result. Integration of both sides of Eq. (1) with respect to $\hat{\theta}_1$ from 0 to π and use of the boundary condition $p(\pi,\hat{\theta}_2,t) = p(-\pi,\hat{\theta}_2,t)$ gives

$$-A_2K_2\frac{\partial}{\partial\hat{\theta}_2}\left\{[A\sin\hat{\theta}_2 - B\cos\hat{\theta}_2]p(\hat{\theta}_2,t)\right\} + \frac{N_{02}K_2^2}{4}\frac{\partial^2}{\partial\hat{\theta}^2}p(\hat{\theta}_2,t) = \frac{\partial p(\hat{\theta}_2,t)}{\partial t} \tag{2}$$

where

$$A = E[\cos\hat{\theta}_1,t|\hat{\theta}_2], \qquad B = E[\sin\hat{\theta}_1,t|\hat{\theta}_2]$$

and $E[\cdot]$ denotes the expectation operator. In the steady-state, the solution to Eq. (2) is

$$p(\hat{\theta}_2) = \frac{\exp\left[\alpha_2(A^2+B^2)^{1/2}\cos\left(\hat{\theta}_2 - \tan^{-1}\frac{B}{A}\right)\right]}{2\pi I_0[\alpha_2(A^2+B^2)^{1/2}]}, \qquad |\hat{\theta}_2| \le \pi \tag{3}$$

where we have made use of the boundary condition $p(\pi) = p(-\pi)$, and where $\alpha = 4A_2/K_2N_{02}$. If, for example, $N_{01} = 0$, then Eq. (3) reduces to the well-known Tikhonov (Ref. 3) distribution, i.e.,

$$p(\hat{\theta}_2) = \frac{\exp[\alpha_2\cos\hat{\theta}_2]}{2\pi I_0(\alpha_2)}, \qquad |\hat{\theta}_2| \le \pi \tag{4}$$

since $B = 0$, $A = 1$. The parameter α_2 is the loop signal-to-noise ratio (Ref. 1). The solution, therefore, requires knowledge of the conditional expectations, which may be approximated or measured by computer simulation.

The utility of the above results becomes obvious when one considers the complexity of the equipment (Ref. 4) and the amount of time required to measure only a few of the many statistical parameters at work in the loop in DSIF receivers, e.g., mean square phase-error or mean time to first loss of synchronization. On the other hand, the amount of time required to measure the conditional expectations A and B via computer simulation methods is not necessarily prohibitive. Once these expectations are

[15]Consultant, Electrical Engineering Department, University of Southern California, Los Angeles, California.

measured or approximated, the validity of the model distributions discussed in Ref. 5 can be checked.

References

1. Lindsey, W. C., *Nonlinear Analysis and Synthesis of Generalized Tracking Systems, Part I,* Technical Report 317. Department of Electrical Engineering, University of Southern California, Los Angeles, Calif., Oct. 1968 (Pending publication in the IEEE Proceedings).
2. Lindsey, W. C., and Weber, C. L., "On the Theory of Automatic Phase Control," in *Stochastic Optimization and Control,* pp. 101–133. John Wiley & Sons, Inc., New York, N. Y., 1968.
3. Tikhonov, V. I., "The Effects of Noise on Phase-Lock Oscillation Operation," *Automatika i Telemekhanika,* Vol. 22, No. 9, 1959.
4. Charles, F. J., and Lindsey, W. C., "Some Analytical and Experimental Phase-Locked Loop Results for Low Signal-to-Noise Ratios," *Proc. IEEE,* Vol. 55, No. 9, pp. 1152–1166, Sep. 1966.
5. Lindsey, W. C., *A Theory for the Design of One-Way and Two-Way Coherent Communication Systems,* Technical Report 32-986. Jet Propulsion Laboratory, Pasadena, Calif. (to be published).

4. Information Systems: Efficiency of S/N Ratio Estimator, G. Lorden[16]

a. Introduction. The large-sample efficiency of the bit signal-to-noise (S/N) ratio estimator described by Layland (SPS 37-48, Vol. III, pp. 209–212) is found for arbitrary S/N ratio.

b. A bound on the accuracy of any S/N estimator. Let $y(t)$ be the received base-band signal, $\hat{\tau}_i$ the estimated data transition time at the start of the ith bit, and

$$I_i = \int_{\hat{\tau}_i}^{\hat{\tau}_{i+1}} y(t)dt$$

the ith data bit integral. A bit S/N estimator is based on the n most-recent data bit integrals, which are assumed to be independent random variables of the form $Y + Z$, where Y represents the transmitted signal and equals $\pm M$ ($M > 0$) with equal probabilities, while Z (independent of Y) is normally distributed with mean zero and variance σ^2. The most efficient scheme for estimating the S/N ratio M/σ would involve determining the transmitted plus-and-minus sequence (assuming reliable decoding is available), thus converting the data to samples from a normal population. The gain in efficiency is outweighed, however, by other considerations, such as the desirability of having an estimator which is available quickly to indicate changes in the S/N ratio, without the time lag required to obtain and make use of the decoded message.

The data bit integrals each have probability density

$$f_{\rho,\sigma}(x) = \frac{1}{(2\pi)^{1/2}\sigma}\left\{\frac{1}{2}\exp\left[-\frac{1}{2}\left(\frac{x}{\sigma}-\rho\right)^2\right] + \frac{1}{2}\exp\left[-\frac{1}{2}\left(\frac{x}{\sigma}+\rho\right)^2\right]\right\}$$

where ρ is the S/N ratio M/σ.

We will investigate the asymptotic efficiency of the estimator S_n described by Layland (SPS 37-48, Vol. III) by looking at the asymptotic normal distribution of $(n)^{1/2}(S_n - \rho)$ and comparing its variance $V(\rho)$ with a lower pound $V^*(\rho)$ on the asymptotic variance of any estimator. We first compute $V^*(\rho)$ by applying an inequality (Ref. 1, p. 266), based on the so-called information numbers

$$I_{\rho\sigma} = E\left[-\frac{\partial^2 \log f_{\rho,\sigma}(X)}{\partial\rho\,\partial\sigma}\right], \qquad I_{\sigma\rho} = E\left[-\frac{\partial^2 \log f_{\rho,\sigma}(X)}{\partial\sigma\,\partial\rho}\right]$$

$$I_{\sigma\sigma} = E\left[-\frac{\partial^2 \log f_{\rho,\sigma}(X)}{\partial\sigma^2}\right], \qquad I_{\rho\rho} = E\left[-\frac{\partial^2 \log f_{\rho,\sigma}(X)}{\partial\rho^2}\right]$$

[16]Consultant, Mathematics Department, California Institute of Technology, Pasadena, California.

where E denotes the expectation computed under $f_{\rho,\sigma}$. This inequality establishes that

$$V(p) \geq V^*(\rho) = I_{\sigma\sigma}\,(I_{\rho\rho}\,I_{\sigma\sigma} - I_{\rho\sigma}\,I_{\sigma\rho})^{-1}$$

and we obtain from the definitions

$$I_{\rho\rho} = E\,(Z + \rho)^2\,\mathrm{sech}^2 \mid \rho Z + \rho^2 \mid - 1$$

$$I_{\sigma\sigma} = \frac{1}{\sigma^2}\,[-2 - 3\rho^2 + \rho^2\,E\,(Z + \rho)^2\,\mathrm{sech}^2 \mid \rho Z + \rho^2 \mid + 2\rho\,E \mid \rho + Z \mid \tanh \mid \rho^2 + \rho Z \mid]$$

$$I_{\rho\sigma} = I_{\sigma\rho} = \frac{1}{\sigma}\,[-\rho\,E(Z + \rho)^2\,\mathrm{sech}^2 \mid \rho Z + \rho^2 \mid - E \mid \rho + Z \mid \tanh \mid \rho^2 + \rho Z \mid]$$

where the expectations are now computed with Z, a standard normal random variable. Note that $V^*(\rho)$ is independent of σ.

The values of $V^*(\rho)$ were computed for values of ρ in the range 0.1 to 10.0. The results are shown in Table 21.

c. The efficiency of the estimator S_n. In the strong signal case, ρ is large and the $|X_i|$'s are approximately normal with mean $\rho\sigma$ and variance σ^2. In this case, the estimator

$$R_n = \frac{\dfrac{1}{n}\sum_1^n |X_i|}{\left[\dfrac{1}{n}\sum_1^n X_i^2 - \left(\dfrac{1}{n}\sum_1^n |X_i|\right)^2\right]^{1/2}}$$

is nearly optimal for large n, since it is the maximum likelihood estimator if we assume the $|X_i|$'s are exactly normal (Ref. 2).

Table 21. Values of $V^*(\rho)$, $V(\rho)$, and $V^*(\rho)/V(\rho)$ for values of ρ

ρ	$V^*(\rho)$	$V(\rho)$	$V^*(\rho)/V(\rho)$
0.1585	0.1157×10^4	0.4386×10^5	0.0264
0.2512	0.9402×10^3	0.3154×10^4	0.2981
0.3981	0.1841×10^3	0.2682×10^3	0.6865
0.6310	0.2704×10^2	0.3226×10^2	0.8384
1.0000	0.6759×10^1	0.7151×10^1	0.9453
1.5849	0.3665×10^1	0.3696×10^1	0.9915
2.5119	0.4398×10^1	0.4407×10^1	0.9978

For small ρ, however, R_n is badly biased and converges in probability to a limit larger than ρ. Layland (SPS 37-48, Vol. III) determined the asymptotic bias of $\frac{1}{2}R_n^2$ as an estimator of $\frac{1}{2}\rho^2$ and proposed correcting the bias by using the estimator $R^{-1}\,(\frac{1}{2}R_n^2)$, where R is the asymptotic expected value of $\frac{1}{2}R_n^2$, as a function of $\frac{1}{2}\rho^2$.

To determine the large sample efficiency of the corresponding estimator of ρ, we consider the asymptotic normal distribution of

$$(n)^{1/2}\left(\frac{\theta_n^2}{\beta_n} - \frac{\theta^2}{\beta}\right)$$

where

$$\theta_n = \frac{1}{n}\sum_1^n |X_i|\,, \qquad \beta_n = \frac{1}{n}\sum_1^n X_i^2$$

and

$$\theta = E|X_i|\,, \qquad \beta = E\,X_i^2$$

First, we apply the multivariate central limit theorem (Ref. 1, p. 118) to determine that the random vector

$$(n)^{1/2}\,(\theta_n - \theta, \beta_n - \beta)$$

is asymptotically bivariate normal with mean zero and covariance matrix

$$\lim_{n\to\infty} n \begin{bmatrix} \mathrm{var}\,\theta_n & \mathrm{cov}\,(\theta_n, \beta_n) \\ \mathrm{cov}\,(\theta_n, \beta_n) & \mathrm{var}\,\beta_n \end{bmatrix}$$

By straightforward calculation, we obtain

$$\lim_{n\to\infty} n \operatorname{var} \theta_n = 4\theta^2(\beta - \theta^2)$$

$$\lim_{n\to\infty} n \operatorname{var} \beta_n = \alpha - \beta^2$$

and

$$\lim_{n\to\infty} n \operatorname{cov}(\theta_n, \beta_n) = 2\theta(\gamma - \beta\theta)$$

where

$$\gamma = E\,|X_i|^3 \text{ and } \alpha = E\,X_i^4$$

We now apply the following theorem (Ref. 1, p. 321): If the asymptotic distribution of

$$(n)^{1/2}(T_n^1 - \theta_1, \cdots, T_n^k - \theta_k)$$

is k-variate normal with mean zero and covariance matrix $||\sigma_{ij}||$, then the asymptotic distribution of

$$(n)^{1/2}[g(T_n^1, \cdots, T_n^K) - g(\theta_1, \cdots, \theta_k)]$$

is normal with mean zero and variance

$$V(\theta_1, \cdots, \theta_k) \neq \sum_{i,j} \sigma_{ij} \frac{\partial g}{\partial \theta_j} \frac{\partial g}{\partial \theta_i}$$

provided $V(\theta_1, \cdots, \theta_k) = 0$ and g is totally differentiable in a neighborhood of $(\theta_1, \cdots, \theta_k)$.

Using $g(\theta, \beta) = \theta^2/\beta$, we observe that

$$(n)^{1/2}\left(\frac{\theta_n^2}{\beta_n} - \frac{\theta^2}{\beta}\right)$$

is asymptotically normal with mean zero and variance

$$V = \left(\frac{\theta^2}{\beta}\right)^2 \left(\frac{\alpha}{\beta^2} - 1\right) - 4\frac{\theta^2}{\beta}\left(\frac{\theta\gamma}{\beta^2} - 1\right)$$

Letting

$$I_0(\rho) = \int_0^\rho \frac{1}{(2\pi)^{1/2}} e^{-t^2/2}\, dt$$

and

$$\phi(\rho) = \frac{1}{(2\pi)^{1/2}} e^{-\rho^2/2}$$

we find that

$$\frac{\theta^2}{\beta} = \frac{4[\rho I_0(\rho) + \phi(\rho)]^2}{1 + \rho^2} \triangleq h(\rho)$$

Since h is an increasing function, it has an inverse and, applying the theorem above,

$$(n)^{1/2}\left[h^{-1}\left(\frac{\theta_n^2}{\beta_n}\right) - \rho\right] =$$

$$(n)^{1/2}\left[h^{-1}\left(\frac{\theta_n^2}{\beta_n}\right) - h^{-1}\left(\frac{\theta^2}{\beta}\right)\right]$$

is asymptotically normal with mean zero and variance

$$\frac{V}{[h'(\rho)]^2}$$

with

$$V = h^2(\rho)\left(\frac{\alpha}{\beta^2} - 1\right) - 4h(\rho)\left(\frac{\theta\gamma}{\beta^2} - 1\right)$$

By further calculation, we get

$$\frac{\alpha}{\beta^2} - 1 = \frac{4\rho^2 + 2}{(1 + \rho^2)^2}$$

$$h'(\rho) = \frac{8(1 - \rho^2) I_0(\rho)\phi(\rho) + 8\rho[I_0^2(\rho) - \phi^2(\rho)]}{(1 + \rho^2)^2}$$

and

$$\frac{\theta\gamma}{\beta^2} - 1 = -1 + (1 + \rho^2)^{-2}[(4\rho^4 + 12\rho^2) I_0^2(\rho)$$

$$+ (4\rho^2 + 8)\phi^2(\rho) + (8\rho^3 + 20\rho) I_0(\rho)\phi(\rho)]$$

The asymptotic variance of

$$S_n = h^{-1}\left(\frac{\theta_n^2}{\beta_n}\right)$$

was computed for the same values of ρ as were used for $V^*(\rho)$ above. The resulting values of $V(\rho)$ and of the asymptotic efficiency $V^*(\rho)/V(\rho)$ are shown in Table 21 and graphed in Fig. 31. Note that the efficiency approaches one as ρ gets large and approaches zero as ρ approaches zero.

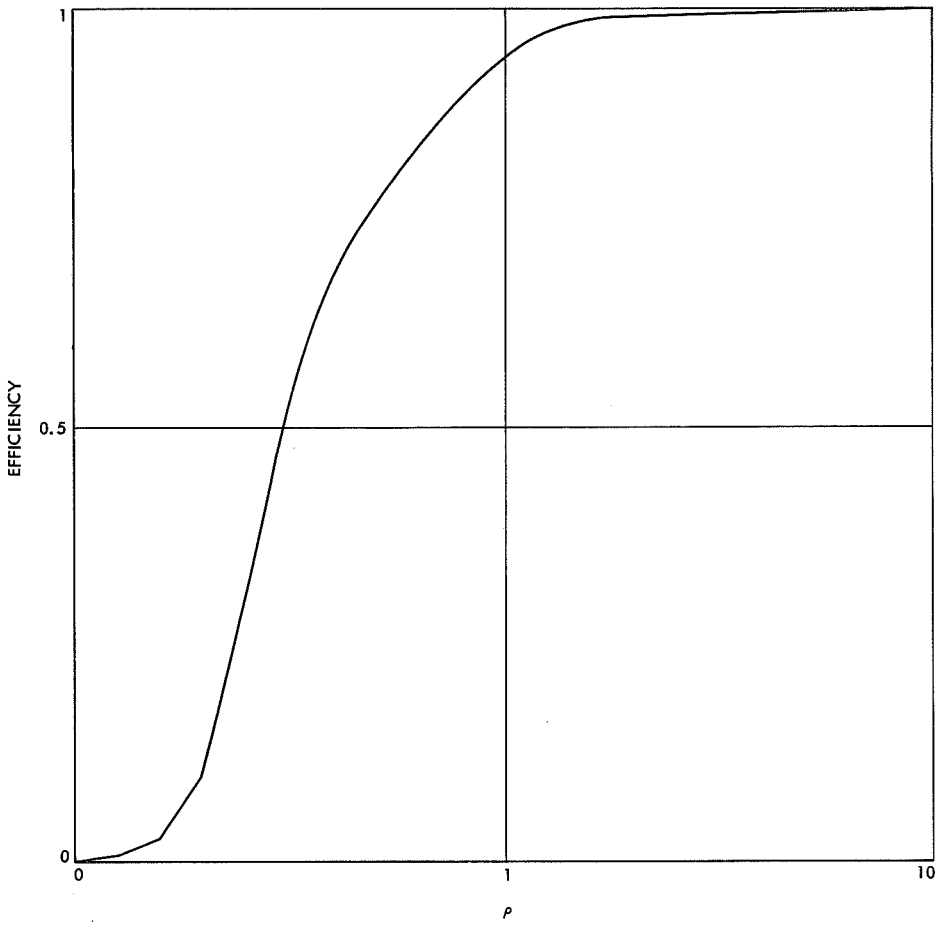

Fig. 31. Efficiency vs ρ

References

1. Rao, C. R., *Linear Statistical Inference and its Applications.* John Wiley & Sons, Inc., New York, N. Y., 1965.

2. Gagliardi, R. M., and Thomas, C. M., "PCM Data Reliability Monitoring Through Estimation of Signal-to-Noise Ratio," *IEEE Trans. Commun. Technol.*, Vol. COM-16, No. 3, Jun. 1968.

C. Tracking and Data Acquisition Elements Research

1. Low-Noise Receivers: Microwave Maser Development,

R. Berwin, R. Clauss, and E. Wiebe

a. Introduction. Investigation of ruby and iron-doped rutile for 8- to 15.3-GHz maser application is in progress. Material samples are used as dielectric resonators and immersed in liquid helium at any desired temperature between 1.7 and 4.5°K. The spectrometer in use employs amplitude and phase sensitive detection at signal frequencies between 8 and 18 GHz. Measured values are: material linewidth, signal and pump power absorption, signal amplification, and amplification bandwidth. Pump frequencies up to 40 GHz are presently in use. Computed energy levels and transition probabilities serve as a guide for crystal orientations having characteristics suitable for high-gain applications. An improved X-band maser is being designed.

b. Magnetic Q and computed values of transition probabilities. From first-order, time-dependent perturbation theory, the probability per unit time that an applied signal will induce a transition from state i to state j of a spin system in a magnetic field H is given by

$$W_{ij} = \frac{1}{4}\gamma^2\rho(f)|\langle i|H^* \cdot S|j\rangle|^2 \qquad (1)$$

where $\gamma = g\beta\mu_0/\hbar$, β = Bohr magneton, g = gyromagnetic ratio, μ_0 = permeability of free space, and $\rho(f)$ = density of states (Ref. 1). If $\rho(f)$ is a slowly varying

function of energy, the matrix element $<i|H^* \cdot S|j>$ determines the probability of transition. The term $H^* \cdot S$ is a total energy operator that is proportional to the energy of the ion in a magnetic field. It is the spin Hamiltonian and, in the general case, includes terms that take into account internal fields due to the crystalline structure. Defining $\sigma_{ij} = <i|S|j>$, Eq. (1) becomes

$$W_{ij} = \frac{1}{4}\gamma^2\rho(f)\,|H^* \cdot \sigma_{ij}|^2 = \frac{1}{4}\gamma^2\rho(f)\,(H^* \cdot \sigma\sigma^* \cdot H) \tag{2}$$

where $\sigma\sigma^*$ is a dyadic product (Ref. 2, p. 178).

The magnetic Q of the maser material is defined as

$$Q_m = \frac{2\pi f_{ij} W}{P_m}$$

where W is the energy stored in the cavity (dielectric resonator), and P_m is the power emitted by the material spins. Using Eq. (2) and $P_m = hf_{ij}W_{ij}\Delta n_{ij}$,

$$\frac{1}{Q_m} = \frac{1}{4}\hbar\,\gamma^2\Delta n_{ij}\rho(f)\,\frac{\int H^* \cdot \sigma\sigma^* \cdot HdV}{\int H^* \cdot HdV} \tag{3}$$

where the integration is over the maser material volume in the case of a dielectric resonator, and Δn_{ij} is the inverted population difference between levels i and j.

In Eq. (3), Q_m^{-1} can be expressed in terms of an inversion ratio, transition probability matrix elements, filling factor, and material linewidth in the following way: the inversion ratio $I = \Delta n_{ij}/\Delta N_{ji}$, where ΔN_{ji} is the thermal equilibrium population difference. The integral terms in Eq. (3) can be interpreted as taking into account the fraction of the RF field in the resonator which is optimum for transitions.

Then

$$\frac{\int H^* \cdot \sigma\sigma^* \cdot HdV}{\int H^* \cdot HdV} = \eta\sigma^2$$

where σ is the maximum value of the transition probability if all the spins in the crystal were optimized with the RF field, and η is the filling factor that varies from 0 to 1. At microwave frequencies,

$$\Delta N_{ji} \approx \frac{hf_{ij}}{kT}\,\frac{N}{n}$$

where N is the density of spins, and n is the number of energy levels over which the spins are distributed. In terms of a Lorentzian line shape with linewidth Δf_L (Ref. 2, p. 255),

$$\frac{1}{Q_m} = \frac{2g^2\beta^2\mu_0}{h}\,\frac{hf}{kT}\,\frac{N}{n}\,\frac{I\sigma^2\eta}{\Delta f_L} \tag{4}$$

Siegman has shown that the midband power gain of a cavity maser for high gain is proportional to $1/Q_m$. Equation (4) shows the important relationship that the gain is proportional to the transition probability matrix elements $\sigma^2\eta$, and inversely proportional to the linewidth and temperature.[17] The transition probability matrix elements and the energy levels were computed on the IBM 7094 (SPS 37-55, Vol. II, pp. 44–45), using the spin Hamiltonians given by Siegman (Ref. 2) for ruby and by Carter and Okaya (Ref. 3) for iron-doped rutile.

c. Figure of merit for materials. A figure of merit applicable to materials for future traveling-wave maser (TWM) applications should relate to the gain and bandwidth capability of the maser material. The interpretation of computed transition probabilities and energy levels as a guide for material selection depends upon the relationship between the computed values and the figure of merit.

In a TWM the gain expression shows the importance of a low magnetic Q (Q_m).

$$G_{dB} = \frac{27.3\,SN}{Q_m} \tag{5}$$

where

G_{dB} = electronic gain, dB

S = TWM slowing factor

N = TWM length in wavelengths

The TWM amplification bandwidth is related directly to the material linewidth (Δf_L).

[17]Refer to Siegman (Ref. 2, p. 255) for a more thorough discussion of the relationship among the quantities in Eq. (4).

$$\Delta f = \Delta f_L \left(\frac{3}{G_{dB} - 3} \right)^{1/2} \quad (6)$$

where

Δf = ½ power amplification bandwidth

Broadbanding techniques must be used when the material linewidth does not result in sufficient amplification bandwidth. The gain reduction occurring with artificial line broadening is discussed by Siegman (Ref. 2). Previous experience with stagger-tuning of the resonance line (SPS 37-45, Vol. III, pp. 40–42) supports the relationship

$$G_{dB} = \frac{k\ell}{\Delta f_L} \quad (7)$$

where

$\ell = SN$ = circuit length

k = a constant, characteristic of maser material

The indicated linear trade-off between circuit length and resonance linewidth for constant gain (Eq. 7) and the gain expression (Eq. 5) lead to the use of $\Delta f_L/Q_m$ as a figure of merit for a maser material.

Inversion ratios calculated for the optimum case are compared with measured inversion ratios as a function of temperature. This information is useful when comparing samples of different doping.

Investigation of the sample material in the form of a dielectric resonator simplifies the evaluation process. Resonator dimensions and crystal orientation are arranged to support RF field components in the direction of maximum transition probability-fill factor product.

The magnetic Q (Q_m) is obtained from the midband gain expression for a reflection cavity maser:

$$G_0 = \left(\frac{\frac{1}{Q_e} + \frac{1}{Q_m}}{\frac{1}{Q_e} - \frac{1}{Q_m}} \right)^2 \quad (8)$$

where

G_0 = power-gain ratio

Q_e = resonator external Q

The figure of merit $\Delta f_L/Q_m$ for each sample is obtained from three measured values: gain, cavity Q, and material linewidth.

d. Cryogenics. A versatile cryogenic system is used to test maser materials. Ease of use at temperatures between 1.7 and 4.5°K is accomplished with a cryogenic "well" cooled by a closed cycle helium refrigerator (CCR). Important features are:

(1) Easy access. The sample is immersed in liquid helium and can be installed or removed in a matter of minutes.

(2) Rapid cooling of sample. The CCR runs continuously, maintaining 0.7 liter of liquid helium at 4.5°K. This quantity of helium is sufficient to cool a sample to 4.5°K in minutes.

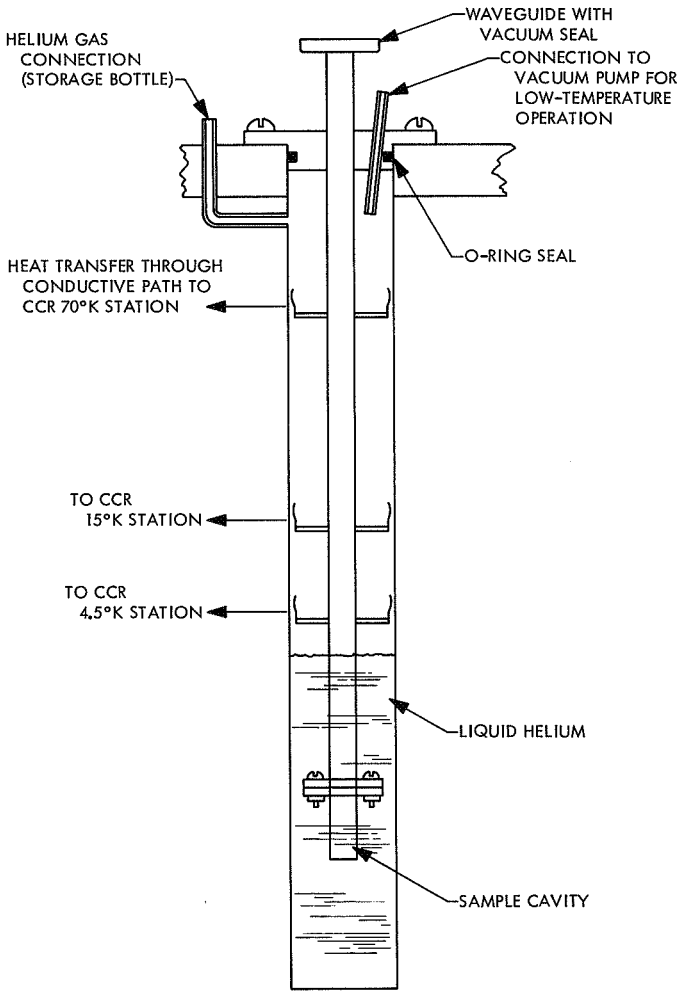
WAVEGUIDE WITH VACUUM SEAL
HELIUM GAS CONNECTION (STORAGE BOTTLE)
CONNECTION TO VACUUM PUMP FOR LOW-TEMPERATURE OPERATION
O-RING SEAL
HEAT TRANSFER THROUGH CONDUCTIVE PATH TO CCR 70°K STATION
TO CCR 15°K STATION
TO CCR 4.5°K STATION
LIQUID HELIUM
SAMPLE CAVITY

Fig. 32. Cryogenic well

(3) Rapid heat transfer from sample during test. Liquid helium is in contact with the sample.

(4) Liquefies helium gas. There is no need to store and transfer liquid helium.

(5) Long life. The CCR is of the same basic design that has demonstrated 9000 h of operation between mechanical maintenance periods (Ref. 4).

(6) Small size. The CCR assembly is contained in a 9-in.-diam by 12-in.-long housing. A drive motor extends 7 in. above the housing. The well extends below the housing into the 3-in. gap, between 12-in.-diam pole pieces, of a 10-kG electromagnet. The CCR compressor operates remotely.

The helium gas supplied for liquefaction to the well is independent of the gas system for the CCR. Helium gas, from a storage bottle, enters the cryogenic well at the top (Fig. 32). Cooling and liquefaction is accomplished by heat removal and conductive heat transfer to the three stages of the CCR.

Heat leak into the well has been minimized by vacuum insulation and by radiation shielding at 70°K. Measurements of liquid temperature (1.7 to 2.0°K during "sealed" well operation) indicate a heat leak of 12 mW. Operation at temperatures below 4.5°K is accomplished by reduction of gas pressure in the well. Evacuation through the well cover causes cooling (to as low as 1.7°K) by evaporation. The system can be used at 1.7°K until the well is empty (35 h continuous operation). When empty, the well returns to the 4.5°K CCR temperature and requires 4 h to fill with liquid.

e. Experimental results. Data have been recorded at 1.7 and 4.5°K, using magnetic fields between 0 and 10 kG and pump frequencies between 26 and 40 GHz. The signal frequency range is 8 to 18 GHz. Evaluation of ruby and rutile is in progress within the above limitations.

Table 22 presents data obtained in orientations that showed promise on the basis of computed transition probabilities. The present pump frequency range eliminates investigation of several favorable orientations of rutile. Ruby samples of excellent crystal quality were tested at the push–pull pumping angle (54.7 deg). The resulting inversion ratio for 0.05% Cr_2O_3 ruby is in excellent agreement with the calculated inversion ratio.

f. Conclusions. Rutile performance suffered from poor inversion ratios. The narrow linewidth measured also degraded the figure of merit. Transition probabilities for

Table 22. Computed and measured material characteristics

Parameter	Ruby	Ruby	Ruby	Ruby	Rutile	Rutile
Doping, %	0.05	0.05	0.075	0.075	0.035	0.035
Orientation, deg	65.7	54.7	54.7	54.7	$\theta = 25$ $\phi = 5$	$\theta = 25$ $\phi = 5$
Signal transition	3–4	2–3	2–3	2–3	1–2	1–2
Pump transition	2–4 (1–2 = 2–3)	1–3, 2–4	1–3, 2–4	1–3, 2–4	1–3	1–3
Magnetic field, G	4485	6780	5720	5560	5700	5710
Signal frequency, GHz	17.2	17.2	14.4	13.9	14.8	14.9
Pump frequency, GHz	29.9	38.0	32.9	32.0	38.0	38.1
Calculated inversion ratio	2.5	3.4	3.6	3.6	1.6	1.6
Measured inversion ratio	0.9	3.3	2.8	3.0	0.40	0.5
Temperature, °K	4.5	4.5	4.5	1.8	4.5	1.8
Q_m (measured)	140	53	37	10.5	130	34
Δf_L (measured), MHz	60	60	60	60	20	20
$\Delta f_L/Q_m$ (merit), MHz	0.43	1.13	1.62	5.7	0.15	0.59
Signal transition probability	2.0	1.88	1.85	1.84	2.0	2.0

rutile that require pump frequencies above 40 GHz are favorable and further investigation is necessary. Ruby displays excellent inversion ratios, good linewidth, and an inverse magnetic Q that exceeds values previously measured at 2300 and 8500 MHz (SPS 37-46, Vol. III, pp. 67–72, and SPS 37-42, Vol. III, pp. 42–46).

References

1. Schiff L. I., *Quantum Mechanics*, Second Edition, p. 199. McGraw-Hill Book Co., Inc., New York, 1955.
2. Siegman, A. E., *Microwave Solid. State Masers*, McGraw-Hill Book Company, Inc., New York, 1964.
3. Carter, D. L., and Okaya, A., "Electron Paramagnetic Resonance of Fe^{3+} in TiO_2 (Rutile)," *Phys. Rev.*, Vol. 118, No. 6, p. 1485, June 15, 1960.
4. Higa, W. H., and Wiebe, E., "A Simplified Approach to Heat Exchanger Construction for Cryogenic Refrigerators,' *Cryogenic Technology*, Vol. 3, No. 2, p. 15, Mar.–Apr. 1967.

2. Design of an Operational Atomic Hydrogen Frequency Standard, *H. Erpenbach and C. Finnie*

a. Introduction. The *Mariner* Mars 1969 mission will provide an opportunity for field testing of two hydrogen masers as frequency standards at DSS 14. The design goals of the masers, which are now being fabricated, are to provide stabilities of the order of one part in 10^{13} for short (1 s) and long terms (days to weeks) with reliability over long periods of weeks and months.

b. Physics of the hydrogen maser. A complete theory of the hydrogen maser is available in Ref. 1. The summary given here is intended only to make the discussion on the design more meaningful.

Figure 33 shows a schematic view of the maser. Hydrogen gas is admitted at the bottom of the device to a dissociator, where molecular hydrogen is converted into atomic hydrogen by an RF discharge. The atomic hydrogen emerges vertically through the collimator and enters the hexapole focusing magnet, where the proper state atoms are focussed while others are defocussed.

The excited atoms then enter a Teflon-coated quartz bulb which is mounted in the resonant cavity. The Teflon film allows the hydrogen atoms to bounce many times without disturbing its quantum state. Hence, the atoms interact with the RF magnetic field in the cavity for nearly a second before escaping through the entry. Some of the atoms make the proper transition from the $F = 1$, $M = 0$ state to the $F = 0$, $M = 0$ state and emit energy at 1420 MHz.

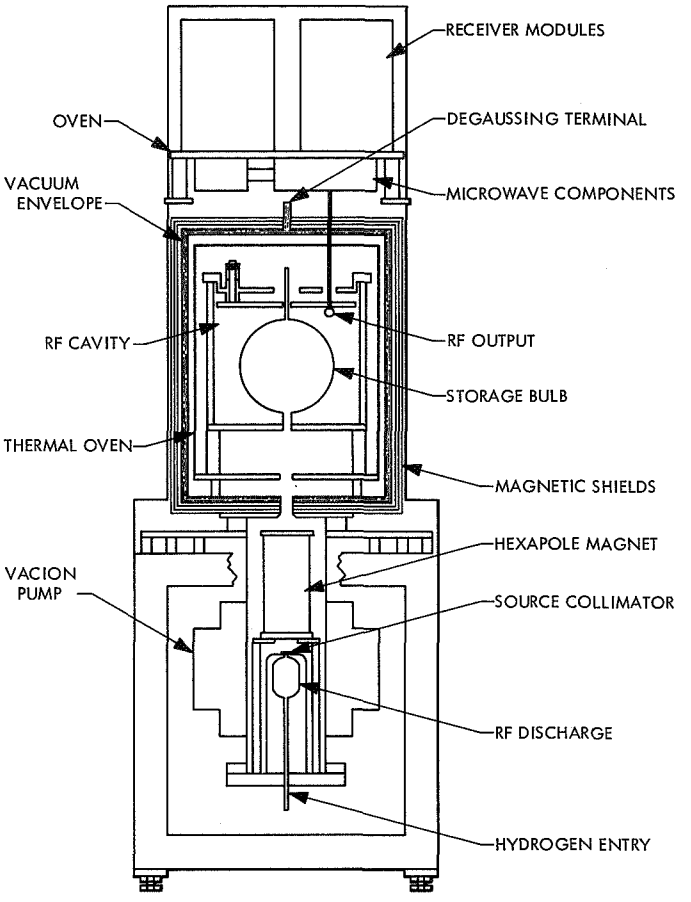

Fig. 33. Schematic view of atomic hydrogen maser

The spent hydrogen gas is pumped out by the vacion pump which maintains the proper high-vacuum environment for the hydrogen beam. Proper operation of the maser also requires careful control of the temperature of the cavity and maintenance of a weak but constant and uniform magnetic field in the region of the quartz storage bulb.

c. Design features. A description of a commercially available hydrogen frequency standard is given in Ref. 2. The principal deviation here, in order to achieve a fieldworthy device, was to provide ready accessibility to all components of the system. Most of the control electronics modules have been removed to a rack for easy servicing and maintenance. (The electronics modules are being designed and fabricated by the JPL Communications Systems Research Section.)

The disposition of the cavity is an innovation and is inverted for ready accessibility from the top. The location of the output coupling loop at the top poses a mechanical stability problem, but with adequate caution it should not cause difficulties. The microwave components are mounted in a temperature-controlled compartment adjacent to the receiver modules.

The main oven has been enclosed inside the vacuum chamber to eliminate convective heat transfer. A secondary oven will be used to reduce the temperature gradient between the primary oven and the environment. In order to provide thermal stability, the cavities are made of Cer-Vit,[18] a material with a very low expansion coefficient.

[18]Tradename of material manufactured by Owens-Illinois, Inc., Toledo, Ohio.

The Cer-Vit cavities were coated with copper in accordance with the methods described in SPS 37-54, Vol. II, pp. 36–39. The thickness of the copper film deposited by high-vacuum evaporation techniques appears to be adequate and provides the necessary Q.

Figure 34 shows the front view of the masers. The upper cylinder contains the microwave components and receiver. The lower cylinder contains the maser cavity and associated components. The vacion pump is visible in the picture at the right.

Figure 35 shows the top view of the microwave cavity. The top plate contains the mechanical tuning devices as well as the output connector.

Current plans are to install two maser systems in an instrument van which will be located near the antenna

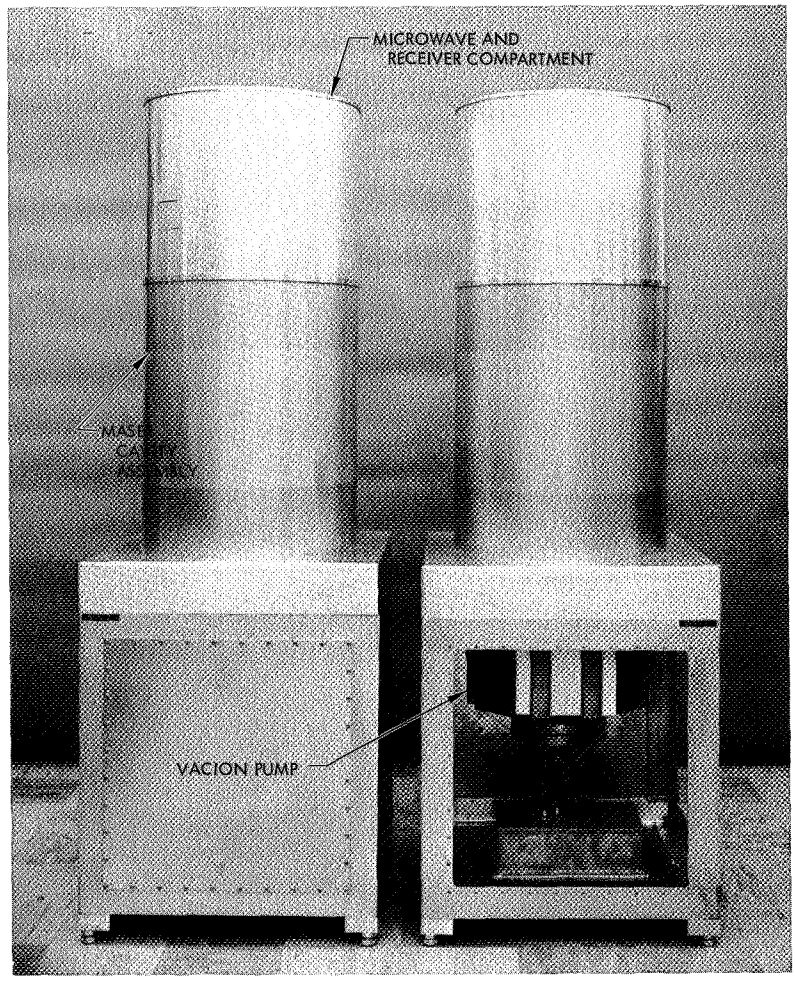

Fig. 34. Front view of maser assembly

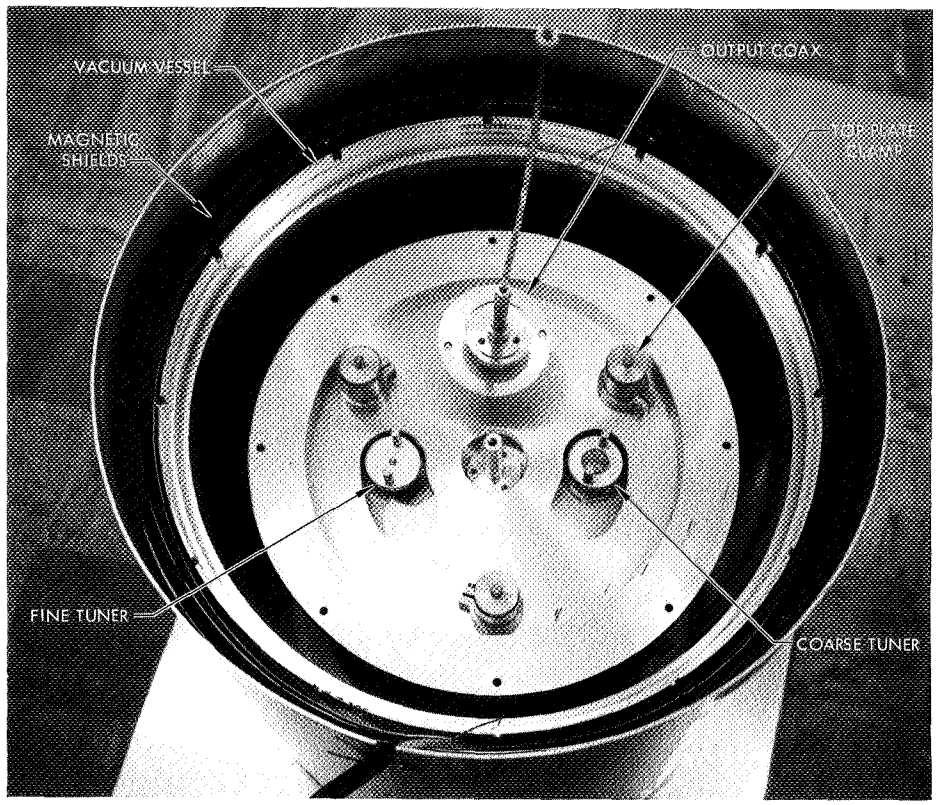

Fig. 35. Top view of maser cavity and other components

at DSS 14. Specific experiments to be performed during the *Mariner* Mars 1969 mission will be designed by the Inherent Accuracy Project.

References

1. Kleppner, D., Goldenberg, H. M., and Ramsey, N. F., "Theory of the Hydrogen Maser," *Phys. Rev.*, Vol. 126, No. 2, pp. 603–615, 1962.

2. Vessot, R. F. C., and Peters, H. E., "Design and Performance of an Atomic Hydrogen Maser," *IRE Trans.*, PG I-11, No. 3 and 4, p. 183, Dec. 1962.

3. Improved RF Calibration Techniques: Scattering Matrix of a Reduced Multiport, *T. Y. Otoshi*

a. Introduction. A microwave receiving system often contains a multiport (such as a directional coupler, polarizer, or hybrid junction) that has been calibrated in the laboratory. In the laboratory the multiport scattering parameters are usually evaluated under matched-load conditions. However, when the multiport is installed in the system, the terminations as seen looking out of the various ports are not generally matched.

For many system analysis problems, it is of interest to determine how the various load reflection coefficients affect the attenuation and phase shift of a signal that is transmitted through the multiport. If analysis is only required of the signal transmission between two of the ports on the multiport, the problem is more easily handled if an equivalent two-port scattering matrix can be derived in terms of (1) the original multiport scattering parameters, and (2) the reflection coefficients of the terminations on the auxiliary ports.

When some of the ports on a multiport are terminated with fixed loads so that these ports are not available, the multiport is sometimes referred to as a "reduced multiport" (Ref. 1). Numerous methods can be used for deriving the scattering parameters of a reduced multiport. Five methods, most of which have been described in literature, are: (1) the *algebraic method*, which involves substitutions and algebraic manipulations of the scattering equations (Ref. 2); (2) the *determinant method*, which involves solving for the desired ratios of voltage waves by use of determinants; (3) the *signal flow graph method* (Ref. 3); (4) the *multipole interconnection method* (Ref. 4); and (5) the *equivalent generator method* (Ref. 1). The

advantage of using one method over another depends upon the size of the multiport involved and also the user's familiarity with the procedures and rules associated with a given method.

The purpose of this article is to discuss a basic matrix method for deriving the equivalent scattering parameters of the reduced multiport. Due to the inherent compactness of matrix notation, all scattering parameters can be derived in an efficient manner even when the size of the multiport becomes large. The method described is similar to the *multipole interconnection method*[19] but is believed to be more convenient to use for solving this particular problem.

The method described in this article is restricted to the analysis of reduced multiports while the *multipole interconnection method* can be used for solving many types of multiport problems.

b. General case. Figure 36 shows an n-port waveguide junction that is to be reduced to an m-port by placing terminations on the ports numbered $m + 1$ through n. The a's and b's, respectively, represent the amplitudes of the voltage waves that travel toward and away from the multiport. To derive the scattering parameters of the equivalent m-port, begin by placing partitioning lines after the mth row and the mth column of the original n-port scattering equations as shown below.

$$\left[\begin{array}{c} b_1 \\ b_2 \\ \cdot \\ \cdot \\ \cdot \\ b_m \\ \hline b_{m+1} \\ \cdot \\ \cdot \\ \cdot \\ b_n \end{array}\right] = \left[\begin{array}{cccc:ccc} S_{11} & S_{12} & \cdots & S_{1m} & S_{1,m+1} & \cdots & S_{1n} \\ S_{21} & S_{22} & \cdots & S_{2m} & \cdot & \cdots & \cdot \\ \cdot & \cdot & \cdots & \cdot & \cdot & \cdots & \cdot \\ \cdot & \cdot & \cdots & \cdot & \cdot & \cdots & \cdot \\ \cdot & \cdot & \cdots & \cdot & \cdot & \cdots & \cdot \\ S_{m1} & S_{m2} & \cdots & S_{mm} & S_{m,m+1} & \cdots & S_{mn} \\ \hdashline S_{m+1,1} & \cdot & \cdots & S_{m+1,m} & S_{m+1,m+1} & \cdots & S_{m+1,n} \\ \cdot & \cdot & \cdots & \cdot & \cdot & \cdots & \cdot \\ \cdot & \cdot & \cdots & \cdot & \cdot & \cdots & \cdot \\ \cdot & \cdot & \cdots & \cdot & \cdot & \cdots & \cdot \\ S_{n1} & \cdot & \cdots & S_{nm} & S_{n,m+1} & \cdots & S_{nn} \end{array}\right] \left[\begin{array}{c} a_1 \\ a_2 \\ \cdot \\ \cdot \\ \cdot \\ a_m \\ \hline a_{m+1} \\ \cdot \\ \cdot \\ \cdot \\ a_n \end{array}\right] \tag{1}$$

[19]The *Multipole Interconnection Method* was brought to the author's attention by W. V. T. Rusch of USC and C. Finnie of JPL.

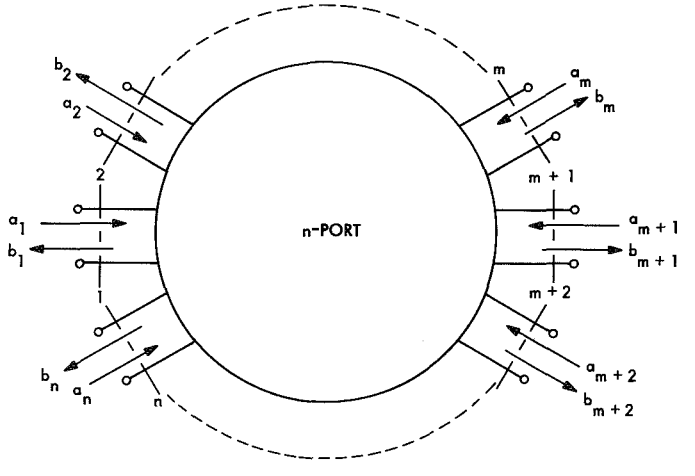

Fig. 36. Incident and emergent waves associated with an *n*-port waveguide junction

Equation (1) can then be written as

$$\left[\begin{array}{c} \mathbf{B}_1 \\ \hline \mathbf{B}_2 \end{array}\right] = \left[\begin{array}{c:c} \mathbf{P}_1 & \mathbf{P}_2 \\ \hdashline \mathbf{P}_3 & \mathbf{P}_4 \end{array}\right] \left[\begin{array}{c} \mathbf{A}_1 \\ \hline \mathbf{A}_2 \end{array}\right] \tag{2}$$

where

$$\mathbf{B}_1 = \begin{bmatrix} b_1 \\ b_2 \\ \cdot \\ \cdot \\ \cdot \\ b_m \end{bmatrix}, \qquad \mathbf{A}_1 = \begin{bmatrix} a_1 \\ a_2 \\ \cdot \\ \cdot \\ \cdot \\ a_m \end{bmatrix}$$

$$\mathbf{B}_2 = \begin{bmatrix} b_{m+1} \\ b_{m+2} \\ \cdot \\ \cdot \\ \cdot \\ b_n \end{bmatrix}, \qquad \mathbf{A}_2 = \begin{bmatrix} a_{m+1} \\ a_{m+2} \\ \cdot \\ \cdot \\ \cdot \\ a_n \end{bmatrix}$$

and $\mathbf{P}_1$, $\mathbf{P}_2$, $\mathbf{P}_3$, and $\mathbf{P}_4$ represent the partitioned submatrices of the original n-port scattering matrix.

By treating the partitioned submatrices as though they were matrix elements and performing the matrix multiplications of Eq. (2), we obtain

$$\mathbf{B}_1 = \mathbf{P}_1 \mathbf{A}_1 + \mathbf{P}_2 \mathbf{A}_2 \tag{3}$$

$$\mathbf{B}_2 = \mathbf{P}_3 \mathbf{A}_1 + \mathbf{P}_4 \mathbf{A}_2 \tag{4}$$

If the loads that terminate ports $m + 1$ through n have voltage reflection coefficients $\Gamma_{L,m+1}$ through Γ_{Ln}, respectively, then

$$\mathbf{A}_2 = \mathbf{\Gamma}_L \mathbf{B}_2 \tag{5}$$

where $\mathbf{\Gamma}_L$ is a diagonal matrix expressed as

$$\mathbf{\Gamma}_L = \begin{bmatrix} \Gamma_{L,m+1} & & & \\ & \Gamma_{L,m+2} & & \\ & & \ddots & \\ & & & \Gamma_{Ln} \end{bmatrix} \tag{6}$$

Substitutions of Eq. (5) into Eqs. (3) and (4) give

$$\mathbf{B}_1 = \mathbf{P}_1 \mathbf{A}_1 + \mathbf{P}_2 \mathbf{\Gamma}_L \mathbf{B}_2 \tag{7}$$

$$\mathbf{B}_2 = \mathbf{P}_3 \mathbf{A}_1 + \mathbf{P}_4 \mathbf{\Gamma}_L \mathbf{B}_2 \tag{8}$$

Obtaining the explicit relationship for $\mathbf{B}_2$ from Eq. (8) and substitution into Eq. (7) results in

$$\mathbf{B}_1 = {}^m\mathbf{S}\, \mathbf{A}_1 \tag{9}$$

where

$${}^m\mathbf{S} = \begin{bmatrix} {}^mS_{11} & {}^mS_{12} & \cdots & {}^mS_{1m} \\ {}^mS_{21} & {}^mS_{22} & \cdots & \vdots \\ \vdots & \vdots & \ddots & \vdots \\ {}^mS_{m1} & \cdots & \cdots & {}^mS_{mm} \end{bmatrix}$$

$$= \mathbf{P}_1 + \mathbf{P}_2 \mathbf{\Gamma}_L (\mathbf{I} - \mathbf{P}_4 \mathbf{\Gamma}_L)^{-1} \mathbf{P}_3 \tag{10}$$

The front superscript m is used to denote that the scattering parameters are associated with the reduced (m-port) system; $\mathbf{I}$ is a unit matrix having the same size as $\mathbf{\Gamma}_L$. Since $\mathbf{\Gamma}_L$ is a simple diagonal matrix, the products $\mathbf{P}_2 \mathbf{\Gamma}_L$ and $\mathbf{P}_4 \mathbf{\Gamma}_L$ can usually be written from inspection.

c. Sample case: four-port to two-port reduction. A multiport frequently encountered in many microwave systems is the four-port. It is of interest to terminate ports 3 and 4 and analyze the device as an equivalent two-port whose input and output ports correspond to ports 1 and 2. Then, according to the procedure discussed previously, the four-port scattering matrix is partitioned so that

$$\left[\begin{array}{c|c} \mathbf{P}_1 & \mathbf{P}_2 \\ \hline \mathbf{P}_3 & \mathbf{P}_4 \end{array}\right] = \left[\begin{array}{cc|cc} S_{11} & S_{12} & S_{13} & S_{14} \\ S_{21} & S_{22} & S_{23} & S_{24} \\ \hline S_{31} & S_{32} & S_{33} & S_{34} \\ S_{41} & S_{42} & S_{43} & S_{44} \end{array}\right] \tag{11}$$

and the load matrix is written as

$$\mathbf{\Gamma}_L = \begin{bmatrix} \Gamma_{L3} & 0 \\ 0 & \Gamma_{L4} \end{bmatrix} \tag{12}$$

Substitutions into Eq. (10) result in

$$\begin{bmatrix} {}^2S_{11} & {}^2S_{12} \\ {}^2S_{21} & {}^2S_{22} \end{bmatrix} = \begin{bmatrix} S_{11} & S_{12} \\ S_{21} & S_{22} \end{bmatrix} + \begin{bmatrix} S_{13}\Gamma_{L3} & S_{14}\Gamma_{L4} \\ S_{23}\Gamma_{L3} & S_{24}\Gamma_{L4} \end{bmatrix} \begin{bmatrix} 1 - S_{33}\Gamma_{L3} & -S_{34}\Gamma_{L4} \\ -S_{43}\Gamma_{L3} & 1 - S_{44}\Gamma_{L4} \end{bmatrix}^{-1} \begin{bmatrix} S_{31} & S_{32} \\ S_{41} & S_{42} \end{bmatrix} \tag{13}$$

Performing the indicated matrix operations yields

$${}^2S_{ij} = S_{ij} + \left\{ \frac{\Gamma_{L3}\left[S_{i3}S_{3j}(1 - S_{44}\Gamma_{L4}) + S_{i3}S_{34}S_{4j}\Gamma_{L4}\right] + \Gamma_{L4}\left[S_{i4}S_{43}S_{3j}\Gamma_{L3} + S_{i4}S_{4j}(1 - S_{33}\Gamma_{L3})\right]}{(1 - S_{33}\Gamma_{L3})(1 - S_{44}\Gamma_{L4}) - S_{43}S_{34}\Gamma_{L3}\Gamma_{L4}} \right\} \tag{14}$$

where

$i = 1, 2$

$j = 1, 2$

The above expression is in a form that is useful for determining how the equivalent scattering parameters vary with load reflection coefficients. As was pointed out by Beatty (Ref. 2), when the loads are non-reflecting, i.e., $\Gamma_{L3} = \Gamma_{L4} = 0$, the scattering parameters of the reduced multiport become those of the original multiport.

References

1. Nemoto, T., and Wait, D. F., "Microwave Circuit Analysis Using the Equivalent Generator Concept," *IEEE Transactions on Microwave Theory and Techniques*, Vol. MTT-16, No. 10, pp. 866–873, Oct. 1968.
2. Kerns, D. M., and Beatty, R. W., *Basic Theory of Waveguide Junctions and Introductory Microwave Network Analysis*, p. 108. Pergamon Press, Inc., New York, 1967.
3. Hunton, J. K., "Analysis of Microwave Measurement Techniques by Means of Signal Flow Graphs," *IRE Transactions on Microwave Theory and Techniques*, Vol. MTT-8, No. 2, p. 206, Mar. 1960.
4. Abele, T. A., "Über die Streumatrix Allgemein Zusammengeschalteter Mehrpole," *Archiv der Elektrischen Ubertragung*, Band 14, Heft 6, pp. 262–268, 1960.

4. Improved RF Calibration Techniques: Operating Noise Temperature Calibrations of the JPL Research Cones,

C. T. Stelzried

Low-noise receiving-system operating noise temperature calibrations using an ambient termination have been discussed in SPS 37-42, Vol. III, pp. 25–32. The maser input is switched between the antenna and the ambient termination. The principal advantage of this technique is the stability and reliability of the ambient termination. It is not necessary to evaluate the waveguide losses when the system operating noise temperature is defined at the maser input.

The present (February 1969) JPL research cones using this technique are designated:

(1) S-band planetary radar (SPR) cone.

(2) S-band multifrequency (SMF) cone.

(3) S-band cassegrain ultra (SCU) cone.

(4) X-band cassegrain experimental (XCE) cone.

These cones are operated on antennas at DSSs 13 and 14 in a cassegrain configuration.[20] A summary of the calibration parameters necessary for the operating noise temperature computer program (JPL ID 5841000, CTS 20B) for these cones is presented in Table 23. Maser 1 is installed in the cone while maser 2 is installed in the DSS 14 3A module. Table 24 indicates the configuration designation used for various maser and receiver combinations.

Figure 37 shows a graph of the measurement results taken with the SPR cone operating on the 85-ft DSS 13 antenna. The averaged operating noise temperature calibration for the various research cone/antenna configurations is presented in Table 25 for the period October 1, 1968 through February 1, 1969. The various cases are defined in Table 26. The operating noise temperature of the XCE cone on the DSS 13 85-ft antenna (case 2)

[20]Most of the calibration data were taken by personnel at DSSs indicated.

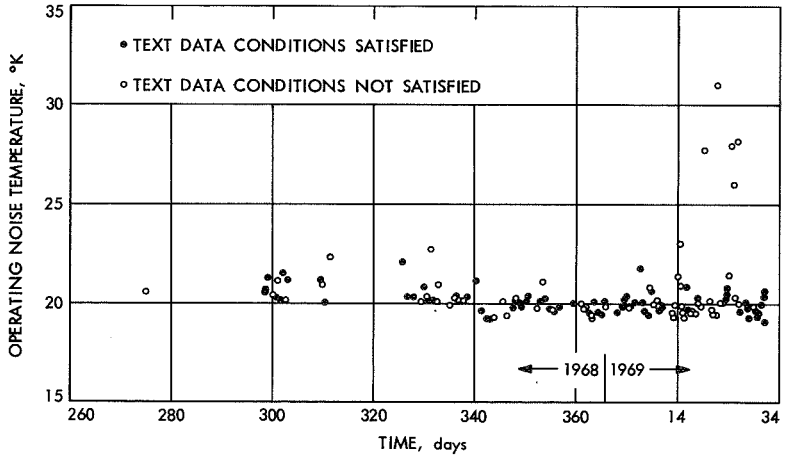

Fig. 37. Operating noise temperature of SPR cone operating on 85-ft DSS 13 antenna (Oct. 1, 1968 to Feb. 1, 1969)

Table 23. Calibration parameter summary of JPL research cones

Cone			Construction date	Configuration	Frequency, MHz	Noise box correction,[a] dB		Maser temperature, °K	VSWR[b]			Approximate zenith low-noise path operating noise temperature, °K		Comments[c]
Model	SN	Mod				C_1 (gain)	C_2 (VSWR)		S_A	S_P	S_e	Ground located	Antenna mounted	
SPR	01	01	7/66		2295	26.0	20.0	5.3	1.237	1.352	1.172			SPS 37-40, Vol. III, p. 98
					2388	26.0	20.0	5.0	1.015	1.006	1.094			
SPR	01	02	5/68		2295	26.0	20.0	5.3	1.250	1.280	1.174			TWM SN02
					2388	26.0	20.0	5.0	1.084	1.020	1.463	17.5	21.0	
SMF	01	00			2297	26.0	20.0	7.2	1.026	1.033	1.252			
					2388	26.0	20.0	7.0	1.040[d]	1.300[d]	1.050[d]			
SMF	01	00	9/68	0–4 (maser 1)	2295	26.0	17.0	4.5	1.120	1.003	1.130	19.0	22.8	TWM SN04
					2388	26.0	17.0	5.5	1.220	1.133	1.230[d]			
SMF	01	01	9/68	5–9 (maser 2)	2295	36.0	20.0	4.5	1.100[d]	1.300[d]	1.300[d]		25.0	SPS 37-54, Vol. II, p. 47 TWM SN03
					2388	36.0	20.0	5.5	1.100[d]	1.300[d]	1.300[d]			
SCU	01	00	7/67		2295	33.0	20.0	4.1	1.013	1.005	1.222			SPS 37-48, Vol. II, p. 52
					2388	33.0	20.0	5.1	1.030	1.253	1.252	20.5	24.0	
SCU	01	01	3/68	0–4 (maser 1)	2295	33.0	20.0	4.5	1.044	1.001	1.266	13.5	17.0	SPS 37-51, Vol. II, p. 82 TWM SN04
					2388	33.0	20.0	5.5	1.147	1.263	1.249	16.5	20.0	
SCU	01	01	3/68	5–9 (maser 2)	2295	36.0	20.0	4.5					27.0	TWM SN03
					2388	36.0	20.0	5.5						
XCE	01	00			8448	36.0	20.0	9.8	1.010	1.006	1.020	32.5		SPS 37-43, Vol. III, p. 59

[a] C_1 = greater path loss to maser input than to maser output. C_2 = greater path loss to maser input than to termination or antenna evaluated.

[b] S_A, S_P, S_e = VSWR, defined at maser input, of antenna (right-handed circular polarization), ambient termination, and maser input, respectively.

[c] TWM = traveling-wave maser.

[d] Estimated.

was considerably higher than anticipated due to problems with the maser. The indicated errors are the standard deviation of the individual measurements and of the means and do not include instrumentation bias errors.

Table 24. Maser/receiver configuration designation

Configuration designation	Maser	Receiver	Frequency, MHz	Diplexed
0	1	R&D	2295	No
1	1	1	2295	No
2	1	2	2295	No
3	1	R&D	2388	No
4	1	1 or 2	2295	Yes
5	2	1	2295	No
6	2	2	2295	No
7	2	1	2295	Yes
8	2	2	2295	Yes

The system operating noise temperature averages were computed using only data with:

(1) Antenna at zenith.

(2) Clear weather.

(3) No RF spur in receiver passband.

(4) $PE_{T_{op}/D}$ less than 0.10°K (from computer program CTS 20B).

The maser gain is nominally optimized prior to each noise temperature calibration. Measurements are made approximately twice a month to check for amplifier saturation (system linearity verification).

Figure 38 shows measured data points and a least-squares second-order curve fit of the low-noise gas-tube noise temperature calibration performed with the SPR cone. The computed value of the least-squares curve fit at the mid-point (December 1968) of the operating period is 4.09°K, which agrees with the averaged 4.01°K reported for August 1968. The standard deviation of the 123 data points is 0.19°K.

Table 25. Average calibration parameters (Oct. 1, 1968 to Feb. 1, 1969)[a]

Case	Reflectometer, dB		Maser gain, dB	Follow-up noise temperature contribution, °K	Operating noise temperature, °K
	Ambient load	Antenna			
1	35.7 ± 0.85/0.07 (136)	33.2 ± 4.9/0.41 (136)	38.6 ± 0.83/0.07 (136)	0.75	20.1 ± 0.60/0.07 (64)
2	38.6 ± 1.90/0.40 (22)	37.2 ± 2.1/0.45 (22)	31.1 ± 5.4/0.11 (22)	4.0	51.5 ± 3.5/0.94 (14)
3	38.7 ± 8.4/0.98 (74)	33.7 ± 9.6/1.1 (74)	49.3 ± 0.93/0.11 (74)	0.66 ± 0.78/0.11 (52)	22.5 ± 0.59/0.08 (52)
4	—	—	50.5 ± 0.73/0.12 (40)	0.43 ± 0.09/0.02 (19)	26.1 ± 0.40/0.09 (19)

[a]Numbers in parentheses indicate number of measurements performed to obtain respective values.

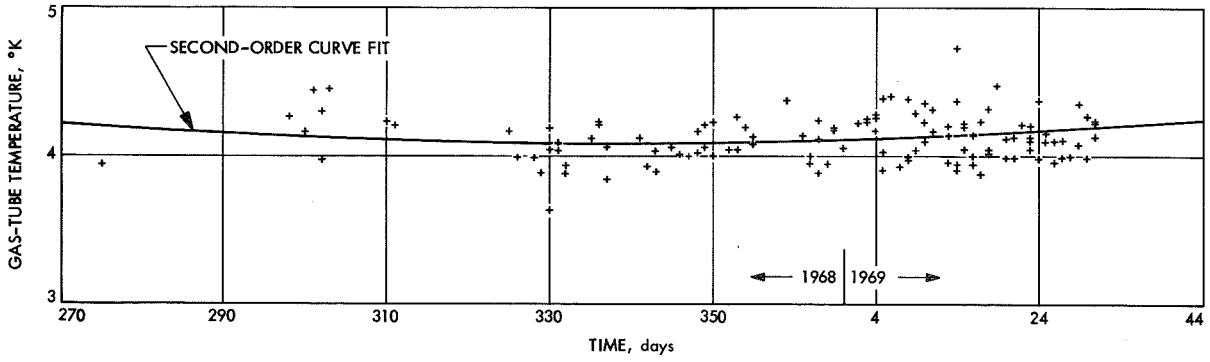

Fig. 38. DSS 13 low-noise gas-tube calibration (Oct. 1, 1968 to Feb. 1, 1969)

Table 26. Case number definitions

Case	DSS	Frequency, MHz	Cone	Maser	Configuration
1	13	2388	SPR SN01 Mod 01	—	—
2	13	8448	XCE SN01 Mod 01	—	—
3	14	2295	SMF SN01 Mod 01	1	0,1 or 2
4	14	2295	SMF SN01 Mod 01	2	5 or 6

5. X- and K-Band Anechoic Antenna Range, *D. E. Neff and S. A. Brunstein*

a. Introduction. In order to take accurate antenna patterns, an antenna range must be essentially reflectionless. For example, a reflection that is 20 dB below the desired signal can cause measurement errors as high as 0.5 dB in amplitude, or 6 deg in phase. Since accurate patterns are usually desired down to at least 40 dB below the pattern peak, reducing the reflection level to the desired negligible level is often a considerable problem.

For this reason, antenna ranges are often built outdoors where reflection-producing objects are far removed from the antennas being measured. The outdoor ranges of the JPL Mesa Antenna Facility are typical of this class. However, outdoor ranges suffer from weather dependence, thus reducing their usefulness. Beside the obvious problem of rain, thermal distortion caused by uneven solar heating of test hardware and the relative movements caused by wind have significantly affected test results in the past. For this reason, many organizations have built indoor antenna ranges. In order to overcome the problem of reflections from floor, walls, and ceiling, these indoor ranges are lined with material that partially absorbs radio waves. These indoor ranges (called anechoic chambers or anechoic antenna ranges) are usable regardless of weather, and even though the materials used are not perfect absorbers, the ranges can usually be designed to give results with accuracy comparable to outdoor ranges.

b. Range characteristics. JPL has just completed the instrumentation of an anechoic range at the Mesa Antenna Facility. Figure 39 shows an X-band dual-mode horn mounted in the anechoic range. The multi-pointed material is the microwave absorber. Its characteristics are such that the range is only usable above 6 GHz. Since antennas for lower frequencies can generally be scaled to the higher frequencies, and because a high-quality absorber for the normal JPL S-band frequencies is extremely bulky, it was decided to utilize the high-frequency absorber.

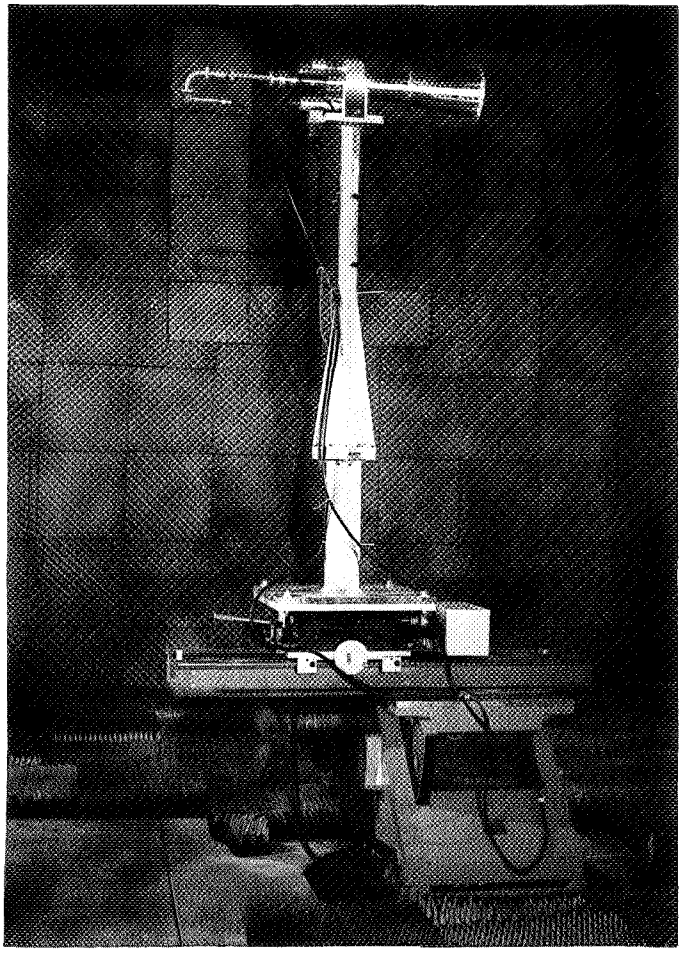

Fig. 39. X-band horn, mounted in the anechoic antenna range

Two illumination horns are mounted in the end of the chamber (Fig. 40). One horn is for use over the frequency range of 7 to 11 GHz and the other for 15 to 21 GHz. Both are permanently connected to the appropriate transmitting equipment so that changing from one horn to the other may be accomplished in minutes.

c. Instrumentation. Racks are used to mount the X-band (7–11 GHz) and K-band (15–21 GHz) transmitting equipment. The racks also contain equipment for monitoring and stabilizing the frequency and for monitoring and automatically regulating the RF power at the illuminating horn input. An RF frequency synthesizer is used as a reference for the signal generator frequency stabilizer. Any frequency in the previously mentioned frequency bands can be rapidly set with a resolution of 2 Hz, and

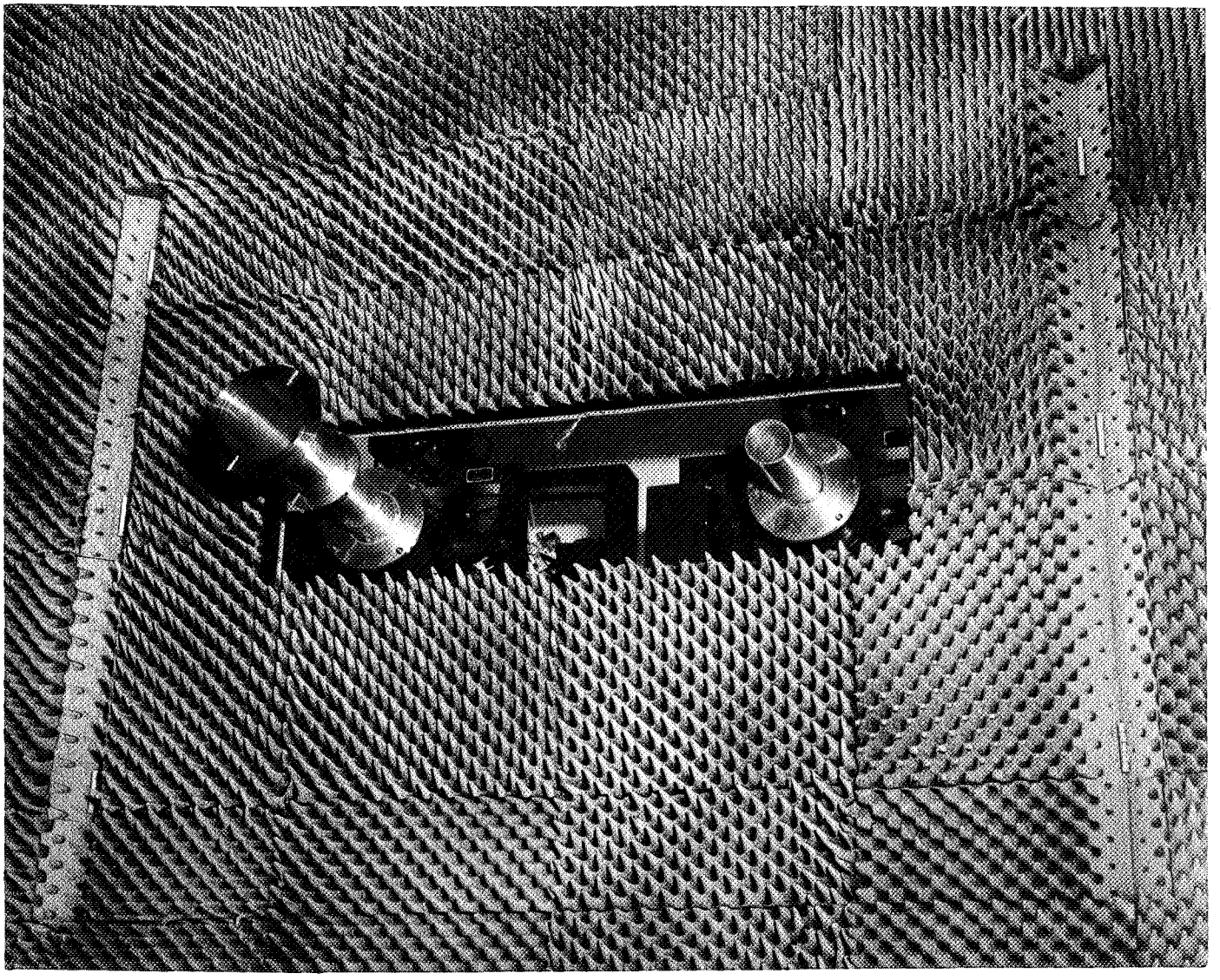

Fig. 40. X- and K-band illuminating horns

can be stabilized to permit accurate patterns to be taken of the relative phase of the radiated energy as a function of angular position of the test horn.

A wide-band tunable, phase-locked loop amplitude and phase receiver is tuned by means of a single knob to any frequency within the two bands mentioned, although the receiver mixer (mounted on the test horn) must be changed from band to band. The dual amplitude and phase pattern recorders allow simultaneous recording of amplitude and phase patterns. The position control and indicating equipment allows operator control of the elevation, azimuth, and polarization of both illuminating horns, and also of the test horn.

d. Preliminary evaluation and usage. No detailed evaluation of the anechoic range has yet been made. Patterns have been taken of a JPL X-band dual-mode horn. A typical pattern taken on the anechoic range is shown in Fig. 41. The symmetry and smoothness of the pattern lead to the preliminary conclusion that the reflections are sufficiently low, at least for high-gain ($\simeq$20 db) antennas. No evaluation with wide beamwidth antennas has yet been attempted.

Since the horn patterns showed the range to be valid for qualitative horn development work, the anechoic range is now in use for the experimental development of advanced feeds for the JPL Advanced Antenna System.

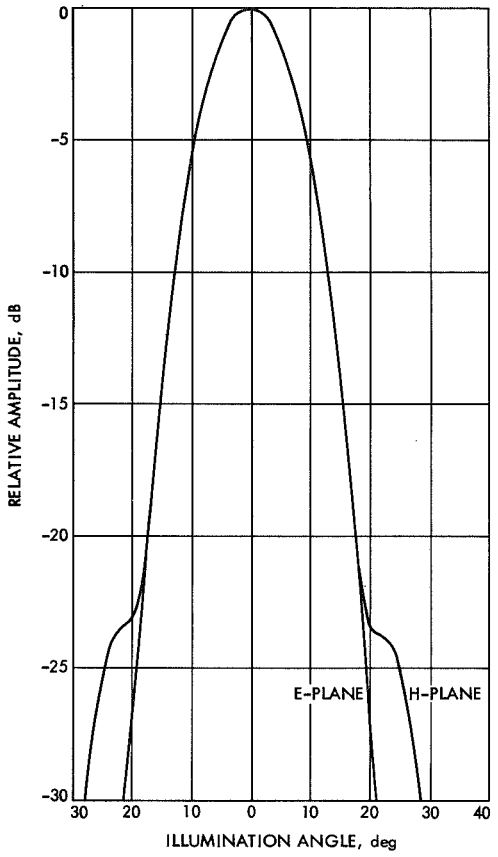

Fig. 41. Typical dual-mode horn pattern

6. *Pioneer VI* Solar Faraday Rotation Occultation Experiment, *T. Sato and C. T. Stelzried*

This experiment has been described in SPS 37-55, Vol. II, pp. 57–59. The polarization measurements of *Pioneer VI* were made under weak-signal (approximately −162 dBmW), high-noise conditions. The polarization of *Pioneers VII, VIII,* and *IX* was also measured to obtain additional information on the receiving system polarizer instrumentation during strong-signal conditions. In addition, further data were obtained on the Faraday rotation due to the earth's ionosphere for view periods that differ from *Pioneer VI.*

Figure 42 shows polarization data for *Pioneer IX* taken shortly after launch. The downward slope is due to the decreasing electron density with time in the ionosphere, which is characteristic of night conditions. The received signal strength at this time (pass 4, Nov. 12, 1968) was approximately −115 dBmW. The decrease in electron density dominates the increasing path length through the ionosphere at lower elevation angles.

The peak-to-peak polarization jitter of approximately 0.1 deg seen on the graph is not due to instrumentation noise but is probably due to spacecraft wobble. This wobble is well within the spacecraft tolerance of 0.5 deg. The uneven density seen on the graph could be explained by the instrumentation sample rate that is nearly synchronous with the spacecraft wobble rate. The spacecraft wobble rate is expected to be several times faster than the instrumentation rate (approximately 20 s per sample for these data).

The above indicates the ability of the polarization instrumentation to provide a direct measurement of spacecraft wobble amplitude.

D. Supporting Research and Technology

1. Accuracy of Single Precision Univac 1108 Subroutine Library Functions, *C. J. Devine, Jr., and C. L. Lawson*

a. Introduction. A new Univac 1108 Multi-Processor System is being implemented at JPL for use in the Scientific Computing Facility. This article discusses the tests conducted on the accuracy of the Univac 1108 library of elementary function subroutines. An elementary function subroutine is defined to be a mathematical algorithm programmed so that it can be referenced from basic Fortran (i.e., contained in the Fortran library) and, when given an independent argument x, computes a dependent value $y = f(x)$, where $f(x)$ is an elementary function, e.g., $f(x) = \sin(x)$.

The efficiency of the coded algorithm is of the utmost importance. Care must be taken to avoid error, ensure rapid execution, and to use the smallest possible number of storage locations in the machine.

b. Method. The accuracy of a single precision mathematical function subroutine in this article is checked by comparing it with a corresponding double precision subroutine and recording the differences in the form of usable error indications. The information is collected to determine where possible improvements could be made in the mathematical algorithm and in the coding of the algorithm. It is also a check against blunders.

Closed intervals $[a, b]$ of the independent variable x are chosen to coincide approximately with the intervals over which the different approximations of the same function are defined within the computing algorithm.

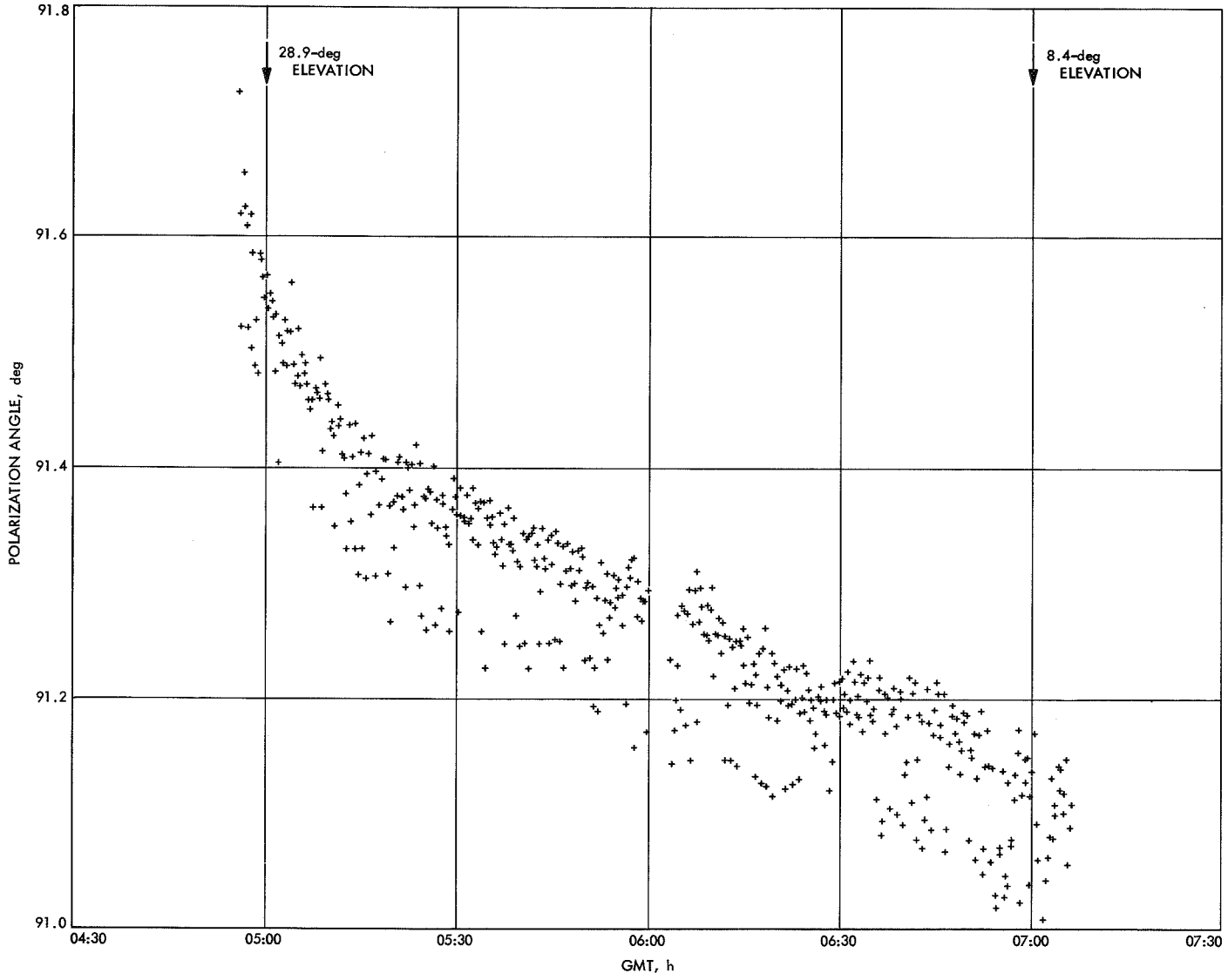

Fig. 42. *Pioneer IX* polarization vs time (Nov. 12, 1968)

The intervals are also chosen to isolate certain points on the real line where the approximating function is liable to large errors.

The program used to compute the errors discussed in this article is ST3, which is an adaptation of the program ST1,[21] written and used in 1963 for testing the IBM 7094 library. In the program, the closed interval $[a, b]$ is partitioned into N contiguous subintervals, each of length $(|b - a|/N)$, where $N = 3000$. In each of these subintervals a number is picked at random assuming a uniform distribution over the subinterval. This number x is used as the independent variable in computing the function $SY = f(x)$ in single precision and also in double precision, $DY = f(DX)$, for comparison.

The absolute error is defined as $D = SY - DY$, and the relative error is defined as $R = D/|DY|$. The maximum magnitudes of these errors are tabulated for the different cases in Tables 27, 28, and 29. Another quantity of interest tabulated was the percentage of results correct to 27 bits. (The length of the fraction part of a single precision floating point number on the two machines tested is 27 bits.) To understand this concept, let 2^n be the value of the twenty-seventh bit position of the fraction part of SY. Then the quantity

$$E = \frac{D}{2^n} * \text{sign}\,(DY)$$

is computed, where E is the error of SY in units of the last bit position of SY and is positive if $(SY - DY)$ has the same sign as DY. Note that the condition $|E| \leq 1/2$ characterizes SY as being a correctly rounded value. More generally, if $2^{m-1} < |E| \leq 2^m$, then SY is correct to $(26 - m)$ bits but not to $(27 - m)$ bits. The desired result, of course, is a correctly rounded one, but this is not always possible (see Ref. 1).

The quantity $|E|$ may be greater than 1/2 due to the properties of a particular function. If we assume that $y = f(x)$ is the computed value of the function at some argument x, then the relative error may be represented as

$$\frac{dy}{y} = \frac{f'(x)\,dx}{f(x)} = \frac{xf'(x)}{y}\left(\frac{dx}{x}\right) \qquad (1)$$

where the quantity (dx/x) is the relative error made in representing the argument x in a finite word length. It is multiplied by the factor $x\,f'(x)/y$, which may decrease it or magnify it. For example, in approximating the elementary function $f(x) = \sin x$, it is difficult to keep the relative error dy/y small in a small interval around π. On the other hand, in the case of the elementary function $f(x) = x^{1/2}$, it is possible to produce a correctly rounded result, since Eq. (1) becomes

$$\frac{dy}{y} = \frac{1}{2}\left(\frac{dx}{x}\right) \qquad (2)$$

and the relative error made in representing x inexactly is reduced by 1/2.

For our purposes the results in the last column of Tables 27, 28, and 29 were used mainly for comparison with subroutines in the IBM 7094 library. It is tacitly assumed that with a few exceptions they represent the state of the art in computing elementary functions and, therefore, serve as a standard for comparison.

c. Results and discussion. From the comparison of results summarized in Tables 27 and 28, it can be seen that the IBM 7094 subroutines, with a few exceptions, are superior to those of the Univac 1108. This indicates that the Univac 1108 routines fall below the standards presently attainable.

The results obtained after JPL improvements were made to the Univac 1108 routines are compiled in Table 29. The condition of the Univac 1108 routines can be improved in some cases with minor alterations. For example, if a comparison is made of the cube root (CBRT) $[f(x) = x^{1/3}]$ results between Tables 28 and 29, a decided improvement is noted. This is a result of one rounding operation added to the original CBRT subroutine. Table 28 also indicates that in computing $f(x) = x^{1/3}$, by using the exponentiation routine available in the IBM 7094 library, the error is worse than that given by the original Univac 1108 CBRT routine, thus indicating that it is worthwhile to carry a CBRT elementary function routine on the library system.

In the case of the tanh and arctan routines, actual coding blunders existed that could be most easily corrected by writing new routines. These new routines were coded in Fortran V without the benefit of rounding instructions and, as indicated in Table 29, surpassed the accuracy of the Univac 1108 routines detailed in Tables 27 and 28.

[21] Lawson, C. L., *ST1, Single Precision Test Program No. 1*, 1963 (JPL internal document).

Table 27. Comparative results of Univac 1108 and IBM 7094 subroutines for trigonometric functions

Function	Interval[a]	Maximum relative error, 10^{-8}		Maximum absolute error, 10^{-8}		Results correct to 27 bits, %	
		7094	1108	7094	1108	7094	1108
Sin	$[0, \pi/2]$	1.0	10.0	0.7	1.0	86.6	39.1
	$[\pi/2, \pi]$	2.0	9.0	0.9	1.0	82.2	38.6
	$[\pi, 2\pi]$	3.0	25.0	1.0	1.0	74.3	40.1
	$[2\pi, 8\pi]$	3.0	109.0	1.0	1.0	75.2	40.3
	$[-10^{-4}, +10^{-4}]$	0	0	0	0	100.0	100.0
Cos	$[0, \pi/2]$	2.0	3.0	0.8	1.0	84.9	39.1
	$[\pi/2, \pi]$	2.0	17.0	1.0	1.0	64.6	38.2
	$[\pi, 2\pi]$	2.0	26.0	1.0	1.0	74.5	38.2
	$[2\pi, 8\pi]$	124.0	2686.0	1.0	1.0	73.6	39.9
	$[\pi/2 - 10^{-4}, \pi/2 + 10^{-4}]$	18430.0	127300.0	0.0003	0.008	0	0
Tan	$[0, \pi/4]$	1.0	9.0	1.0	2.0	77.9	21.2
	$[\pi/4, \pi/2]$	3.0	4.0	29960.0	71290.0	71.3	52.9
	$[\pi/4, 8\pi]$	26.0	146.0	4808.0	457600.0	62.9	39.8
	$[\pi/2 - 10^{-3}, \pi/2 + 10^{-3}]$	1070.0	127300.0	∞	27970.0	42.6	9.5
Arcsin	[0, 1/2]	2.0	18.0	0.8	4.0	72.7	17.2
	[1/2, 1]	3.0	24.0	2.0	40.0	62.8	14.9
Arccos	[0, 1/2]	2.0	2.0	2.0	3.0	54.2	41.7
	[1/2, 1]	2.0	761.0	2.0	20.0	64.9	18.5
Arctan	[0, 1/2]	1.0	17.0	0.3	3.0	79.9	13.2
	[1/2, 1]	0.8	6.0	0.4	4.0	98.9	2.8
	[1, 10]	0.7	4.0	0.8	3.0	98.5	33.6
	$[10, 10^5]$	0.5	1.0	0.8	2.0	98.4	53.4
Sinh	[0, 0.7]	2.0	1512.0	1.0	2.0	52.8	25.5
	[0.7, 24]	2.0	2.0	∞	19390.0	87.5	45.3
	[24, 88]	0.8	2.0	∞	∞	95.5	25.6
Cosh	[0, 0.7]	0.9	2.0	1.0	2.0	94.6	34.2
	[0.7, 24]	1.0	3.0	∞	19690.0	88.2	24.5
	[24, 88]	0.8	2.0	∞	∞	96.4	24.8
Tanh	[0, 0.55]	1.0	3313.0	0.7	2.0	60.7	14.0
	[0.55, 11]	1.0	11.0	0.8	11.0	96.9	27.5
	$[11, 10^5]$	0	—	0	—	100.0	—

[a]Based on 3000 random arguments uniformly distributed over each interval.

Table 28. Comparative results of Univac 1108 and IBM 7094 subroutines for non-trigonometric functions

Function	Interval[a]	Maximum relative error, 10^{-8}		Maximum absolute error, 10^{-8}		Results correct to 27 bits, %	
		7094	1108	7094	1108	7094	1108
Exp	[0, 1/2]	0.7	2.0	0.8	2.0	98.7	38.4
	[1/2, 1]	0.7	2.0	2.0	4.0	97.6	40.8
	[1, 10]	0.7	2.0	12280.0	36760.0	97.4	38.5
	[10, 88]	0.8	2.0	∞	∞	96.1	25.9
Log_e	[0, 0.1]	0.7	1.0	6.0	18.0	99.8	91.2
	[0.1, 0.9375]	0.8	13.0	2.0	2.0	98.3	38.2
	[0.9375, 1.065]	5.0	12280.0	0.1	0.1	66.8	0.5
	[1.065, 4]	0.7	12.0	0.8	1.0	99.0	60.4
	$[4, 10^4]$	0.7	1.0	6.0	10.0	99.8	74.3
	$[10^4, 10^{30}]$	0.7	12.0	50.0	77.0	99.9	70.1
Log_{10}	[0, 0.1]	2.0	2.0	6.0	4.0	47.2	74.7
	[0.1, 0.9375]	2.0	13.0	2.0	1.0	42.3	34.4
	[0.9375, 1.065]	4.0	23520.0	0.04	0.7	40.1	0.7
	[1.065, 4]	2.0	11.0	1.0	1.0	43.3	57.5
	$[4, 10^4]$	2.0	1.0	6.0	5.0	34.6	59.5
	$[10^4, 10^{30}]$	2.0	1.0	50.0	39.0	34.4	52.9
SQRT	[0, 1/4]	0.7	2.0	0.2	0.4	100.0	53.2
	[1/4, 1/2]	0.7	2.0	0.4	0.7	100.0	54.4
	[1/2, 1]	0.5	1.0	0.4	0.7	100.0	53.4
	[1, 16]	0.7	1.0	2.0	3.0	100.0	55.6
CBRT	[0, 1/8]	6.0	1.0	1.0	0.4	3.8	50.8
	[1/8, 1/4]	3.0	2.0	2.0	0.8	16.5	46.5
	[1/4, 1/2]	2.0	1.0	1.0	0.8	24.7	48.5
	[1/2, 1]	1.0	0.9	1.0	0.8	39.1	48.3
	[1, 64]	3.0	2.0	13.0	3.0	25.5	48.0

[a]Based on 3000 random arguments uniformly distributed over each interval.

Table 29. Results of JPL improvements to elementary routines

Function	Interval[a]	Maximum relative error, 10^{-8}		Maximum absolute error, 10^{-8}		Results correct to 27 bits, %	
		7094	1108	7094	1108	7094	1108
SQRT	[0, 1/4]	—	0.7	—	0.2	—	100.0
	[1/4, 1/2]	—	0.7	—	0.4	—	100.0
	[1/2, 1]	—	0.6	—	0.4	—	100.0
	[1, 16]	—	0.7	—	1.5	—	100.0
SQRT2	[0, 1/4]	0.7	—	0.2	—	98.5	—
	[1/4, 1/2]	0.8	—	0.4	—	98.8	—
	[1/2, 1]	0.5	—	0.4	—	98.6	—
	[1, 16]	0.7	—	1.6	—	98.3	—
CBRT	[0, 1/8]	—	0.7	—	0.2	—	98.6
	[1/8, 1/4]	—	0.4	—	0.4	—	97.4
	[1/4, 1/2]	—	0.6	—	0.4	—	98.5
	[1/2, 1]	—	0.5	—	0.4	—	98.7
	[1, 64]	—	0.7	—	2.0	—	98.6
Tanh (Fortran V)	[0, 0.55]	—	0.8	—	0.4	—	93.0
	[0.55, 11]	—	0.9	—	0.8	—	58.9
	[11, 10^5]	—	0	—	0	—	100.0
Arctan (Fortran V)	[0, 5]	—	2.7	—	1.5	—	57.9
	[5, 10^5]	—	0.9	—	1.4	—	56.4

[a]Based on 3000 random arguments uniformly distributed over each interval.

In selecting the best computational algorithm, factors of timing, accuracy, and storage must be considered. In the case of the square root (SQRT) routine, it is interesting to see the possible trade-off in choosing one condition over the other. The IBM 7094 SQRT routine obtained 100% of the results correct to 27 bits, while the original Univac 1108 routine was much poorer (Table 28).

The IBM routine used a simple linear approximation with three Newton–Raphson iterations of the approximation. The Univac routine was improved to the same accuracy of the IBM routine by adding one more Newton–Raphson iteration, making a total of three (Table 29). However, it is also possible to obtain almost the same accuracy by a more precise linear approximation and only two Newton–Raphson iterations in the algorithm, thus saving approximately 12 μs (SQRT2, Table 29). Hence, there is a decrease in execution time and storage with little loss in accuracy.

Reference

1. Hart, J. F., et al., *Computer Approximations.* John Wiley & Sons, Inc., New York, 1968.

2. Tricone Multiple Cassegrain Feed System for the 210-ft Antenna, *M. S. Katow and K. P. Bartos*

a. Introduction. A solution to satisfy increasing demands for greater versatility of the 210-ft antenna for multifrequency operations, including the need for special primary feeds to satisfy research and developmental missions, is to permanently mount multiple primary feed cones combined with the installation of a rapid, simple, and safe changing means. The present RF feed cone changing method consumes valuable operating time as well as presenting risks of possible damage during the handling procedures.

A previous article (SPS 37-45, Vol. III, pp. 48–51) considered three different configurations of the multiple primary feeds, the hyperboloid, and the paraboloid. It was concluded that the best overall solution was to mount fixed multiple primary RF feeds to the vertex of the paraboloid structure combined with a movable hyperboloid to select the operational primary RF feed. By raising the original location of the primary focus approximately 2.5 ft, standard cabinets and 400-kW transmitter units can be installed in modules II and III (Fig. 43). This arrangement also provides for short minimum-loss waveguide runs to the RF feed horns.

This article describes the main features incorporated in the tricone system by the design effort (phase I); only the basic configurations delineating the functional aspects are outlined. Future articles will present detailed descriptions of the implemented hardware as well as on the manufacturing, testing, and erection of the system.

b. Tricone geometry. The tricone microwave geometry is generated by tilting only the hyperboloid system of the standard cassegrain about its virtual secondary focus, which is coincident with the focus of the paraboloid. Since only spherical wavefronts are radiated from the two foci of the hyperboloid system, the tilt thus maintains the phase relationship of the basic standard cassegrain geometry. To maintain the RF amplitude control, the symmetric axis of the RF feed points to the center of the almost circular surface as described by the intersection of the 60-deg paraboloid's cone and the hyperboloid's surface. This intersection also describes the trimline of the hyperboloid's surface.

c. Hyperboloid assembly. The functional features of the hyperboloid assembly are shown in Fig. 44 with the support torus the main structural member. The support torus is attached to the apex structure of the quadripod by a determinate set of restraint rods and carries the large diameter rotation bearing combined with a drive mechanism and an indexing pin.

The assembly is designed for axial (z) motion of ± 3 in. and lateral (x and y) motions of ± 4 in. Where simultaneous motions of the restraint rods is required, direct-geared connections are made to ensure this. Mechanical means to actuate the change in the length of the restraint bars is supplied by motorized ball jack screws.

As initially installed, all actuations will be remotely indicated and console-controlled at the control room. However, extra cable wires and provision for mounting encoders for future installation of servo controls is provided.

d. Cassegrain cone support modules. Three primary RF feed cones are designed to be closely mesh-mounted on top of the center supporting modules. The RF feed cones used will be similar in size to the existing standard DSIF feed cones with the difference in the use of cylindrical sides in the bottom section. The supporting assembly will consist of three modules supported by the center hub of the reflector structure.

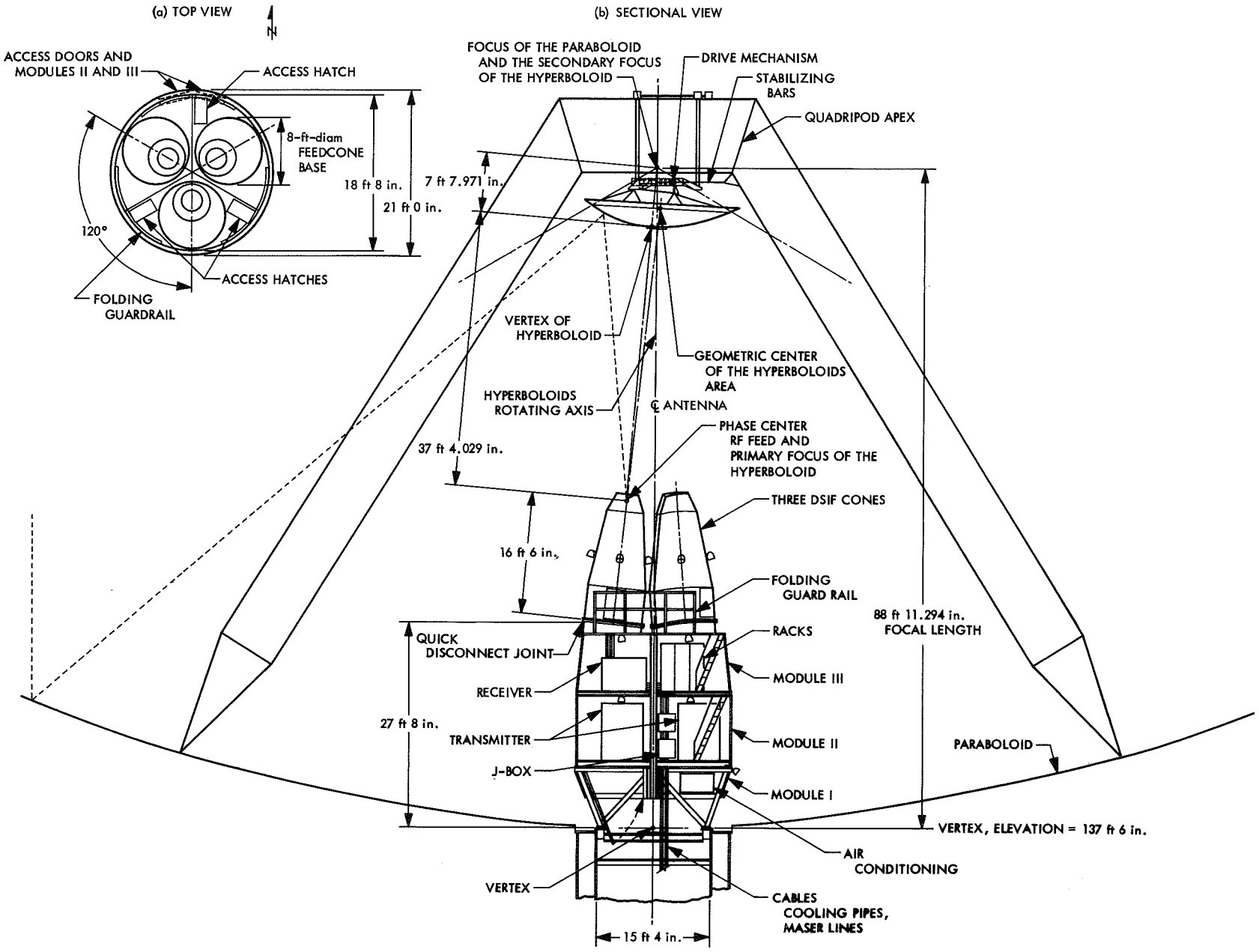

Fig. 43. Multiple primary feed system

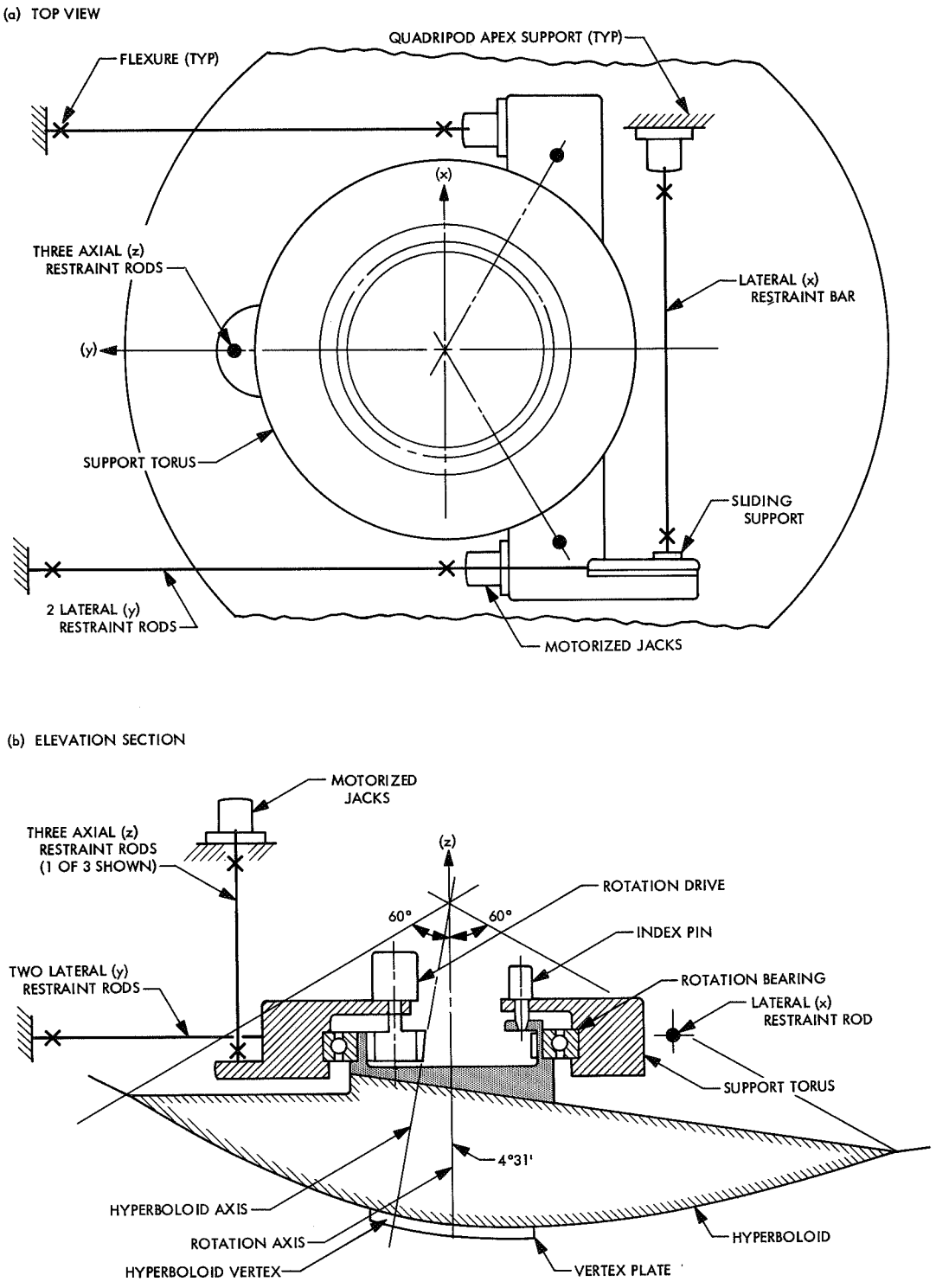

Fig. 44. Hyperboloid assembly

Module I is designed as an open-space truss in order to provide open optical lines of sights to the surface panel targets from the theodolite mounted 15 in. about the vertex. The heat exchanger for the air conditioning unit is located above the optical lines-of-sight envelope. Module I provides the structural support for modules II and III.

Module II is a cylindrical section designed to house three large transmitters. A hoisting means, using the feed-cone hoist, will be provided to raise up to a 5000-lb unit from the ground level into both modules II and III.

Module III has tapered sides in order to minimize the RF blockage and will provide space for mounting standard-size DSIF cabinets.

Hoisting means will be provided to install (1) module I alone, (2) modules II and III separately, (3) modules II and III together, and (4) each of the three standard RF feed cones individually. All means will use the existing feed-cone hoist with pulleys mounted on the upper quadripod legs.

3. Analysis of Bandpass Filtered Phase Modulation by a Non-Ideal Square Wave, *R. C. Coffin*

a. Introduction. In several applications, notably multiple mission telemetry, loss of higher order sidebands, generally due to equipment imperfections, contributes an appreciable loss in signal power or degradation of signal-to-noise ratio. This study has considered the case of square-wave phase modulation (PM) at some index β, using a waveform of equal rise and fall times t_1, dwell time t_0, and period T, passed through a receiver passband B. Two cases are considered:

Case I. The modulation index β is set at its nominal value by observing the peak amplitude of the modulation source while ignoring the degradation due to imperfect rise time and time asymmetry $[T - 2(t_0 + t_1)]$. This case might occur by setting the modulation index at a low frequency, where the above effects can be neglected, and then operating at a higher frequency.

Case II. The modulation index is set at operating conditions such that the nominal carrier suppression is maintained without regard to the imperfect waveform. The result is that, in general, $\beta > \beta_{\text{nom}}$.

The viewpoint of the study is that, by better defining the transmitter signal, more accurate models of the overall system are obtained and, therefore, measurements of receiver performance are more meaningful. It has been initially assumed that the RF bandwidth of the transmitter exceeds both the modulation bandwidth and the receiver bandwidth.

b. Analysis. The approach of this analysis is to compute the ratio of ideal sideband power to actual sideband power. Ideal sideband power is that resulting from the PM of an RF carrier by an ideal square wave ($t_1 = 0$, $t_0 = T/2$). Actual sideband power is the result of modulation by an imperfect source (i.e., a trapezoid) and is truncated because of a finite receiver passband.

A PM function can be expanded into a Fourier series such that (Ref. 1)

$$e = E \sum_{-\infty}^{\infty} C_n \exp\left[j(\omega_0 + n\omega)t\right] \tag{1}$$

where

$$C_n = \frac{\omega}{2\pi} \int_{-\pi/\omega}^{\pi/\omega} \exp\left[j\phi(t)\right] \exp\left(-jn\omega t\right) dt$$

The modulation $\phi(t)$ is, for our purposes, a trapezoid. It has been observed that the modulation sources generally in use have rise and fall times whose differences may be ignored. Hence, a trapezoid of equal rise and fall was chosen for analysis and is expressed as

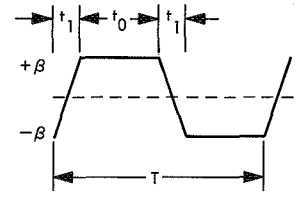

$$\left.\begin{aligned}
\phi(t) &= \frac{2\beta}{t_1} t - \beta, && 0 \le t \le t_1 \\
\phi(t) &= \beta, && t_1 < t < t_0 + t_1 \\
\phi(t) &= -\frac{2\beta}{t_1} t + \beta + 2\beta \frac{(t_0 + t_1)}{t_1}, && t_0 + t_1 \le t \le t_0 + 2t_1 \\
\phi(t) &= -\beta, && t_0 + 2t_1 < t \le T
\end{aligned}\right\} \tag{2}$$

Substituting for $\phi(t)$ and evaluating the integrals, it may be shown that the magnitude of the coefficient term is

$$|C_n| = \frac{\beta}{n\pi} \left| \frac{\sin\left(\beta - n\pi \frac{t_1}{T}\right)}{\beta - n\pi \frac{t_1}{T}} \right. \tag{3}$$

$$\left. - \exp\left[-jn\omega(t_0 + t_1)\right] \left[\frac{\sin\left(\beta + n\pi \frac{t_1}{T}\right)}{\beta + n\pi \frac{t_1}{T}} \right] \right|$$

In the expression for $|C_n|$, there is an imaginary term. This term is a function of the asymmetry $(t_0 + t_1)/(T/2)$ and is commonly called the quadrature term. It contributes to the power loss of each harmonic, but it also causes the carrier to be slightly out of phase with ideal.

The power in the sidebands of a carrier with unity total power defined as in Eq. (1) is

$$P_{sb} = 2 \sum_{1}^{\infty} |C_n|^2$$

and for an ideal square wave (rise time = 0, $t_0 = T/2$), the power in the sideband is

$$P_{sb} = \sin^2 \beta$$

When computing the sideband power for the trapezoid modulation, the power in the even harmonics is ignored. Even order harmonics will not enter into the recovered power if the local model in the receiver is ideal (in the sense that it contains no even harmonics). Hence, the tabulated data are somewhat worse case since the local model may contain some even harmonics. If the local model of the subcarrier were to have time asymmetry in the same sense as the modulation, then the losses could, conceivably, be offset.

The effect of passing the modulated carrier through a receiver of bandwidth B is taken into account by truncating the summation process in the computation of sideband power for the trapezoid case at an odd harmonic equal to, or less than, the noise bandwidth of the system. Since the sideband power for the ideal case is not truncated, the ratio computed is that of truncated odd harmonic sideband power generated by a trapezoid to total sideband power generated by an ideal square wave.

In case I, the peak phase excursion of the trapezoid is assumed to be the same as that of the ideal nominal square wave. Therefore, the difference in sideband power, expressed as a ratio, is caused by losses due to finite rise time, time asymmetry, and finite bandwidth.

In case II, the carrier power for the trapezoid case is made to match the carrier power for the ideal square-wave case by allowing the peak phase excursion β to exceed the nominal. Hence, the differences in sideband power are caused by finite rise time, time asymmetry, finite bandwidth, and the fact that $\beta > \beta_{\text{nom}}$. The sideband power for the ideal square-wave case is computed based on β_{nom}.

The analysis was programmed into the HP 9100 calculator. Case I uses as its inputs t_0, t_1, T, β, N, and displays, as a result, the ratio

$$\frac{\text{Sideband power for trapezoid PM, truncated at } N}{\text{Total sideband power for ideal square-wave PM}}$$

Case II uses as inputs the same information as the case I program. It first computes the carrier power for the trapezoid case using the nominal peak phase excursion β_{nom}. If this power is different from that in the ideal square wave by more than an arbitrarily small amount, then β is iterated until they agree. The program then displays the new peak phase excursion β. When told to continue, the program computes and displays the ratio as above, using β in the numerator calculation and β_{nom} in the denominator calculation. Also displayed is the cosine of the angle between the ideal and actual carrier.

A tabulation of the waveforms is shown in Table 30; Table 31 presents the results. The input data were obtained from published or unpublished sources and, where none existed, photographs were obtained of subcarrier waveforms. In addition to the rise time, dwell time, and period, a measure of the time asymmetry is also given in the form of $\Delta T/T$. A nominal peak phase excursion of 1 rad was arbitrarily chosen. The truncation point was chosen based on a nominal receiver noise bandwidth of 3 MHz.

c. Conclusions. As would be expected, the loss ratios for the low-frequency examples are relatively small and the loss ratios for the high subcarrier rate examples are

Table 30. Source characterizations

Source[a]	Dwell time t_0, s	Rise time t_1, s	$\Delta T/T$, %
24-kHz channel			
M69-4 FTS	2.03×10^{-5}	1.50×10^{-7}	0.96
Mariner Mars 1969 FTS breadboard	2.03×10^{-5}	2.25×10^{-7}	0.78
SDA test rack	2.07×10^{-5}	7.00×10^{-8}	0.19
MMT test rack	2.07×10^{-5}	7.00×10^{-8}	0.19
259-kHz channel			
M69-4 FTS	1.79×10^{-6}	1.15×10^{-7}	0.65
Mariner Mars 1969 FTS breadboard	1.61×10^{-6}	2.25×10^{-7}	2.50
SDA test rack	1.80×10^{-6}	7.00×10^{-8}	1.55
MMT test rack	1.84×10^{-6}	7.00×10^{-8}	0.52
HRT test rack	1.85×10^{-6}	2.75×10^{-8}	1.36

[a]FTS = flight telemetry subsystem
HRT = high-rate telemetry
MMT = multiple-mission telemetry
SDA = subcarrier demodulator assembly.

Table 31. Some representative imperfection losses

Source[a]	Case I, dB	β, rad	Cos α, dB	Case II, dB
24-kHz channel				
M69-4 FTS	−0.100	1.003	−0.0019	−0.083
Mariner Mars 1969 FTS breadboard	−0.083	1.004	−0.0013	−0.061
SDA test rack	−0.033	1.001	−0.0001	−0.028
MMT test rack	−0.033	1.001	−0.0001	−0.028
259-kHz channel				
M69-4 FTS	−0.333	1.016	−0.0009	−0.245
Mariner Mars 1969 FTS breadboard	−0.464	1.041	−0.0132	−0.244
SDA test rack	−0.338	1.008	−0.0051	−0.293
MMT test rack	−0.314	1.007	−0.0006	−0.275
HRT test rack	−0.323	1.006	−0.0039	−0.290

[a]FTS = flight telemetry subsystem
HRT = high-rate telemetry
MMT = multiple-mission telemetry
SDA = subcarrier demodulator assembly.

large enough to be considered significant. However, in the context of 0.1-dB telemetry budgets, the whole range of loss is of interest in refining models of system performance. Notice that the cosine α terms (α is the angle between the ideal and actual carrier) are small enough to be neglected in a system sensitive to carrier phase. In each example, case II gives a smaller loss ratio than case I. This is because the carrier is being over-modulated, causing additional power to be placed in the sidebands and partially compensating for the losses due to imperfections. The data presented here are too limited to be able to draw conclusions as to the separate effects of poor rise time or asymmetry. The study will be continued utilizing the programs already developed to further investigate the effects separately.

Reference

1. Woodbury, R. C., Spectral Analysis Applied to a Digitally Coded PM RF Carrier, Technical Report 32-893. Jet Propulsion Laboratory, Pasadena, Calif., Aug. 15, 1966.

4. DSS 13 Operations, *E. B. Jackson and J. D. Campbell*

a. Experimentation. During the period December 16, 1968 through February 15, 1969, DSS 13 conducted monostatic planetary radar experiments. Additionally, the 85-ft antenna continued to be used for reception of various pulsars at 2388 MHz, as evaluation of pulse-to-pulse spacing stability and average peak-signal strength continued.

Some experimentation and testing have been done with monostatic planetary radar, total spectrum, using a method of frequency sweeping that has been tentatively entitled "chirp radar." This technique promises increased resolution of planetary surface features along with a reduction in the amount of data required to obtain such resolution.

On February 14, range to the planet Venus was measured using a range-gate length of 100 μs at a nominal range of 50.98×10^6 mi. The data indicate that the round-trip range is in error by approximately 40 μs. Figure 45 illustrates the results obtained.

Clock-synchronization transmissions via moon reflection continued to DSS 42 and commenced to DSS 14. However, testing is still underway at DSS 14 and routine correlation of the reflected signals has not yet commenced.

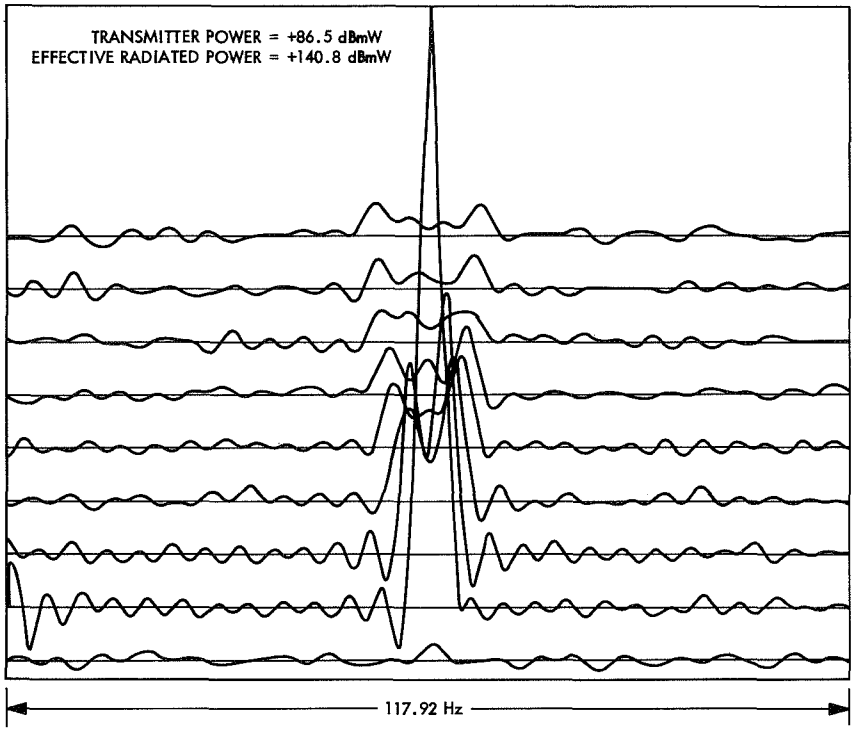

Fig. 45. Range-gated spectra of Venus

b. System performance.

30-ft antenna. A leaking seal in one of the azimuth drive units allowed oil to contaminate the brake and clutch causing erratic operation in that axis. The seal was replaced, the brake and clutch were cleaned, and the system operated normally.

85-ft antenna. The following failures occurred during this period and were repaired with no loss of tracking time:

(1) Azimuth brake failed.

(2) Azimuth brake interlock relay failed.

(3) Azimuth clutch interlock transistor shorted.

(4) Short developed in wiring in servo amplifier.

c. System improvements.

30-ft antenna. After the electronics modification (SPS 37-55, Vol. II, pp. 77–79), the response time to a large step offset was found to be too slow to meet the requirements of the Space Science Tracking Program. Investigation showed that the rate amplifier was being overloaded by large signals. Redistribution of the amplifier gains eliminated this situation and permitted the antenna to respond normally to large offsets.

85-ft antenna. The hardware for the servo automation test (SPS 37-55, Vol. II) has been installed and tested. Although time did not allow complete testing of the automation program software, preliminary tests have been satisfactory. Further tests will be scheduled as time permits.

5. Cable-Driver Circuits, *D. W. Slaughter*

A previous article (SPS 37-55, Vol. II, pp. 89–91) describes a line driver being developed as an addition to the line of Hi-Rel digital logic modules (SPS 37-46, Vol. III, pp. 159–161). This line driver utilized a current-mode output circuit. In the interim, a voltage-mode cable driver has been developed. (The term cable driver has been adopted as preferable to the term line driver.) The relative value of these circuits is being investigated.

In SPS 37-55, Vol. II, the following functional characteristics were listed as desirable:

(1) Provide a bipolar output.

(2) Provide independent selection of the positive and negative logic output voltage levels.

(3) Provide a maximum signal swing large enough to drive all known or reasonable devices.

(4) Produce clean signals for driving analog devices.

(5) Drive long signal lines, 100 ft or more.

(6) Be compatible with the existing line of modules.

Figure 46 diagrams the equivalent circuits for two basic forms of cable drivers. Figure 46a is a Norton equivalent circuit for a current-mode driver. As a digital driver, the current source will assume one of two values representing the binary logic 1 and 0. These values may be a current and absence of a current, or perhaps a change in current polarity from plus to minus. In the Thevenin equivalent circuit of Fig. 46b, the voltage source also assumes one of two discrete values. The purpose of both circuits is usually the production of a voltage across the load resistor at the end of the cable.

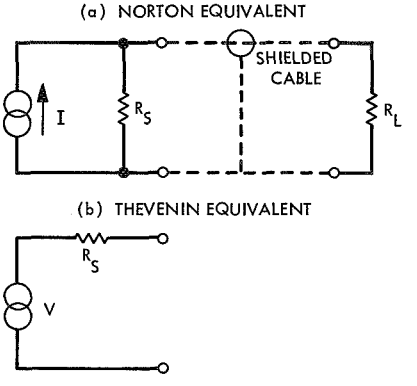

Fig. 46. Equivalent circuits

In cable-driving applications, the minimization of cable reflection and ringing may require that the driving source impedance (designated *Rs* in the equivalent circuits of Fig. 46) be matched to the cable characteristic impedance. For the transmission of linear signals, the cable-driver source impedance may be determined by negative feedback or other internal characteristics of the amplifier. While digital signals may be processed by linear amplifiers, switching circuits are usually more applicable. The transistor switch approaches an infinite impedance when *off* and a zero impedance when *on*.

Figure 47 is a simplified schematic of a voltage-mode driver using saturating transistor switches to switch between a positive and a negative source. Resistor R1 provides the source resistance when transistor Q1 is switched *on* (Q2 is an open circuit), while resistor R2 serves the same purpose when Q2 is switched *on* (and Q1 is an open circuit). For the current-mode driver described in SPS 37-55, Vol. II, the source resistance for matching the cable (if required) was a shunt resistor, 50 Ω for a 50-Ω coax. The following factors are being considered in determining the relative value of the two driver circuits:

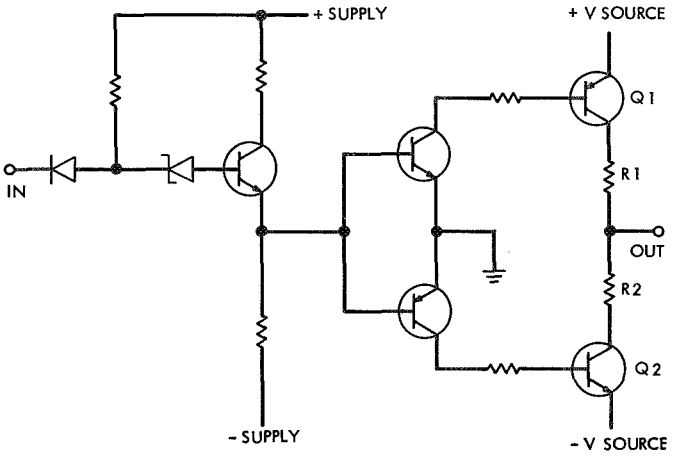

Fig. 47. Simplified schematic of voltage-mode driver

(1) Cost factors, including the cost in space, i.e., the number of circuits that can be placed on one standard module.

(2) Reliability, including both catastrophic failure and ability to remain within the specified performance characteristics.

(3) Ability to provide the desired functional requirements.

The current-mode circuit has one significant disadvantage. The voltage drop across the output transistors produces a significant amount of transistor heat dissipation (depending on the load resistance), whereas the voltage-mode driver utilizes the transistors as switches dissipating very little power. Transistor dissipation in the current mode requires that the transistors be mounted on an adequate heat sink, and possibly limits the number of circuits to one per logic module. Unless the heat sinking is adequate, transistor dissipation poses a reliability problem.

One advantage of the current-mode arrangement is its insensitivity to ground potential. The current supplied to the cable by the current source is independent of the ground potential existing between the current generator and the load impedance at the user end of the cable.

However, the value of this performance characteristic may not be significant because:

(1) When coaxial cables are used, significant ground potential does not usually exist.

(2) When the cable driver is utilized for signal coupling between Hi-Rel logic modules, these logic modules provide a high degree of noise immunity.

The current-mode driver also provides better waveforms at the terminal end of cables which are mismatched or which possess an uncertain characteristic impedance.

The two circuits are also significantly different in their arrangements for independent adjustment of the positive and negative logic levels. The logic levels of the current-mode driver reported in SPS 37-55, Vol. II, are adjustable by selecting resistor values. The voltage-mode circuit requires variable power supplies although their circuitry need not be very complex.

One application of the cable driver is the phase modulation of RF carriers. While the modulation is binary, the degree of phase displacement (depth of modulation) may be a function of the logic voltage level. The voltage-mode driver provides better logic voltage stability than does the current-mode circuit.

A tentative decision has been made to utilize the voltage-mode driver, whose complete circuit is shown in Fig. 48. A design review has been held at which a number of potential engineering users reviewed the circuit, worst-case analysis, and applications data. An etched circuit layout has been completed and 20 sets of parts have been ordered for the fabrication of prototype models. However, work is continuing on the development of a packaging design for the current-mode circuit. Two-thirds of the components can be used in either circuit.

The characteristics of the voltage-mode cable-driver module are summarized in Table 32.

Table 32. Characteristics of voltage-mode cable-driver module

Characteristic	Value
Input voltage, V	
Logic 0[a]	−1 to +3
Logic 1	+5 or more
Output impedance, Ω	50
Output voltage, open circuit, V	
Logic 1 input	+12
Logic 0 input	−12
Output voltage, 50-Ω load, V[b]	
Logic 1 input	+6 ± 3%
Logic 0 input	−6 ± 3%
Propagation delay, ns	
Typical	25
Worst case (estimated)	40
Switching speed, 50-Ω load (90 to 10% points), ns	
Typical	8
Worst case (estimated)	15
Frequency, MHz	0 to 3
Operating temperature, °C	10 to 100

[a]Signal source must sink 2 unit loads.

[b]Values are for nominal supply voltages with output emitters tied to supply voltages. These emitters may be connected to external supplies of 2 to 12 V, independently adjustable.

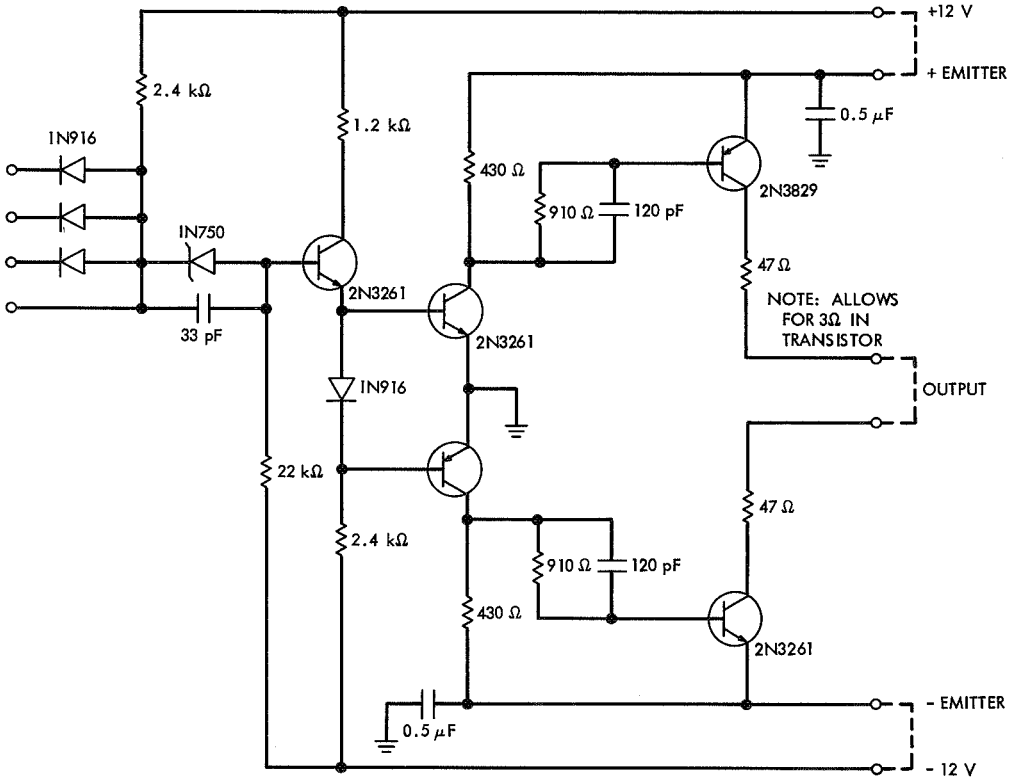

Fig. 48. Cable-driver schematic

IV. Development and Implementation

A. DSIF Development

1. DSIF Systems Test Analysis and Verification, *R. W. Burt*

a. Introduction. DSIF system performance is evaluated by measurements made on each of the various system functions, e.g., the telemetry, command, ranging, signal level tracking functions, and comparison of the results against a theoretical model. The methods and results used for the high-rate telemetry function and the signal level tracking function were presented in SPS 37-51, Vol. II, pp. 118–121 and 132–136. This article presents the method used for evaluating the weak-signal performance of the doppler tracking function. Testing techniques are given and predicted and measured results compared for test data obtained at Compatibility Test Area 21 (CTA 21). A test description (DXZ-1150-6-TD), along with the required computer programs, has been released through the DSN and used successfully to verify doppler tracking performance at several stations.

b. Predicted performance. The parameter chosen for evaluation of weak-signal doppler tracking function performance is the phase-error variance appearing at the output of the doppler extractor detector. The variance was predicted using a computer analysis program by Tausworthe (SPS 37-42, Vol. III, pp. 60–61), which solves the formulas

$$\sigma^2 = \frac{\pi^2}{3}\left\{1 - \exp\left[-\frac{3a^2}{\pi}(1 + 0.13a^2)\right]\right\} \tag{1}$$

and

$$a^2 = \frac{1}{2\rho_0 m w_{L_0}}\left(\frac{w_{L(eq)}\Gamma}{\gamma^2}\right) \tag{2}$$

where

m = receiver margin above loop design signal power P_0

ρ_0 = signal-to-noise ratio (SNR) in receiver passband w_{L_0} Hz wide at the power level P_0, $\rho_0 = P_0/kTw_{L_0}$

w_{L_0} = two-sided linear theoretic bandwidth at design point (often designated $2B_{L_0}$)

The parameters in brackets in Eq. (2) are discussed in SPS 37-42, Vol. III, as well as operation of the program. Some of the receiver parameters, also required by the program, are:

Values from DSIF specifications

$$T_1 = 2468.0 \text{ s}$$

$$T_2 = 0.1388 \text{ s}$$

$$\rho_0 = 1$$

Values measured at CTA 21

$$\text{Loop gain} = 4.895 \times 10^6$$

$$BH = 2474 \text{ Hz}$$

The receiver is considered to be the most sensitive portion of the doppler function.

Figure 1 shows the performance predicted by computer analysis. The two-sided linear theoretic bandwidth at design point w_{L_0} was also predicted (12.1 Hz). Therefore, according to the definitions given, $P_0/kTw_{L_0} = 1$ for a margin m of 0 dB. This results from the DSIF design specification of $\rho_0 = 1$. The requirement of the test and evaluation is, then, to set various margins, measure the resulting phase variance, and compare with the predicted performance.

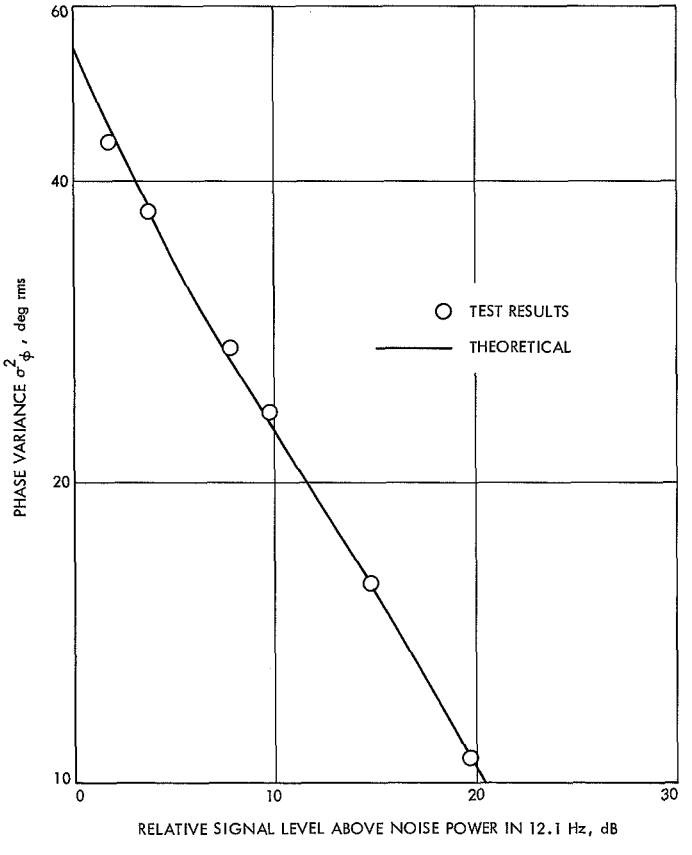

Fig. 1. Doppler phase noise above relative signal level

c. Test setup. Figure 2 shows the test setup used at CTA 21. Coherent two-way lock is attained and various SNRs in $w_{L_0} = 12.1$ Hz are set using the power-level measurement equipment, variable attenuator A3 and the fixed attenuator A2. The step attenuator A1 is maintained at a high value to reduce the effects of leakage. At each margin, doppler phase error is measured at the doppler extractor 0- and 90-deg outputs using a doppler jitter program (DOI-5005-RD).

d. Margin setup technique. The technique used consists of accurately measuring the ratio of carrier-plus-noise power to noise power. First (see Fig. 2), power indicator M1 is adjusted for full-scale deflection with the RF signal turned off. Next, the required Y-factor is inserted in precision attenuator A4 and, with the RF signal turned on, A3 is adjusted until the power indicator is returned to the same value. The required Y-factor is determined from the desired margin m from the relation

$$Y = 10 \log_{10} [(m + A_1 - 10 \log_{10} F) + 1]$$

where F is 9.867 kHz as determined from the average of four bandwidth measurements. Step attenuator A1 is a fixed attenuator of value known to an accuracy of 0.1 dB and is chosen to give values of Y between 5 and 15 dB. The worst-case error in setting SNRs by this technique was evaluated in SPS 37-51, Vol. II, pp. 132–136. There, it was shown to be ±0.25 dB when the error in A2 is included. Experience with multiple-mission telemetry and high-rate telemetry indicates that this is a reasonable number.

e. Data collection and reduction. The digital instrumentation system (DIS) was used to gather and process data. Both doppler phase inputs (0 and 90 deg) are recorded and the one nearest 0 deg for each set of five samples is used for data reduction. This procedure allows the receiver to be followed up to phase errors of 90 deg and during cycle slips. The phase detector is assumed to be sinusoidal and to sample phase angles determined by the formula

$$\theta = \sin^{-1} \frac{V}{V_{\text{peak}}}$$

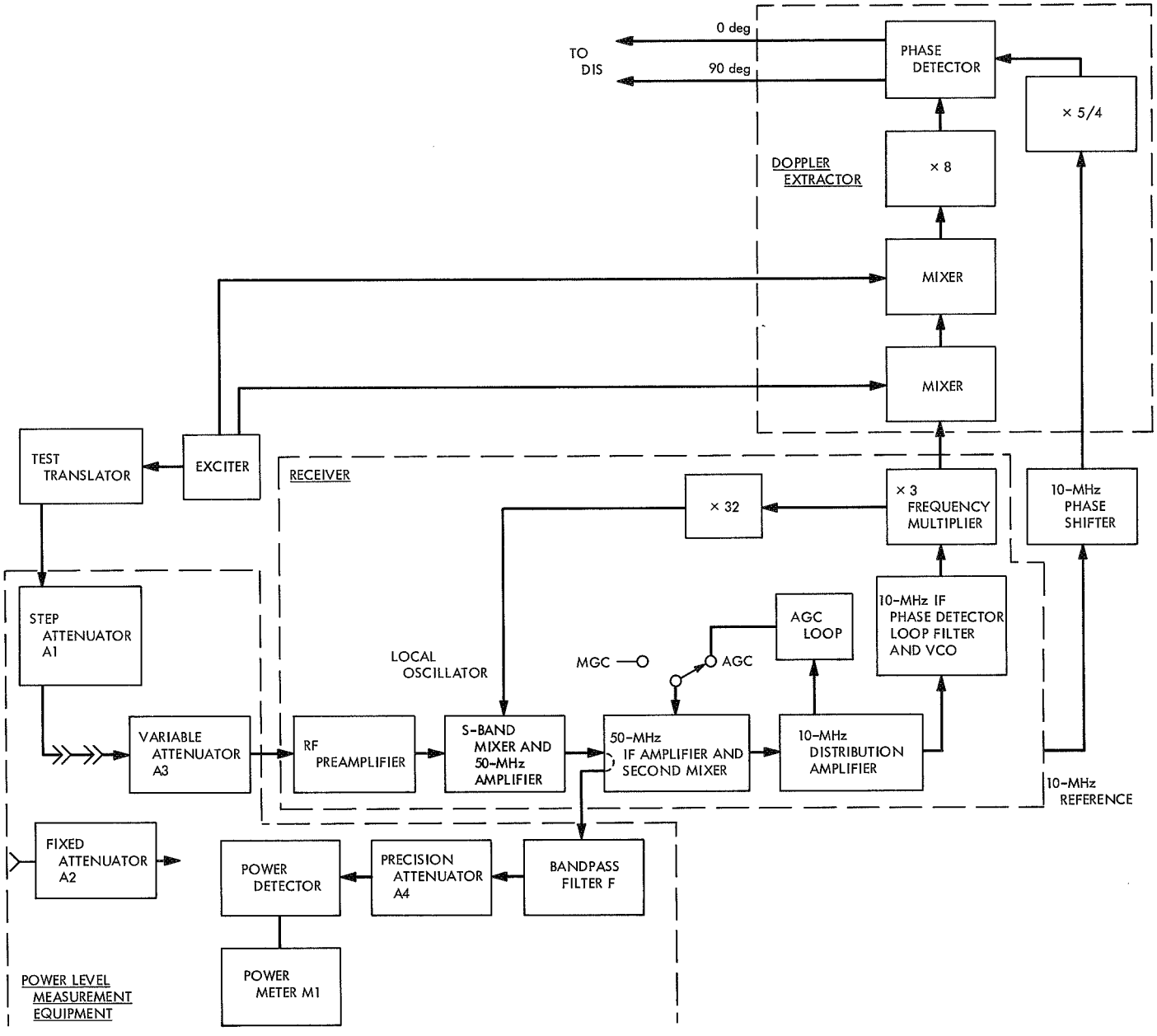

Fig. 2. Doppler phase variance test setup

where V_{peak} is the peak output of the detector and V is the sampled voltage. Data are reduced by the formula

$$S^2 = \frac{1}{n}\sum_{i=1}^{n}\theta_i^2 - \bar{\theta}^2$$

where

S^2 = sample variance

θ_i = sample values

$\bar{\theta}$ = sample mean

n = number of samples

Enough sets of 5000 samples were taken at 1-ms intervals; the results were averaged to produce a smooth curve.

f. Test results and conclusions. Results of testing at CTA 21 are shown in Fig. 1. The mean error in data versus theoretical is ~0.2 dB. This close agreement indicates that

(1) The weak signal model of the doppler tracking function is valid.

(2) The two-sided linear theoretic bandwidth w_{L_0} is very close to the design value of 12.0 Hz at CTA 21.

These conclusions are predicated on the measurement errors involved. The worst-case error in setting margins is thought to be no more than 0.25 dB as discussed previously. There is also some error below margin values of ~6 dB due to sampling in and around transitions (cycle slips), which will require further investigation.

2. Programmable Frequency Divider and Pulse Generator for Receiver AGC Calibrations, *A. C. Shellbetter*

a. Introduction. The "pulsed-gate" method of carrier-level attenuation (SPS 37-53, Vol. II, pp. 102–107) requires a stable trigger pulse of constant width and variable repetition frequency to operate the P-intrinsic-N (PIN) diode modulator in a switching mode. By gating the PIN modulator *off* and *on* with a variable duty cycle, the test translator carrier is spread into a spectrum with a sin x/x envelope such that the change in magnitude of the carrier component from a reference level is a function of the change in duty cycle of the PIN modulator output. If the *on* pulse-width is constant, the change in carrier level is only a function of the change in pulse-repetition frequency (PRF).

$$\Delta(\text{dB}) = 20\log_{10}\left(\frac{PRF}{PRF_0}\right) \qquad (1)$$

where

Δ = change in carrier component magnitude from a reference level at initial PRF, dB

PRF = present PRF, Hz

PRF_0 = initial reference PRF, Hz

The pulse generator must provide a stable pulse-width, stable and precisely determined repetition frequencies, be remotely programmable, and also provide the proper wave shape and bias levels to facilitate rapid switching of the PIN modulator.

Figure 3 shows the block diagram of a programmable frequency divider and pulse generator which provides a simple and inexpensive means of fulfilling the above requirements. The programmable divider allows the clock frequency (500 kHz) to be divided by any integer between 1 and 999 and produces a stable 1-μs pulse at that repetition frequency. With this means, a reference power level (at unity divisor) could be provided by a Y-factor measurement or a similar method. Then a previously calculated sequence of divisors, corresponding to PRF changes of the proper proportion to give the desired attenuation increments, could be read into the divider to generate a receiver automatic gain control (AGC) curve. The divider can be programmed manually with thumbwheel switches or, with the addition of the proper interfacing hardware, by a computer.

b. Functional description (Fig. 4).

Clock shaper. A Signetics 526 high-speed comparator integrated circuit is connected as a zero crossing detector in such a way that, when the input 1-MHz sine wave is positive, the output of the shaper is +4 V. When the input is negative, the output is approximately 0 V. Thus, the output is a square wave with rise and fall times on the order of 10 ns at the same frequency as the input. The high gain of the comparator allows a trigger-level uncertainty of approximately ± 1 mV.

Divide by two. A stable pulse-width of approximately 1 μs is desired for triggering the PIN modulator. This pulse-width is obtained by digitally dividing the 1-MHz square wave by two. The output of the flip-flop is a 500-kHz square wave (thus generating a stable 1-μs *"on"* pulse-width), which is used to clock the counter. The inverted output of the flip-flop supplies the $\overline{clock}$, which is required in the reset logic of the counter. Pulse-width stability, using this method, is greatly improved over the standard RC time constant monostable multivibrator approach.

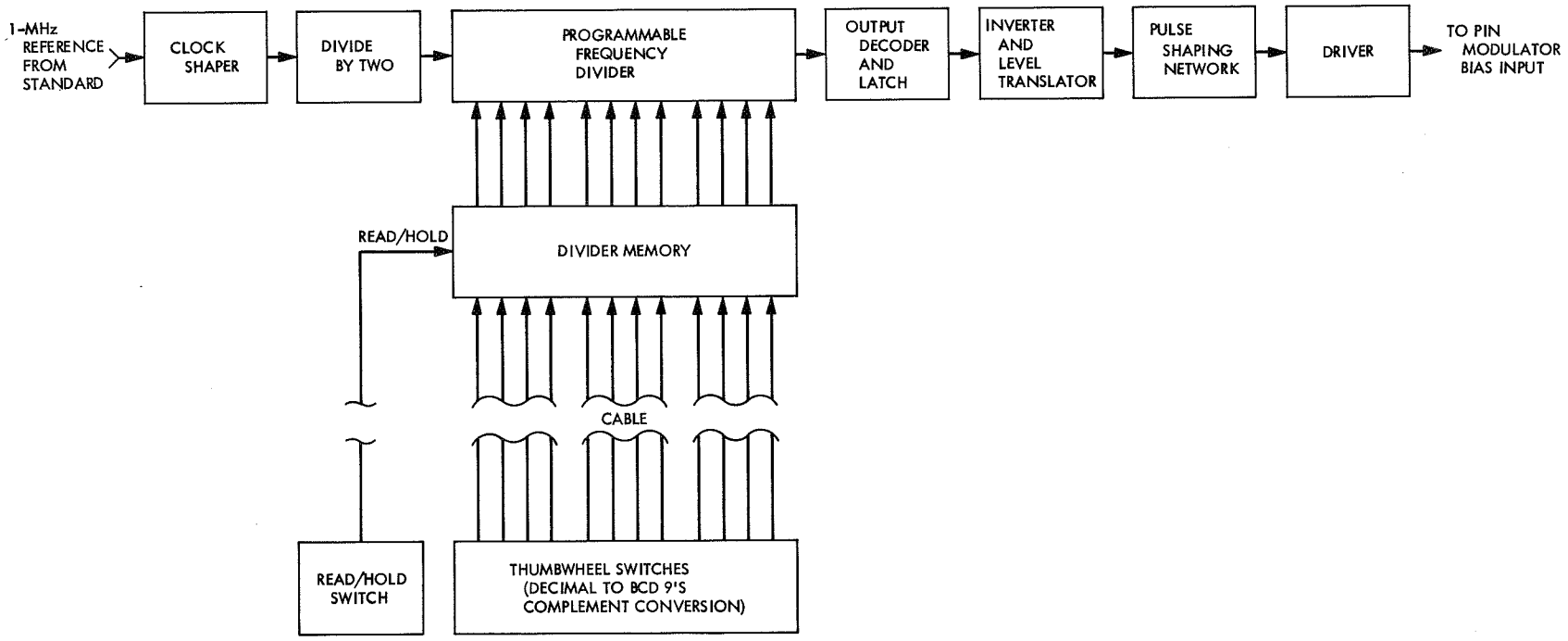

Fig. 3. Block diagram of programmable frequency divider and pulse generator

Counter. The 12-bit counter employs three 4-bit programmable decade counter integrated circuits connected in series to provide a maximum counting capacity or frequency division of 999. Each decade counter consists of four JK flip-flops connected as a synchronous binary-coded decimal (BCD) up-counter which counts logical "1" to logical "0" (high to low) clock transitions. Additional asynchronous input gating also allows the individual flip-flops to be preset to a given state programmed at the *data input* lines when the *data strobe* line is a logical "0". Information at the *data input* lines is locked out when the *data strobe* is at logical "1". In this way, the counter can be forced to any count in its normal sequence by applying the BCD representation of that count to the corresponding *data input* lines and pulsing the *data strobe* to logical "0."

Divider memory. In order to program the modulus of the counter, a means of storing the initial starting count at the *data input* lines is required so that the count will be available for resetting into the counter when the counter has completed its counting sequence. This memory function is provided by three quadruple bistable latch integrated circuits. Each latch has two inputs (*data* and *read*) and two outputs (Q and $\bar{Q}$). When the *read* line is at logical "1," Q follows the input at the *data* line and $\bar{Q}$ provides the complement of the *data*. Upon the *read* transition from logical "1" to logical "0," the information present at the *data* line just prior to the transition is retained at the Q output and its complement at $\bar{Q}$ as long as the *read* line remains low.

In this application, the desired divider is set on the thumbwheel switches, which are coded to convert the decimal number settings to BCD nine's complement at the output terminals. These nine's complement outputs provide the initial counts for each of the programmable counter stages. For example, to divide by 25, the initial count for the counters would be 999 − 25 = 974, or $\overline{0}$010,1110,1001 (most significant bit) in BCD. The latches hold the previous initial counting state until the thumbwheels have been set up for the next divider, thus eliminating extraneous counting sequences while the thumbwheels are being set. When the *read* line is pulsed, the initial state is read into the latches.

Output decoder. The output decoder is merely an eight-input *nand* gate that detects the count 999. When the count reaches 999, the output of the *nand* gate X goes low, which sets the output latch.

Output latch. When X is high, Y is held low and Z is held high by the "latching effect" of the cross-coupled gates. In the counting sequence, X goes low on the negative clock transition of the last count in the sequence. Thus, when X goes low, $\overline{clock}$ goes high, causing Y to go high and Z, the *data strobe*, to go low, which resets the counter to the initial count. The latch remains in this state until $\overline{clock}$ goes low, which resets the latch to its normal state (Y = "0" and Z = "1").

The output of the latch Y is a single pulse of approximately 1-μs width at a PRF of (500/divisor) kHz.

Inverter. The Fairchild μL 9900 buffer is used to invert the Y output of the latch and provide a higher driving capability to rapidly switch the level translator stage.

Level translator and pulse shaper. For optimum switching of the PIN modulator, a special waveform is required such as that shown in Fig. 5. The "spikes" on the leading and trailing edges of the pulse provide the overdrive needed to facilitate rapid injection and withdrawal of charge from the PIN diodes.

The level translator is a single transistor stage operating in a switching mode that transforms the +4- and 0-V logic levels of the μL 9900 to approximately +15 and −5 V, respectively.

The pulse-shaping network is an over-compensated resistive voltage divider which divides the +15, −5-V output of the level translator to the approximately +7, −2.5 V required by the PIN modulator and produces the desired "spikes" on the leading and trailing edges.

Driver. The National semiconductor NH0002C is a hybrid complementary emitter follower-type current amplifier and is used to provide the low-impedance driving capability needed to drive the PIN modulator bias input through a coaxial cable.

c. Sequence of operation. The sequence of the divider will be carried through for a divisor of six to indicate the overall operation of the divider (Fig. 6).

The desired divisor (six) is first set on the thumbwheel switches. The initial count is then available at the inputs of the divider memory. A momentary "1" level on the *read* line allows the initial count to be read into the latches, and the initial counting state (993) is then present at the *data input* lines to the counter. The counter

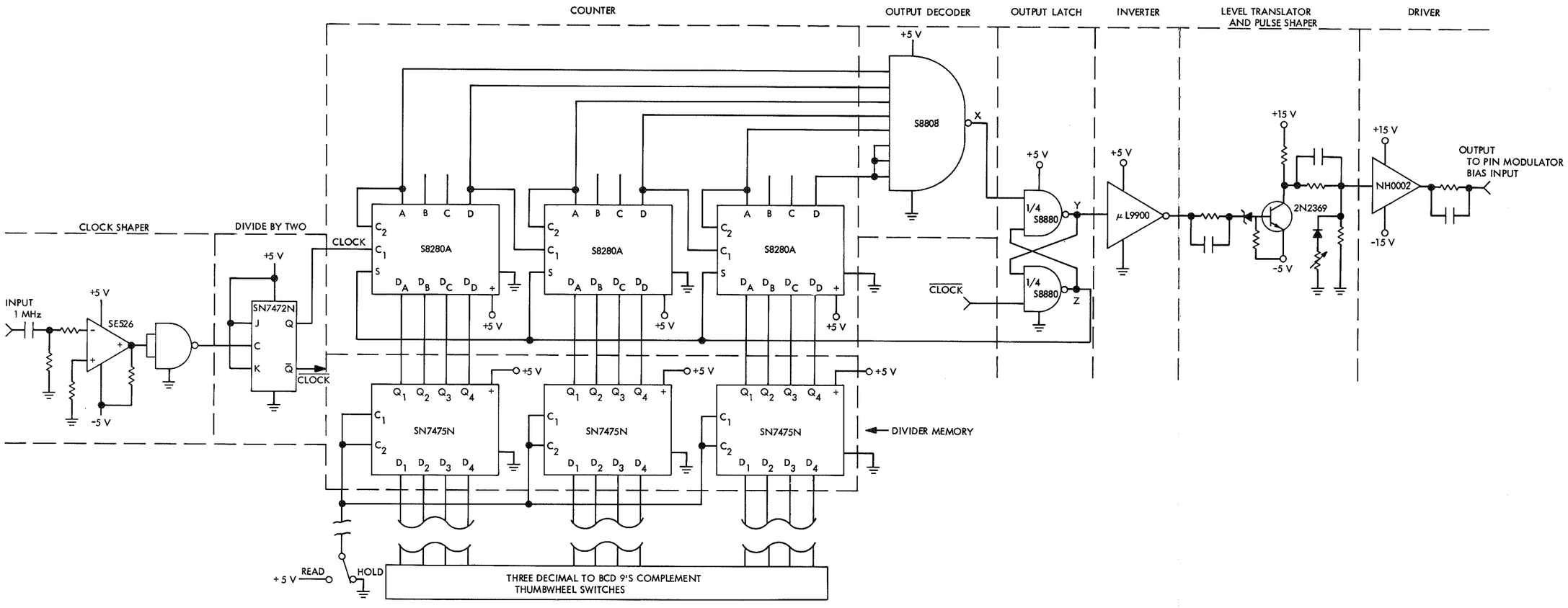

Fig. 4. Schematic of programmable frequency divider and pulse generator

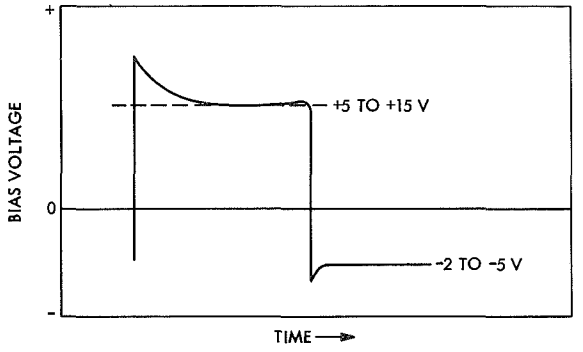

Fig. 5. PIN modulator bias waveform

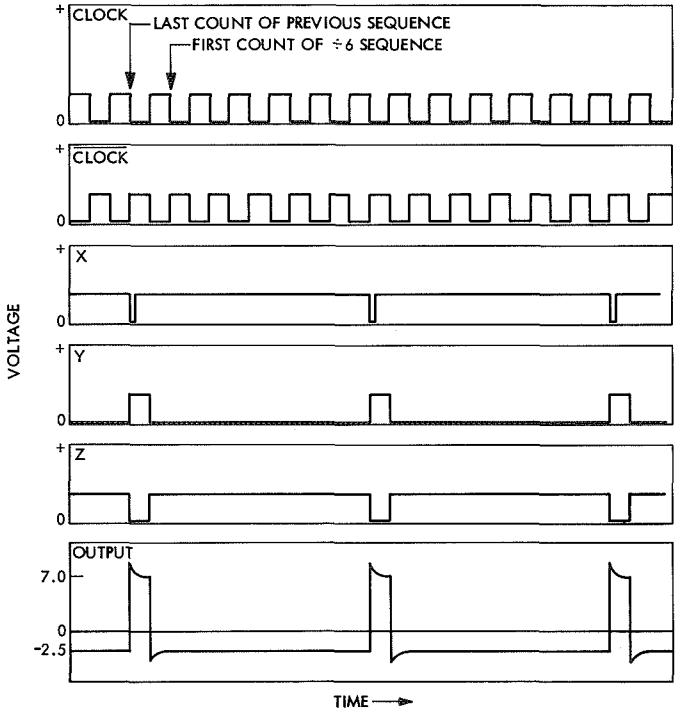

Fig. 6. Timing diagram for division by six

completes its present sequence when the count 999 is reached. The output latch is then set, causing *Y* to go high and *Z* to go low, which reads the initial count of the new sequence into the counter.

Output *X* then goes high, "priming" the latch. After approximately 1 μs, $\overline{clock}$ goes low, resetting the latch to its normal state. On the next "1" to "0" clock transition, the counter begins to count from the initial count of the new sequence and counts up to 999, giving an output pulse at *Y* and resetting the initial state. This cycle repeats until the divisor is changed on the thumbwheels and read into the memory.

d. Conclusions. Precise stability tests have not been conducted as yet. However, preliminary tests indicate that pulse-width variation of less than 0.1% is obtainable. This would allow the portion of the overall attenuation error contributed by pulse-width instability to be less than $\pm$0.01 dB. Other sources of error are the stability of the "*on*" insertion loss of the PIN modulator caused by temperature variations and bias-level changes. These errors contribute approximately an additional $\pm$0.01 dB to the overall attenuation error.

The integral frequency division method provides a simple means of providing discrete frequency increments that would be suitable for AGC calibration. However, for an essentially infinite resolution attenuator, a frequency synthesizer would be required to provide the necessary frequency resolution.

3. DSIF Monitor System Phase I Development, *F. B. Leppla*

The DSIF Monitor System Phase I (MSϕ1) is being developed within the DSIF to provide various monitor data for the DSN and DSIF deep space stations. This system is presently being implemented for use in the digital instrumentation subsystem phase II (DIS II) for support of the *Mariner* operations.

The original intent and design of the MSϕ1 was to provide a mission-independent system that was flexible enough to provide support for various tracking assignments. At the present time an operational version of the MSϕ1 is being implemented and used within the DSIF. This version of the program does not meet the original overall design goals for several reasons.

During the last two months a large amount of effort has been spent in the testing and validation of version I of the MSϕ1. Several discrepancies have been discovered. At the same time, software development personnel have been used to provide on-site training in the use and operation of the system. The testing, validation, and training accomplished within this period have produced much useful information in regards to the overall philosophy of a monitor system. Several problem areas are now being investigated.

To provide the monitoring and performance evaluation of a DSIF tracking station, the MSϕ1 performs the following basic functions:

Configuration monitoring. Tests approximately 120 switch positions or operating modes of other subsystems.

These indicators are tested against one of a series of standard configurations supplied on a magnetic tape.

Status monitoring. Tests approximately 40 status indicators from various subsystems and performs appropriate computations as required.

Performance evaluation. Performs conversion/computation of various input data that are then checked against tolerances supplied on a magnetic tape. This function operates on approximately 40 parameters.

Alarm generation. From inputs supplied by one of the above items, generates output to any of the following devices:

(1) High-speed data line (HSDL).

(2) Teletype (TTY) output.

(3) Line printer output.

(4) Page printer output.

(5) Station manager alarm panel.

Recording. Logs all input data on a magnetic tape.

The DSIF Monitor System is only a part of an overall system design. In order to operate properly, the DSIF portion requires inputs from three computer programs located within the SFOF:

(1) *MCDX.* Provides station configuration, performance tolerances, and nominal values.

(2) *PRDX.* Provides tracking prediction information such as angles, doppler, range, and frequencies.

(3) *CP2M.* Provides signal to noise and received signal strength predictions.

Within the DSIF, the monitor must interface with the following computer programs:

(1) antenna pointing subsystem.

(2) mission-dependent telemetry and command processor programs.

(3) monitor calibration, which provides station calibration data.

The output data generated by the DSIF monitor is processed or manipulated by other computer programs. At this time the list includes the following:

(1) *Post-track report.* On-site generation of the post-track report and direct outputs for TTY transmission.

(2) *Communications processor.* Handles backup TTY messages for display within SFOF.

(3) *7044.* High-speed data message logging and routing to the display buffer.

(4) *DBOS.* Generates digital TV displays of selected monitor data and performs monitor data logging.

Figure 7 presents an overall system interface description and data flow; the overall system is basically operational at this time.

The DSIF portion of the system is also operational. Certain technical discrepancies exist and have been documented. The overall design goals and basic philosophy are being reviewed in order to provide an orderly upgrading in the development of the DSIF Monitor System.

4. Frequency and Timing Subsystem Phase II, *P. C. Harrison*

An attempt to install frequency and timing subsystem phase II (FTS II) at five DSIF stations was thwarted by intermittent failures in the digital isolation amplifier. This amplifier provides isolation and drive power for 50 channels of digital information. After a concerted effort, the problem was isolated and possible solutions were evaluated. The manufacturer of this isolation amplifier will participate in the instrument evaluation and perform the required modifications.

As a test monitor of the modified instrument, the Laboratory SDS 920 computer was utilized. The inputs and outputs of the isolation amplifier are compared and, when a difference is detected, a printout on the line printer gives the input number, output number, and time of occurrence.

It is felt that upon completion of this modification and testing of the FTS II installation may be completed. Due to turn-around and test-time requirements, this will be accomplished after *Mariner* Mars 1969 encounter. Also at that time, the FTS II spares will be completed, evaluated, and distributed to the five stations.

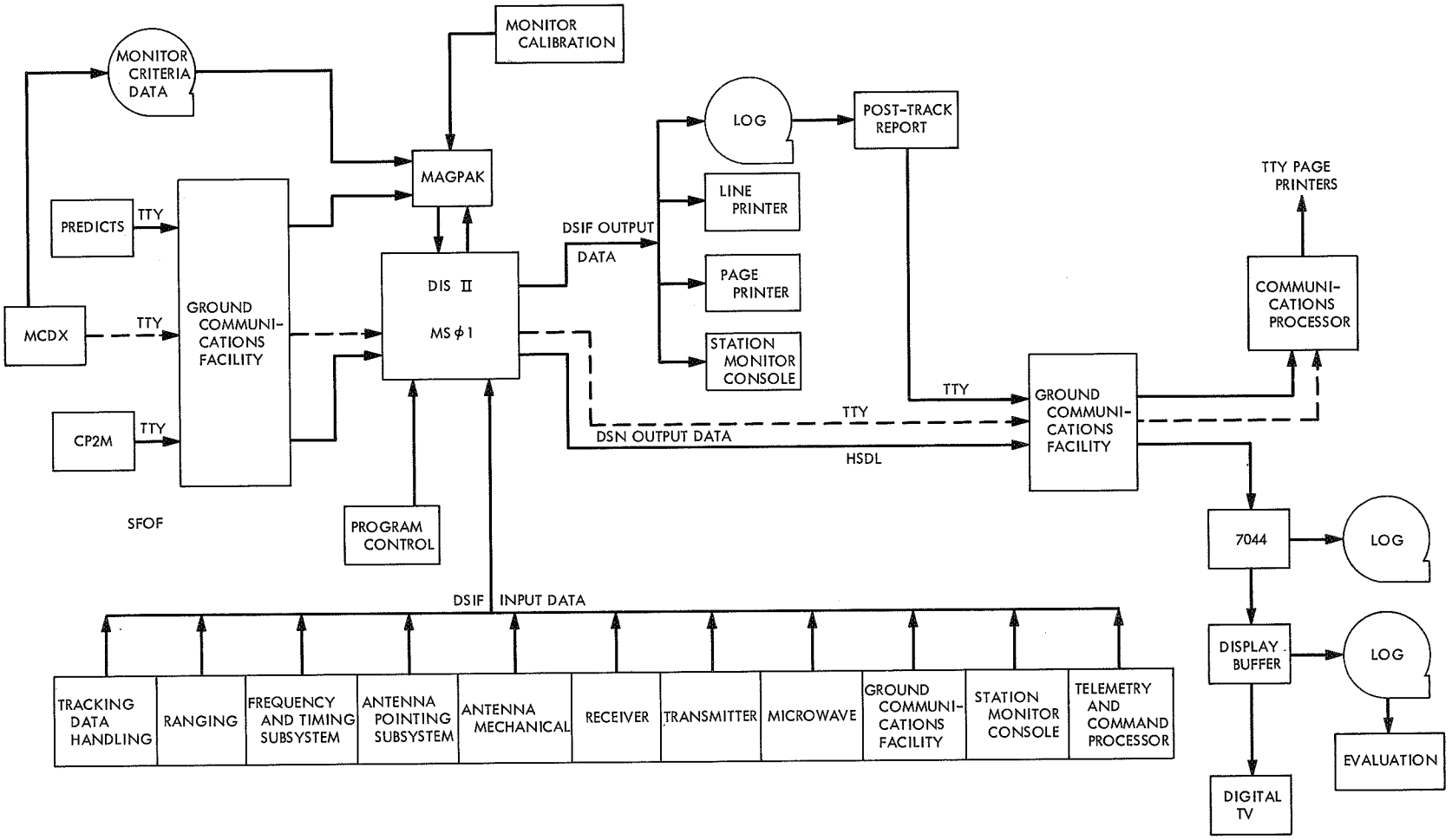

Fig. 7. Monitor system interfaces and data flow

5. Clock-Synchronization System Performance, *H. W. Baugh*

A precision clock-synchronization network is being established to meet the requirements of the DSN. The immediate goal for this system is to provide synchronization between all stations committed to *Mariner* Mars 1969 to within 20 μs at the time of planetary encounter. A second objective is to provide correlation to the National Bureau of Standards (NBS) to within 5 μs for the DSN as a whole.

The system uses a computer-controlled transmitter at DSS 13 to send timing signals to the remote stations by way of an X-band carrier that is reflected from the surface of the moon. The system being used was first described in SPS 37-43, Vol. III, pp. 92–106 and in SPS 37-45, Vol. III, pp. 72–75. Results of field experiments have been described in SPS 37-47, Vol. II, pp. 90–92, SPS 37-50, Vol. II, p. 165, SPS 37-53, Vol. II, pp. 97–99, and SPS 37-54, Vol. II, pp. 82–83. The present article will cover the operations of the system from September 1, 1968 to February 5, 1969.

Clock-synchronization operations are continuing on a near-routine basis whenever the master station at DSS 13 and the receiver at DSS 42 have a common view of the moon during normal working periods. Schedules and predicts are normally sent to the receiving station several weeks in advance, and are followed up with a weekly teletype message confirming the transmission schedule for the next week.

As noted in SPS 37-54, Vol. II, numerous interruptions occurred during September and early October due to transmitter upgrade and overhaul, and to some misunderstanding in the requesting of computer runs to extract predict information from the lunar ephemeris, the latter accounting for one 2-wk interval of down-time during September. From mid-October to mid-November, 70% of the scheduled transmissions resulted in successful checks of the DSS 42 clock. However, sufficient volume of coherent data was not acquired to warrant detailed statistical analysis or plotting of information for this article.

In mid-November, the waveguide switches were removed from the transmitter feed system for modifications to reduce their insertion losses, and hence to offset a heating problem that had accompanied the increase to 20 kW in the output power. The modifications were successfully completed and the transmitter returned to service on December 7, but DSS 42 was unsuccessful in receiving the signals until the end of January 1969. Six days were lost in December when a drive coupling failed in the DSS 42 antenna; another 27 days were lost in January when the main drive clutch failed and a complete unit had to be shipped from JPL.

When the mechanical problems were corrected, the original lack of success was discovered to be the result of an incorrect setting of the transmitter polarization switch. The polarization had inadvertently been changed when the modified waveguide switches were installed; this fact was not discovered until DSS 42 experimentally changed their polarization. The transmitter polarization can only be changed by climbing the 30-ft antenna, so it was decided that it will be left in the "left-hand circular" position, and all receivers will use "right-hand circular" settings. (Needless to say, this will be written into the standard procedures, and all new receivers will be checked to ascertain that they can function with either right- or left-hand polarization on the transmitter by setting their polarization switches accordingly.)

The system became operational again on January 31, 1969, just in time to prepare for a visit to DSS 42 by a portable clock from the Smithsonian Astrophysical Observatory (SAO). The SAO clock had been set (with a tolerance of 5 μs) to the standard time kept by the U.S. Naval Observatory (USNO), and it visited a number of sites in Australia, stopping at DSS 42 and Mount Stromlo on February 4, 1969. On that day there were two other significant events: (1) the moon-bounce between DSS 13 and DSS 42 was successful, and (2) the Radio Standards Laboratory (RSL) at Goldstone provided a portable clock check of the DSS 13 time standard with respect to NBS/USNO. Thus, all the information required for an independent check of the system is available and can be analyzed as follows:

The SAO clock was within 5 μs of USNO, and the DSS 42 clock was found to lead SAO (and hence USNO) by 109 μs. The moon-bounce operation showed that the DSS 42 clock led DSS 13 by 90 μs, so that the DSS 13 clock appears to have led USNO by 19 μs. The RSL check of DSS 13 showed it to be leading NBS/USNO by 22 μs, so that the overall closure error was 3 μs, which is well within the ± 5 μs tolerance of the original check of the SAO clock against USNO. (To be completely objective, it should be noted that the above is being reported before the final re-check of the SAO clock against USNO on its return to the U.S. At that time, the drift of the SAO clock during the trip will be known, but it is unlikely to be more than a few microseconds.)

Thus, the system has been shown to be capable of providing clock-synchronization services well within the requirements of the *Mariner* Mars 1969 mission.

The receiving antennas for the three overseas stations, DSSs 41, 51, and 62, have been shipped and are scheduled to be installed by station personnel early in March 1969. The receivers, which were built by Motorola, have had all the most recent modifications installed and checked out, and are currently being re-packaged into DSIF standard 7-ft racks which will be integrated into the frequency and timing subsystem area in those stations. The stations should be operable by early April.

6. Multiple-Mission Telemetry Baseband Signal Recording,

J. McInnis

a. Introduction. Overall reliability criteria dictate that spacecraft telemetry signals be recorded and preserved until data-recovery evaluation has confirmed correct functioning of downstream system elements.

The first point at which signal recording is technically feasible is at the interface between the receiver–exciter subsystem and the subcarrier demodulator assembly (SDA). At this interface the baseband telemetry signal (data modulated on a subcarrier, but without the IF component) is recorded, using an Ampex FR-1400 recorder.

The difficulties encountered in recording and reproducing this baseband signal have been reported in previous documentation. The problems have been adequately summarized in SPS 37-46, Vol. III, p. 184, as follows: ". . . the tape can be played back through the entire multiple-mission telemetry system (MMTS) in nonreal time to recover any of the telemetry data lost in real time due to failures in the SDAs. A degradation of the performance of the MMTS is encountered in this mode, due to limitations in the bandwidth capability and time-base instability of the tape recorder."

These two basic recording problem areas, bandwidth and time-base instability (or flutter), are actually quite distinct and separately subject to both analysis and corrective action. This article presents the deviations between the system requirements for this recording function and the capabilities of the existing recording equipment. In each case, the technical feasibility of either improving the performance of the recording equipment or providing external compensation for its deficiencies is discussed.

b. Bandwidth requirements. The baseband signal consists of a periodic square-wave subcarrier modulated with a non-periodic square-wave data stream. The SDA is designed and constructed with the objective of removing the square-wave subcarrier signal. Any deviation of the subcarrier from a square-wave format will produce degradation in SDA demodulation performance.

The record/reproduce cycle subjects the signal to the equivalent of a bandpass filter action, and the amount by which the subcarrier squarewave is distorted by such filtering controls the bandwidth-influenced aspect of SDA demodulation performance degradation.

Figure 8 is a normalized representation of a square-wave signal spectrum. It is readily obvious that significant portions of the signal energy are contributed by frequency components far removed from the equivalent fundamental frequency. A summation (or piece-wise integration) of the spectral power represented by the amplitude function curve of Fig. 8 provides a ready

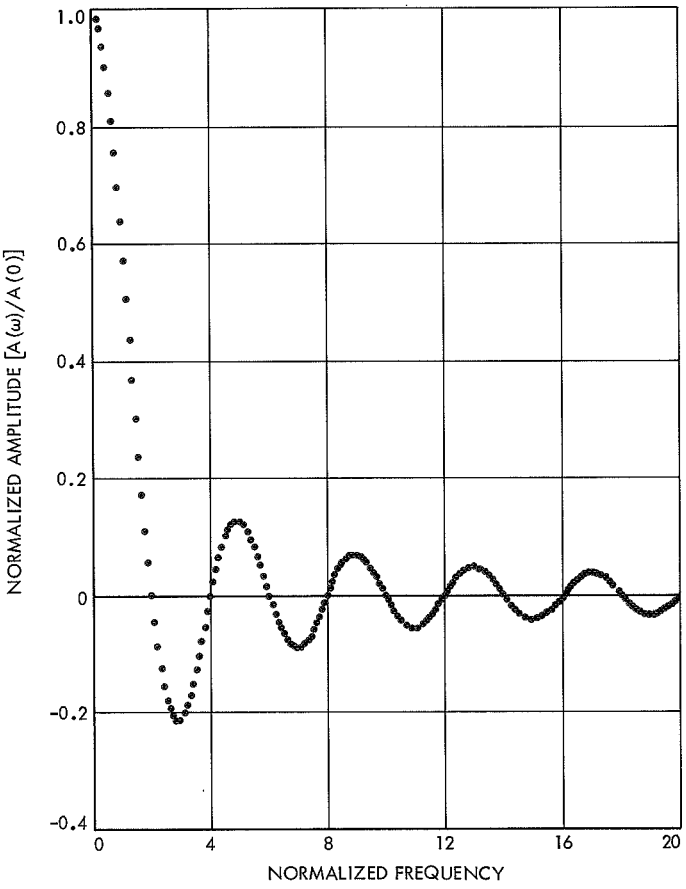

Fig. 8. Square-wave spectrum

determination of the relative effect of any proposed bandwidth limitation within the computed limits. For example, an increase of 12% in spectral power passage can be achieved by using a bandwidth equal to twice the fundamental frequency, rather than one equal to the fundamental frequency itself. A further bandwidth widening from 2 to 4 times the fundamental frequency provides an additional 4.9% improvement in spectral power transmission, but expanding still further to 20 times adds only another 3.8%.

Based on the above, it is reasonable to state that a record/reproduce bandpass characteristic that does not include frequency components out to at least twice the square-wave fundamental frequency will produce severe distortion of the subcarrier waveform. Expansion of the bandpass in the region between two and four times the fundamental frequency will produce successively better approximations of the signal waveform, but at about four times the fundamental, the point of diminishing returns is reached.

The repetition rate (fundamental frequency) of the subcarrier signal takes on discrete values in the range from 20 to 80 kHz,[1] while the equivalent data-stream bit rates occupy the range from 8 to 512 Hz. A record/reproduce system capable of preserving the character of the high-frequency subcarrier signals will not introduce bandwidth-related disturbances of the data stream.

In summary, a bandwidth equal to twice the fundamental square-wave frequency is essential and further widening toward approximately four times the fundamental is desirable. The actual frequencies represented by these requirements are determined by the operational subcarrier frequencies.

c. Bandwidth capabilities. The record/reproduce cycle bandpass capability of a magnetic-tape recorder is mainly dependent on two factors: (1) the record/reproduce head design, and (2) the tape speed. Although the bandpass characteristic of the recorder electronic package could provide a limitation, this factor is so easy to eliminate that it is seldom a decisive factor. Likewise, the grain size of the magnetic-tape oxide coating could, theoretically, represent a limitation, but modern manufacturing techniques have eliminated this factor from need of consideration over the frequency range germane to this study.

[1]If used for *Pioneer* operations, the lower limit of the subcarrier frequency is reduced to 2 kHz.

Query of Ampex Corp. technical representatives at JPL reveals that their company is not prepared to supply any alternative FR-1400 record/reproduce heads that would improve its high-frequency characteristic. Further, they admit to no knowledge of heads of other make that would be compatible with the FR-1400 and that might provide a bandwidth improvement over the existing heads. This leaves only the tape speed as a control factor in the determination of record/reproduce system bandwidth capability.

Table 1 relates FR-1400 tape speed to bandwidth[2] as well as the desirable and absolute maximum subcarrier frequencies for each of the listed speeds. These maxima are subject to interpretation based on the portion of the allowable overall SDA performance degradation that can be allocated to bandwidth-related effects. If other sources of degrading influence are present to any considerable extent, the "desirable" maxima may become the "absolute" maxima, when the system is taken as a whole.

Table 1. Direct record bandwidth and subcarrier frequency limits as a function of tape speed

Tape speed, in./s	Bandwidth (±3 dB), kHz	Desirable $F_{sc(max)}$, kHz	Absolute $F_{sc(max)}$, kHz[a]
7.5	0.40–90	22.5	45.0
15.0	0.40–185	46.0	92.5
30.0	0.40–375	93.5	187.5
60.0	0.40–750	187.0	375.0
120.0	0.40–1500	375.0	750.0

[a]Same SDA degradation results when the tape speeds are used with these subcarrier frequencies.

d. Time-base instability (tape flutter). The second degrading factor encountered in the use of the baseband signal record/reproduce mode is an instability in the reproduced signal's time base. This is caused by local short-term variations in the tape speed (commonly called "flutter") that may occur during the record cycle, the reproduce cycle, or (usually) both.

The flutter problem is quite distinct from considerations of the recorder's long-term time-base accuracy. If a tape that took an hour to record will playback for exactly an hour, or an event that occurred x number of minutes

[2]*Detail Specification for 1.5 MHz Dual Transport Recorder/Reproduce Group Recording Subsystem*, JPL Specification DOK-1219-DTL, Rev. B, p. 8, Nov. 3, 1967.

from the beginning of the recording is reproduced at exactly x minutes from the beginning playback, the long-term accuracy factor is involved. Flutter, on the other hand, regulates the relation between the time duration of a given short-term time interval at playback to its duration at record. Alternatively, flutter can be discussed in terms of the relative durations of two different short intervals within the same tape. Flutter, then, is a short-term effect, typically representing milliseconds or microseconds of instantaneous timing error.

The observed effects of flutter are variations in the frequency (or perhaps phase) of signals reproduced from the tape. The long-term accuracy factor establishes the nominal output signal frequencies, while flutter causes frequency or phase perturbations about these base frequencies. As an example, if tape flutter resulted in time perturbations of 1 μs rms, this would represent approximately 7 deg rms of phase fluctuation for a 20-kHz subcarrier signal or 29 deg rms for an 80-kHz signal. Although not necessarily random in nature, such perturbations adversely affect the effective system signal-to-noise ratio.

In general, tape flutter perturbations occur at rates that are fast when compared with the electro-mechanical time constants of the recorder's tape-drive system. It is not feasible, therefore, to attack the flutter problem through modifications to the tape-drive control system unless there is some underlying abnormality in its operation. Even a well-designed tape machine will exhibit residual flutter and only a redesign of the tape-handling assembly (based on new performance criteria) would provide significant improvement.

e. System flutter specifications and performance. The FR-1400 recorder's maximum permissible flutter, as a function of tape speed, is presented in Table 2.[3]

[3]*Functional Specification Deep Space Instrumentation Facility Recording System*, JPL Specification DFK-1012-FNC, Rev. B, p. 28, Dec. 5, 1967.

Table 2. FR-1400 flutter specification requirements

Tape speed, in./s	Tape flutter tolerance (p–p), %
7.5	1.0
15.0	0.5
30.0	0.4
60.0	0.3
120.0	0.25

Informal conversations with personnel concerned with the operation and maintenance of FR-1400 recorders at JPL Pasadena and Goldstone indicate that the typical flutter figures actually observed range from about one-half to three-quarters of the tolerances specified in Table 2.

Conversion of these peak-to-peak (p–p) flutter values to other forms (e.g., rms flutter values) is complicated by the indeterminate instantaneous spectral characteristic of the flutter waveform itself. While probably not random in nature, the flutter at any given time instant is almost certainly not entirely periodic either. Depending on the choice of a conversion factor, p–p flutter values would probably represent equivalent rms time/frequency perturbation percentages ranging from about one-fifth to about one-third of the values shown in Table 2. Although any conversion factor that might be chosen would be subject to argument pro and con, a compromise of one-fourth (0.25) will be used for convenience in this discussion. Table 3 provides approximate maximum rms flutter percentages based on a one-fourth conversion ratio.

The rms flutter percentages of Table 3 can also be related to equivalent rms frequency or phase errors in the reproduction of a recorded subcarrier signal. Such equivalent error factors are presented in Table 4.

Table 3. Approximate FR-1400 rms flutter tolerances

Tape speed, in./s	Tape flutter tolerance, % rms
7.5	0.25
15.0	0.125
30.0	0.10
60.0	0.075
120.0	0.0625

Table 4. Maximum rms frequency/phase error in reproduced baseband subcarrier signals

Tape speed, in./s	Tape flutter, % rms	Maximum rms frequency/phase error, Hz	
		20-kHz subcarrier	80-kHz subcarrier
7.5	0.25	50.0	200
15.0	0.125	25.0	100
30.0	0.10	20.0	80
60.0	0.075	15.0	60
120.0	0.0625	12.5	50

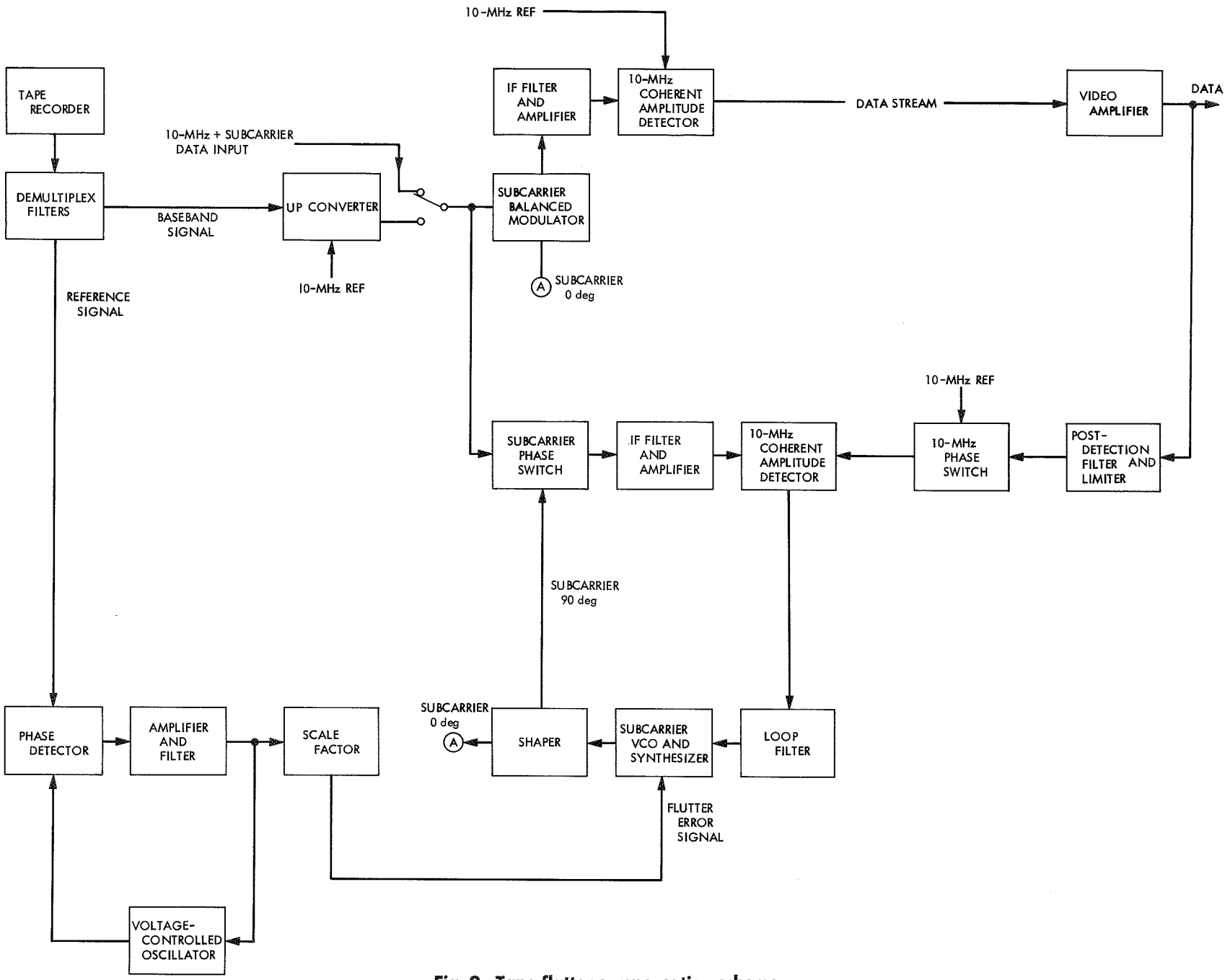

Fig. 9. Tape flutter compensation scheme

It is apparent that unpredictable instantaneous subcarrier frequency perturbations of the magnitudes indicated (Table 4) would seriously degrade the operation of the SDA. At the same time, however, it would be unfair to "blame" the FR-1400 in such a case, inasmuch as it would be operating within its design standards.

f. System flutter performance improvement or compensation. The FR-1400 appears to be operating well within its design standards, but its unassisted baseband-recording performance is not adequate for the operational input requirements of the SDA. Improvement of the system time-base stability by internal modification of the tape-handling mechanism is not practical under these circumstances. Fortunately, however, external tape-speed compensation techniques exist that provide overall performance improvement under just such circumstances.

One applicable technique requires that a high-precision local reference signal be multiplexed with the data signal and both recorded on the *same* tape channel. When reproduced, the reference signal is demultiplexed from the data signal and used to derive a flutter-error compensation signal. Recording the reference on the same channel as the data eliminates inter-channel flutter effects. The circuitry employed for such a compensation scheme would resemble that shown in Fig. 9.

Significant flutter suppression factors may be achieved with this type of technique. It is obvious that such a reduction in system time-base instability will be reflected as an equivalent improvement in SDA performance in the baseband record/reproduce mode.

g. Conclusions. In order to achieve sufficient bandwidth capability, it is necessary that the baseband signal recorder be operated at a tape speed appropriate to the subcarrier frequency (Table 1).

It should be noted that faster tape speeds also exhibit lower tape flutter or time-base instability factors (Table 2). Unfortunately, the FR-1400 exhibits too high a flutter factor at its fastest tape speed for adequate SDA performance, thus indicating a need for external flutter compensation.

Schemes exist that can provide considerable flutter compensation external to the tape recorder. Tests are being conducted to determine whether such compensation schemes can provide a system time base sufficiently stable to permit acceptable SDA operation in the baseband record/reproduce mode.

V. Operations and Facilities

A. DSN Operations

1. Radio-Science Support, *J. R. Hall*

The facilities of the DSN are being made available on a restricted basis for use by the radio-astronomy–radio-science community for experiments which require the unique capability of the 210-ft antenna or the long baseline configurations available in the DSN. An Experiment Selection Committee will select experimenters in much the same manner now used to select spacecraft experimenters. Present schedules allocate 5% of 210-ft antenna time to this activity. Experiments which have been conducted over the past year are listed in Table 1.

B. Facility Engineering

1. 210-ft Antenna Overseas Projects, *P. C. Doster*

a. Introduction. This is the first in a planned series of reports covering the progress of implementation of NASA Projects 9156 and 9157. These projects provide two overseas 210-ft-diam antenna deep space antenna facilities which will complete, along with the existing 210-ft antenna at DSS 14, a three-station network of 210-ft antennas strategically spaced around the earth. The projects represent a continuation of a long-range plan for extending the technical capability of the Deep Space Network in keeping with spacecraft communications requirements. The three-station network will be capable of continuous communication with deep-space vehicles in the declination range 28.5° North to 28.5° South (Fig. 1).

The network is to provide for surveillance of spacecraft during complex planetary reconnoitering and atmospheric probe missions which are evolving from past successful early missions in the vicinity of the moon, Mars, and Venus. The network will also provide for required continuous and reliable positive command control for distant planetary spacecraft.

b. Description of projects. These new facilities will augment the existing DSN facilities located near Canberra, Australia and Madrid, Spain. The projects will provide a fully steerable 210-ft-diam paraboloidal reflector type of antenna, operations facilities, and increased powerplant output to meet the requirements of the advanced system, at each of the two selected sites. All necessary supporting features including utilities, communications, roads, water and fuel storage, site development; safety and security features; and essential electronic equipment associated with the antenna systems are provided.

Figure 2 is a side elevation of the planned configuration of the antenna instrument. The design for the two overseas antenna facilities is identical to the antenna instrument now at DSS 14 with the exception of the foundations, a multi-feedcone configuration, and minor design refinements. The structural/mechanical design

Table 1. DSN radio science support (July 1967–November 1968)

Experiment	Purpose	Experimenter	DSN Facility
Lunar occultation of radio sources (S-band)	To determine intensity and angular size of radio sources	A. Maxwell (Harvard)	DSS 14 DSS 11
Long baseline interferometer (S-band)	To determine angular size of radio sources	D. S. Robertson (Weapons Research Establishment, Adelaide, Australia) A. T. Moffet (Caltech)	DSS 14 DSS 12 DSS 41
Radio source scintillation as a result of passage through the solar corona (S-band)	To determine angular size of radio sources	R. Eckers (Caltech)	DSS 14 DSS 11
Jupiter occultation of radio sources (S-band)	To investigate structure of Jupiter magnetosphere	B. Gary (JPL) Nicholson (South African Central Scientific Institute for Research)	DSS 51
Pulsar measurements (S-band)	To determine structure, spectrum, pulse rate stability, etc., of pulsars	A. T. Moffet (Caltech)	DSS 14
Radiometric observation of Venus (22–24 GHz)	To determine absorptive and emissive properties of Venus in the 22 to 24 GHz region	D. Jones and B. Gary (JPL)	30-ft antenna at DSS 13

was developed over a long period of time, using data developed during the design, fabrication, construction, test and operation phases of the 210-ft antenna facility at DSS 14.

c. Progress. Preliminary engineering has been completed. Site surveys and foundation studies have been made at Tidbinbilla, Australia (SPS 37-48, Vol. II, p. 173) and Robledo de Chavela, Spain (SPS 37-50, Vol. II, p. 191).

On-site construction of the antenna instrument at the DSS 42 location is presently scheduled to begin in December 1969. Work at the second site will follow shortly thereafter. Both overseas antenna facilities are scheduled to be operational in 1973.

2. DSS 14 4-ft Time Sync Antenna Installation,

M. Kron and V. B. Lobb

During the early part of October 1968 a survey was made to determine a new location on the roof of the newly constructed control building at DSS 14 for the time sync system previously located atop the control building at DSS 11.

A visual inspection of the physical conditions of the roof revealed that the southeast corner of the building was the best site for the antenna location, and that the reinforced parapet surrounding the roof was the best support for the antenna's frame foundation.

The selection of the southeastern corner of the roof provided an unobstructed view looking south, whereas the northeastern or northwestern corners would have some blockage due to the heat exchangers on the south central section of the roof. The electrical cable lengths were within permissible lengths, and it was unnecessary to perform a horizon mask to determine the extent of blockage at the other sites.

The roof surface was not flat but arched, with drains located in the corners and directly beneath the antenna. Consequently, the design approach chosen was to mount two channels along the sides of the parapet at right angles to each other. "Red head" anchors were drilled and driven into the wall. The frame structure shown in Fig. 3 was constructed on site by tying a 10-in. beam diagonal member across the corner, closing the triangular frame. Four-inch channels provide future support for decking around the antenna. Six-inch channel sections forming the foundation for the pedestal are tied into the diagonal beam, and the beams are mounted to the parapet wall.

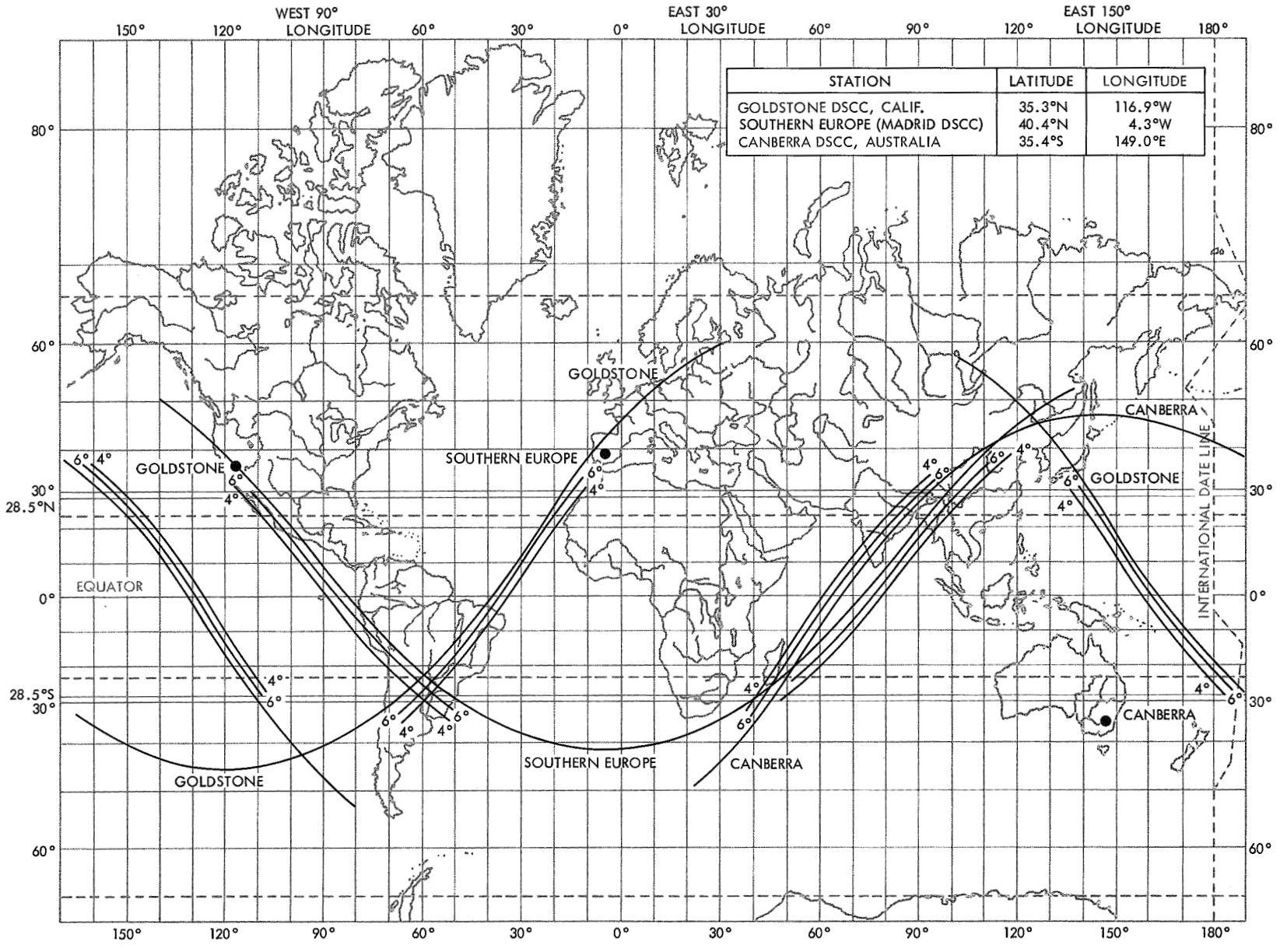

Fig. 1. Deep space antenna (210 ft) facility network coverage plot

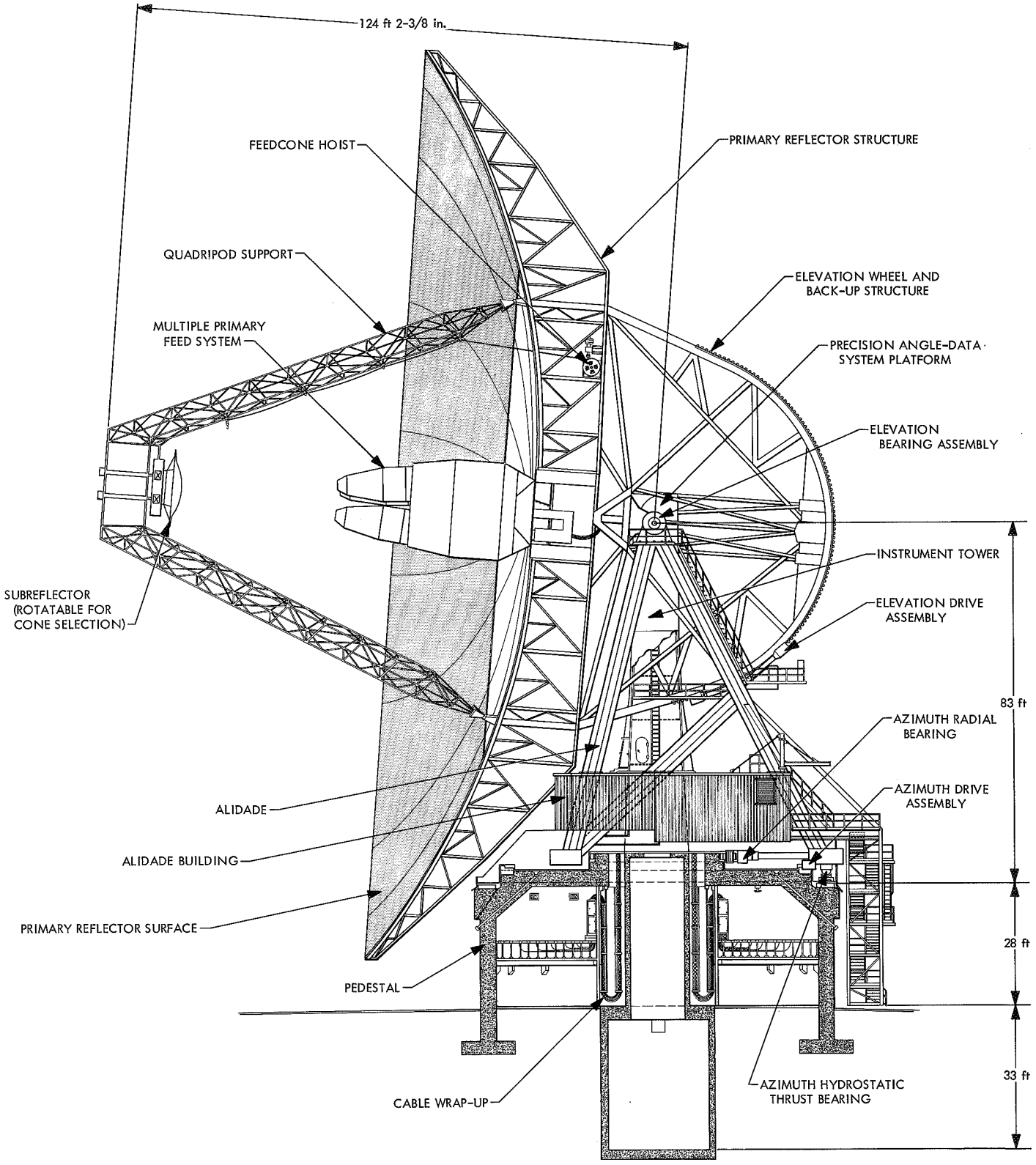

Fig. 2. Antenna instrument side elevations

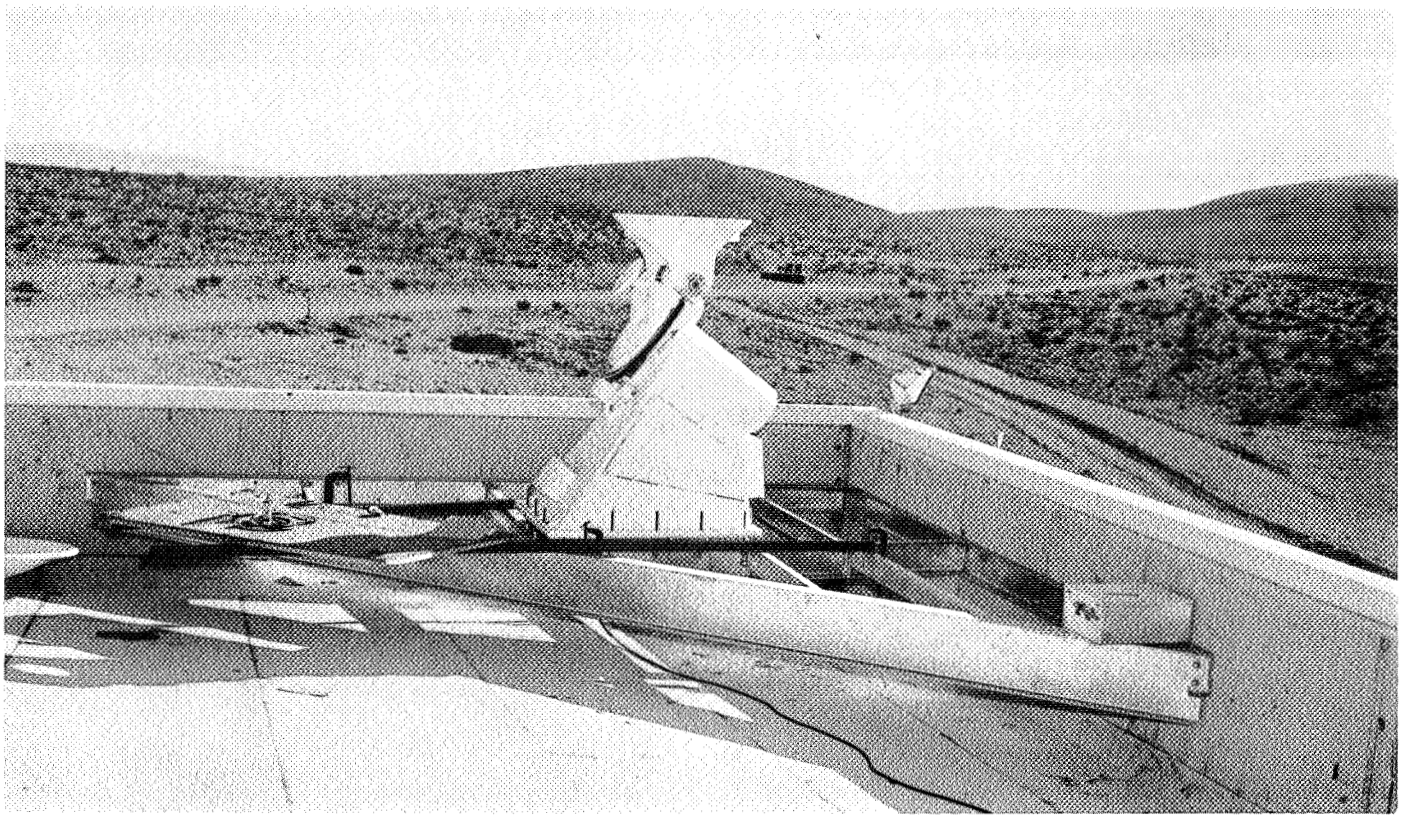

Fig. 3. Time sync antenna mounted on parapet of DSS 14 control building